Author:
Minera Rebulla, Sergio A

Title:
Analysis and Design of Buckling Resistant Thin-Walled Structures via Computationally Efficient 3D Stress Analysis

Analysis and Design of Buckling Resistant Thin-Walled Structures via Computationally Efficient 3D Stress Analysis

By

SERGIO ALEJANDRO MINERA REBULLA

Department of Aerospace Engineering
UNIVERSITY OF BRISTOL

A dissertation submitted to the University of Bristol in accordance with the requirements of the degree of DOCTOR OF PHILOSOPHY in the Faculty of Engineering.

AUGUST 2019

Word count: Fifty nine thousand

To Mary

Abstract

Performing detailed structural analysis of beam-like or thin-walled structures can be a complex task, especially if three dimensional stress profiles are required. Depending on the nature of the problem, i.e. geometry, dimensions, loading and boundary conditions, it may be possible to use simplified (numerical or analytical) beam or shell models. Nevertheless, their accuracy is limited to certain regions and far from singularities. Due to this limitation, three-dimensional finite element methods (FEM) are commonly employed. FEM is a robust methodology, but it may come with a high computational cost. Therefore, when analysing complex structures, it is common practice to split the problem in parts. A coarse mesh and/or a simplified model is used to describe the overall and global behaviour of the structure. After identifying regions (or scales) where more detail is needed, a more refined model is employed. This sub-modelling process can be cumbersome and time consuming. In this work, a new framework for solving this duality is proposed. A model, based on the Serendipity Lagrange (SL) polynomial space, extends the capabilities of the Unified Formulation (UF) model to perform non-linear and large-deflection analyses of non-prismatic and curved beam-like structures. Special attention is given to the modelling of buckling and post-buckling of beams and thin-walled structures. The capability in recovering localised displacement and stress fields, numerical stability and efficiency of the proposed model (UF-SL) are presented, discussed and compared with reference models.

In addition, two new and novel methodologies for the design of buckling-resistant structures are presented. The first, the Localised Nominal Stiffness Method (LNS), exploits the accuracy and efficiency of the UF-SL model to identify and map regions of potential insensitivity to localised low stiffness variations. The result is then used to tailor the structure and improve its buckling and post-buckling performance. The second approach, Eigenstress Method, uses the resultant stress, recovered from the first eigenvector of a linear buckling analysis, as baseline for a new topology. The resulting geometry closely resembles that of the structure that optimises the buckling load, with a given structural weight. This method provides a method that is fast and intuitive for designing buckling-resistant structures.

Acknowledgements

Since my early years I have been amazed by airplanes and the marvel of flying. Having the opportunity of undertaking a Ph.D. in Aerospace Engineering is a dream came true. This would not be possible without the help and support of many. Therefore, I want to give my thankful thoughts and acknowledgements to those who made this a reality.

First of all I would like to thank God, for putting in my way those people and situations that made me who I am today. Secondly, to my wife and best friend Andrea, who has left everything without hesitation to support me. To Luis Pedro, for giving me the last push I needed to finish this journey. To my parents, for their endless love and support.

I would like to express my gratitude to both my great supervisors, for whom I feel very fortunate of having as mentors. To Prof. Paul Weaver, for his incredible patience, time and guidance. For his invaluable advice and willingness to share his knowledge to others. To Dr. Alberto Pirrera, for his support, technical advice and constant follow up. And for always being a carrier of *good-news*. Thanks to you both for giving me the opportunity of being part of a great research team.

To Prof. Erasmo Carrera and his research team, for being always open to help and for hosting me during the secondment at Politechnico di Torino. To Prof. Chiara Bisagni, for giving me the opportunity of doing a research placement at the Faculty of Aerospace Engineering at Delft University. Especial thanks to Dr. Tomas Vronsky, from Vestas Company, for receiving me for the industrial secondment.

To Dr. Rainer Groh, for his time, advice and shared knowledge. To my colleagues and friends Mayank Patni, Aewis Hii and Sander van den Broek, for the endless and rich technical discussions we had during these three years.

This research has been developed in the framework of the FULLCOMP project. The H2020 Marie Skłodowska-Curie European Training Network is gratefully acknowledged.

Bristol, August 9, 2019

Sergio Minera

AUTHOR'S DECLARATION

I declare that the work in this dissertation was carried out in accordance with the requirements of the University's Regulations and Code of Practice for Research Degree Programmes and that it has not been submitted for any other academic award. Except where indicated by specific reference in the text, the work is the candidate's own work. Work done in collaboration with, or with the assistance of, others, is indicated as such. Any views expressed in the dissertation are those of the author.

SIGNED: ..... DATE: .....

Journal Articles

1. S. Minera, M. Patni, E. Carrera, M. Petrolo, P. Weaver, A. Pirrera, Three-dimensional stress analysis for beam-like structures using Serendipity Lagrange shape functions, International Journal of Solids and Structures, 141 (2018) 279-296.

2. M. Patni, S. Minera, R. Groh, A. Pirrera, P. Weaver, Three-dimensional stress analysis for laminated composite and sandwich structures, Composites Part B: Engineering 155 (2018) 299–328.

3. M. Patni, S. Minera, R. Groh, A. Pirrera, P. Weaver, Efficient 3D Stress Capture of Variable-Stiffness and Sandwich Beam Structures, AIAA Scitech 2019 Forum, p. 1763. 2019.

4. M. Patni, S. Minera, C. Bisagni, A. Pirrera, P.M. Weaver, Geometrically nonlinear finite element model for predicting failure in composite structures, Composite Structures, p.111068.

5. M. Patni, S. Minera, R. Groh, A. Pirrera, P.M. Weaver, On the accuracy of localised 3D stress fields in tow-steered laminated composite structures, Composite Structures, 111034.

6. S. van den Broek, S. Minera, A. Pirrera, P. Weaver, E. Jansen, R. Rolfes, Enhanced deterministic derformance of panels using stochastic variations of geometric and material parameters, Submitted to: AIAA.

7. A.K.W. Hii, S. Minera, R.M.J. Groh, A. Pirrera, L.F. Kawashita, A computationally efficient Variable Kinematics Continuum Shell element for 3D stress field analysis of laminated structures, Submitted to: Composite Structures.

8. S. Minera, M. Patni, A. Pirrera, P. Weaver, Design of topologically efficient buckling-resistant structures using the Eigenstress Method, To be submitted to: Thin-Walled Structures.

9. S Minera, M. Patni, A. Pirrera, P. Weaver, Buckling-resistant topological design using sensitivities to variations in localised nominal stiffness, To be submitted to: Thin-Walled Structures.

Conference Papers

1. S. Minera, M. Patni, P.M. Weaver, A. Pirrera, Continuum mechanics of beam-like structures using one-dimensional finite elements based on Serendipity Lagrange cross-sectional discretisations, In: 3rd International Conference of Mechanics of Composites, 4-7 JUL 2017, Bologna, Italy.

2. S. Minera, M. Patni, E. Carrera, P. Weaver, A. Pirrera, Linearised buckling analysis of thin-walled structures using detailed three-dimensional stress fields, In: 20th International Conference of Composite Structures, 4-7 JUL 2017, Paris, France.

3. S. Minera, M. Patni, P.M. Weaver, A. Pirrera, A non-iterative method for designing topologically efficient buckling-resistant structures, In: First International Conference of Mechanics of Advanced Materials and Structures, 17-20 JUL 2018, Turin, Italy.

4. S. Minera, M. Patni, P.M. Weaver, A. Pirrera, M. O'Donnell, Comparing the effect of geometry and stiffness on the effective load paths in non-symmetric laminates, In: AIAA Scitech 2019 Forum, C.A., U.S.

Book Chapter

1. S. van den Broek, S. Minera, F. Jansen, A. Pirrera, P.M. Weaver, R. Rolfes, Improving the Static Structural Performance of Panels with Spatially Varying Material Properties Using Correlations, In: Chapter 9, Advances in Predictive Models and Methodologies for Numerically Efficient Linear and Nonlinear Analysis of Composites, Springer, 2019.

TABLE OF CONTENTS

List of Tables

List of Figures

Figure **Page**

NOMENCLATURE

Roman Symbols

$\boldsymbol{u}$, $\boldsymbol{U}$, u, v, w	Displacement vector; Displacement components in $x-$, $y-$ and z-directions, respectively
E, G, E_{ij}, G_{ij}	Young's modulus and Shear modulus; Normal and shear stiffness in ij direction
D, I, A	Flexural rigidity; Second moment of area; Cross-section area
$\mathscr{B}$, $\mathbf{D}$	Green-Lagrange differential operator and its variation
$\mathbf{C}$	Constitutive material matrix
N_i,N	Finite element shape function; Unified Formulation beam shape function
F,G	Unified Formulation cross-section shape function; Product of shape functions FN
N^{2D}, N^{3D}	2D and 3D Lagrange shape functions, respectively
W	Work
V , M	Volume and mass
$\boldsymbol{K}$, $\boldsymbol{K}_{ij}$	Stiffness matrix; components of stiffness matrix
$\boldsymbol{\kappa}^{ij\tau s}_{\text{(T)}}$, $\boldsymbol{\kappa}^{ij\tau s}_{\text{(O)}}$, $\boldsymbol{\kappa}^{ij\tau s}_{\text{(G)}}$	Components of the tangent, secant and geometrical stiffness Unified Formulation nuclei
$\boldsymbol{f}$, P	Force vector; Applied force
a, b, t, L	Length of cross-section/plate; width of cross-section/plate; thickness; Length of beam
R, h	Radius and thickness of cylinder, respectively
m, n	Number of half waves
p, L	Serendipity Lagrange 1D and 2D polynomials, respectively
$\mathscr{J}$, J	Jacobian matrix and its determinant
$Q(n)$	Complexity in terms of the size of the input
x_i, y_i, z_i	Metric components ($i,j = 1,2,3$)
$\boldsymbol{E}$, $\boldsymbol{S}$	Green-Lagrange strain tensor and Second Piola stress tensor
c, p	Unit cell radius and length
OF	Optimality Factor

Greek Symbols

$\boldsymbol{\varepsilon}$, ε_{ij}. γ_{ij}	Strain vector; Normal and shear strain components in the ij direction, respectively
ϕ_x, ϕ_z	Rotation angles in the $z-$ and x-directions, respectively
$\boldsymbol{\sigma}$, σ_{ij}, τ_{ij}	Stress vector; Normal and shear stress components in the ij direction

ν, ν_{ij}	Poisson's ratio in the ij direction
δ	Variation respect of displacements. Relative shortening.
ξ, η, α, β	Natural coordinates
λ	Eigenvalue, buckling loads
α	Initial post-buckling scale factor
κ	Curvature parameter
$\hat{\sigma}_{\text{VM}}$	von Mises normalised eigenstress

Superscripts

$\hat{}$	Normalised quantity
i, j	Indexes related to the beam shape function
τ, s	Indexes related to the cross-section shape function
2D, 3D	Quantity in two or three-dimensions
(e)	Quantity at element level

Subscripts

k	k^{th} element
i, j	Indexes related to the beam shape function
τ, s	Indexes related to the cross-section shape function
(e)	Quantity at element level
int, ext	Internal or external work quantity
VM	Quantity related to von Mises eigenstress
o	initial or original quantity
cr	Critical value quantity

Acronyms

FE	Finite Element
FEM	Finite Element Method
UF	Unified Formulation
CUF	Carrera Unified Formulation
SL	Serendipity Lagrange
LNS	Localised nominal stiffness method
EB	Euler Bernoulli Theory
TB	Timoshenko Beam Theory

CHAPTER 1

INTRODUCTION

Modelling and simulation of structural members have become an essential part in the research and development of complex structures, especially in aerospace engineering. Predicting the mechanical response of thin-walled or beam-like structures accurately can be a complicated task, particularly if detailed and localised stress profiles are required. For simple cases, subject to very specific loading and boundary conditions, analytical models can be used, but in general, advanced non-linear finite element methods (FEM) have to be employed. These models are robust, but in many cases they come with a high computational cost in terms of degrees of freedom and time. This can result in a potential, and undesirable, bottleneck in the design process. Developing mathematical models and algorithms that are efficient, with high-fidelity and accurate, is still an open research topic.

The most common approach for performing detailed structural analysis of complex structures is to split the problem in parts. A global analysis with a coarse mesh and/or a simplified model[1] is used for describing the overall and general behaviour of the structure subject to some loading and boundary conditions. After identifying regions (or scales) where more detail is needed, a more refined model is employed[2]. One of the motivations of this thesis is to solve this duality. Developing a model that is suitable for both, global and local analyses, without the need of sub-modelling.

1.1 Fullcomp Project

Composite materials are widely exploited in aerospace applications. Take for example the Airbus A350 or Boeing 787 Dreamliner, whose structures are made approximately of 55% of composite

[1] Depending on the application this can be an analytical model, beam, or shell FEM model,.

[2] This can be a FEM model with a refined mesh, or an *ad hoc* analytical, or semi-analytical model.

materials by weight. Designing structures with composite materials opens a new realm of complexity, since their mechanics are completely different to that of, for example, metallic structures. The analysis schemes for metals are often inadequate for modelling composite materials.

The *FULLy integrated analysis, design, manufacturing and health-monitoring of COMPosite structures* (FULLCOMP) project aimed at of creating a multidisciplinary, inter-sectoral and international research training network. Twelve researchers have worked closely with academic and industrial partners to develop a framework of integrated analysis tools to improve the design and production of composites. The project includes the full spectrum in the development of composites: manufacturing, health-monitoring, failure, modelling, multiscale approaches, testing, prognosis, and prognostic.

The project was funded by the European Commission under the H2020 Marie Skłodowska-Curie European Training Network grant for the European Training Networks (ETN).

1.2 Aim and Motivation

My role within FULLCOMP was to extend the capabilities of one of the main tools used for the analysis: the Unified Formulation, developed by Carrera and co-workers [11]. Particularly, to study the buckling phenomena of beam-like and thin-walled structures and to develop new methodologies for the analysis and design of buckling-resistant structures. The following points summarise the aims of this work:

1. To develop a high-fidelity, numerically stable, and efficient model, within the framework of the Unified Formulation. The model must have hierarchical properties as well as local expansion control, and have the capability of capturing localised displacement and stress fields.

2. To develop an efficient Unified Formulation Linearised Buckling Model for analysing thin-walled structures, capable of capturing localised displacement and stress fields at buckling and initial post-buckling.

3. To extend the capabilities of the existing Unified Formulation framework to perform non-linear and large displacement analyses of non-prismatic, 3D-like, beam structures.

4. To develop a methodology for analysing the effect of localised low stiffness regions in the buckling and post-buckling behaviour of thin structures.

5. To develop a new and non iterative methodology for designing topologically efficient buckling resistant structures.

1.3 Chapters Outline

Chapter 2. Literature Review. This chapter provides a short historical review of the two main topics treated in the manuscript: beam models and buckling. Traditional beam models (Euler and Timoshenko models) and hierarchical models are explained in more detail. Buckling equations for some analytical cases are also provided.

Chapter 3. Serendipity Lagrange Expansion Model. This chapter presents the expansion model based on the Serendipity Lagrange polynomial space. The model is developed within the framework of the Unified Formulation. Its hierarchical capability, local expansion control, numerical stability and efficiency are explained.

The contents of this chapter are based on the paper: *Three-dimensional stress analysis for beam-like structures using Serendipity Lagrange shape functions* [12]. Approximately $60\% - 70\%$ of its contents have been re-used to write the chapter.

Chapter 4. Unified Formulation Linearised Buckling Model. This chapter presents a linearised buckling model based on the Unified Formulation and the Serendipity Lagrange expansion model. The derivation of the model, its capabilities of recovering localised through thickness stresses and efficiency are discussed in detail.

The contents of this chapter are partly based on the paper: *Buckling-resistant topological design using sensitivities to variations in localised nominal stiffness* [13]. Approximately $20\% - 30\%$ of its contents have been re-used to write the chapter.

Chapter 5. Unified Formulation 3D-Beam model. This chapter provides an extension of the Unified Formulation, and all its known capabilities, to non-linear and large deflections analysis of non-prismatic and curved 3D-like beam structures. Mathematical derivations and illustrative examples are discussed in detail.

Chapter 6. Local Nominal Stiffness Method. This chapter presents a new methodology for identifying and mapping regions in thin-walled structures that may be less sensitive to localised nominal stiffness variations. It is shown how these regions can be used as a baseline for reducing the weight of the structure, keeping its buckling and post-buckling integrity relatively unaltered.

The contents of this chapter are partly based on the paper: *Buckling-resistant topological design using sensitivities to variations in localised nominal stiffness* [13]. Approximately $70\% - 80\%$ of its contents have been re-used to write the chapter.

Chapter 7. Eigenstress Method. This chapter presents a new and novel methodology for designing topologically-efficient buckling resistant structures. The method is based on the resultant stress recovered from the first eigenvector of a linear buckling analysis. It is shown how the

method provides a topology that resembles the optimum case, and can be used for reducing the weight of the structure keeping its buckling capacity or, alternatively, to increase the buckling performance keeping the weight constant.

The contents of this chapter are based on the paper: *Design of topologically efficient buckling-resistant structures using eigenstresses* [14], 100% of its contents have been re-used to write the chapter.

Chapter 8. Concluding Remarks. Conclusions of the work are summarised in this chapter.

Complementary information and details of some mathematical derivations are included as appendices.

CHAPTER 2

LITERATURE REVIEW

"Mechanics is the paradise of mathematical science because here we come to the fruits of mathematics"

- Leonardo Da Vinci

Beam models are commonly used by scientists and engineers for performing structural analysis of slender structures, because of their simplicity and acceptable levels of accuracy. Depending on the assumptions of each particular theory, the accuracy of the predicted displacement and stress fields is often limited to regions far from edges or singularities (e.g. corners or points of load application). Moreover, classical theories, like Euler-Bernoulli or Timoshenko Beam Theory, do not take into account complex cross-sectional behaviours, like warping or torsion. High-order theories are needed to describe these effects. Another limitation of classical beam theories is the correct prediction of another important mechanical phenomena: buckling. Only the overall and global buckling behaviour is captured accurately.

The aim of this chapter is to provide the reader with a general picture on these two topics. A brief historical overview is given, followed by a description of classic, high-order and unified beam formulations. Some classical results on buckling are provided as well.

2.1 Brief Historical Overview

The two core topics of this manuscript are three-dimensional refined beam models and buckling. A brief historical overview is presented for both.

(a) Leornado Da Vinci.

(b) Da Vinci's discussion of the deformation of a beam.

Figure 2.1: Da Vinci and part of a manuscript on beam bending. Figures taken from [1, 2]

2.1.1 Beam Models

For centuries scientists, engineers and architects have had the need of describing as accurately as possible the mechanical behaviour of structures. Beam-like slender structural members have been an important, and ever-present, element in structural engineering. The correct mathematical description of these is, and has been, of paramount importance. One of the first attempts to understand the mechanics of beams was made by Leonardo Da Vinci (1452-1519), Figure 2.1(a). He was greatly interested in mechanics as he stated on one of his notes: *"Mechanics is the paradise of mathematical science because here we come to the fruits of mathematics"* [1]. He studied several mechanical problems, particularly the bending of a square cross-section beam supported on its mid section. The manuscript, shown in Figure 2.1(b), describes how the structure is bent, and how the convex part becomes shorter and its concave part, linger [2]. In this regard, he stated a general principle as follows: *"In every article that is supported, but is free to bend, and is of uniform cross section and material, the part that is farthest from the supports will bend the most"* [1]. Inspired by Da Vinci's work, Galileo Galilei (1564-1642) became interested in the mechanics of beams as well. He published some of his findings in his famous treatise *Discorsi e Dimostrazioni Matematiche, intorno a due nuove Scienze*, Figure 2.2(a), where he discussed the resistance to fracture of a cantilever beam with a load at the end, Figure 2.2(b).

With the invention and development of the new mathematical field of Calculus, mainly by Newton (1643-1727) and Leibniz (1646-1716), a new era on the mathematical modelling of beams started. Jacob Bernoulli (1654-1705), trying to expand Leibniz's work in mechanics, studied the *Elastica* problem, paying more attention to the deformation of the beam rather than on the strength of the materials, as done by his contemporaries (e.g. Hooke and Mariotte). He gave an expression for the deflection of a cantilever beam, however, due to an erroneous


DISCORSI
E
DIMOSTRAZIONI
MATEMATICHE,
intorno à due nuoue ſcienze
Attenenti alla
MECANICA & i MOVIMENTI LOCALI;
del Signor
GALILEO GALILEI LINCEO,
Filoſofo e Matematico primario del Sereniſſimo
Grand Duca di Toſcana.
Con vna Appendice del centro di grauità d'alcuni Solidi.
IN LEIDA,
Appreſſo gli Elſevirii. M. D. C. XXXVIII.

(a) Galileo's Treatise

(b) Galileo's cantilever beam

Figure 2.2: Galileo's manuscript and bending test. Figures taken from [1].

assumption regarding the axis of rotation this was wrong [1]. Nevertheless, stating that the curvature of the deflection curve at each point is proportional to the bending moment at that point, was correct and it was later used by others (particularly Euler) in similar studies of elastic curves [15]. Some years later, Daniel Bernoulli, son of John Bernoulli (Jacob's brother), suggested to Euler (1707-1783) the use of calculus of variations (and together with Jacob's theory) to investigate the *Elastica*. For solving the problem using the variational method (called *"The method of final causes"*) Euler needed an expression for the strain energy, and at this point he used the information given by Daniel; Euler states *"The most illustrious and, in this sublime fashion of studying nature, most perspicacious man, Daniel Bernoulli, had pointed out to me that he could express in a single formula, which he calls the potential force, the whole force which inheres in a curved elastic strip, and that this expression must be a minimum in the elastic curve"* [1]. The principal results of Euler's work in this direction were published in his book *Methodus Inveniendi Lineas Curvas* [16], Figure 2.3. The resulting mathematical formulation is now known as *Euler-Bernoulli Beam Theory* (EB). It is described in more detail in further sections. During the following decades many other pioneers (such as Lagrange, Navier, Barre de Saint-Venant, to mention only a few) contributed to the development of this early, but successful theory. Due to its simplicity and assumptions, the theory has some limitations: it decouples bending and torsion as well as having difficulties evaluating normal and shear components for stress. Its validity is limited by Saint-Venant's Principle, i.e. to regions remote from boundary constraints, discontinuities and points of load application. Many refinements of the original EB

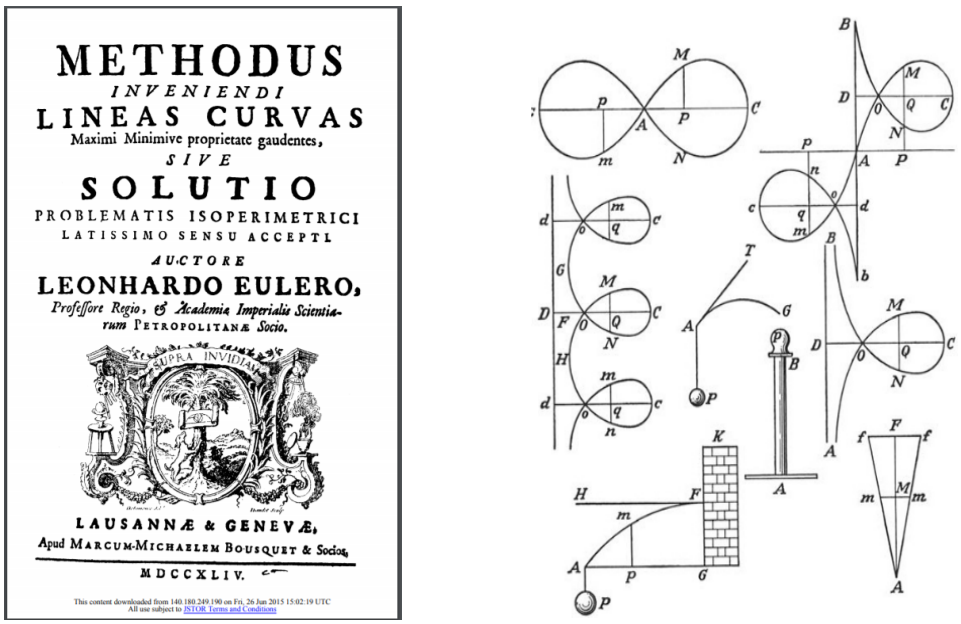

(a) Euler's Treatise

(b) Deflection curves studied by Euler

Figure 2.3: Euler's book and the *Elastica* problem. Figures taken from [1].

theory have been proposed. Among these the one attributed to Timoshenko (1878-1972), in which transverse shear deformations are included in the theory, allows a more accurate description of the mechanics of a beam. *Timoshenko Beam Theory* (TB) is discussed in more detail in subsequent sections. A comprehensive comparison of these two theories can be found in [17].

These theories assume that the effect of through-thickness deformations on overall behaviour are negligible and that axial displacements vary linearly through-thickness. Timoshenko's beam model enhances Euler-Bernoulli's model by considering the effects of shear deformations. Still, only a uniform cross-sectional shear distribution can be obtained. To account for shear-free boundary conditions along the beam's longitudinal surface, correction factors are commonly employed in a TB setting [18–20].

To account for effects that are not captured by classical axiomatic theories, several refined finite element (FE) models have been developed in recent decades. However, geometric complexities and accurate approximations of the displacement field can lead to computationally expensive models, where a large number of unknown variables is required. These new techniques made it possible to implement and exploit refined high-order theories [21–24] of both, displacement based and mix formulations [25].

More recently, Giavotto et al. [26] developed a method for analysing anisotropic beams, where the cross-section and beam axis are described separately and combined using a set of coupled linear equations. Some years later, an approach developed by Ladevèze and co-workers [27] reduces a three-dimensional (3D) model to a beam-like structure thereby simplifying the 3D

elasticity equations. Using this method a beam model can be constructed as the sum of a Saint-Venant part and a residual, higher-order part. In a following work, Ladevèze [28] used linear shape functions on beams with general cross-section and developed an exact beam theory for calculating 3D displacements and stresses. However, the theory only works if one neglects localised effects that occur at extremities and geometric discontinuities. Surana [29] developed a two-dimensional (2D) curved beam element using Lagrange interpolating polynomials along the cross-section to describe transverse shear stress distributions in composite structures. Although accurate, the computational cost of Surana's model grows rapidly as the number of composite layers increases. Kameswara [30] used Taylor series to include displacement components along the cross-section and proposed an analytical solution based on a mixed formulation, whereby, to ensure continuity, transverse stresses are invoked as degrees of freedom (DOFs). Kameswara's model has been employed for static and dynamic analyses of laminated plates and beams.

Another powerful tool to develop structural models is the asymptotic method. In the beam model scenario, the works by Berdichevsky and co-workers [31, 32] are among the earliest contributions that exploited the Variational Asymptotic Method (VAM). More recently, Yu et al. [33, 34] have developed the so called variational asymptotic beam sectional analysis (VABS) which uses VAM to split the 3D elastic problem into a 2D linear problem in the cross-section and a 1D beam problem in longitudinal direction.

Classical approaches have also been enhanced by the Generalized Beam Theory (GBT) for thin-walled structures, as given by Silvestre and Camotim [35], where transverse cross-sectional displacements are obtained from the axial ones. In GBT, in order to obtain a displacement representation compatible with classical beam theories, each component of displacement is expressed as a product of two single-variable functions—one depending on the longitudinal position along the reference axis and the other on cross-sectional coordinates. However, since thin plate assumptions are adopted [35], through-thickness strains are set to be zero and full 3D stress fields cannot be captured. Following on from early implementations of the GBT, many other high-order theories, based on enriched cross-section displacement fields, have been developed in order to describe effects that classical models cannot capture. A complete account of the literature, however, goes beyond the scope of this work. The keen reader is referred to [36] for further details.

Of relevance to the present work, is one of the most recent contributions to the development of refined beam theories and that is the Unified Formulation by Carrera and co-workers [37]. The formulation provides one-dimensional (beam) [38] and two-dimensional (plate and shell) [39] models that extend the classical approximations by exploiting a compact, hierarchical notation that allows most classic and recent formulations to be retrieved from one, hence *unified*, model. The displacement field is expressed over the cross-section (beam case) and through the thickness (plate and shell cases) by employing various expansion functions including Taylor polynomials [38], Lagrange polynomials [37], exponential and trigonometric functions [40], Chebyshev [41] and Legendre polynomials [42]. Amongst these, Taylor (TE) and Lagrange expansion (LE) models

are most widely adopted. TE models are hierarchical and the degree of accuracy with which kinematic variables are captured is enriched by increasing the order of the cross-sectional expansion. On the other hand, LE models are based on cross-sectional discretisations using Lagrange elements of given kinematic order and refinement is obtained by increasing the mesh density, i.e. by increasing the number of Lagrange elements in the cross-section. Both models are explained in detail if further sections.

2.1.1.1 Mix Variation Formulations

In a displacement-based method, the equations are written in terms of the displacement field by eliminating some of the stresses by means of kinematic and constitutive relations [3]. Conversely, in a stress-based method, the governing equations are expressed in terms of stresses by taking the constitutive equation in terms of compliance matrix and substituting it in the kinematic equation. In a mixed formulation, originally developed by Reissner [25, 43], the displacement and stress fields are solved simultaneously. Solving the resultant linear system is difficult, therefore, the governing equations are solved using a variational principle, such as the Principle of Virtual Displacements (PVD). Using this principle, some of the governing field equations are solved exactly, whereas other equations produce a residual. In a finite element context, using the PVD gives accurate solutions for displacements, but stresses are less reliable. This is due to the fact that the equilibrium and natural boundary conditions are only satisfied globally in an average sense. The accuracy of the solution is then improved by refining the kinematics. In contrast, when the stress-based method is employed, i.e. the stress computations are exact, then the displacement fields obtained lacks accuracy. The mixed stress/displacement-based fromulation overcomes these limitations and is widely adopted in the solid mechanics research community, particularly in the context of the Unified Formulation [44, 45].

2.1.2 Buckling and Stability

The first mathematical study on buckling is attributed to Euler, who used Bernoulli's Calculus of Variations to describe the stability (and the buckling load) of an elastic beam under compression. His work on this topic was published in the appendix of this manuscript *Methodus Inveniendi Lineas Curvas* [16], Figure 2.3. Some years later, Lagrange (1736-1813) developed the energy approach, which is a more general formulation compared to Newton's vector approach, to study the mechanics of bodies. This led to the energy theorem, which states that minimum total potential energy is sufficient for elastic stability.

Buckling is related to a mathematical instability, in particular a limit point or singularity, in the equilibrium path. Henry Poincaré (1854-1912) is the founder of bifurcation theory, and one of the first to classify singularities. Approximately at the same time, Aleksandr Liapunov (1857-1918) developed the basic definitions of stability and created the generalised energy functions that we now call the Liapunov Functions, which are used to study stability [46]. The topological

concept of stability was introduced by A. Andronov and Lev Pontryagin (1908-1988). A well known treatise on classification theory can be found in a work by R. Thom [47].

T. von Kármán (1881-1963) studied the inelastic buckling of beams, cylindrical shells under compression [48], spherical shells under pressure [49] and the influence of curvature on buckling [50]. Warner T. Koiter (1914-1997) introduced the classical non-linear bifurcation theory for studying post-buckling of structures, his worked was published in his doctoral dissertation at the Univeristy of Delft: *Over de stabiliteit van het elastisch evenwicht* [51, 52]. An account on non-linear branching of elastic structures under conservative force fields was given by Budiansky [53].

Some recent contributions to important areas are [4]: G.R. Kirchhoff on buckling of the elastica; Timoshenko [54], H. Wagner [55] and N.S. Trahair [56] on flexural-torsional buckling of beams; B. Chandler [57] and R. von Mises on buckling of frames; Timoshenko [54], T. von Kármán [48] and A. Kromm [58] on buckling and post-buckling of plates; H. Donnell [59], K. M. Marguerre and K. M. Mushtari on post-buckling of shells; M. Hyer and H. H. Lee [60]„ P.M. Weaver [61] on buckling and post-buckling of composite plates and shells; B. S. Cox, A. Pirrera and R. Groh [62] on post-buckling branching. The keen reader is referred to [4, 18, 63] for more and complete references.

2.2 Structural Beam Models

A beam is a structure whose axial length is much larger than its other two dimensions (length to thickness, or height, ratio $\sim L/t > 10$). In this section a brief summary and explanation of the most common and widely used beam theories is presented. The Euler Bernoulli Beam Theory (EB), Timoshenko Theory (TB), High-Order Theories and the Unified Formulation (UF) are explained. The main assumptions, equations, scope and limitations are discussed.

2.2.1 Euler-Bernoulli Beam Theory

Starting from *a priori* hypotheses for the kinematics of a beam under bending, the displacement, strain, stress field, and resulting forces are derived. A coordinate system where the beam axis of length L is coincident with the y axis, and the cross-section with the xz-plane is used. This coordinate system is adopted through out the whole manuscript, unless stated otherwise.

In EB the following assumptions are made [64], refer to Figure 2.4:

1. The cross-section is rigid[1] in its plane
2. The cross-section rotates around a neutral axis remaining plane
3. The cross-section remains perpendicular to the neutral axis

[1]The cross-section is, effectively, not rigid, since it can change its size. The theory allows for deformations of size such as a consequence of the Poisson effect. This is a common term used in the literature and therefore included here.

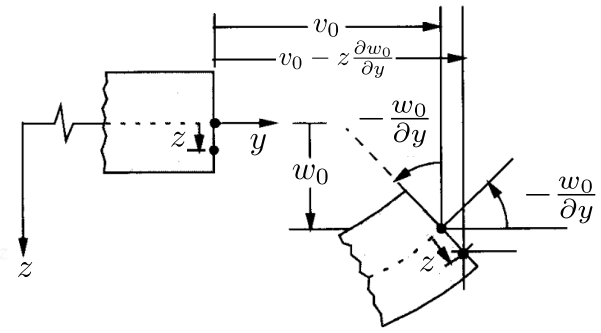

Figure 2.4: Bending of an Euler-Bernoulli Beam. Figure adapted from [3].

According to the first assumption, the in-plane deformations are not taken into account. Therefore, the displacements in the x and z directions, u and w, respectively, depend only on the axial coordinate:

$$\begin{aligned} u &= u_0(y) \\ w &= w_0(y), \end{aligned} \tag{2.1}$$

and the normal strains in-plane are zero:

$$\begin{aligned} \gamma_{xx} &= \frac{\partial u}{\partial x} = 0 \\ \gamma_{zz} &= \frac{\partial w}{\partial z} = 0 \\ \gamma_{xz} &= \frac{\partial u}{\partial z} + \frac{\partial w}{\partial x} = 0. \end{aligned} \tag{2.2}$$

The second assumption is equivalent to approximating the axial displacement v as being a linear function of the cross-section coordinates:

$$v = v_0(y) + \phi_z(y)x + \phi_x(y)z, \tag{2.3}$$

where the functions ϕ_z and ϕ_x are the rotations angles along the z and x axis respectively[2]. The third assumption is satisfied if shear strains[3] are neglected

$$\gamma_{yz} = \gamma_{yx} = 0, \tag{2.4}$$

and these can be written in terms of the rotation angles as

$$\begin{aligned} \gamma_{xy} &= \phi_z + \frac{\partial u_0}{\partial y} = 0 \\ \gamma_{yz} &= \phi_x + \frac{\partial w_0}{\partial y} = 0, \end{aligned} \tag{2.5}$$

[2] ϕ_z is positive when, by suing the *right-hand-rule*, the thumb points in the positive z-axis; ϕ_x is positive when the thumb points in negative x-direction.

[3] Here we are using *engineering strains*, that is, the definition without the $\frac{1}{2}$, see [18].

so the rotation angles are $\phi_z = -\frac{\partial u_0}{\partial y}$ and $\phi_x = -\frac{\partial w_0}{\partial y}$. The displacement field of the EB theory is given by:

$$\begin{aligned} u &= u_0 \\ v &= v_0 - \frac{\partial u_0}{\partial y}x - \frac{\partial w_0}{\partial y}z \\ w &= w_0. \end{aligned} \tag{2.6}$$

The displacement field can be seen as a Taylor expansion for the three components, the in-plane terms are of zero-order, and the axial term is of order one. This fact is important since it will be used as motivation, and starting point, for higher order theories. According to the kinematic assumptions, EB theory accounts only for axial strain, which is written as:

$$\varepsilon_{yy} = \frac{\partial v}{\partial y} = \frac{\partial v_0}{\partial y} - \frac{\partial^2 u_0}{\partial^2 y}x - \frac{\partial^2 w_0}{\partial^2 y}z, \tag{2.7}$$

where the terms $\frac{\partial v_0}{\partial y}$, $\frac{\partial^2 u_0}{\partial^2 y}$ and $\frac{\partial^2 w_0}{\partial^2 y}$ are interpreted as membrane stretching and curvatures in x and z directions, respectively. The axial stress is obtained by using the constitutive equation

$$\sigma_{yy} = E\varepsilon_{yy}, \tag{2.8}$$

where E is the Young's modulus in the axial direction. The EB formulation is intended to work well with slender beams ($L/t > 10$), and describe accurately axial strains, displacements and stress far from boundaries. It starts to fail if the beam is indeed highly orthotropic or anisotropic [17], that is if three-dimensional effects are important.

2.2.2 Timoshenko Beam Theory

In the TB beam model the first two of the kinematic assumptions of EB are kept, the third is relaxed [18]. For this theory the cross-sections are not constrained to remain perpendicular to the beam axis, Figure 2.5.

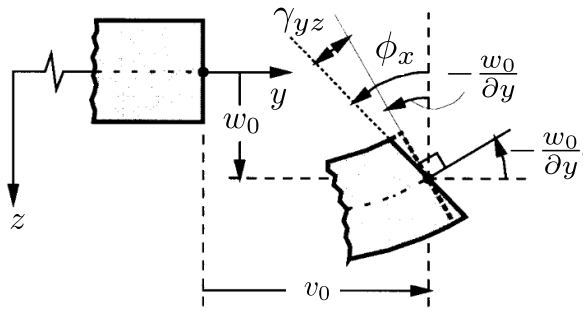

Figure 2.5: Bending of a Timoshenko Beam. Figure adapted from [3].

Shear deformations γ_{xy} and γ_{yz} are taken into account and all the non-null strain components are written as:

$$\begin{aligned}\varepsilon_{yy} &= \frac{\partial v_0}{\partial y} + \frac{\partial \phi_z}{\partial y}x + \frac{\partial \phi_x}{\partial y}z \\ \gamma_{xy} &= \phi_z + \frac{\partial u_0}{\partial y} \\ \gamma_{yz} &= \phi_x + \frac{\partial w_0}{\partial y}.\end{aligned} \tag{2.9}$$

The displacement field is written in terms of the rotation angles[4]:

$$\begin{aligned}u &= u_0(y) \\ v &= v_0(y) + \phi_z(y)x + \phi_x(y)z \\ w &= w_0(y).\end{aligned} \tag{2.10}$$

The constitutive relations are used to obtain the axial and shear stress components. For an isotropic material with Young's modulus E and shear modulus G the stresses are:

$$\begin{aligned}\sigma_{yy} &= E\varepsilon_{yy} = E\left(\frac{\partial v_0}{\partial y} + \frac{\partial \phi_z}{\partial y}x + \frac{\partial \phi_x}{\partial y}z\right) \\ \sigma_{xy} &= \kappa G\left(\phi_z + \frac{\partial u_0}{\partial y}\right) \\ \sigma_{yz} &= \kappa G\left(\phi_x + \frac{w_0}{\partial y}\right),\end{aligned} \tag{2.11}$$

where κ is a shear correction factor. This is needed since the TB model predicts a constant shear distribution through thickness and the correct profile is at least parabolic, in order to satisfy the stress-free boundary condition on the unloaded faces. Many shear correction factors are found in the literature [19, 65–68]. TB model contains all the capabilities of the EB model, plus the fact that can recover displacements and shear stresses more accurately, see [17].

2.2.3 High-Order Beam Theories

Euler-Bernoulli and Timoshenko Beam Theories can be considered as first-order theories, where some of the displacements are expanded in a Taylor-like series of order one or less. As mentioned in previous sections, these models can only describe displacements and (some) stresses accurately in particular situations: slender beams and far from singularities or points of load applications, i.e. limited by the Saint-Venant Principle. Another problem that arises in these theories is the phenomenon called *Poisson's Locking*. This is because there is a contradiction on how the coupling of normal strains (ε_{xx}, ε_{yy} and ε_{zz}) is related when using the constitutive equation (all three have linear distributions) in contrast with that from the kinematic description (one is linear and the other two constant) [11]. This type of locking can cause over-stiff response of the structure. Two

[4]Notice the dependency on y.

possible remedies can be used: (1) is to modify the constitutive relations and consider a reduced form, as in [3]; (2) the use of high-order models. Only the latter is of interest for the present work.

One-dimensional beam models perform well in describing the bending of slender beams with compact cross-sections, however, for more complex structures subject to complicated boundary and loading conditions (e.g. torsion), these might not be enough. Refinements to the classical theories are often performed in order to describe the mechanical response more accurately. It is possible to find many refined models in literature [21–24], however, the refinements are usually problem dependent. In general, we can describe the high-order (displacement-based) beam theories as being a model in which each component of the displacement is expanded in a Taylor expansion in terms of the cross-sectional coordinates:

$$\begin{aligned} u &= u_0 + u_1 x + u_2 z + u_3 x^2 + u_4 xz + u_5 z^2 + ... \\ v &= v_0 + v_1 x + v_2 z + v_3 x^2 + v_4 xz + v_5 z^2 + ... \\ w &= w_0 + w_1 x + w_2 z + w_3 x^2 + w_4 xz + w_5 z^2 + ... \end{aligned} \tag{2.12}$$

where u_i, v_i and w_i with $i = 0, 1, ...$, are functions depending only on the axial coordinate y. By setting some values to zero and using the appropriate constitutive equations, classical beam models (e.g. EB, TB or Reddy's third-order theory[5] [24]) can be easily recovered. High-order models like the one described in Equation (2.12) have three-dimensional fidelity, at least to some extent[6]. Therefore, three-dimensional strains

$$\varepsilon^{\mathrm{T}} = \left\{ e_{xx}, e_{yy}, e_{zz}, \gamma_{yz}, \gamma_{zx}, \gamma_{xy} \right\}$$

can be computed by using the geometrical relation between displacements and strains[7]:

$$\boldsymbol{\varepsilon} = \mathscr{B}\boldsymbol{u} \tag{2.13}$$

where $\mathbf{u}^{\mathrm{T}} = \{u, v, w\}$ and

$$\mathscr{B} = \begin{bmatrix} \frac{\partial}{\partial x} & 0 & 0 \\ 0 & \frac{\partial}{\partial y} & 0 \\ 0 & 0 & \frac{\partial}{\partial z} \\ 0 & \frac{\partial}{\partial z} & \frac{\partial}{\partial y} \\ \frac{\partial}{\partial z} & 0 & \frac{\partial}{\partial x} \\ \frac{\partial}{\partial y} & \frac{\partial}{\partial x} & 0 \end{bmatrix};$$

the six components of the stress

$$\boldsymbol{\sigma}^{\mathrm{T}} = \left\{ \sigma_{xx}, \sigma_{yy}, \sigma_{zz}, \tau_{yz}, \tau_{zx}, \tau_{xy} \right\}$$

can be computed using the constitutive equation

$$\sigma = \mathbf{C}\varepsilon, \tag{2.14}$$

[5] In this case boundary conditions are also taken into account.

[6] Beam Taylor-based models may be also limited by Saint-Venant Principle depending on how refined the model is.

[7] Here the linear relation is presented, in further sections the full non-linear Strain Tensor is considered.

where the stiffness matrix of the material is defined as

$$\mathbf{C} = \begin{bmatrix} C_{11} & C_{12} & C_{13} & C_{14} & C_{15} & C_{16} \\ & C_{22} & C_{23} & C_{24} & C_{25} & C_{26} \\ & & C_{33} & C_{34} & C_{35} & C_{36} \\ & & & C_{44} & C_{45} & C_{46} \\ & Symmetric & & & C_{55} & C_{56} \\ & & & & & C_{66} \end{bmatrix}. \tag{2.15}$$

The explicit form of the coefficients C_{ij} can be found in [3] .

2.3 Finite Element Model

Throughout this work a displacement-based finite element formulation is used as the main tool for the analysis. Fundamental equations are summarised here for completeness and clarity of exposition.

Consider an elastic continuum of volume V, embedded in $\mathbb{R}^3$. In a finite element setting, the volume is discretised into a series of N-noded sub-domains (the elements), so that displacement fields of the form

$$\boldsymbol{U}(x,y,z) = \begin{bmatrix} U_x(x,y,z) \\ U_y(x,y,z) \\ U_z(x,y,z) \end{bmatrix}$$

can be approximated element-wise by means of local shape functions, N_i, and generalised nodal displacements, $\boldsymbol{u}_i$, such that

$$\boldsymbol{U}_{(e)}(x,y,z) = N_i(x,y,z)\boldsymbol{u}_i, \qquad \text{with} \qquad i = 1,\ldots,N. \tag{2.16}$$

In the previous expression and throughout remainder of the manuscript, the Einstein summation convention is implied over repeated indices.

Using equation (2.16), the strain-displacement relationship in its linear form may be recast as

$$\boldsymbol{\varepsilon} = \mathscr{B}_i \boldsymbol{u}_i, \tag{2.17}$$

where

$$\mathscr{B}_i = \begin{bmatrix} \frac{\partial N_i}{\partial x} & 0 & 0 \\ 0 & \frac{\partial N_i}{\partial y} & 0 \\ 0 & 0 & \frac{\partial N_i}{\partial z} \\ 0 & \frac{\partial N_i}{\partial z} & \frac{\partial N_i}{\partial y} \\ \frac{\partial N_i}{\partial z} & 0 & \frac{\partial N_i}{\partial x} \\ \frac{\partial N_i}{\partial y} & \frac{\partial N_i}{\partial x} & 0 \end{bmatrix}.$$

Elastic equilibrium is enforced via the Principle of Virtual Displacements, which, in a quasi-static setting, states that

$$\delta W_{\text{int}} = \delta W_{\text{ext}}, \tag{2.18}$$

where W_{int} and W_{ext} are the internal and external works, respectively, and δ denotes virtual variation with respect to displacements.

By definition, the internal work is the work done by stresses over corresponding virtual strains. Noting that $W_{\text{int}} = \sum_{\text{e}} W_{\text{int}}^{(\text{e})}$ and letting $V_{(\text{e})}$ be the volume of the generic element

$$\delta W_{\text{int}}^{(\text{e})} = \int_{V_{(\text{e})}} \delta \boldsymbol{\varepsilon}^{\text{T}} \boldsymbol{\sigma} \, dV, \tag{2.19}$$

where[2]

$$\begin{aligned} \delta \boldsymbol{\varepsilon} &= \delta \left[\mathscr{B}_j \boldsymbol{u}_j \right] \\ &= \mathscr{B}_j \delta \boldsymbol{u}_j. \end{aligned} \tag{2.20}$$

Substituting (2.14) and (2.17) into (2.19)

$$\begin{aligned} \delta W_{\text{int}}^{(\text{e})} &= \int_{V_{(\text{e})}} \delta \boldsymbol{\varepsilon}^{\text{T}} \boldsymbol{\sigma} \, dV \\ &= \int_{V_{(\text{e})}} \delta \boldsymbol{\varepsilon}^{\text{T}} \boldsymbol{C} \boldsymbol{\varepsilon} \, dV \\ &= \int_{V_{(\text{e})}} \delta \boldsymbol{u}_j^{\text{T}} \mathscr{B}_j^{\text{T}} \boldsymbol{C} \mathscr{B}_i \boldsymbol{u}_i \, dV \\ &= \delta \boldsymbol{u}_j^{\text{T}} \left(\int_{V_{(\text{e})}} \mathscr{B}_j^{\text{T}} \boldsymbol{C} \mathscr{B}_i \, dV \right) \boldsymbol{u}_i \\ &= \delta \boldsymbol{u}_j^{\text{T}} \boldsymbol{K}_{ij}^{(\text{e})} \boldsymbol{u}_i. \end{aligned} \tag{2.21}$$

If we now denote body forces per unit volume as $\boldsymbol{g}$, surface forces per unit area as $\boldsymbol{p}$, line forces per unit length as $\boldsymbol{q}$ and concentrated forces acting on Q as $\boldsymbol{P}$, the external work is

$$\delta W_{\text{ext}}^{(\text{e})} = \int_{V_{(\text{e})}} \delta \boldsymbol{u}^{\text{T}} \boldsymbol{g} \, dV + \int_S \delta \boldsymbol{u}^{\text{T}} \boldsymbol{p} \, dS + \int_l \delta \boldsymbol{u}^{\text{T}} \boldsymbol{q} \, dl + \delta \boldsymbol{u}^{\text{T}} |_Q \boldsymbol{P}. \tag{2.22}$$

Recasting equation (2.22) as $\delta W_{\text{ext}}^{(\text{e})} = \delta \boldsymbol{u}^{\text{T}} \boldsymbol{f}_{(\text{e})}$ and substituting with (2.21) into (2.18) we get

$$\delta \boldsymbol{u}_j^{\text{T}} \boldsymbol{K}_{ij}^{(\text{e})} \boldsymbol{u}_i = \delta \boldsymbol{u}_j^{\text{T}} \boldsymbol{f}_{(\text{e})}, \tag{2.23}$$

which is a statement of elastic equilibrium in weak form, where $\boldsymbol{K}_{ij}^{(\text{e})}$ and $\boldsymbol{f}_{(\text{e})}$ are, respectively, the structural stiffness matrix and the generalised load vector of the generic element. After assembly the linear system to solve[8] is given by:

$$\boldsymbol{K} \boldsymbol{u} = \boldsymbol{f}. \tag{2.24}$$

[2] Note the change of subscript for consistent summations using Einstein notation.

[8] On this system boundary conditions should be applied.

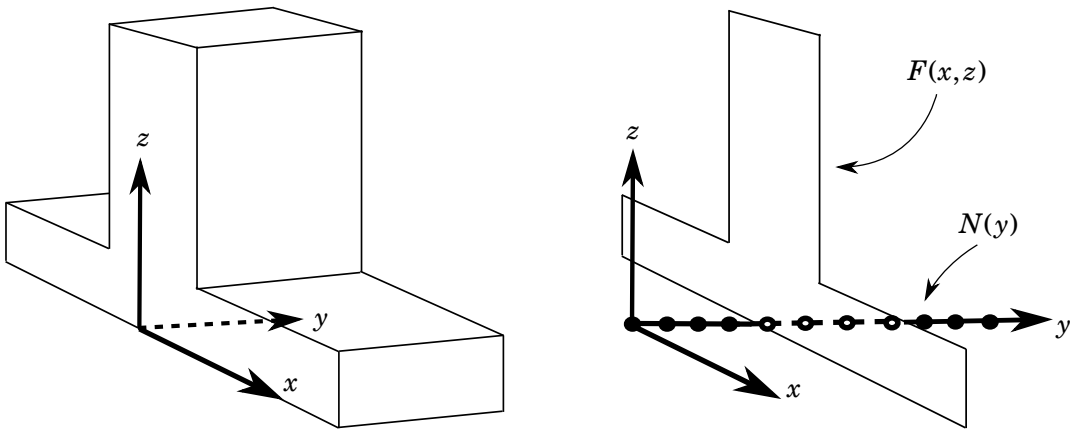

(a) Beam element and axes orientation.

(b) Beam axis and element cross-section.

Figure 2.6: Unified formulation beam element and relative reference system.

2.4 Unified Formulation

A typical way to overcome the limitations of classical beam models and to refine the structural analyses that employ them is to enrich the kinematics of the approximated displacement field. The use of Taylor expansions, for instance, is common to many theories where high-order terms are included to enrich the kinematic approximation. In general, the higher the order, the higher the computational effort required. One of the advantages of the Unified Formulation (UF) is that, owing to the notation adopted, beam models of increasing kinematic refinement are readily developed.

Let us consider a beam-like structure as shown in Figure 2.6, where the beam extends along the y-axis and cross-sections lie in the xz-plane. In UF, the beam is discretised along the length with traditional 1D finite elements. Cross-sectional deformations can be approximated using different expansions as explained in sections 2.4.1. Mathematically, this means that the displacement field and its virtual variations may be written as a product of two functions: cross-sectional expansion functions, $F(x,z)$, and 1D Lagrange shape functions, $N(y)$, along the beam axis. In principle, these functions can have as many terms as desired. The more terms there are, the richer the kinematics. With reference to equation (2.16),

$$\begin{aligned} \boldsymbol{U}_{(\mathrm{e})} &= F_\tau(x,z)N_i(y)\boldsymbol{u}_{i\tau}, \\ \delta\boldsymbol{U}_{(\mathrm{e})} &= F_s(x,z)N_j(y)\delta\boldsymbol{u}_{js}, \end{aligned} \qquad \text{with} \quad \tau,s = 1,...,M \quad \text{and} \quad i,j = 1,...,N_\mathrm{e} \tag{2.25}$$

where M is the number of terms in the cross-sectional expansion depending on the order; N_e is the number of Lagrange nodes within each element along the beam; and $\boldsymbol{u}_{i\tau}$ and $\boldsymbol{u}_{js}$ are generalized displacement vectors. Substituting (2.25) into equation (2.19) and following the steps

as shown in (2.21) gives

$$\begin{aligned}\delta W_{\text{int}}^{(\text{e})} &= \delta \boldsymbol{u}_{js}^{\text{T}} \left(\int_{V_{(\text{e})}} \mathfrak{B}_{js}^{\text{T}} \boldsymbol{C} \mathfrak{B}_{i\tau} \, dV \right) \boldsymbol{u}_{i\tau} \\ &= \delta \boldsymbol{u}_{js}^{\text{T}} \boldsymbol{k}_{(\text{e})}^{ij\tau s} \boldsymbol{u}_{i\tau}\end{aligned} \tag{2.26}$$

and substituting (2.25) into equation (2.22) gives

$$\delta W_{\text{ext}}^{(\text{e})} = \delta \boldsymbol{u}_{js}^{\text{T}} \boldsymbol{f}_{(\text{e})}. \tag{2.27}$$

Finally, equating internal and external work

$$\delta \boldsymbol{u}_{js}^{\text{T}} \boldsymbol{k}_{(\text{e})}^{ij\tau s} \boldsymbol{u}_{i\tau} = \delta \boldsymbol{u}_{js}^{\text{T}} \boldsymbol{f}_{(\text{e})}, \tag{2.28}$$

which is a statement of elastic equilibrium in weak form in UF notation. The term $\boldsymbol{k}_{(\text{e})}^{ij\tau s}$ is referred to as the element *Fundamental Nucleus*. Its explicit form can be found by taking the linear part of the equations in Appendix C. Fundamental nuclei may be assembled in a global stiffness matrix following the standard finite element procedure resulting in

$$\boldsymbol{K}\boldsymbol{u} = \boldsymbol{f}. \tag{2.29}$$

The latter equation is then solved to find the generalised displacements.

In UF, the choice of F_τ and M is arbitrary. In the literature, different kinds of expansion functions have been used, including Taylor, Lagrange, Legendre[9], exponential trigonometric and Chebyshev polynomials [37, 40–42, 69].

2.4.1 Cross-sectional expansion models

As mentioned in the previous section, in the Unified formulation, cross-sectional expansion functions can be chosen arbitrarily. That said, the most widely adopted expansions are based on Taylor and Lagrange polynomials. These two types of functions are used in fundamentally different ways, with profound implications on some computational and numerical aspects of the implementation.

2.4.1.1 Taylor expansion model

In Taylor expansion models, the cross-sectional displacement field at the i^{th} Lagrange beam node is expressed with complete, Taylor polynomials containing terms of the form $F_\tau = x^n z^m$. For example, a second-order expansion ($N = 2$) has constant, linear and quadratic terms as follows

$$\boldsymbol{u}_i = \{u_{x_i}, u_{y_i}, u_{z_i}\}^T = \boldsymbol{u}_{i1} + x\boldsymbol{u}_{i2} + z\boldsymbol{u}_{i3} + x^2\boldsymbol{u}_{i4} + xz\boldsymbol{u}_{i5} + z^2\boldsymbol{u}_{i6}, \tag{2.30}$$

where the terms $\boldsymbol{u}_{i\tau}^{\text{T}} = \{u_{x_{i\tau}}, u_{y_{i\tau}}, u_{z_{i\tau}}\}$ on the right hand side are unknown variables to be determined. High-order models, i.e. models with high-order kinematics, can be obtained by enriching the polynomial expansion. The reader is referred to [11] for a more detailed treatment of TE models.

[9]The Legendre model has shown to have similar capabilities to the SL model presented in Chapter 3.

2.4.1.2 Lagrange expansion model

In Lagrange expansion models, beam elements are further discretised by dividing cross-sections into a number of local sub-domains as shown in Figure 2.7(b). Two-dimensional Lagrange polynomials are used as expansion functions over the sub-domains. The order of the Lagrange polynomials spanning each sub-domain depends on the number of computational nodes therein. For instance, a 9-noded Lagrange type element (`L9`) is spanned by quadratic expansions so that the displacement field at the i^{th} beam node becomes

$$\boldsymbol{u}_i = L_1\boldsymbol{u}_{i1} + L_2\boldsymbol{u}_{i2} + L_3\boldsymbol{u}_{i3} + L_4\boldsymbol{u}_{i4} + L_5\boldsymbol{u}_{i5} + L_6\boldsymbol{u}_{i6} + L_7\boldsymbol{u}_{i7} + L_8\boldsymbol{u}_{i8} + L_9\boldsymbol{u}_{i9}, \tag{2.31}$$

where the expansion functions, $F_\tau = L_\tau$, are 2D Lagrange polynomials and the terms $\boldsymbol{u}_{i\tau}$ on the right hand side are unknown variables. Unlike in TE models, these global unknowns are pure displacement components at the computational nodes defined across the sub-domains. Refined model accuracy is obtained by increasing the number of sub-domains or the number of nodes therein, or in other words, by increasing the cross-sectional mesh density. A more detailed description of LE models can be found in [70].

2.4.2 Numerical integration over UF elements

Sections 2.4.1.1 and 2.4.1.2 highlight one of the fundamental differences between TE models and LE models. Taylor expansions are defined to span cross-sections starting from the origin of xz-planes along the y-axis. Lagrange expansions are defined on quadrilateral sub-domains. This difference is illustrated graphically in Figures 2.7(a) and 2.7(b).

In practical terms, the fact that Lagrange expansions are defined on cross-sectional sub-domains implies that an additional mapping is required for integrations over $V_{(e)}$. To clarify, like traditional beam elements, N-noded UF elements based on Taylor expansions are obtained through integration of $\int_{V_{(e)}} \mathscr{B}_j^{\mathrm{T}}\boldsymbol{C}\mathscr{B}_i\, dV$ over a master element defined in $\zeta \in [-1,1]$, which is then mapped onto $(x,y,z) \in [x_1^{(e)}, x_N^{(e)}] \times [y_1^{(e)}, y_N^{(e)}] \times [z_1^{(e)}, z_N^{(e)}]$, i.e. the element position in global coordinates. An identical operation is required, for elements based on Lagrange expansions, to integrate $\int_{V_{(e)}} \mathfrak{B}_j^{\mathrm{T}}\boldsymbol{C}\mathfrak{B}_i\, dV$, however an additional mapping is required to link physical sub-domains in cross-sectional xz-planes to the master computational domain $(\xi,\eta) \in [-1,1] \times [-1,1]$. A visual representation of this two-dimensional map is given in Figure 2.8.

Cross-sectional sub-domains defined in (x,z) are mapped and interpolated using linear Lagrange polynomials L_k

$$\boldsymbol{\xi} = L_k\boldsymbol{x}_k, \qquad \text{with} \qquad k = 1,\ldots,4 \tag{2.32}$$

where $\boldsymbol{\xi}$ is the vector of mapped coordinates and $\boldsymbol{x}_k$ are the physical positions of the nodes of the generic quadrilateral sub-domain. As customary, by using (2.32) one can compute the Jacobian of the transformation, which is required for integrals oven the master domain.

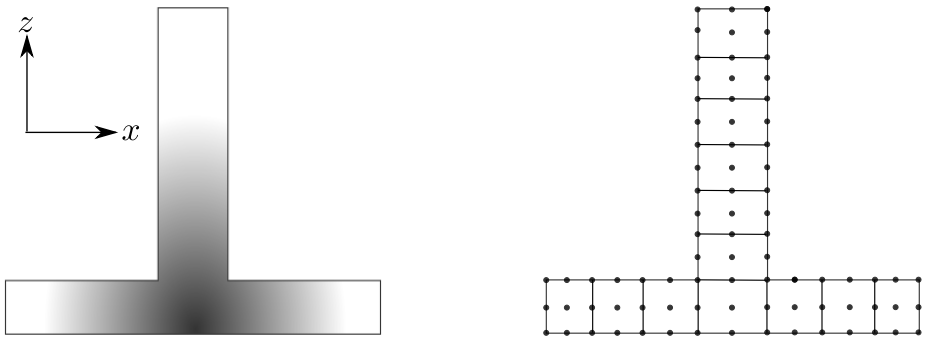

Figure 2.7: Typical cross-sectional discretisation for: (a) Taylor expansions (hierarchical); (b) Lagrange expansions (node-based). Grey shading indicates hierarchical shape functions over the section.

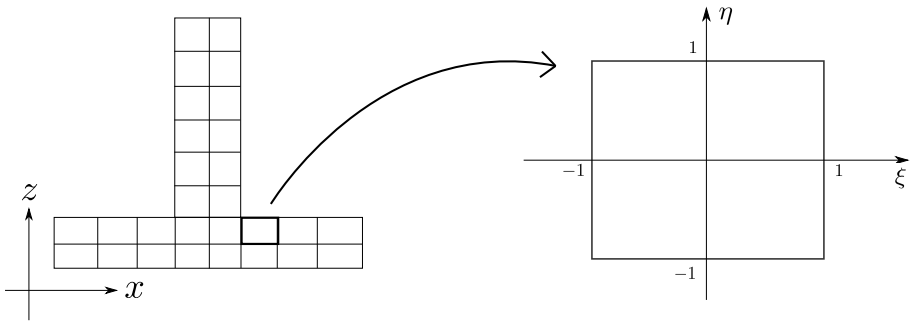

Figure 2.8: Schematic depiction of the mapping from physical cross-sectional sub-domains to computational master reference system.

2.5 Buckling

The design of structures is commonly based on strength and stiffness criteria. The *strength* is the ability of the structure to withstand the applied load without breaking[10], while *stiffness* is the resistance to deformation. However, a structure may become unstable long before the strength and stiffness allowed maximums are reached. The study of buckling is an essential step towards understanding the behaviour of complex structures.

In this section some elementary results on buckling are presented, including buckling of beams, plates and cylinders under some cases of loading and boundary conditions.

2.5.1 Stability

When an elastic slender beam is loaded compressively in its axial direction, with a small enough load, its geometry slightly shrinks in the same direction. On reaching a critical load, the structure

[10]There are many types of failure, for details see [71].

loses stability and it experiences large lateral deflections. The structure has buckled.

Buckling, or structural instability as it is also known, is classified into two categories: bifurcation buckling and limit load buckling [4, 72, 73]. In the former the structure's deflection changes suddenly from one direction to a different direction (e.g. from axial shrinking to lateral deflection). Take for example a hinged beam under axial compression. The applied load P vs lateral displacement w is shown in Figure 2.9. The load at which the structure buckles is called *critical-load* or *buckling-load* P_{cr}. The path prior to the buckling point is called *Primary path* or *Pre-buckling path* and after the bifurcation is called *Secondary path* or *Post-buckling path*. In this case the Secondary path is symmetric and stable.

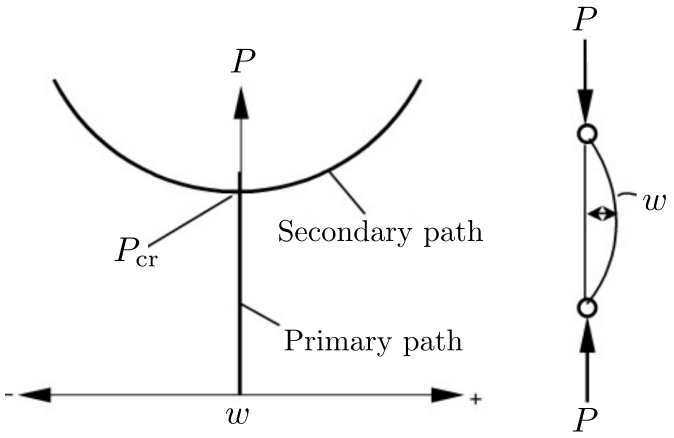

Figure 2.9: Load-deflection curve for a beam under compression. Figure adapted from [4].

Depending on the type of structure, loads and boundary conditions, the load-deflection curve may change. Take for instance a guyed tower subject to a vertical load at its cusp, Figure 2.10. Before the critical load the structure is stable, when the load is equal to the critical load, the structure buckles and two symmetric, but unstable paths, appear.

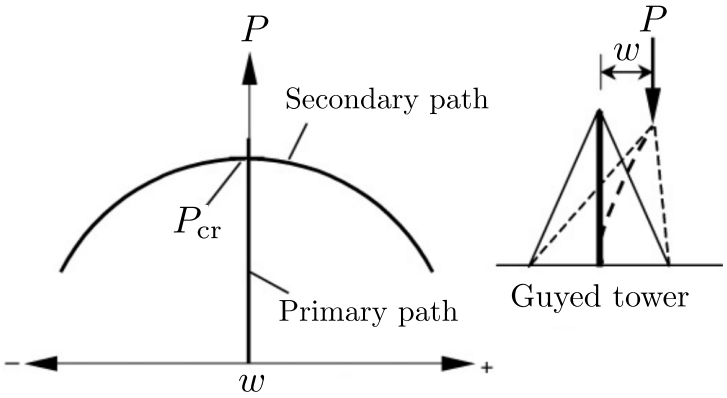

Figure 2.10: Load-deflection curve for a guyed tower under vertical load. Figure adapted from [4].

For some structures, like an L-shape frame subject to a vertical force, Figure 2.11, the load-deflection (load P vs angle θ) path is asymmetric. At buckling, the structure can take any path, stable or unstable, depending on factors such as geometrical, material, boundary or load imperfections.

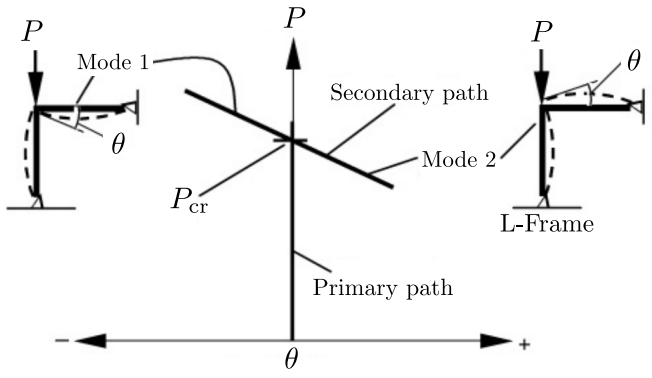

Figure 2.11: Load-deflection curve for an L-shape frame under vertical load. Figure adapted from [4].

In limit load bifurcation, the structure can be loaded to a maximum load before snap-buckling, i.e. only one mode shape is developed. One example is a shallow arch, where snap-through behaviour is observed, as in Figure 2.12(a). Another example of single-mode structure is the buckling of an imperfect thin cylinder under compression (finite disturbance buckling), Figure 2.12(b).

2.5.2 Buckling of an Euler Beam under Axial Compression

Consider an isotropic straight beam with length L, Young's modulus E and second moment of area I, subject to an axial compression load P. The equation governing the buckling of the beam is [4]

$$\frac{d^4\hat{w}}{dy^4} + \alpha\frac{d^2\hat{w}}{dy^2} = 0 \quad , \alpha = \frac{P_{\text{cr}}L^2}{EI} \tag{2.33}$$

where $\hat{w} = \frac{w}{L}$ is the normalised transverse displacement and y the axial coordinate. The constant value α defines the critical buckling load P_{cr}. The general solution to this equation is:

$$\hat{w} = C_1 \sin\left(\sqrt{\alpha}y\right) + C_2 \cos\left(\sqrt{\alpha}y\right) + C_3 y + C_4, \tag{2.34}$$

where C_i ($i = 1,2,3,4$) are constants that depend on the boundary conditions. The function $\hat{w}(y)$ describes the shape of the buckled beam, herein we present the mode shapes and buckling modes for five boundary cases: clamped-free (CF), hinged-hinged (HH), clamped-hinged (CH), clamped-clamped (CC) and clamped with sliding restraint (CS). Figure 2.13 summarises these cases.

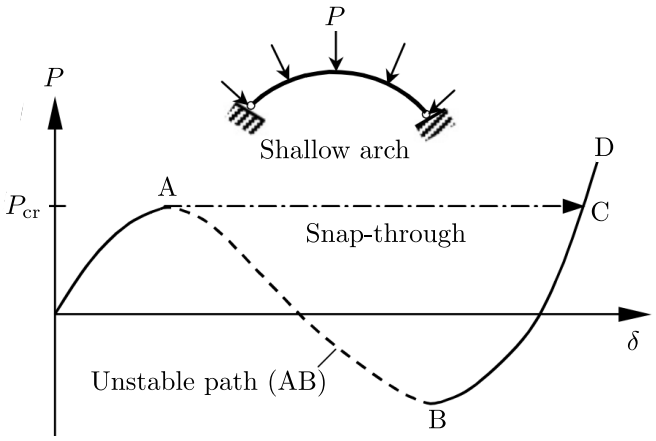

(a) Snap through buckling

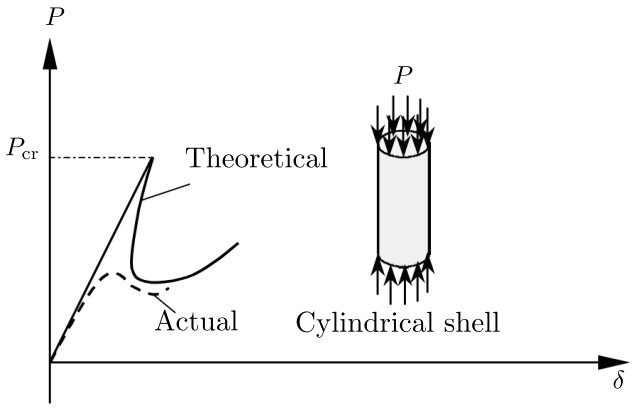

(b) Finite disturbance buckling

Figure 2.12: Limit load bifurcation examples. Figure adapted from [4].

2.5.3 Buckling of a Simply-Supported Plate

Consider a simply-supported (SSSS)[11] rectangular plate with width a, length b and thickness t, made of an isotropic material with Young's modulus E, Poisson's ratio ν and flexural rigidity $D = Et^3/\left[12(1-\nu^2)\right]$. Let the mid surface coincide with the xy-plane as in Figure 2.14. In the *Classical Plate Theory* (CPT), the equation governing the linear buckling problem reduces to

[11] Only rotations are allowed, loading conditions are expected in form of prescribed fordes and in-plane displacements are restricted. See Equation (2.35).

Case	CF	HH	CH	CC	CS
Buckling shape					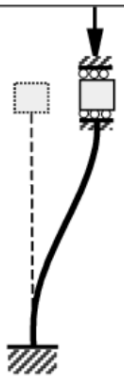
Buckling parameter	$\alpha = \frac{\pi^2}{4}$	$\alpha = \pi^2$	$\alpha = 2.0457\pi^2$	$\alpha = 4\pi^2$	$\alpha = \pi^2$

Figure 2.13: Euler beam buckling cases. Figure adapted from [4].

[4, 54]:

$$\begin{aligned} \frac{\partial^4 w}{\partial x^4} + 2\frac{\partial^4 w}{\partial x^2 \partial y^2} + \frac{\partial^4 w}{\partial y^4} &= \frac{1}{D}\left(\hat{N}_x \frac{\partial^2 w}{\partial x^2} + 2\hat{N}_{xy}\frac{\partial^2 w}{\partial x \partial y} + \hat{N}_y \frac{\partial^2 w}{\partial y^2}\right) \\ w(0,y) = w(a,y) &= 0 \\ w(x,0) = w(x,b) &= 0 \\ M_{xx}(0,y) = M_{xx}(a,y) &= 0 \\ M_{yy}(x,0) = M_{yy}(x,b) &= 0, \end{aligned} \tag{2.35}$$

where w is the displacements in z direction, M_{xx} and M_{yy} moments per unit length, $\hat{N}_x$, $\hat{N}_y$ and $\hat{N}_{xy}$ are the applied forces per unit length.

2.5.3.1 Plate Uni-axially Compressed

Assume that the rectangular plate is compressed in its middle plane by forces uniformly distributed along the sides $x = 0$ and $x = a$, therefore $\hat{N}_y = \hat{N}_{xy} = 0$. At some critical value of $\hat{N}_x = N_{\text{cr}}$ the structure becomes unstable and buckling occurs. The critical load is given by [54]

$$N_{\text{cr}} = \frac{\pi^2 D}{b^2}\left(\frac{b}{a} + \frac{a}{b}\right)^2. \tag{2.36}$$

The buckling mode, the solution to Equation (2.35), is

$$w(x,y) = c\sin\left(\frac{n\pi x}{a}\right)\sin\left(\frac{\pi y}{b}\right) \tag{2.37}$$

where c is an arbitrary constant and n is the number of half-waves in the x direction. The structure develops one half-wave in each direction.

2.5.3.2 Plate Bi-axially Compressed

Consider the rectangular plate submitted to two uniformly distributed compressive forces $\hat{N}_x$ and $\hat{N}_y = \alpha \hat{N}_x$, where the α constant positive α is the ratio of the two the in-plane forces. Given a value of α, the critical buckling load is given by [4]:

$$N_{\text{cr}} = \frac{D\pi^2}{b^2}\left(\frac{s^4 + 2\nu s^2 + 1}{s^2 + \alpha}\right) \tag{2.38}$$

where ν is the Poisson's ratio and $s = \frac{b}{a}$. The buckling shape takes the form

$$w(x,y) = c \sin\left(\frac{\pi x}{a}\right)\sin\left(\frac{\pi y}{b}\right) \tag{2.39}$$

with c an arbitrary constant.

2.5.4 Buckling of Cylinder under Axial Compression

Consider an isotropic cylinder with Young's modulus E and Poisson's ratio ν, thickness h, radius R and length L, subject to a compressive load, N as in Figure 2.15. The boundary conditions are simply-supported at the edges. The equation governing the axisymmetric buckling of the structure is given by [4, 74, 75]

$$D\frac{d^4w}{dy^4} + N\frac{d^2w}{dy^2} + \frac{Eh}{R^2}w = 0 \tag{2.40}$$

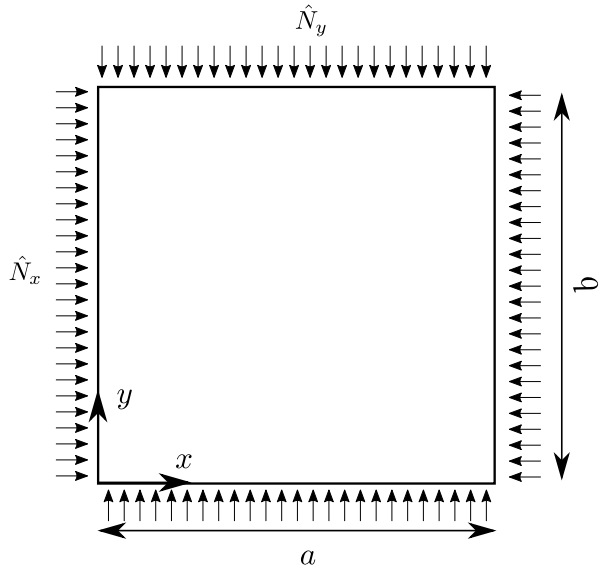

Figure 2.14: Rectangular plate

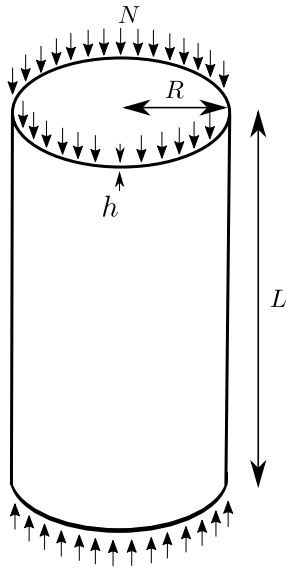

Figure 2.15: Cylindrical Shell

where y the axial coordinate, w the radial deflection, $D = Eh^3/\left[12(1-\nu^2)\right]$ the bending rigidity.

This equation is similar to the equation governing the buckling of a beam (2.33), with an extra term, which in the beam analogy represents an elastic foundation. If the length of the cylinder is long and if m is a multiple of the half sine waves, then the critical load buckling load is given by[12] [74]

$$N_{\text{cr}} = \frac{1}{\sqrt{3(1-\nu^2)}}\left(\frac{Eh^2}{R}\right); \tag{2.41}$$

and the buckling mode takes the form

$$w = c \sin \frac{m\pi y}{L} \tag{2.42}$$

with c an arbitrary constant.

[12]This formula has limited practical applications due to the sensitivity to imperfections (i.e. it leads to substantial overestimations of the buckling loads).

CHAPTER 3

SERENDIPITY LAGRANGE EXPANSION MODEL

"Those who appreciate mathematical analysis will see with pleasure mechanics becoming a new branch of it and hence, will recognize that I have enlarged its domain."

- J.L. Lagrange

Simple analytical and finite element models are widely employed by engineers for the stress analysis of beam structures, because of their simplicity and accuracy at global level. However, the validity of these models is limited by assumptions of material heterogeneity, geometric dimensions and slenderness, and only applicable to regions remote from boundary constraints, discontinuities and points of load application (Saint-Venant's Principle). To predict accurate stress fields in these locations, computationally expensive three-dimensional (3D) finite element analyses are commonly used. Alternatively, displacement based high-order beam models are often employed to capture localised three-dimensional stress fields analytically. Herein, a novel approach for the analysis of beam-like structures is proposed. The approach is based on the Unified Formulation by Carrera, and is able to capture complex, 3D stress fields in a computationally efficient way. As a novelty, purposely adapted, hierarchical shape functions are used to define cross-sectional displacements. Due to the nature of the vector space used, these functions are named Serendipity Lagrange (SL) polynomials. This new cross-sectional expansion model is benchmarked against traditional finite elements and other implementations of the Unified Formulation by means of static analyses. It is shown that Serendipity Lagrange elements solve some of the shortcomings of the most commonly used Unified Formulation beam models based on Taylor and Lagrange expansion functions. Additionally, due to their hierarchical nature, they can be combined with additional high order geometrical mappings to model complex curved

cross-sections, without increasing the amount of degrees of freedom. Furthermore, significant computational efficiency gains over 3D finite elements are achieved for similar levels of accuracy.

The model described herein is used thoughout the whole manuscript as the main expansion for the Unified Formulation model. The work presented in this chapter is the outcome of a collaboration with MUL2 Group in Politecnico di Torino, Italy, together with the Bristol Composites Institute Fullcomp team, specially with Mayank Patni. The contents of the chapter are the contributions of the author.

3.1 Aim and Motivation

Studying the mechanical behaviour of structures can be a difficult task, especially if detailed three-dimensional stress fields close to singularities are to be computed. As mentioned in Chapter 2, there are several ways to approach the problem, depending on the geometry, dimensions, loading and boundary conditions. Engineers have the difficult task to balance the trade-off between accuracy and computational efficiency. In some cases accuracy can be sacrificed if only global or approximate response of the structure is needed, e.g. in the first stages of design; in others, high computational cost in unavoidable for the sake of accuracy. Therefore, the need of an efficient and accurate tool for analysing complex structures is desirable. Moreover, efficient and accurate tools allows to anticipate for especific and complex design challenges. Therefore, efficiency and accuracy are the main motivation for the developments presented in this chapter.

The aims of this new formulation can be summarised as:

1. Develop a hierarchical model.
2. Local expansion control in terms of mesh and order expansion.
3. Reduce computational effort in terms of degrees of freedom.
4. Capture localised stress fields accurately.
5. Improve numerical stability.

3.2 Introduction

One of the most recent contributions to the development of refined beam theories is the Carrera Unified Formulation [37] as explained in detail in Section 2.4. Among all the possible shape functions that can be used to describe the cross-section expansion, the most commonly used are the Taylor (TE) and Lagrange (LE) models. TE models are hierarchical in nature, so the degree of accuracy with which the displacement fields are captured is enriched by increasing the order of the polynomial of the cross-sectional expansion. On the other hand, LE models are based on cross-sectional discretisations using Lagrange 2D-elements. Refinement is obtained by refining

the mesh in the cross section. Both models are found to be accurate and computationally efficient, but have limitations. TE models can be numerically unstable if the order of expansion is too high (order ~ 8 or higher), whilst LE models can have slow mesh convergence rates. Another known limitation of Carrera Unified Formulation is the oscillation of shear stresses along the beam axis that appears if the mesh along the beam length is not sufficiently fine.

A new approach for the analysis of beam-like structures that overcome all of the above limitations is proposed. The approach is based on the Unified Formulation and, as a novelty, hierarchical Lagrange polynomials are used to define cross-sectional displacement fields. The new model, called *Serendipity Lagrange* (SL), is based on the Trunk (or Serendipity) Space which is a polynomial space whose base is the set of monomials $\xi^i\eta^j$, $i,j = 0,1,2,\ldots,N$, where N is the order of the polynomial [5]. SL expansions combine the two best features of TE and LE models, i.e. they are hierarchical and facilitate numerically stable cross-sectional refinements via re-meshing. The advantages of using SL elements for beams of general cross-section compared with finite elements, Taylor and Lagrange type models are discussed. In addition the effect of collocating beam nodes towards the boundaries using Chebyshev biased grids is investigated, which reduce oscillations in numerical solutions (the Runge effect) [76].

3.3 Finite Element Implementation

The Unified Formulation (UF) relies on a displacement-based finite element method. A brief summary of the fundamental equations is presented here for clarity.

Consider a volume discretised into a series of N-noded subdomains (elements), so that displacement fields of the form

$$\boldsymbol{U}(x,y,z) = \begin{bmatrix} U_x(x,y,z) \\ U_y(x,y,z) \\ U_z(x,y,z) \end{bmatrix}$$

are approximated element-wise by means of local shape functions, G_i, and generalised nodal displacements, $\boldsymbol{u}_i^{\mathrm{T}} = \{u_i, v_i, w_i\}$ as

$$\boldsymbol{U}_{(e)}(x,y,z) = G_i(x,y,z)\boldsymbol{u}_i, \qquad \text{with} \qquad i = 1,\ldots,N, \tag{3.1}$$

where the summation convention is implied over repeated indices. In the context of the Unified Formulation the three-dimensional shape function G in equation (5.7), is written such that it becomes the product of two functions, one defined on the cross-section $F(x,z)$ and the other on the beam axis $N(y)$, as explained in detail in Section 2.4: $G(x,y,z) = F(x,z)N(y)$. Therefore the displacement field and its variation becomes

$$\begin{aligned} \boldsymbol{U}_{(e)} &= F_\tau(x,z)N_i(y)\boldsymbol{u}_{i\tau}, \\ \delta\boldsymbol{U}_{(e)} &= F_s(x,z)N_j(y)\delta\boldsymbol{u}_{js}, \end{aligned} \qquad \text{with} \quad \tau,s = 1,\ldots,M \quad \text{and} \quad i,j = 1,\ldots,N_{\mathrm{e}} \tag{3.2}$$

where M is the number of terms in the cross-sectional expansion depending on the order; N_{e} is the number of Lagrange nodes within each element along the beam; and $\boldsymbol{u}_{i\tau}$ and $\boldsymbol{u}_{js}$ are generalized displacement vectors. Herein, a novel expansion function $F(x,z)$, with special properties, is derived and tested.

Given the displacements, the six components of the linear strain tensor

$$\boldsymbol{e}^{\mathrm{T}} = \left\{e_{xx}, e_{yy}, e_{zz}, \gamma_{yz}, \gamma_{zx}, \gamma_{xy}\right\}$$

can be computed using the differential relation

$$\boldsymbol{e} = \mathscr{B}_i \boldsymbol{u}_i, \tag{3.3}$$

where

$$\mathscr{B}_i = \begin{bmatrix} \frac{\partial G_i}{\partial x} & 0 & 0 \\ 0 & \frac{\partial G_i}{\partial y} & 0 \\ 0 & 0 & \frac{\partial G_i}{\partial z} \\ 0 & \frac{\partial G_i}{\partial z} & \frac{\partial G_i}{\partial y} \\ \frac{\partial G_i}{\partial z} & 0 & \frac{\partial G_i}{\partial x} \\ \frac{\partial G_i}{\partial y} & \frac{\partial G_i}{\partial x} & 0 \end{bmatrix}.$$

Using Hooke's law and the material's stiffness matrix $\boldsymbol{C}$, the six components of the Cauchy stress tensor

$$\boldsymbol{\sigma}^{\mathrm{T}} = \left\{\sigma_{xx}, \sigma_{yy}, \sigma_{zz}, \tau_{yz}, \tau_{zx}, \tau_{xy}\right\},$$

are related to strains by

$$\boldsymbol{\sigma} = \boldsymbol{C}\boldsymbol{e}. \tag{3.4}$$

Elastic equilibrium is enforced via the Principle of Virtual Displacements, which implies

$$\delta W_{\mathrm{int}} = \delta W_{\mathrm{ext}}. \tag{3.5}$$

δW_{int} is the variation of the internal work given by

$$\begin{aligned} \delta W_{\mathrm{int}}^{(\mathrm{e})} &= \delta \boldsymbol{u}_{js}^{\mathrm{T}} \left(\int_{V_{(\mathrm{e})}} \mathfrak{B}_{js}^{\mathrm{T}} \boldsymbol{C} \mathfrak{B}_{i\tau} \, dV \right) \boldsymbol{u}_{i\tau} \\ &= \delta \boldsymbol{u}_{js}^{\mathrm{T}} \boldsymbol{k}_{(\mathrm{e})}^{ij\tau s} \boldsymbol{u}_{i\tau} \end{aligned} \tag{3.6}$$

where (7.3) and (3.3) have been used. The external work δW_{ext} is given by

$$\delta W_{\mathrm{ext}}^{(\mathrm{e})} = \int_{V_{(\mathrm{e})}} \delta \boldsymbol{u}^{\mathrm{T}} \boldsymbol{g} \, dV + \int_S \delta \boldsymbol{u}^{\mathrm{T}} \boldsymbol{p} \, dS + \int_l \delta \boldsymbol{u}^{\mathrm{T}} \boldsymbol{q} \, dl + \delta \boldsymbol{u}^{\mathrm{T}}|_Q \boldsymbol{P}. \tag{3.7}$$

where we denote body forces per unit volume as $\boldsymbol{g}$, surface forces per unit area as $\boldsymbol{p}$, line forces per unit length as $\boldsymbol{q}$ and concentrated forces acting on Q as $\boldsymbol{P}$. The last equation can be written as $\delta W_{\mathrm{ext}}^{(\mathrm{e})} = \delta \boldsymbol{u}^{\mathrm{T}} \boldsymbol{f}_{(\mathrm{e})}$ and equating to (3.6) we get

$$\delta \boldsymbol{u}_{js}^{\mathrm{T}} \boldsymbol{k}_{(\mathrm{e})}^{ij\tau s} \boldsymbol{u}_{i\tau} = \delta \boldsymbol{u}_{js}^{\mathrm{T}} \boldsymbol{f}_{(\mathrm{e})}, \tag{3.8}$$

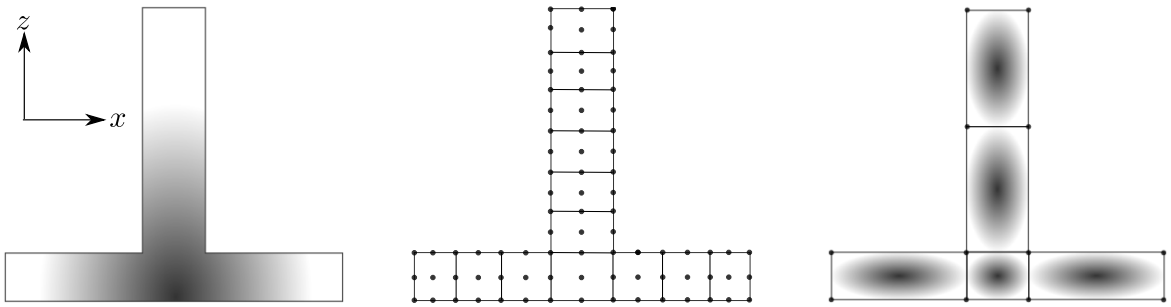

Figure 3.1: Typical cross-sectional discretisation for: (a) Taylor expansions (hierarchical); (b) Lagrange expansions (node-based); (c) Serendipity Lagrange expansions (hierarchical and node-based). Grey shading indicates hierarchical shape functions over the section or section sub-domain.

which is the classical statement for a finite element formulation, where $\boldsymbol{k}^{(e)}_{ijrs}$ and $\boldsymbol{f}^{(e)}$ are, respectively, the Unified Formulation element stiffness Fundamental Nucleus and the generalised load vector of the generic element. The explicit form of the Fundamental Nucleus can be found by taking the linear part of the equations described in Appendix C.

3.3.1 Serendipity Lagrange Expansion Models

One of the main advantages of using TE models is that enriching the displacement field is straightforward, by increasing the order of expansion. On the other hand, LE models require a mesh refinement for the same purpose. The trade-offs between choosing TEs over LEs is on numerical stability and loss of accuracy close to singularities, in order to avoid re-meshing. Furthermore, TE models can be categorised as Equivalent Single Layer (ESL) or Local models, since the material properties are homogenised by integrating over the entire cross-section. LE models are Layer-wise or Non-Local models, the material properties are related to each element in the cross-section. By adopting the SL expansion model the two best properties of TE and LE are combined. Cross-sections are discretised using four-noded Lagrange sub-domains and the displacement field, within sub-domains, can be enriched by increasing the order of the local Serendipity Lagrange expansion as depicted in Figure 3.1(c), where the shading represents enrichment hierarchy. The proposed expansion model is based on the hierarchical finite element shape functions as derived from Trunk (or Serendipity) polynomial spaces in [5].

In order to construct the new expansion functions, a set of 1D polynomials and a set of 2D polynomials are required. These polynomials are combined and used as shape functions for the displacement field within the computational sub-domains. Enrichment of the kinematics can then be achieved by increasing the expansion order and/or the number of elements in the cross-section.

3.3.1.1 1D Lagrange-type Polynomials

The shape functions are constructed in two steps, one is to assemble 1D polynomials with certain properties followed by the 2D polynomials. This section explains the former.

Consider the set $\Xi^{1D} = \{\xi \in \mathbb{R} : -1 \leq \xi \leq 1\}$ and let $N \geq 2$ be the number of equally spaced points ξ_i within Ξ^{1D}. By construction N will also be the order of the polynomial. Starting at $\xi = -1$,

$$\xi_i = -1 + \frac{2}{(N-1)}(i-1), \qquad \text{where} \qquad i = 1, \ldots, N. \tag{3.9}$$

An N^{th}-order polynomial, $p_N(\xi)$, can be found such that

$$\begin{aligned} p_N(-1) &= 0, \\ p_N(1) &= 0, \\ p_N(\xi_i) &= 0. \end{aligned} \tag{3.10}$$

The explicit form of this Lagrange-type polynomial is

$$p_N(\xi) = (\xi - \xi_1)(\xi - \xi_2)\cdots(\xi - \xi_{N-1})(\xi - \xi_N), \tag{3.11}$$

such that, for instance,

$$\begin{aligned} p_2(\xi) &= (\xi+1)(\xi-1), \\ p_3(\xi) &= (\xi+1)\xi(\xi-1), \\ p_4(\xi) &= (\xi+1)(\xi+\tfrac{1}{3})(\xi-\tfrac{1}{3})(\xi-1), \\ p_5(\xi) &= (\xi+1)(\xi+\tfrac{1}{2})\xi(\xi-\tfrac{1}{2})(\xi-1), \\ p_6(\xi) &= (\xi+1)(\xi+\tfrac{3}{5})(\xi+\tfrac{1}{5})(\xi-\tfrac{1}{5})(\xi-\tfrac{3}{5})(\xi-1), \\ p_7(\xi) &= (\xi+1)(\xi+\tfrac{2}{3})(\xi+\tfrac{1}{3})\xi(\xi-\tfrac{1}{3})(\xi-\tfrac{2}{3})(\xi-1). \end{aligned} \tag{3.12}$$

These polynomials are proportional to the traditional Lagrange polynomials, which can be easily derived from (3.11), for details see [76, 77].

The property of vanishing values on the boundary of Ξ^{1D} is essential to ensure continuity of the displacement field at the interfaces between cross-sectional sub-domains, and the completeness of the vector space basis.

3.3.1.2 2D Lagrange-type Polynomials

Polynomials $p_N(\xi)$ derived in the previous section can be used to define their N^{th}-order 2D counterparts in $\Xi^{2D} = \{(\xi, \eta) \in \mathbb{R}^2 : -1 \leq \xi \leq 1, -1 \leq \eta \leq 1\}$. These 2D polynomials are to be employed as hierarchical Lagrange-type shape functions. Three different sets of functions are needed, each with specific requirements:

1. A set of four first-order Lagrange polynomials. These are bi-linear polynomials that take value 1 at each of the four nodes and 0 on the others. These are named polynomials of type I.

2. A set of N^{th}-order polynomials that vanish along three sides of $\Xi^{2\text{D}}$ in order to satisfy the continuity of displacements across cross-sectional sub-domains. These are named polynomials of type IIA and IIB.

3. A set of N^{th}-order polynomials defined in the interior subset of $\Xi^{2\text{D}}$ that vanish along its four sides. These are named as polynomials of type III.

Letting $r = 1,\ldots,N$, and $s = 1,2,3,4$, the SL expansion functions are indicated by

$$L_\tau^{(\text{t})}(\xi,\eta), \tag{3.13}$$

where the subscript τ is an index defined as

$$\tau = \begin{cases} s & \text{for} \quad r = 1 \\ 4(r-1)+s & \text{for} \quad r = 2,3 \\ 4(r-1)+\frac{(r-3)(r-4)}{2}+s & \\ (4r+1)+\frac{(r-3)(r-4)}{2},\ldots,4r+\frac{(r-2)(r-3)}{2} & \text{for} \quad r \geq 4 \end{cases}, \tag{3.14}$$

and the superscript (t) denotes the polynomial type as follows

$$\text{t} = \begin{cases} \text{I} & \text{for} \quad r = 1 \quad \text{and} \quad \tau \in [s] \\ \text{IIA} & \text{for} \quad r = 2,3 \quad \text{and} \quad \tau \in [4(r-1)+s] \\ \text{IIB} & \text{for} \quad r \geq 4 \quad \text{and} \quad \tau \in \left[4(r-1)+\frac{(r-3)(r-4)}{2}+s\right] \\ \text{III} & \text{for} \quad r \geq 4 \quad \text{and} \quad \tau \in \left[(4r+1)+\frac{(r-3)(r-4)}{2},\ldots,4r+\frac{(r-3)(r-4)}{2}\right] \end{cases}. \tag{3.15}$$

Following on from equations (3.14) and (3.15),

$$L_\tau^{(\text{I})} = \frac{1}{4}(1+\xi_s\xi)(1+\eta_s\eta), \tag{3.16}$$

where (ξ_s,η_s) are the coordinates of the four corner nodes in $\Xi^{2\text{D}}$.

$$L_\tau^{(\text{IIA,IIB})} = \frac{1}{2}\begin{bmatrix}(1-\eta)\\(1+\xi)\\(1+\eta)\\(1-\xi)\end{bmatrix}^{\text{T}}\begin{bmatrix}\delta_{1s} & 0 & 0 & 0\\ 0 & \delta_{2s} & 0 & 0\\ 0 & 0 & \delta_{3s} & 0\\ 0 & 0 & 0 & \delta_{4s}\end{bmatrix}\begin{bmatrix}p_r(\xi)\\p_r(\eta)\\p_r(-\xi)\\p_r(-\eta)\end{bmatrix}, \tag{3.17}$$

where δ_{ij} is the Kronecker delta and the argument of $p_r(-\xi)$ and $p_r(-\eta)$ is negative to ensure that all $L_\tau^{(\text{IIA,IIB})}$ polynomials of odd order are identical and separate by a 90 degree rotation, a property of shape functions required to ensure completeness. And finally,

$$L_\tau^{(\text{III})} = p_n(\xi)p_m(\eta), \tag{3.18}$$

with $n,m = 2,3,...N$, constrained by $n+m = r$ and $n+m \leq N$.

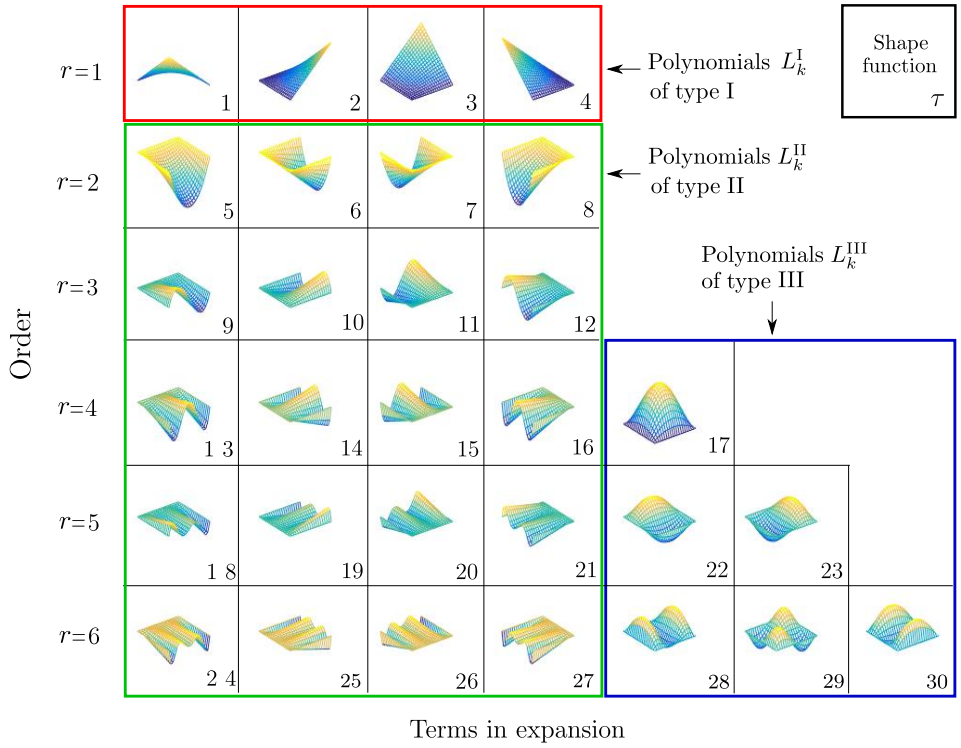

Figure 3.2: Serendipity Lagrange hierarchic shape functions (adapted from [5]).

The first few polynomials $L_\tau^{(\mathrm{t})}$, sorted by type, order and index τ are presented in Figure 3.2. The N^{th}-order Serendipity Lagrange models are implicitly assumed to include all of the shape functions of orders 1 to N, no reduced models are possible. As an example, a model of order $N = 5$ contains:

1. Four bi-linear Lagrange polynomials (type I). Subscripts 1 to 4;
2. Four second-order polynomials (type II). Subscripts 5 to 8;
3. Four third-order polynomials (type II). Subscripts 9 to 12;
4. Five fourth-order polynomials (4 type II, 1 type III). Subscripts 13 to 17;
5. Six fifth-order polynomials (4 type II, 2 type III). Subscripts 18 to 23.

The explicit form of the shape functions can be found in Appendix A. Similarly, cross-sectional displacements of order $N = 2$, at the i^{th} Lagrange beam node, take the form (using the notation $F_\tau = L_\tau^{(\mathrm{t})}$):

$$\boldsymbol{u}_i = \sum_{k=1}^{4} L_k^{(\mathrm{I})} \boldsymbol{u}_{ik} + L_5^{(\mathrm{II})} \boldsymbol{u}_{i5} + L_6^{(\mathrm{II})} \boldsymbol{u}_{i6} + L_7^{(\mathrm{II})} \boldsymbol{u}_{i7} + L_8^{(\mathrm{II})} \boldsymbol{u}_{i8}. \tag{3.19}$$

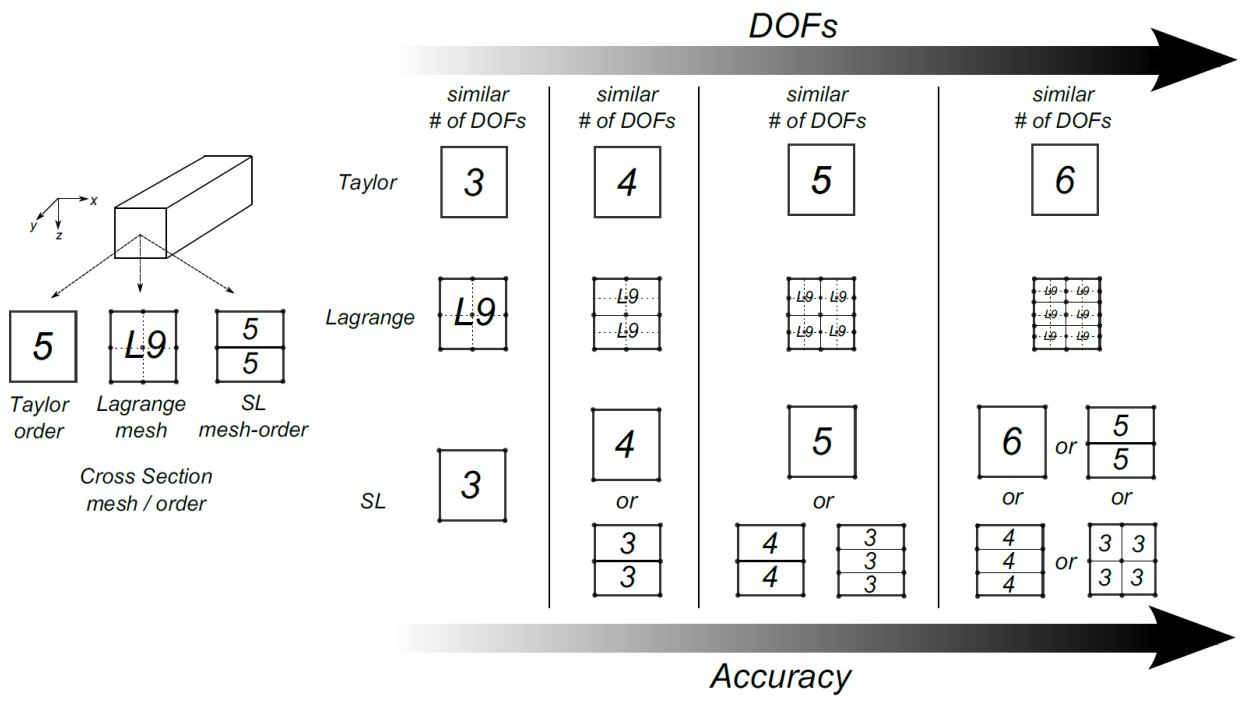

Figure 3.3: Schematic summary of possible cross-sectional discretisation strategies in Taylor, Lagrange and Serendipity Lagrange expansion models.

The SL expansion model combines the two main characteristics of both TE and LE models, because: (a) SL shape functions have the same hierarchical nature of TEs; (b) as in LE models, they are defined on sub-domains thus enabling local refinement and improved numerical stability, as it is shown in the following sections. A schematic representation of the trade-offs between the three expansion models is shown in Figure 3.3.

3.4 Cross-Sectional Shape Mapping

The element stiffness matrix is obtained by integrating the terms of equation (3.6) throughout the element domain. When dealing with complex geometries and curved section beams, the integration domain, in general, is curved. The correct geometrical description is of fundamental importance. The SL expansion functions, as defined in Section 3.3.1, are used to enrich the kinematics in the cross-section. These functions are integrated over the beam's cross section, which requires transformation of the coordinates. If the edges of a quadrilateral element are straight, the approximation of the geometry is obtained through linear mapping by using linear Lagrange polynomials, which in this case coincide with SL functions of order 1. However, if the cross-section is curved a different approach is needed, and an alternative cross-sectional shape mapping is used. In an isoparametric formulation the same functions describing the displacement

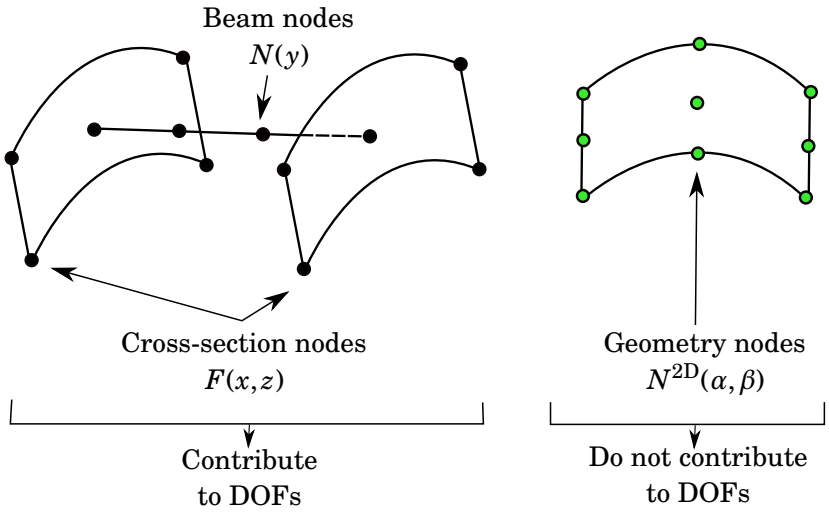

Figure 3.4: Element discretisation and shape functions.

field are used to describe the geometry, which has an advantage: modelling the geometry correctly, automatically improves the accuracy of the field. This may come with a high computational cost, especially if the UF is used. Another possibility is to model the geometry independently from the displacement field, this approach is adopted herein.

The hierarchical nature of the SL shape functions allows to employ these inside a general curved element, as the order of expansion can be increased as needed. The aim is to describe the curved geometry without increasing the number of DOFs of the model. Some possible ways of modelling the geometry are:

1. Blending-method and high-order polynomials [78]

2. Exact geometry description using non-linear functions [5]

3. Using a CAD-like approach with Lagrange 2D-shape functions

The first method requires a polynomial description for each of the four sides of the element, situation that can be cumbersome if the element is highly distorted or if a large number of elements are used. The second method requires the exact description, therefore only a limited amount of cases can be studied[1], or else, complicated functions have to be constructed. The third method, which is of common use in finite element analysis, makes use of Lagrange interpolation functions. These are easy to implement and can be combined with existing CAD software's[2]. The latter is adopted in this chapter, and is now described in more detail.

[1]This method is used in Chapter 4

[2]For must of the examples, a software called Gmsh [79] has been used to discretise and mesh the structures.

Three sets of independent, yet coupled, shape functions are used: cross-section shape-functions $F(x,z)$, beam shape-functions $N(y)$ and cross-section geometry shape-functions $N^{2D}(\alpha,\beta)$. Let $N^{2D}(\alpha,\beta)$ be a function, defined in $[-1,1]\times[-1,1]$, describing the geometry such that the position vector $\boldsymbol{x}$ of any given point in the structure, in the global Cartesian system, can be represented as

$$\boldsymbol{x} = N_k^{2D}(\alpha,\beta)\boldsymbol{x}_k, \tag{3.20}$$

where $\boldsymbol{x}_k \in \mathbb{R}^2$ are the position vectors of the nodes of the element, and $k = 1,...,N_{ne}$, with N_{ne} the number of nodes; 9-noded or 16-noded Lagrange elements are commonly used. The number of nodes used to represent the element geometry is not related to those used for the discretisation of the kinematic field in the cross-section and beam axis, as the shape functions are independent from each other. Therefore, only the functions $F(x,z)$ and $N(y)$ contribute to the DOFs, while $N^{2D}(\alpha,\beta)$ describes the geometry and does not increase the computational cost. Figure 3.4 shows how the displacement field is approximated by decoupling the cross-section and beam axis elements. The connection between the displacement shape functions[3] $F(\alpha,\beta)N(\xi)$, the 2D-mapping function $N^{2D}(\alpha,\beta)$ and the structure's geometry is via the Jacobian matrix, defined as

$$\mathcal{J} = \begin{bmatrix} x_\alpha & z_\alpha \\ x_\beta & z_\beta \end{bmatrix}.$$

The entries of $\mathcal{J}$ are the derivatives of (3.20), and can be interpreted as the local curvilinear basis vectors. The relationship between the cross-section function derivatives in the local and global coordinate system is

$$\begin{bmatrix} F_x \\ F_z \end{bmatrix} = \begin{bmatrix} x_\alpha & z_\alpha \\ x_\beta & z_\beta \end{bmatrix}^{-1} \begin{bmatrix} F_\alpha \\ F_\beta \end{bmatrix}. \tag{3.21}$$

Equation (3.2) together with (3.20) and (3.21) are used to describe the displacement field in a curved cross-section element. Is important to note that, with this description, only the cross-section is curved and not the beam axis. This formulation works only for prismatic elements, and therefore only piece-wise prismatic structures can be modelled. This is a limitation of the current Unified Formulation. In Chapter 5 a novel solution to this problem is provided.

3.5 Chebyshev Node Distribution

It is well known that the Unified formulation models can lead to inaccurate prediction of shear stresses along the axis and close to singularities. The theoretical reason is still a topic of research, nevertheless, one hypothesis is that it may be caused by the incompatibility[4] and/or low order of expansion in both, the cross-section and beam directions. One possible solution is to increase the number of beam elements along the axial direction, but this inevitably increases the degrees

[3] Note that the displacement shape function is a product of both F and N as a single unit, additionally, the functions are defined in the local coordinate system and then transformed to the global system.

[4] In the sense that the resultant polynomials are not a complete and/or orthogonal base.

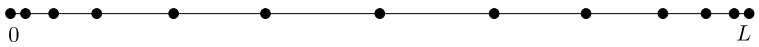

Figure 3.5: Sample Chebyshev grid in $[0, L]$.

of freedom required for convergence. Another possible solution is to use the Mix Interpolation of Tensorial Components Method (MITC) [80], which, in some cases, might introduce spurious modes. We propose a simple and effective alternative: to redistribute the nodes with a bias towards boundaries and features. Namely, the nodes are distributed using a Chebyshev biased mesh. Chebyshev polynomials are known to give better convergence rates and minimise Runge phenomena [81].

Chebyshev Polynomials The polynomials of the first kind of order n, denoted as $T_n(y) \in [-1, 1]$, are a set of orthogonal functions defined as the solutions to the Chebyshev differential equation and may be defined using a series expansion:

$$T_n(y) = \frac{n}{2} \sum_{i=0}^{\lfloor \frac{n}{2} \rfloor} \binom{n}{2i} y^{n-2i} \left(y^2 - 1\right)^i . \tag{3.22}$$

Chebyshev meshes are defined using the set of roots of (3.22) in $[-1, 1]$, i.e.

$$y_k = \cos\left(\frac{2k-1}{2n}\pi\right), \qquad k = 1, \ldots, n, \tag{3.23}$$

which are mapped in $[0, L]$ as follows:

$$y_k = \frac{L}{2} - \frac{L}{2}\cos\left(\frac{2k-1}{2n}\pi\right). \tag{3.24}$$

Refer to Figure 3.5, where y_k were used to place n nodes along the axis of the beam. The nodes are positioned more compactly towards the boundaries.

3.6 Numerical Examples

In this section the capabilities of the SL model are explored and assessed. For this purpose two examples are used, one is a cantilever square cross-section beam and the second is a cantilever curved stiffened structure. For the former, the convergence, numerical stability and stress analysis are studied; for the latter, a detailed stress analysis is performed[5].

3.6.1 Square Cross-Section Cantilever Beam

The structure considered is a clamped-free, square cross-section beam with length $L = 1\,\text{m}$, height $h = 0.1\,\text{m}$ and width $b = 0.1\,\text{m}$. The loading condition is $P_z = -10\,\text{N}$ applied at the end ($y = L$) as

[5]Even though only two examples are presented in this chapter, the SL formulation is used throughout the whole manuscript.

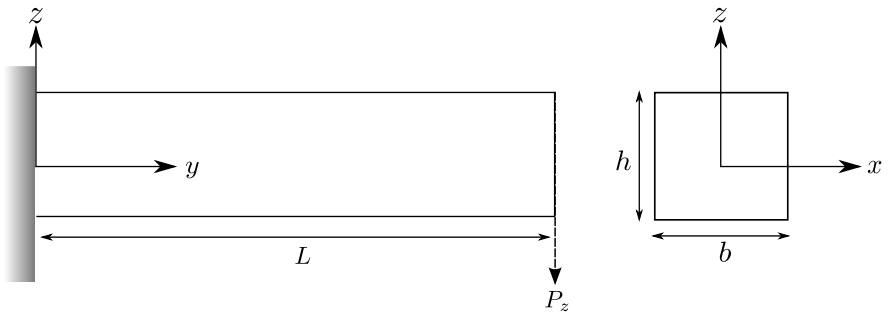

Figure 3.6: Square cross-section cantilever beam with applied tip load.

shown in Figure 3.6. The constituent material is isotropic with Young's modulus $E = 71$ GPa and Poisson's ratio $\nu = 0.33$. A 3D FE analysis with 40,000 `SOLID186` (3D 20-noded) elements is performed with ANSYS and used as verification.

3.6.1.1 Convergence Analysis

Herein the SL models are compared with the traditional Unified Formulation models: TE and LE. Convergence rates for displacement and stresses, accuracy and DOFs are compared among models. Analytical results are also provided, obtained with classical theories such as Euler-Bernoulli (EB) and Timoshenko beam (TB). In addition, results are also compared to Timoshenko's enhanced analytical (TB-EN) solution[6] obtained using Airy's stress function [18]. The following analytical expressions are employed to calculate deflection and stresses [18, 41]:

$$u_z^{\text{EB}} = \frac{P_z L^3}{3EI} \tag{3.25}$$

$$u_z^{\text{TB}} = \frac{P_z L^3}{3EI} + \frac{P_z L}{AG} \tag{3.26}$$

$$\sigma_{yy}^{\text{EB,TB,TB-EN}} = \frac{P_z (L-y) z}{I} \tag{3.27}$$

$$\tau_{yz}^{\text{TB}} = -\frac{3P_z}{2A} \tag{3.28}$$

$$\tau_{yz}^{\text{TB-EN}} = \tau_{yz}^{\text{TB}} \left[\frac{-\nu}{1+\nu} \left(\frac{1}{3} + \sum_{n=1}^{\infty} \frac{4}{\pi^2} \frac{(-1)^n}{n^2 \cosh(n\pi)} \right) + 1 \right] \tag{3.29}$$

where G is the shear modulus, I is the second moment of area with respect to the x axis and A is the area of the cross-section.

Transverse displacement, normal and shear stresses are evaluated at various locations as shown in Table 3.1. The through-thickness distribution of shear stress at midspan is shown in

[6] This enhanced formulation predicts accurate transverse shear stress distribution. In chapter 11 of reference [18], the formulation is termed as "exact". However, it is derived by enforcing certain stress components to be zero and assumes that the bending stress varies linearly along the thickness coordinate. As such, strictly speaking, the formulation is not exact.

Table 3.1: Displacement and stress components of the square cross-section beam.

	$u_z(0,L,0)$ [m] $\times 10^{-6}$	$\sigma_{yy}(0,0.21437L,h/2)$ [Pa]	$\tau_{yz}(0,L/2,0)$ [Pa]	DOFs #
ANSYS				
SOLID186	-5.330	47138.0	-1392.4	541059
Analytical				
EB	-5.333	47137.8	-	-
TB	-5.368	47137.8	-1500	-
TB-Enhanced	-5.333	47137.8	-1388.8	-
Taylor Expansions				
T1	-5.369	47139.9	-1000.0	279
T2	-5.314	47137.6	-1000.0	558
T3	-5.322	47148.0	-1396.6	930
T4	-5.326	47137.4	-1396.6	1395
T5	-5.328	47140.8	-1387.6	1953
T6	-5.328	47123.4	-1387.6	2604
T7	-5.329	47131.1	-1389.6	3348
Lagrange Expansions				
1×1 L4	-4.462	47139.7	-1000.0	372
2×1 L4	-4.939	49928.9	-1091.4	558
2×2 L4	-5.064	49761.3	-934.3	837
1×1 L9	-5.315	47145.3	-958.6	837
2×1 L9	-5.322	47139.7	-1579.9	1116
2×2 L9	-5.325	47138.6	-1583.2	2325
3×2 L9	-5.326	47136.4	-1341.2	3255
3×3 L9	-5.327	47136.5	-1342.3	4557
Serendipity Lagrange Expansions				
SL1	-4.462	47139.7	-1000.0	372
SL2	-5.315	47146.9	-958.6	744
SL3	-5.324	47149.1	-1396.6	1116
SL4	-5.327	47136.1	-1409.2	1581
SL5	-5.328	47139.2	-1387.6	2139
SL6	-5.329	47123.5	-1387.3	2790
SL7	-5.329	47134.0	-1389.6	3534

Figure 3.7 for SL ($N = 5$), Taylor ($N = 5$) and three Lagrange models with different cross-sectional discretisations. Plots of the percentage error of displacement, normal and shear stress (with respect to the reference 3D FE solution) versus DOFs are presented in Figure 3.8.

From the results it is clear that the SL model, with one cross-sectional element and order

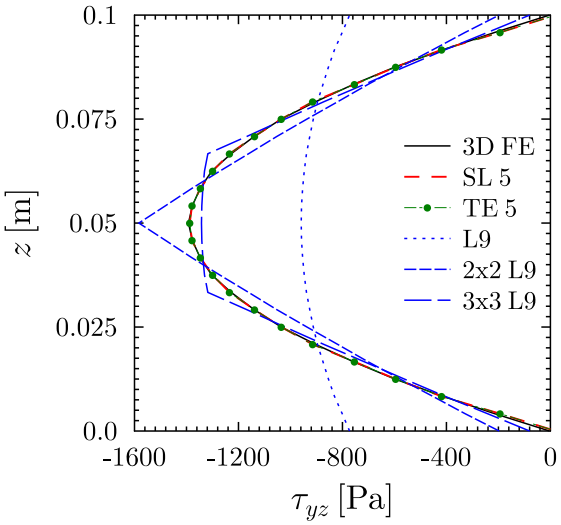

Figure 3.7: Through-thickness plot of shear stress (τ_{yz}) at beam mid span, $(x, y) = (0, L/2)$.

$N = 1$, provides the same results as the Lagrange model with one `L4` element. This is expected since the models have identical kinematical descriptions. The benefits of using the SL elements are evident for expansions of order greater than one ($N > 1$). SL, TE and LE models perform similarly in terms of convergence of displacement and normal stress. On one hand, the fast convergence in displacement can be explained due to the fact that the formulation is displacement based; on the other hand, similar convergence behaviour for normal stress for all the models is expected, since the discretisation along the beam is the same. Turning our attention to shear stresses, SL and TE expansions achieve convergence at around 2,000 DOFs. Conversely, as shown in Figure 3.8c, Lagrange expansions fail to do so. Even upon further cross-sectional discretisation and a number of DOFs in excess of 26,000, Figure 3.9 shows that τ_{yz} does not fully converge. This numerical behaviour is attributed to the use of low order—linear (`L4`) or quadratic (`L9`)—shape functions for the cross-sectional elements, which upon differentiation can only provide piecewise constant or linear stress variations respectively. Is worth to mention that a further discretisation would result in a converged solution at some point, this case is not presented in the present example.

3.6.1.2 Numerical Stability

In some cases Unified Formulation models may lead to numerical instabilities in the form of locking, as in the case of the oscillations in shear stresses along the axial direction and towards singularities, and as ill conditioned systems, if the order of expansion is high ($\sim N \geq 9$). These phenomena are addressed and discussed in this section. Solution for both cases are provided.

As mentioned in Section 3.5, one possible way of solving the oscillations in shears is to use a Chebyshev-bias beam mesh, therefore here a comparison between the convergence behaviour

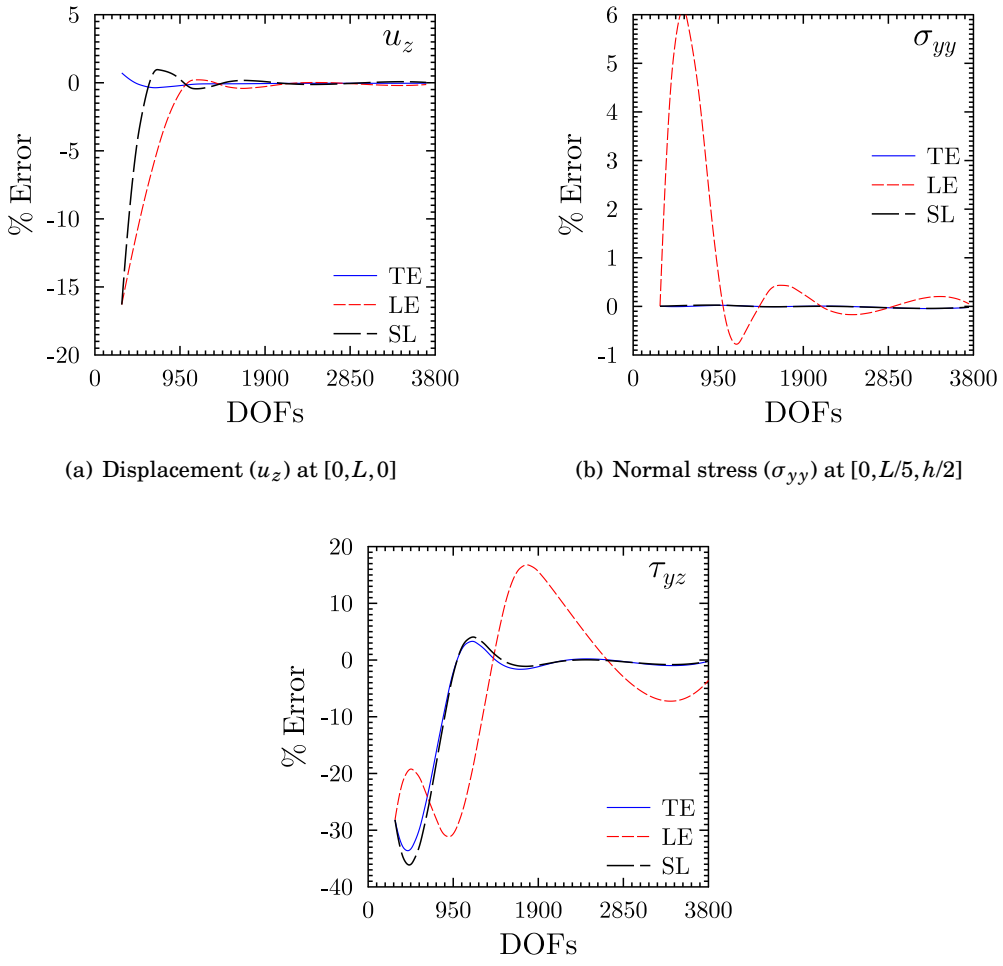

(a) Displacement (u_z) at $[0, L, 0]$

(b) Normal stress (σ_{yy}) at $[0, L/5, h/2]$

(c) Shear stress (τ_{yz}) at $[0, L/2, 0]$

Figure 3.8: Relative error with respect to reference 3D FE solution.

of stress fields obtained using the proposed mesh and uniform beam meshes is presented. The structure considered is the same as in the previous section.

In the case of the Unified Formulation model a SL expansion with one element in the cross-section and with order $N = 5$ is used. The analyses are carried out with two different uniform meshes of 4-noded (B4) elements: 10 and 20 B4; for the case of Chebyshev-biased mesh, a 10 B4 mesh is chosen. Node distribution and degrees of freedom are shown in Figure 3.10. It can be seen that the Chebyshev and uniform meshes, with 10 B4 elements, have almost half the DOFs of the uniform mesh with 20 B4 elements.

Normal stress (σ_{yy}) values along the beam, at $x = 0$, $z = h/2$, are plotted in Figure 3.11(a). For further clarity, Figure 3.11(b) zooms in on the deviations displaying σ_{yy} from root up to 10% of the beam length, i.e. for $y \in [0, 0.1L]$. Similarly, shear stress (τ_{yz}) distributions along the beam at $x = 0$, $z = 0$, are shown in Figures 3.12(a) and 3.12(b). Finally, through-thickness variations of σ_{yy}

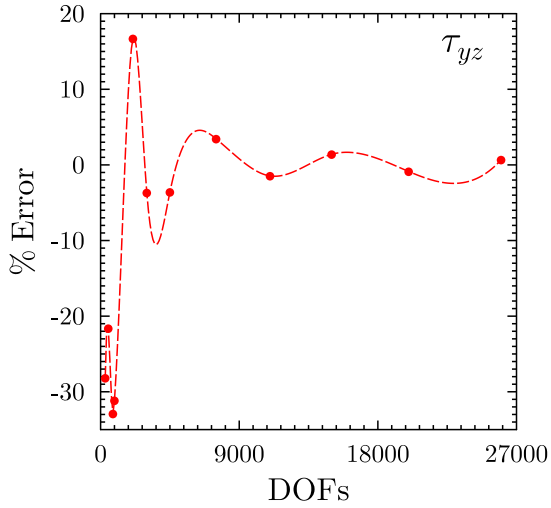

Figure 3.9: Relative error of shear stress (τ_{yz}) at $[0, L/2, 0]$ with respect to reference 3D FE solution for refined Lagrange expansion models.

and τ_{yz} at $x = 0$, $y = 0.1L$ are plotted in Figures 3.13(a) and 3.13(b).

Theses results show clearly that using a Chebyshev bias mesh is sufficient to improve the accuracy and to alleviate the shear oscillations without increasing the number of DOFs. Ten Chebyshev elements give even better results than using double number of uniform elements. For this reason, Chebyshev meshes are adopted for longitudinal discretisations in all of the following analyses.

Ill conditioned matrices appear more commonly in TE models, due to the way the stiffness matrix is assembled. Higher order terms are at the bottom of the element stiffness matrix, creating regions with very small, close to zero, values. When using TE models this might be unavoidable, since the only way of refining the displacement field is to increase the order of expansion[7]. The instability, which may be measured by computing the conditioning number (r_c)

[7] By using orthogonal polynomials this problem may ease and stability might be improved.

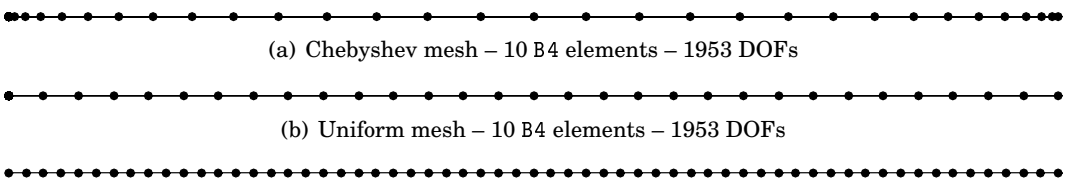

(a) Chebyshev mesh – 10 B4 elements – 1953 DOFs

(b) Uniform mesh – 10 B4 elements – 1953 DOFs

(c) Uniform mesh – 20 B4 elements – 3843 DOFs

Figure 3.10: Chebyshev and uniform node distributions along the beam length and their respective DOFs for Taylor model with $N = 5$.

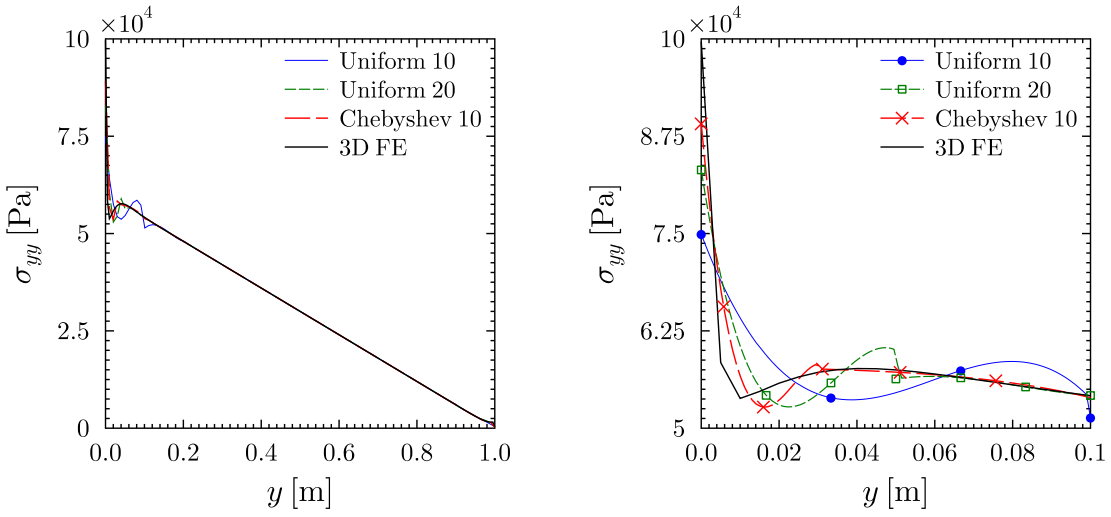

(a) σ_{yy} for $(x,z) = (0, h/2)$ and $y \in [0, L]$.

(b) σ_{yy} for $(x,z) = (0, h/2)$ and $y \in [0, 0.1L]$.

Figure 3.11: Variation of normal stress (σ_{yy}) along the length of the cantilever, square cross-section beam meshed with uniform and Chebyshev grids.

of the ensuing stiffness matrix [76]. Figure 3.14 is a plot of $1/r_c$, reciprocal of the conditioning number, versus, N, the expansion order of SL and TE models with one cross-sectional element. From the figure, we observe that, for increasing N, the stiffness matrix of TE models becomes ill-conditioned (i.e. r_c diverges). Conversely, the conditioning properties of SL models are almost

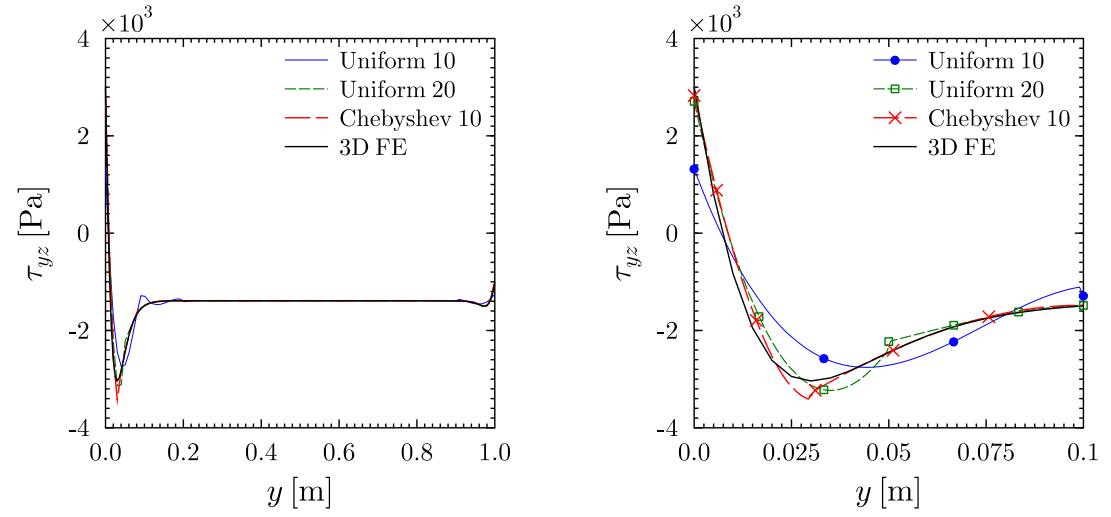

(a) τ_{yz} for $(x,z) = (0,0)$ and $y \in [0, L]$.

(b) τ_{yz} for $(x,z) = (0,0)$ and $y \in [0, 0.1L]$.

Figure 3.12: Variation of shear stress (τ_{yz}) along the length of the cantilever, square cross-section beam meshed with uniform and Chebyshev grids.

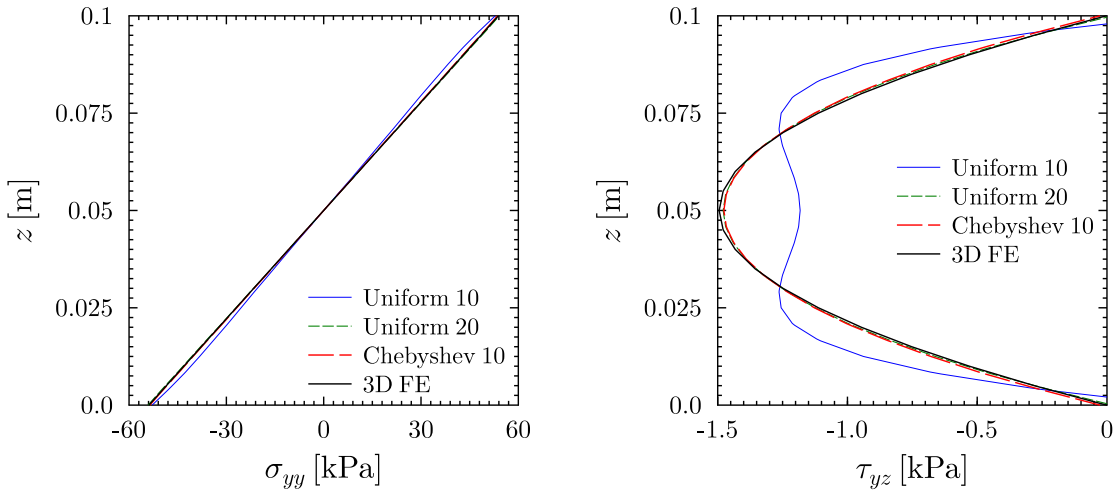

(a) Normal stress.

(b) Shear stress.

Figure 3.13: Through the thickness variation of normal (σ_{yy}) and shear stress (τ_{yz}) at $(x, y) = (0, 0.1L)$ for the cantilever, square cross-section beam meshed with uniform and Chebyshev grids.

independent from the expansion order. This is shown to be the case also for LE models, proving that cross-sectional discretisation improves numerical stability. The reader is referred to [12] for further examples on the stability of the model.

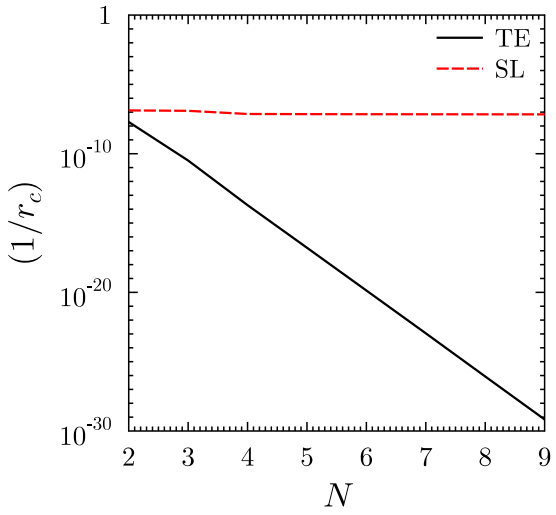

Figure 3.14: Conditioning number of the system's stiffness matrix versus expansion order for Taylor and Serendipity Lagrange models.

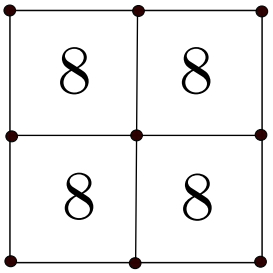

Figure 3.15: Refined cross-section: 2×2 L4 elements and order 8.

3.6.1.3 Localised Stresses

To demonstrate the capabilities of the SL model in capturing the local variation of 3D stresses towards the clamped edges, relevant stress components are measured at several locations along the beam. In the this example, in order to capture 3D stress fields accurately, the beam's cross-section discretisaion is different from the previous case: it is now divided into a 2×2 mesh of SL domains of order $N = 8$. Figure 3.15 shows the cross-section mesh and order of expansion, where the number represents the order of expansion inside each Lagrange element.

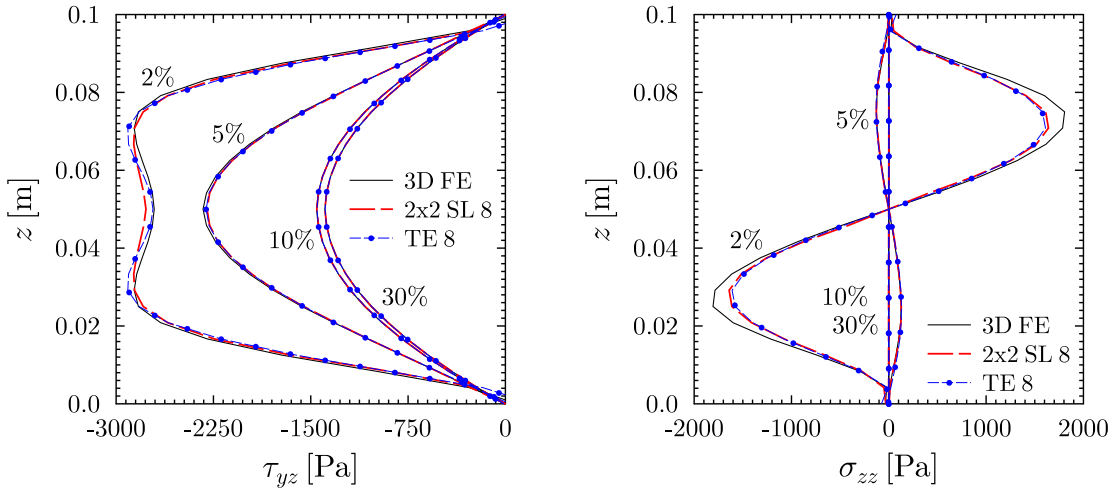

(a) Transverse shear stress

(b) Transverse normal stress

Figure 3.16: Through-thickness plot of shear and transverse normal stresses (τ_{yz} and σ_{zz}) at 2%, 5%, 10% and 30% of the beam length from the clamped end and $x = 0$.

Figure 3.16 shows the through-thickness distribution of shear (τ_{yz}) and transverse normal stress (σ_{zz}) at different locations from the clamped support. In this region, significant localised gradients in σ_{zz} occur, which can be characterized by the presence of an inflection point. Moving away from the clamped end, boundary layer effects diminish. SL calculations are in good agreement with 3D FE results at a significantly reduced computational cost ($\approx$ 1/10 of DOFs). Similar

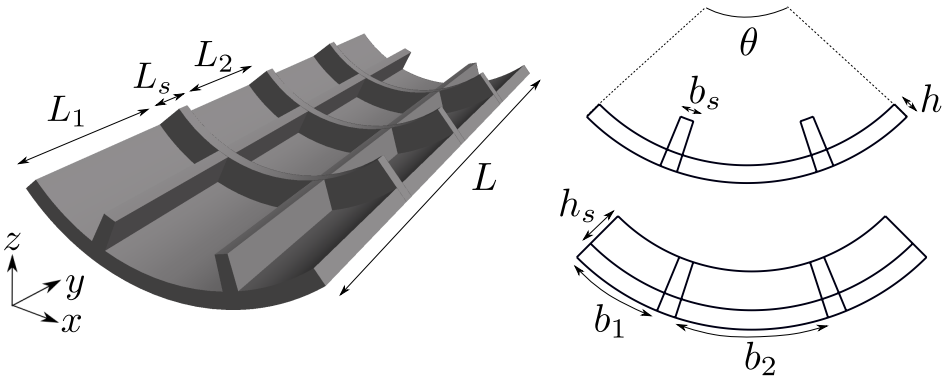

Figure 3.17: Stiffened curved panel geometry. Skin cross-section: top-right; Rib cross-section: bottom-right.

analyses, carried out with a TE model of order $N = 8$, are found to produce similar results, with some differences. For example, Figure 3.16b shows σ_{zz} to match the reference solution almost everywhere, except in a small region near the free surfaces, where $\partial\sigma_{zz}/\partial z$ is expected to vanish. Unlike the SL model, the TE expansion fails to capture this localised feature. This discrepancy can be explained by the fact that SLs allow not only the order of expansion to be increased, but also to discretise the cross-section at the same time. Owing to these capabilities, boundary effects in the stress profiles can be more readily captured. The reader is refer to [12] for further examples on the capabilities of the model in capturing localised stress fields in more complex structures.

3.6.2 Curved Stiffened Panel

The purpose of this section is to asseses the SL model in capturing the structural response of a complex curved structure by using the technique described in Section 3.4. The problem considered is a curved panel, stiffened with stringers and ribs, whose modelling usually requires the use of 2D or 3D finite elements. Figure 3.17 shows the geometry of the structure where: $L = 1\,\text{m}$, $L_1 = 0.24\,\text{m}$, $L_2 = 0.23\,\text{m}$, $L_s = 0.02\,\text{m}$, $b_1 = b_2 = 0.1\,\text{m}$, $b_s = 0.02\,\text{m}$, $h = 0.02\,\text{m}$, $h_s = 0.04\,\text{m}$ and $\theta = 90^o$. Notice that the structure can be described as having two different types of cross-sections: one related to the stringer-stiffened skin and one to the rib. The loading condition is $P = 1\,\text{kN}$ applied at $y = 1\,\text{m}$ in positive z-direction. The other end is clamped. Material is isotropic with Young's modulus $E = 71.7\,\text{GPa}$ and Poisson's ratio $\nu = 0.3$.

The discretisation of the cross-sections is explained first. The skin cross-section is discretised using 20 Lagrange 9-noded curved elements as shown in Figure 3.18(a) and the rib cross-section with 36 Lagrange 9-noded curved elements, as shown in Figure 3.18(b). As it can be seen in the geometry, the structure contains 4 segments with the skin cross-section, and 3 segments with the rib cross-section. The mesh is such that, at the interface between segments, the nodes coincide. The beam is discretised with 34 B4 elements. The skin segments contains 4 beam elements, and each rib, 6 beam elements. In every segment a Chebyshev distribution is used locally (the nodes

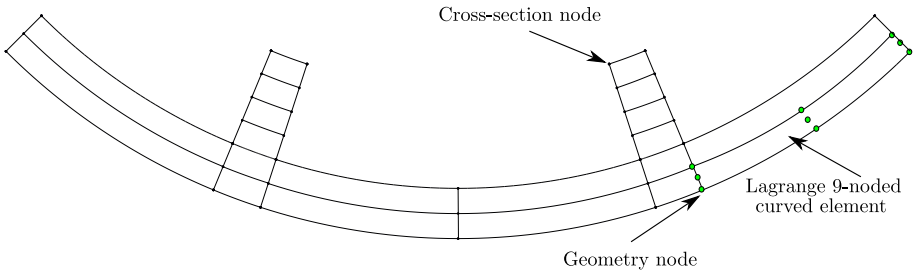

(a) Skin cross-section discretisation

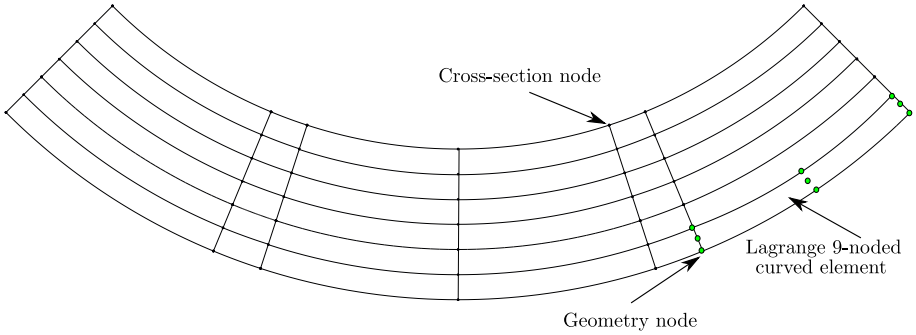

(b) Rib cross-section discretisation

Figure 3.18: Curved stiffened panel cross-section discretisation. Showing geometry nodes for one curved element only.

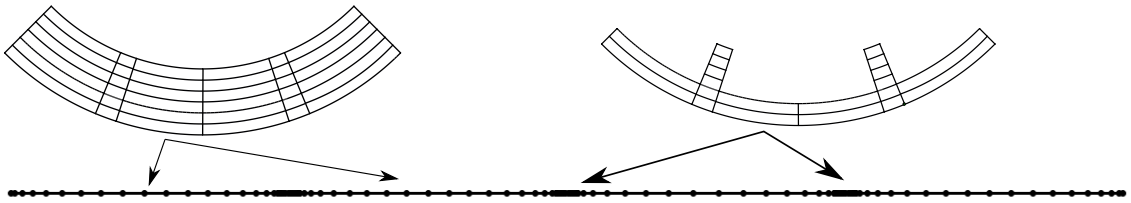

Figure 3.19: Beam axis mesh and cross-section segments.

are biased towards the edges of the individual segment), as shown in Figure 3.19. The order of the SL expansion is $N = 7$. The total number of DOFs is 246,645. An ANSYS 3D FE solid model with 9,286,608 DOFs is used as verification. Only the converged results are presented in this section.

Normal and shear stresses at several positions are now calculated and compared. Figure 3.20 shows the variation of the bending stress σ_{yy} at the top of the stringer and the skin along its length. Through-thickness variation of σ_{yy}, transverse shear τ_{yz}, computed at the rib-stringer junction at two different positions (25% and 50%) from the clamped end , are shown in Figure 3.21. The results shown in these figures are computed in the local coordinate system. The plots show that the model is able to capture accurate through thickness stress gradients.

Additionally, to highlight the model's ability in capturing localised regions accurately, contour

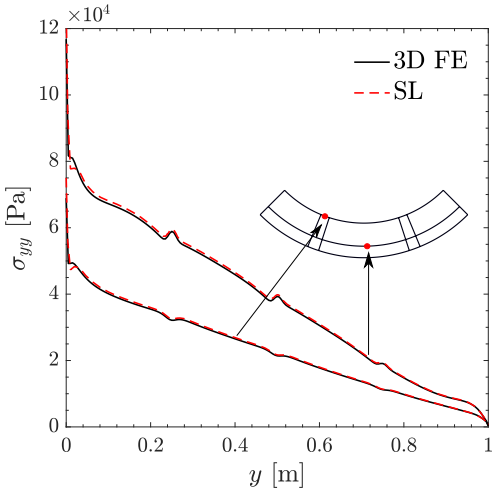

Figure 3.20: Variation of σ_{yy} stress along the length at two positions: top of the stinger and skin.

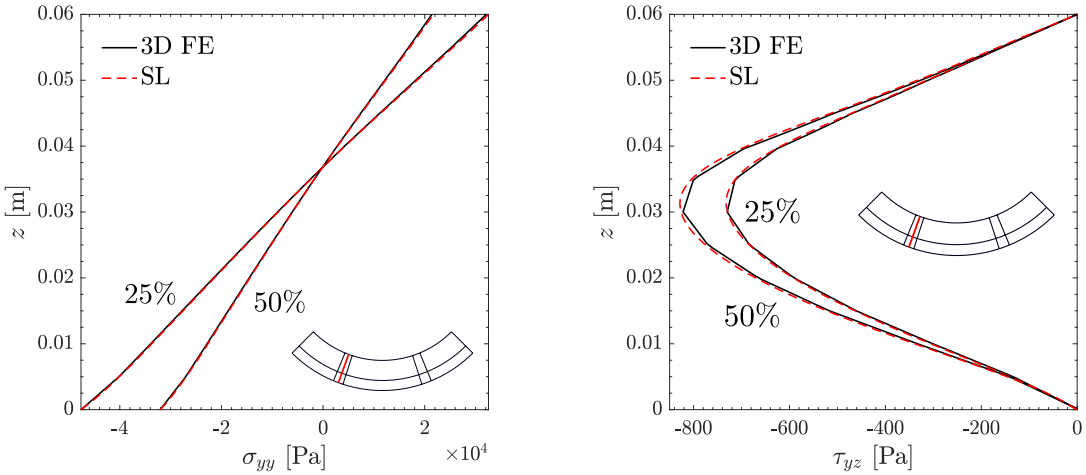

(a) Normal stress

(b) Shear stress

Figure 3.21: Normal σ_{yy} and shear τ_{yz} stress through thickness of the rib, at two positions from the clamped end.

plots[8] of normal and shear stresses across the entire cross-section, at 25% from the clamped end, are also shown in Figure 3.22. Contour plots show that the stress distributions are practically the same, with a maximum difference of 2.5% in the case of normal stress, and of 4.7% for the shear. The discrepancies are close to singularities, such as corners, as expected.

[8]Results are shown in global coordinate system.

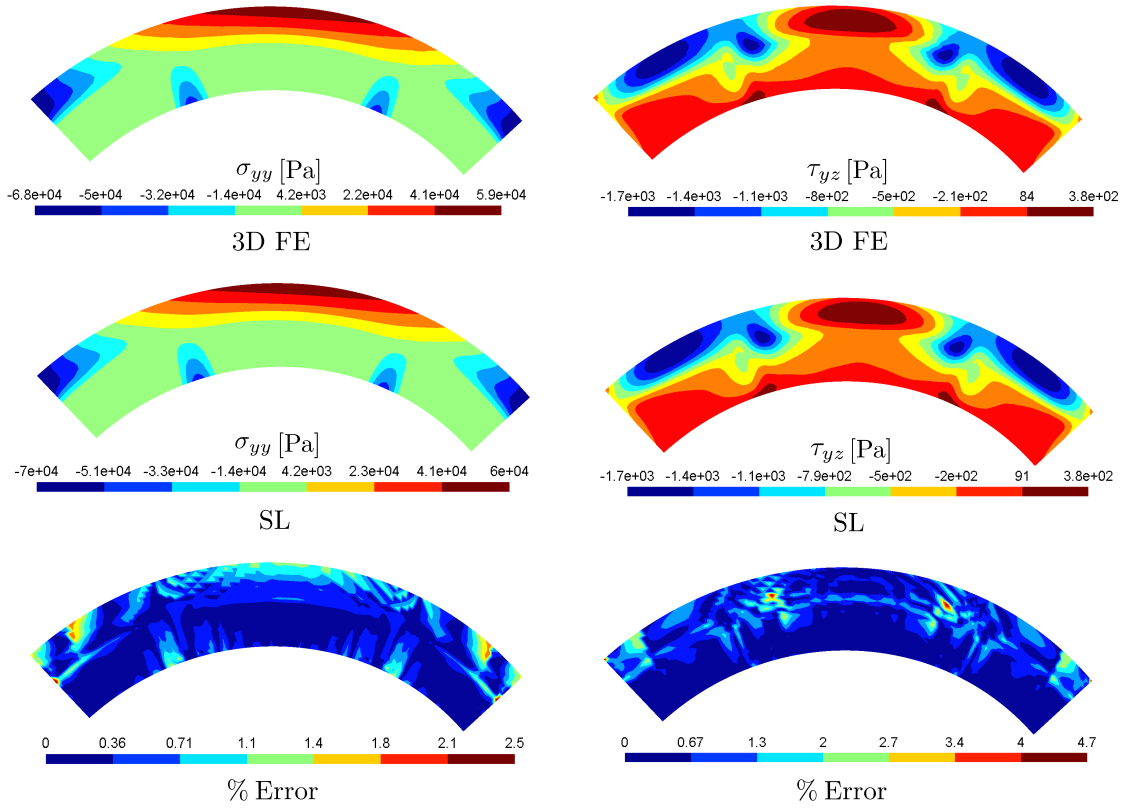

(a) Normal stress (b) Shear stress

Figure 3.22: Distribution of normal σ_{yy} and shear stress τ_{yz} in the cross-section at 25% of the clamped end.

3.7 Discussion

The Serendipity Lagrange Expansion Model intends to overcome some of the drawbacks of the most commonly used Unified Formulation models, namely Taylor and Lagrange expansions. For the TE model the drawback is numerical stability of the matrix and the *non-local*[9] nature of the expansion. LE models need re-meshing for the refinement of the kinematics, a situation that can be cumbersome if the structure is complex. The proposed solution is to combine the hierarchical property of Taylor with the local meshing capability of Lagrange expansion. The model is constructed by parts, first by defining hierarchical Lagrange-type 1D polynomials, which are easily built by locating equally space nodes along the beam element. Secondly, using as domain a 4-noded 2D Lagrange element, construct a set of polynomials that will serve as basis of a vector space, called Serendipity or Trunk space. These polynomials, defined inside a local element, are used as expansion functions for the cross-section displacement field. Refinement is achieved by first meshing the cross-section, and/or controlling the expansion order, which gives

[9] *Non-local* models are known also as *Equivalent Single Layer* models, where local features are not modelled exactly. *Local* models, or *Layer-wise* models, do have the capability of modelling these features.

the designer much more control and possibilities on how to proceed.

The first example shows the main capabilities of the model. SL convergence rate was compared to that of TE and LE models, and verified by using 3D FE and analytical formulas. For this case, results show that SL has a similar convergence rate as TE and LE in terms of displacements, which is expected since the models are displacement based. For stresses, especially through-thickness shears, the model behaves similar to TE, but significantly better than LE, since this last tends to have a slower rate due to the nature of the discretisation shape functions.

Combining the SL model with a Chebyshev biased mesh solved one of the known problems of the UF, namely, shear oscillations along the axial direction. The proposed solution is simple, effective and efficient, since the no additional DOFs were introduced. Additionally, it is shown that the SL model improves the conditioning of the matrix (i.e. the stability of the system), which allows to use higher-order of expansions without the potential problems caused by ill conditioned systems.

Results show that the local stresses close to the clamped end are three-dimensional in nature. Features as boundary layer effects, zero or high gradients, as close as 2% of the edge, were captured accurately by the SL model. Results matched with the 3D reference solution with a fraction ($\sim 1/10$) of the DOFs.

The second example showed how the model can be used to model complex prismatic curved structures. The hierarchical property of SL shape functions allows to use curved elements as local domains. These curved elements can be described in various ways, here an approach similar to CAD, but with Lagrange 2D-shape functions, has been used. General curved sections are discretised using Lagrange elements with arbitrary number of nodes. These do not increase the number of DOFs since they are used only to compute the Jacobian and shape function gradients. Combining these with Chebyshev-biased beam meshes allows to build complex structures as a connected set of prismatic (and curved) segments.

The curved stiffened panel contains a series of complicated regions, like corners and junctions, which can be a challenge for modelling, even with 3D FE models. In this case a solid model with $\sim$ 9M DOFs was needed to achieve converged results. An SL model with two different cross-sections and six beam segments, with $\sim$ 200k DOFs, was used to describe the structure. Local bending and shear stresses close or at singularities were computed with both SL and FE models. Results show that SL model is capable of capturing accurate stress profiles as good as FE with a small fraction ($\sim$ 2%) of DOFs.

3.8 Concluding Remarks

The propose model: the Serendipity Lagrange Expansion Model, provides a beam-like model (in the framework of the Unified Formulation), that combines two of the main advantages of TE and LE models: hierarchical property and local expansion control. In order to challenge and exemplify

the merits of the proposed approach, static linear analyses of square and stiffened curved panel beams have been carried out. The model was benchmarked against TE and LE expansions, 3D FE model as well as analytical formulae (where available). The main findings can be summarised as follows:

1. The effect of collocating beam nodes using a Chebyshev biased mesh has been assessed. The mesh was refined in the regions where stress fields are expected to change rapidly. It has been observed that, by employing this method, shear stress oscillations are mitigated and accurate results can be obtained near constraints, without the need to increase the total number of beam nodes.

2. For the numerical cases assessed, the Serendipity Lagrange expansion model retains benefits of both the Lagrange model (cross-sectional discretisation) and the Taylor model (hierarchical property), eliminating their disadvantages, as described in the following points.

3. In order to capture the response of beam-like structures accurately, high-order models may be required. For TE models, as the order of expansion increases, the conditioning number of the stiffness matrix decreases exponentially, and the system becomes ill-conditioned. SL expansions overcome this limitation and are therefore suitable for analysing beams with complex cross-sections.

4. Similarly to LE model, the Serendipity Lagrange ones allow for cross-sectional discretisation. This feature, together with the hierarchical nature of the local expansions, makes SL elements particularly suited for capturing localised stress fields near boundaries and discontinuities, unlike the TE expansion model.

5. Cross-sections are also discretised in the LE model, however model building can be cumbersome because re-meshing is the only way to refine the kinematics.

The proposed Serendipity Lagrange expansion models proved to be an efficient and effective means for computing 3D stress fields for solid and complex isotropic beam structures.

CHAPTER 4

UNIFIED FORMULATION LINEARISED BUCKLING MODEL

"Algebra is generous; she often gives more than is asked of her."

- J. D'Alembert

For design engineers, predicting the buckling behaviour of a thin-walled structure subject to axial compression can be a complex task. For some cases analytical and closed form solutions can be found. In general, it is not always possible and alternative methods have to be utilised. The Finite Element Method is common practice, but it may come with a high computational cost. In this chapter, we intend to provide an accurate, efficient and reliable design tool for performing linearised buckling analysis. The model is based on the Unified Formulation framework which allows to describe the structure as a one-dimensional beam with a general cross-section. Serendipity Lagrange expansions are employed in all the cases presented, due to their efficiency and accuracy. The use of curved elements and the hierarchical property of the shape functions allows to describe the cross-section geometry in an exact way. The combination of all of these capabilities in a single model provides a new analysis technique that could be of great interest in industry. The formulation is verified against traditional finite element models. Results in terms of buckling loads, modes, stresses and efficiency are provided.

4.1 Aim and Motivation

Studying the buckling behaviour of complex thin walled structures can be challenging, especially if one needs to compute localised three-dimensional stresses at buckling. If this is the case, sub-modelling is a common practice: take for example the case where a 2D shell model is used for obtaining the global buckling response and 3D solid FE model for computing the stress profile in

localised regions. This can be computationally expensive and cumbersome. The aim is to solve this duality as follows:

1. To extend the Unified Formulation SL model to linearised buckling analysis.
2. To develop a single tool suitable for both, linear buckling and stress analysis, without the need of sub-modelling.
3. To develop a model that is as accurate as 3D solid FE and as efficient as 2D shell FE.
4. To develop a fast and reliable design tool.

4.2 Introduction

As stated previously, the Unified Formulation was chosen as the main tool for the proposed framework due to its versatility, accuracy and efficiency in modelling complex beam structures.

There are many ways to measure computational efficiency. One possibility is to count the total number of variables needed to solve an specific problem. For example, analytical models use a relatively few number of variables. On the other hand, finite element models may require much more DOFs. In a finite element context, the number of unknowns will depend on several factors such as: (1) how complex the model is; (2) the size of the mesh; and (3) the target accuracy, among others. In practice, using models with many DOFs (in the order of millions) may have negative impact, e.g. when doing parametric studies, since the calculations have to be repeated many times. Computer memory may also be a limiting factor, since more space and RAM are required to save and manipulate data. One of the advantages of using Unified Formulation is its efficiency in terms of DOFs. This model is capable not only on recovering 3D fields accurately, but to accomplish it using many less DOFs, compared with equally accurate FEM models.

Time is another possible way of measuring efficiency, and a more difficult one. Computationally speaking, time is a measurement of how slow or fast an algorithm runs, but it is highly dependent on several factors such as: (1) computer hardware; (2) code architecture; (3) programming language, etc.. Therefore, defining an objective way of measuring time is important. Every algorithm[1] performs a specific number of operations relative to the size of its input, so, counting operations gives an alternative (an equivalent) measure of time. A function that returns the number of operations (or time) as a function of the size of the input is called the *Complexity* of the algorithm [82, 83]. In subsequent sections it is shown how the proposed model can reduce the computing time, given an algorithm complexity, compared to FEM models. In other words, it is shown that the formulation provides the same accuracy with less computational time effort.

The difficulty of predicting the buckling behaviour of compression loaded thin-walled structures is a concern for design engineers. Current industry approaches for the design of thin

[1] e.g. inversion schemes, eigenvalue solvers or factorisation algorithms.

structures for buckling resistance include empirical guide-lines [84, 85], statistic-based techniques [86, 87] or the use of experimental data sets, among others. However, for some of these approaches the appropriate parameters to apply are often unknown, so experimental testing and validation are usually required. This highlights the need for an analysis methodology able to provide accurate predictions, rapidly. With FEM, precise results for a wide variety of cases can be obtained, but often with a high computational cost. Many techniques have been proposed by several authors during recent years [88–92]. In this chapter an efficient, reliable and fast design tool capable of performing linearised buckling analysis of thin-walled curved structures is presented.

4.3 Linearised Buckling Model

Buckling is an inherently non-linear process partly driven by geometrical non-linearities. Solving the complete set of non-linear governing equations is a complex task. Analytical solutions are available for some specific or simplified cases, and only for some combination of boundary conditions and loads. Therefore, approximate or numerical methods are employed. A common tool for solving these kinds of problems is by means of finite element models. This method usually requires high computational effort, in terms of degrees of freedom and time. Additionally, the use of non-linear solvers such as Riks or Newton-Raphson [93] is needed. An alternative approach is to perform a linearised buckling analysis, which provides accurate results in many practical cases, as long as the assumptions are satisfied. In this section, the Unified Formulation linearised buckling model *Geometrical Stiffness Matrix* is presented. A more detailed explanation can be found in Appendix B.

There are several ways to derive the Geometrical Stiffness nucleus. One possibility is to linearise the second variation of the non-linear stress tensor, as presented in [94, 95]. The incremental approach is another option as shown in [96]. The latter method is adopted here. Carrera and co-authors have presented approximated versions of the nucleus as in [64, 92].

Consider a purely static process where time does not play a role. Instead, the concept of time is used to order a series of small[2] incremental loading steps. The linearised stability equation is derived by using the Principle of Virtual Displacements (PVD) at the incremental step. The following assumptions are made:

1. Strains are small;

2. All the integrals are computed using the undeformed geometry, that is, a Total Lagrangian Formulation;

3. Some non-linear incremental displacement terms are neglected;

[2] In this context *small* means that quadratic and higher order terms are negligible.

4. Pre-buckling behaviour is linear.

It is assumed that all quantities (strains, stress and displacements) are known at the time step t. The values of these quantities at the incremental loading step $t+\Delta t$ are written as the value at time t plus the incremental (Δ) value. If the strain is written as a sum of a linear part $\boldsymbol{e}$ and non-linear part $\boldsymbol{\nu}$, that is[3] $\boldsymbol{\varepsilon} = \boldsymbol{e} + \boldsymbol{\nu}$, and by using the material stiffness matrix $\boldsymbol{C}$, the strain-stress relation and the PVD we obtain

$$\int_V \delta\Delta\boldsymbol{e}^{\mathrm{T}}\boldsymbol{C}\Delta\boldsymbol{e} + \delta\Delta\boldsymbol{e}^{\mathrm{T}}\boldsymbol{\sigma}_t + \delta\Delta\boldsymbol{\nu}^{\mathrm{T}}\boldsymbol{\sigma}_t \, dV = \delta\Delta\boldsymbol{u}^{\mathrm{T}}\boldsymbol{f}_{\mathrm{ext}} \tag{4.1}$$

where the left-hand side is the variation of the internal energy at the load step, and the right-hand side is the variation of the external energy. Writing the external applied load as a multiple λ of a reference load $\boldsymbol{f}_{\mathrm{ref}}$

$$\boldsymbol{f}_{\mathrm{ext}} = \lambda \boldsymbol{f}_{\mathrm{ref}}, \tag{4.2}$$

the UF approximation of the element displacement field is written as a product of a shape function defined in the cross-section $F(x,z)$, and a function $N(y)$ defined in the element beam axis. Figure 2.6 shows the decoupling of the element cross-section and beam axis shape functions. Therefore, the displacement field takes the form:

$$\begin{aligned} \boldsymbol{U}_{(\mathrm{e})} &= F_\tau(x,z)N_i(y)\boldsymbol{u}_{i\tau}, \\ \delta\boldsymbol{U}_{(\mathrm{e})} &= F_s(x,z)N_j(y)\delta\boldsymbol{u}_{js}, \end{aligned} \tag{4.3}$$

where $\boldsymbol{u}$ are the generalised displacements and τ, s, i, j are the indices for the cross-section and beam axis shape functions. The cross-section and axis expansions can be chosen and enriched independently from each other. In this chapter we have taken the *Serendipity Lagrange Expansion Model* (SL) [12] for the cross-sectional shape functions, and a 4-noded 1D Lagrange polynomial for the beam expansion. From this point onwards the Unified Formulation Linearised Buckling Model is refer to as UF-SL[4]. By substituting equation (4.3) into equation (4.1) and by simplifying, one obtains

$$\left(\boldsymbol{k}_{(\mathrm{e})}^{ij\tau s} + \lambda\boldsymbol{\kappa}_{(\mathrm{e})}^{ij\tau s}\right)\boldsymbol{u}_{i\tau} = \boldsymbol{0}, \tag{4.4}$$

where $\boldsymbol{k}_{(\mathrm{e})}^{ij\tau s}$ is the element *Stiffness Matrix* nucleus [11] and $\boldsymbol{\kappa}_{(\mathrm{e})}^{ij\tau s}$ the *Geometric Stiffness Matrix*.

The 3×3 nucleus defining the element *Geometrical Stiffness Matrix* is given by:

$$\boldsymbol{\kappa}_{(\mathrm{e})}^{ij\tau s} = \kappa^{ij\tau s}\begin{bmatrix} 1 & 0 & 0 \\ 0 & 1 & 0 \\ 0 & 0 & 1 \end{bmatrix} \tag{4.5}$$

[3] See Appendix B for details.

[4] In some cases it is refer only as SL.

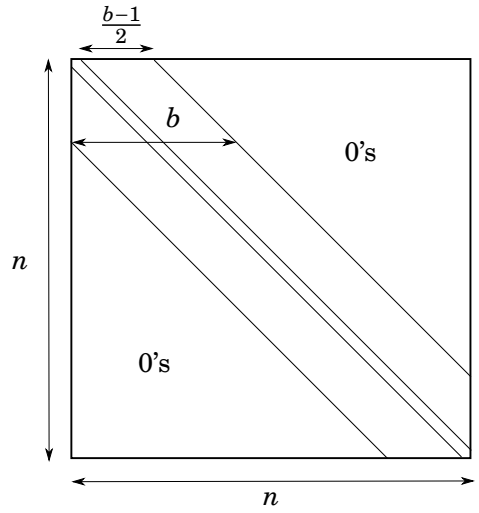

Figure 4.1: Band size of a matrix.

with

$$\begin{aligned}\kappa^{ij\tau s} = \int_{V_{(e)}} & \sigma_{xx} N_i N_j F_{\tau,x} F_{s,x} + \sigma_{yy} N_{i,y} N_{j,y} F_\tau F_s + \sigma_{zz} N_i N_j F_{\tau,z} F_{s,z} + \\ & \sigma_{yz}(N_i N_{j,y} F_{\tau,z} F_s + N_{i,y} N_j F_\tau F_{s,z}) + \\ & \sigma_{xz}(N_i N_j F_{\tau,z} F_{s,x} + N_i N_j F_{\tau,x} F_{s,z}) + \\ & \sigma_{xy}(N_{i,y} N_j F_\tau F_{s,x} + N_i N_{j,y} F_{\tau,x} F_s)\, dV,\end{aligned} \tag{4.6}$$

which contains all six components of the pre-buckling stress state $\boldsymbol{\sigma}^{\mathrm{T}} = \{\sigma_{xx}, \sigma_{yy}, \sigma_{zz}, \sigma_{yz}, \sigma_{zx}, \sigma_{xy}\}$.

After assembly the problem reduces to finding the non-trivial solution to the eigenvalue problem

$$\det(\boldsymbol{K} + \lambda \boldsymbol{K}_{\mathrm{G}}) = 0. \tag{4.7}$$

The solution gives the buckling loads (eigenvalues) λ and the buckling shapes (eigenvectors). In Section 4.4 a detail explanation on the *Complexity* of the solution algorithms (inversion and eigenvalue) and how the proposed Unified Formulation Linearised Buckling Model reduces the computational effort is presented. Numerical evidence is also provided in Section 4.6.

4.4 On the Complexity of the Inversion and Eigenvalue Solvers

For performing a buckling analysis two main steps are needed: the first is to solve the system $\boldsymbol{K}\boldsymbol{u} = \boldsymbol{f}$, which involves an inversion of a $n \times n$ matrix. This is usually performed by employing a sparse solver [97], or if the system is too large, an iterative algorithm [98]. Second, the eigenvalue problem $\det(\boldsymbol{K} + \lambda \boldsymbol{K}_{\mathrm{G}}) = 0$ is solved, by using one of the many existing iterative methods [99–101]. These steps are computationally expensive. One of the goals of the present chapter it to compare computational efficiency, in terms of DOFs and time, of the models used.

In computer science, complexity refers to a way of objectively measuring how slow or fast a particular algorithm performs [82, 83]. Complexity is defined as a function $T(n)$, time vs input size. The aim is to measure time taken by an algorithm regardless of the implementation details. The same algorithm takes different amounts of time on the same inputs depending on factors such as computer hardware, software architecture, or programing language. The way around this issue is to estimate the time efficiency asymptotically and by counting the number of floating operations $Q(n)$ instead[5]. Given $Q(n)$ and the speed of a computer's processor it is possible to estimate the required time. For example, if the computer processor speed is 1GHz, then it can perform $\sim 1\times 10^9$ floating operations per second. If 2.5×10^9 operations are needed, then it takes ~ 2.5 seconds.

In finite element software various solvers are employed. Given a specific solver, it is possible to objectively compare *times* between models by counting the number of operations required. Although efficiency may change if different algorithms are used. Herein we assume that, hypothetically, every model (FEM and UF-SL) uses the same algorithm. In the case of matrix inversion, the *Gaussian Elimination Method* for sparse matrices [102] is assumed. For the eigenvalue analysis a *Simple Subspace Method* [6] [101] is used. These algorithms were chosen because their complexity is well known. The number of floating operations for inverting the matrix using *Gaussian Elimination Method*[7] depends not only on the size of the matrix $n\times n$, but also on the band size b. Figure 4.1 shows how to compute b. Asymptotically, $Q_{\text{inv}}(n)$ is given by [100]

$$Q_{\text{inv}}(n) = \frac{nb^2}{4} \tag{4.8}$$

The number of operations is of the order $Q_{\text{inv}}(n) \sim O(nb^2)$. If, for example, the band is twice as big (i.e. twice less sparse), then the number of operations quadruple.

The Subspace algorithm is more complex. Before showing an expression for $Q_{\text{eig}}(n)$, a brief description of the algorithm is given. Suppose that the eigenvalues and vectors of a $n\times n$ matrix $\mathbf{A}$ with band size b are to be computed. Let $\mathbf{X_0} = [\mathbf{x_1}, ..., \mathbf{x_m}]$ be a system of $n\times m$ vectors [8], the iterations are computed as follows [101]:

- **Start**: Choose initial system of $\mathbf{X_0}$.
- **Iterate**: Until convergence[9], do:
  - Compute $\mathbf{X_k} = \mathbf{A}\mathbf{X_{k-1}}$;

[5] This is used throughout the chapter as a measurement of *time*.

[6] *Subspace Method* is indeed used in both, Abaqus and in the Linearised Buckling Model implementation (Matlab). Nevertheless, the specifics of the algorithm, such as the use of accelerators or re-normalizations steps [100], etc., is not known.

[7] This is a direct method, meaning that the process is performed only once in order to invert the matrix.

[8] The total number m of vectors depends on the number of eigenvalues requested and on the method used. If only the first eigenvector is needed, $m = 2$ or 3.

[9] In terms of the norm of the vectors in $\mathbf{X_k}$.

- Compute $\mathbf{X_k} = \mathbf{QR}$ the $\mathbf{QR}$ factorization of $\mathbf{X_k}$;
- Set $\mathbf{X_k} = \mathbf{Q}$.

This method converges to the set $\mathbf{X_k}$ of eigenvectors. Eigenvalues are computed from the matrix factorizations. For details refer to [101, 103]. The complexity, or number of operations $Q_{\text{eig}}(n)$, *per iteration*, is now given for each of the steps. The product $\mathbf{X_k} = \mathbf{AX_{k-1}}$ is a matrix multiplication and uses approximately

$$Q_1(n) = bn^2m \tag{4.9}$$

operations. The QR-factorization step has a complexity of [101]

$$Q_2(n) = \frac{4n^3}{3}. \tag{4.10}$$

Notice that the number of operations does not depend on the band size b, only on the size of the matrix (i.e. DOFs). In total, *per iteration*[10], the number of operations is given by the sum:

$$\begin{aligned} Q_{\text{eig}}(n) &= Q_1 + Q_2(n) \\ &= bn^2m + \frac{4n^3}{3}, \end{aligned} \tag{4.11}$$

which is dominated by $Q_2(n)$ if the matrix is banded and $m < n$, therefore $Q_{\text{eig}} \sim O(n^3)$. In summary, for both steps:

- **Inversion Step**: $Q_{\text{inv}}(n) \sim O(nb^2)$, done only once.
- **Eigenvalue Step**: $Q_{\text{eig}} \sim O(n^3) \times$ *number of iterations*.

In general, the Unified Formulation Linearised Buckling Model's stiffness matrices are less sparse than those from solid or shell finite element models. This has an effect on the inversion step. On the other hand, solid and shell FEM's stiffness matrices are larger than those in ours which affects the eigenvalue step. The effect is worse in the latter than in the former, since calculations must be repeated many times.

4.5 Curved Elements. Exact Representation

As mentioned before, the Stiffness Matrix elements require integrating the terms throughout a cross-sectional domain. This domain is, in general, curved, and the accurate representation of its geometry is important. One possibility is to represent curved edges using higher-order polynomials [78]. In Chapter 3 a cross-sectional shape mapping that approximates curved cross-sections using Lagrange 2D expansions was explained. This approach prove to be accurate in modelling curved sections, nevertheless, it is still an approximate representation of the geometry.

[10]The number of iterations depends on many factors, such as the size problem, boundary conditions, mesh quality, etc.

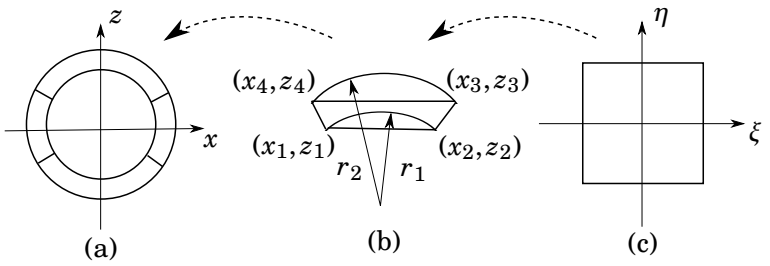

Figure 4.2: Mapping of curved element using the blending function method.

In this chapter, structures with circular cross-sections are analysed, therefore the approximate representation using Lagrange 2D functions is replaced with an exact approach. Non-linear functions representing the equation of a circle are used instead. The choice of this function guarantees the exact description of cross-sectional shape, unlike using higher-order polynomials which can lead to numerical errors due to approximation. To understand the procedure, consider a section as shown in Figure 4.2(a) which is discretised using quadrilateral domains. Using the blending function method [5], two of the sides of the domain are curved and the coordinates of these sides are represented by

$$\begin{aligned} x &= \frac{1}{2}(1-\eta)x_{c_1} + \frac{1}{2}(1+\eta)x_{c_3}, \\ z &= \frac{1}{2}(1-\eta)z_{c_1} + \frac{1}{2}(1+\eta)z_{c_3}, \end{aligned} \tag{4.12}$$

where $x_{c_1}(\xi)$, $x_{c_3}(\xi)$, $z_{c_1}(\xi)$ and $z_{c_3}(\xi)$ are functions, as given below, that represents the curved edges with radius of curvature r_1 and r_2.

$$\begin{aligned} x_{c_1}(\xi) &= \frac{1}{2}(1-\xi)x_1 + \frac{1}{2}(1+\xi)x_2, \\ x_{c_3}(\xi) &= \frac{1}{2}(1-\xi)x_4 + \frac{1}{2}(1+\xi)x_3, \\ z_{c_1}(\xi) &= \sqrt{r_1^2 - x_{c_1}(\xi)^2}, \\ z_{c_3}(\xi) &= \sqrt{r_2^2 - x_{c_3}(\xi)^2} \end{aligned} \tag{4.13}$$

where (x_i, z_i) with $i = 1,2,3,4$, are the coordinates of the corners of a quadrilateral element as shown in Figure 4.2(b). These functions are defined in such a way that $x_{c_1}(-1) = x_1$ and $x_{c_1}(1) = x_2$. Similarly, $x_{c_3}(-1) = x_4$ and $x_{c_3}(1) = x_3$. The functions z_{c_1} and z_{c_3} map the z coordinates to a circular arc. This procedure maps all the coordinates of the quadrilateral domain to a curved domain. The derivatives of the previous equations give the components of the tangent and normal vectors (local curvilinear basis) at each point. This procedure can be expanded to all the edges in case of a domain with all sides curved.

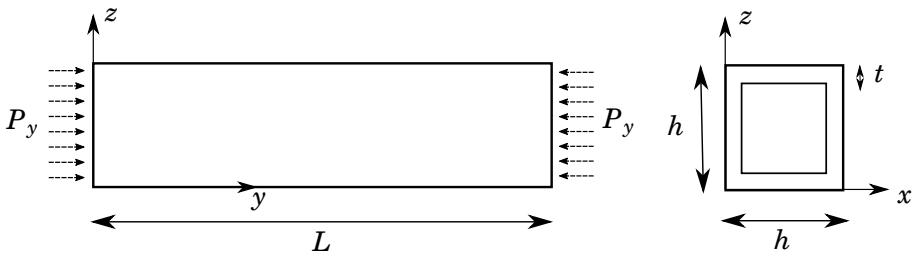

Figure 4.3: Thin box geometry.

4.6 Numerical Examples

In this section a series of examples involving thin-walled structures subject to buckling are presented. Results in terms of buckling loads, shapes and model efficiency are reported. Additionally, a second analysis is performed, the original structure is modified with a geometrical imperfection proportional to the first normalised eigenvector of the buckled shape. The idea is to resemble the geometry just after it has buckled[11]. With this geometry, some localised stresses of the original structure at pre-buckling and of the modified geometry are also given. The displacement field of the modified geometry is taken as [52, 88]

$$\boldsymbol{u}_{\mathrm{b}} = \lambda \boldsymbol{u} + a\boldsymbol{v}, \tag{4.14}$$

where a is a perturbation parameter and $\boldsymbol{v}$ is the first eigenvector. This gives an approximation of displacements close to the buckling point. For all the cases $a = t$ is used, where t is the thickness of the structure. The material is isotropic with Young modulus $E = 71$ GPa and Poisson's ratio of $\nu = 0.33$. The same material is used for all cases.

The first three cases are used as benchmark problems. The last part of the section is dedicated to show the capabilities of the model as an efficient and reliable design tool. Different models were employed: `ABAQUS` 3D Solid model and the UF- SL buckling model. A 2D Shell FEM is also used in some cases. Convergence was achieved in terms of buckling loads, modes and stresses. The specifics of each model: type, number of DOFs, order, etc., are given in each example.

4.6.1 Buckling of a Thin Box

Consider a thin box as shown in Figure 4.3, with dimensions $L = 1$ m, $h = 0.1$ m and $t = 0.002$ m. Unless stated otherwise, these dimensions are use throughout the example. The applied load is $P_y = 1$ N. Three different sets of results are presented. First, the effect of slenderness (L/h) and variable thickness (h/t) on the first two buckling loads; second, some stress distributions; and third, the buckling load and mode.

[11] Special attention and caution should be take by using this approach, since this is not a proper post-buckling simulation, it does not involve the effects of the load redistribution, which can be captured only with a second order analysis.

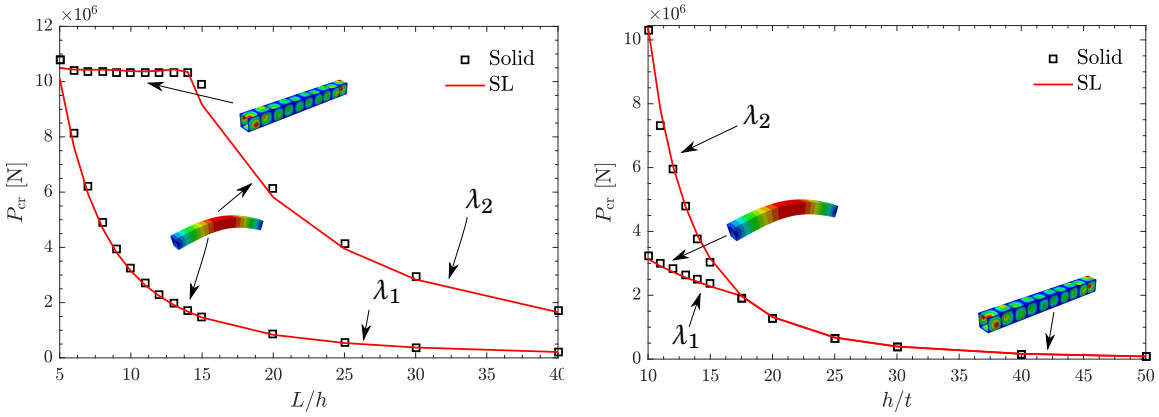

(a) Buckling loads vs L/h.

(b) Buckling loads vs h/t.

Figure 4.4: First two buckling loads for variable slenderness and thickness for a thin box with $t = 0.01\,\text{m}$ and $h = 0.1\,\text{m}$.

4.6.1.1 Variable Slenderness and Thickness

The effect of the variable slenderness and thickness on the first two buckling loads is studied. For this case, the boundary conditions are such that the two edges are free to move only in the axial direction. Two different models are used, a Solid (`C3D20R`) model with 2,060,940 DOFs and a UF-SL model with 8 elements in the cross-section, 34 4-noded Lagrange beam elements (B4) along the length and of SL order 4, which results in 26,208 DOFs.

Variable slenderness The thickness of the box is set to $t = 0.01$ m, the height as $h = 0.1$ m and variable L. The range studied is from a short beam, $L/h = 5$, to a long beam, $L/h = 40$. Figure 4.4(a) shows the variation of the first (λ_1) and second (λ_2) buckling loads versus slenderness. The first buckling load decreases monotonically with increasing length and its buckling mode corresponds to that of a beam-like structure. The second buckling mode has a different behaviour, for the range from $L/h = 5$ to $L/h = 15$ its value is close to constant, and the box's skin buckles; for values greater than $L/h = 15$, the load decreases monotonically and the structures buckles as a beam. Meaning that for thick and short beams, larger loads have to be applied in order for the skin to buckle, otherwise it buckles like an Euler beam.

Variable thickness For this case the length of the beam is taken as $L = 1\,\text{m}$, height as $h = 0.1\,\text{m}$ and thickness t is varied. The range used is from $h/t = 0.02$ (thick box) to $h/t = 0.002$ (thin box). Figure 4.4(b) shows the results. The first buckling load decreases monotonically as thickness decreases (h/t increasing), with a change of slope at $h/t = 18$. Before this inflection point, the structure buckles as an Euler beam, afterwards, the box's skin buckles. The second buckling load decreases as h/t increases as well, and its skin buckles for all the cases.

4.6.1.2 Localised Stresses

The purpose of this section is to test the capability of the UF-SL model to recover 3D stresses (mainly through thickness) and to show that the equivalent 3D FEM model is computationally expensive for the same level of accuracy.

Original structure's pre-buckling stresses and modified geometry's stresses at some locations are presented and discussed. Comparison with two different 3D Solid models is provided. The first Solid model was meshed with 784,000 linear elements (`C3D8R`), which gives two elements through thickness. This model is denoted in the results as 2-Lin. The second model was meshed with 98,000 quadratic elements (`C3D20R`), which gives one element through thickness. Denoted in the results as 1-Quad.

Given that the applied force is in the axial direction, the stress distribution in the pre-buckling state consists mainly of an axial normal stress σ_{yy}, and is equal to the pre-buckling pressure. The distribution along the length of the beam, and measured at the top centre ($x = 0.05$ and $z = 0.1$), is shown in Figure 4.5. Stress is constant, except for regions within approximately 15% from the boundaries.

At the point where the structure changes shape, ie. considering the modified geometry, other stresses develop, in particular normal stresses σ_{xx}. Through thickness axial normal σ_{yy} and normal σ_{xx} stresses were measured at the point where buckling displacement is maximum ($x = 0.05$, $z = 0.1$ and $y = 0.04$). Figure 4.6 shows the results for the three different models. Both distributions are linear, therefore, the 2-Lin model provides only a rough approximation of the distribution. At least one quadratic element through thickness is needed to accurately capture the stress profile. For these stresses, 3D plot distributions from the UF-SL model are shown in Figure 4.7 and 4.8. Plots show only one quarter of the structure and at three different layers ($z = 0.1$ -top-, $z = 0.099$ -mid- and $z = 0.098$ -bottom-).

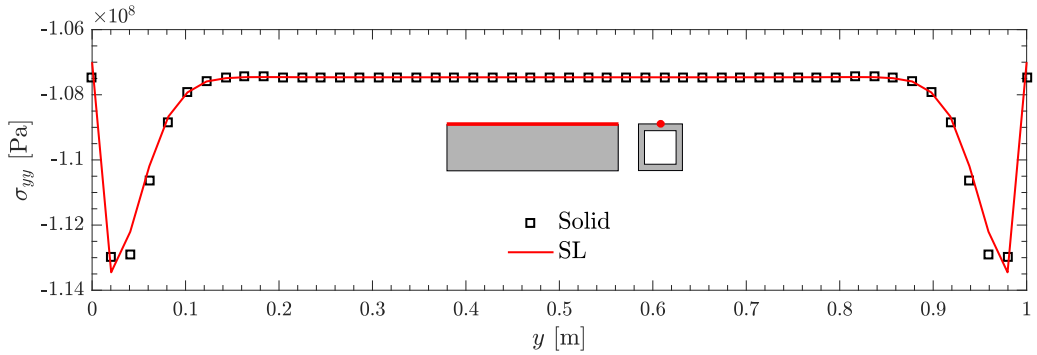

Figure 4.5: Pre-buckling axial stress σ_{yy} vs length y at $x = 0.05$ and $z = 0.1$. Thin box.

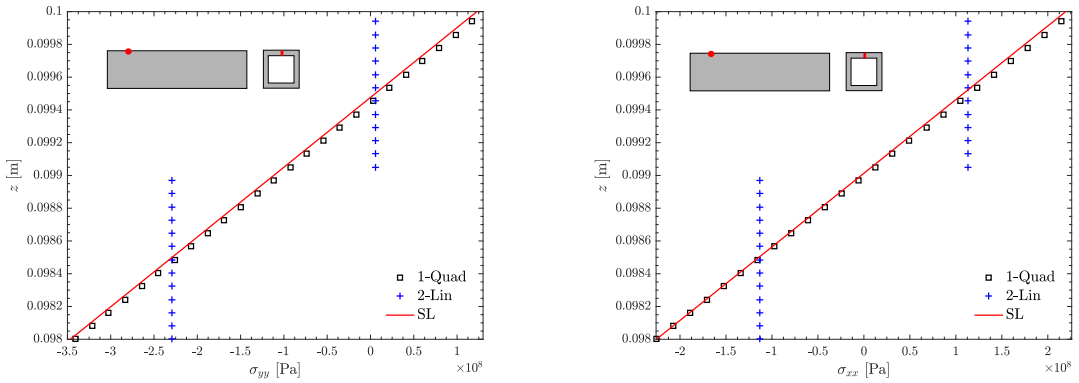

(a) Axial normal stress σ_{yy} through thickness.

(b) Normal stress σ_{xx} through thickness.

Figure 4.6: Original structure and modified structure normal stresses at $y = 0.04$ and $x = 0.05$ from $z = 0.098$ to $z = 0.1$. Thin box.

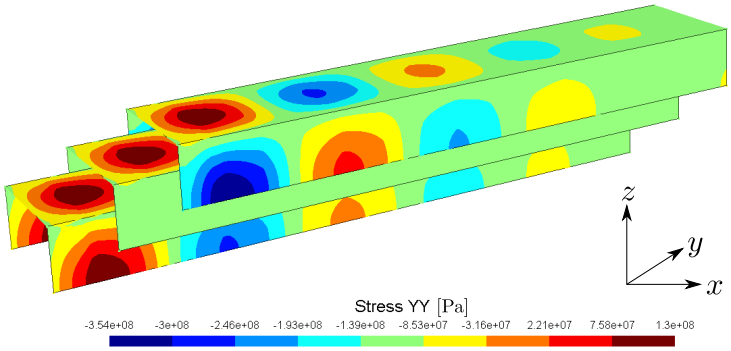

Figure 4.7: Axial normal stress σ_{yy} at three different layers ($z = 0.1$, $z = 0.099$ and $z = 0.098$). Box, UF-SL model.

4.6.1.3 Buckling Load and Mode

Buckling loads and shapes are probably the most important output from a linearised buckling analysis. They provide information on the stability of the structure, i.e. the load at which stability is lost, and the buckling shape. Three models are used, Solid model, Shell model and UF-SL.

Table 6.4 shows the results of the critical load, DOFs and efficiency for the three models. The buckling load P_{cr} predictions are all similar ($\sim 1\%$ error). Vertical displacements along the length and at top centre ($x = 0.05$ and $z = 0.1$) are shown in Figure 4.9. All models show similar results for displacements, expect for some differences close to the centre of the beam axis. The displacements at this region are expected to be very small compared to the size of the structure, therefore, these small differences are acceptable. Moreover, it was noticed that these differences ($\lessapprox 1\%$) were probably due to numerical noise related to the eigenvalue solver; since when the solid and shell mesh/order were slightly changed, there was no apparent convergence pattern.

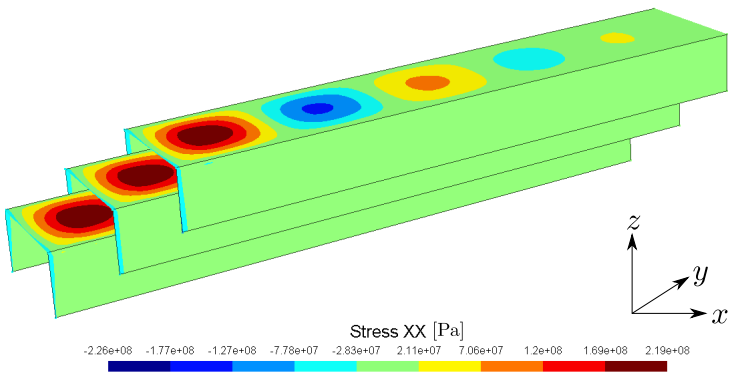

Figure 4.8: Normal stress σ_{xx} at three different layers ($z = 0.1$, $z = 0.099$ amd $z = 0.098$). Box, UF-SL model.

Eleven half-waves are developed along the span, and four (one on each face) along the perimeter of the cross-section. The position of maximum displacements coincide with positions of maximum stresses. A 3D plot of the buckling pattern is shown in Figure 4.10.

Table 4.1: Critical load, DOFs, Number of operations for Sparse and Eigenvalue Solvers for linear buckling analysis of a box.

	P_{cr} [N] $\times 10^4$	DOFs #	Ops. Inversion #	Ops. Eigenvalue *# per iteration*
Model				
Solid	8.537	2,060,940	$\sim 10^9$	$\sim 10^{18}$
Shell	8.526	288,960	$\sim 10^7$	$\sim 10^{16}$
UF-SL	8.523	26,208	$\sim 10^9$	$\sim 10^{13}$

Regarding the efficiency, the Solid model is the most computationally expensive in terms of DOFs, followed by the Shell and UF-SL models. The number of operations for inverting the

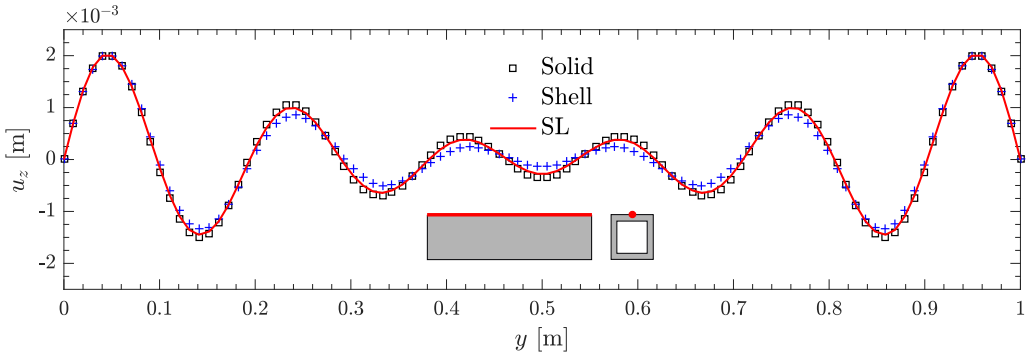

Figure 4.9: Vertical displacements u_z at buckling vs y at $x = 0.05$ and $z = 0.1$. Thin box.

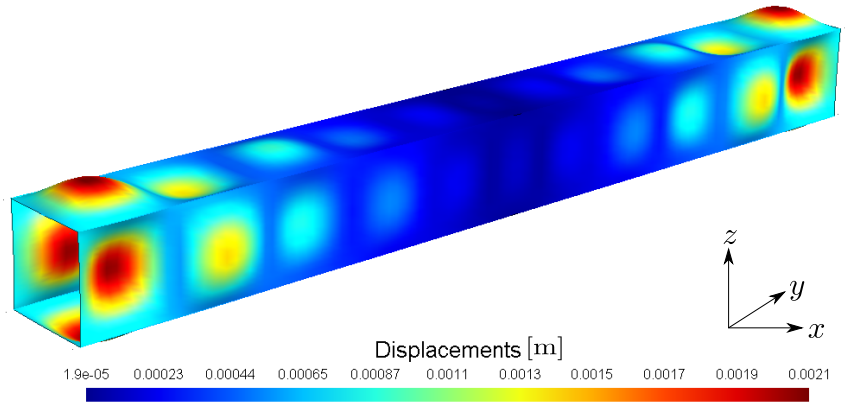

Figure 4.10: Buckling 3D shape of a thin box. UF-SL model.

matrix are of the same order of magnitude for Solid and UF-SL model. The shell model is most efficient in the solution step. In the eigenvalue step, UL-SL outperforms both Solid and Shell models.

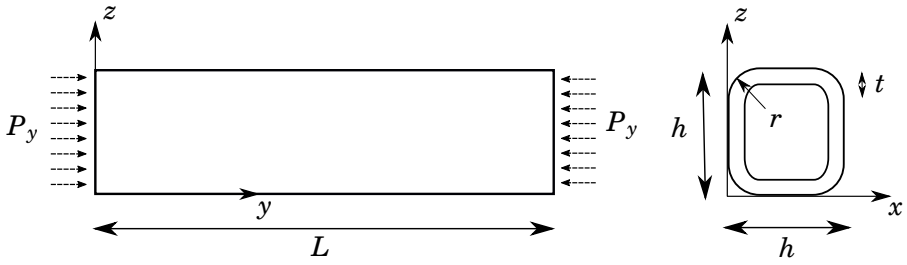

Figure 4.11: Thin box with round fillets geometry.

4.6.2 Buckling of a Thin Box with Curved Fillets

In addition to the example shown in the previous section, a modified geometry is now studied. The sharp corners are replaced by round fillets. The new geometry is depicted in Figure 4.11. The dimensions are $L = 1$ m, $h = 0.1$ m, $t = 0.002$ m and $r = 0.01$ m. The load and boundary conditions are the same as for the thin box.

4.6.2.1 Localised Stresses

As discussed in Section 4.6.1.2 a Solid model with two linear elements through thickness is not enough for capturing stresses properly, therefore, a Solid model with one quadratic element through thickness is used in this example. An UF-SL model with 8 cross-section elements, 30 B4 beam elements and of order 4 is used. Results from a Shell model are also provided. Details of the FE models can be found in Table 4.2.

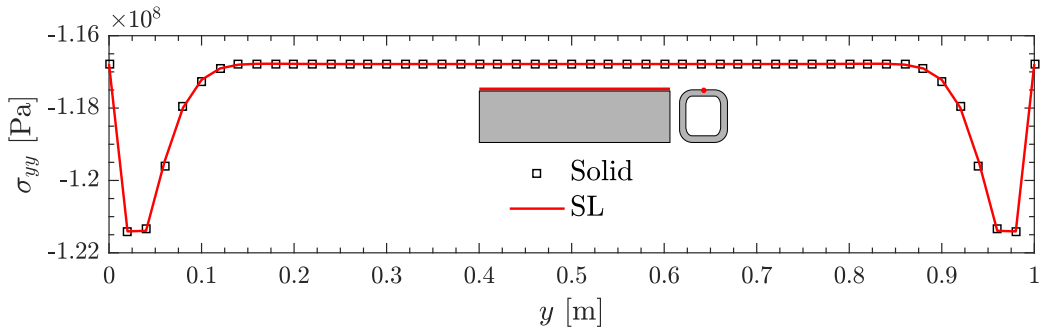

Figure 4.12: Pre-buckling axial normal stress σ_{yy} along y at $x = 0.05$ and $z = 0.1$. Box with curved fillets.

Figure 4.12 shows the distribution of pre-buckling axial normal stress along the length of the beam. Stress is constant throughout the beam axis, except close to the boundaries (~ 15%). Axial normal stress σ_{yy} and normal stress σ_{xx}, for the modified geometry, are measured through thickness at the point where displacement is maximum ($y = 0.04$ and $x = 0.05$). Figure 4.13 shows that both stresses have a linear distribution, similar to the case a box with straight edges. 3D plots showing the distributions of theses stresses obtained using the UF-SL model are shown in Figure 4.14 and 4.15.

4.6.2.2 Buckling Load and Mode

Linear buckling analyses are performed with the same three FE models. Comparison between buckling load predictions and computational efficiency is reported in Table 4.2. The critical load obtained with the UF-SL model is within 1% of error compared with both Solids and Shells. The replacement of sharp corners with round fillets has the effect of increasing the load carrying

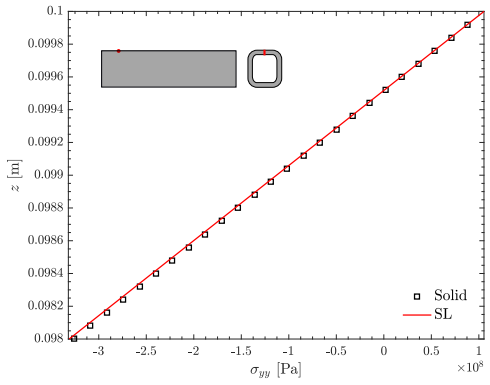

(a) Axial normal stress σ_{yy} through thickness.

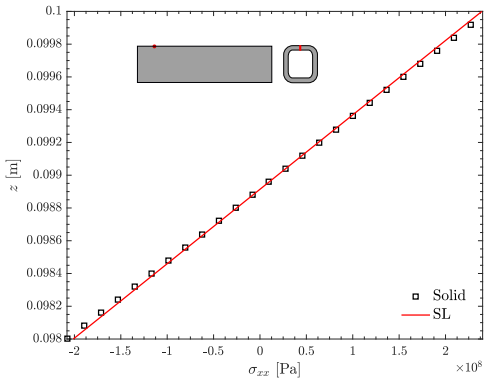

(b) Normal stress σ_{xx} through thickness.

Figure 4.13: Original structure and modified structure normal stresses at $y = 0.04$ and $x = 0.05$ from $z = 0.098$ to $z = 0.1$. Box with curved fillets.

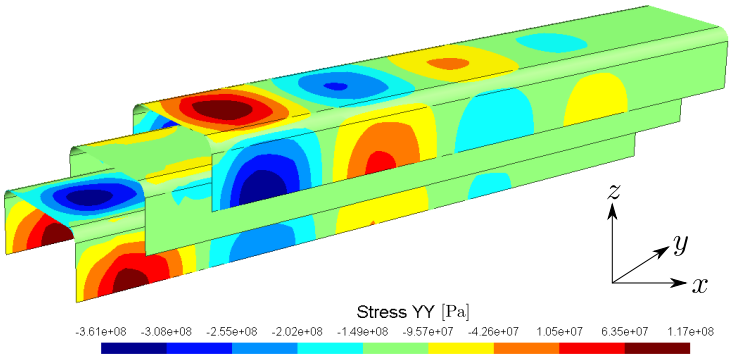

Figure 4.14: Axial normal stress σ_{yy} at three different layers ($z = 0.1$, $z = 0.099$ and $z = 0.098$). Box with curved fillets, UF-SL model.

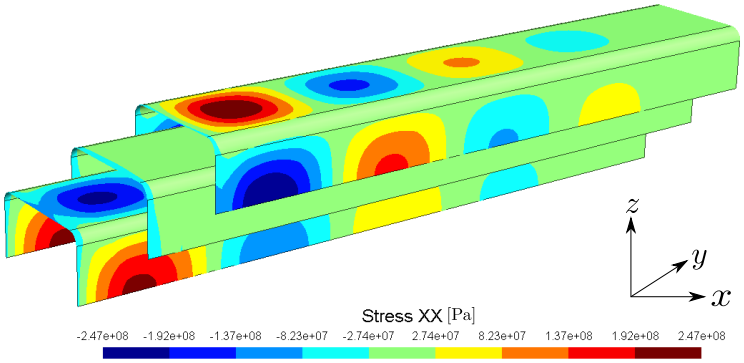

Figure 4.15: Normal stress σ_{xx} at three different layers ($z = 0.1$, $z = 0.099$ amd $z = 0.098$). Box with curved fillets, UF-SL model.

capability by ~ 5%, compared with the box's critical load.

Nine half-waves develop along the span of the beam and four appear along its perimeter, as shown in Figure 4.17. Vertical displacement u_z along the length of the beam is shown in Figure 4.16. UF-SL predicts displacements similar to those given by the Shell model. Results slightly differ from Solid's prediction, particularly where the displacements are expected to be small, i.e. close to the centre of the structure. The probable reason for this discrepancy was explained in Section 4.6.1.3.

Efficiency is similar to the case of the box with straight edges: UF-SL requires less DOFs and uses less time for solving the eigenvalue problem, nevertheless, the Shell model is more efficient in the inversion step.

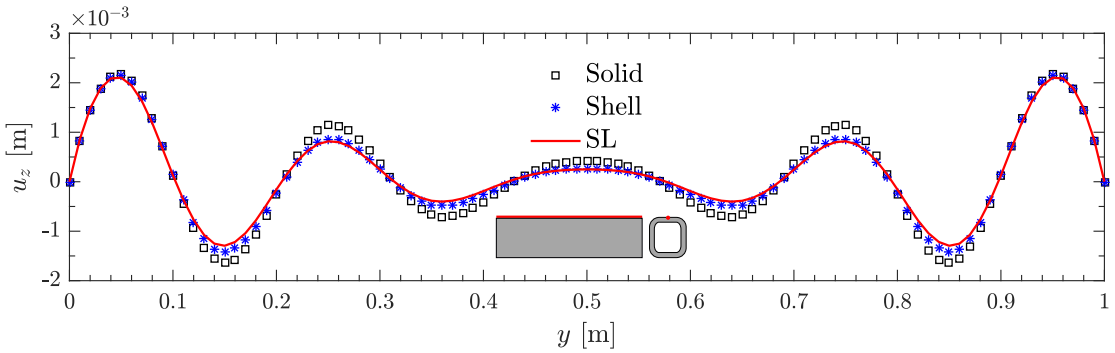

Figure 4.16: Vertical displacements u_z at buckling vs y at $x = 0.05$ and $z = 0.1$. Box with curved fillets.

Table 4.2: Critical load, DOFs, Number of operations for Sparse and Eigenvalue Solvers for linear buckling analysis of a box with curved fillets.

	P_{cr} [N] $\times 10^4$	DOFs #	Ops.Inversion #	Ops. Eigenvalue *# per iteration*
Model				
Solid	9.005	1,976,820	$\sim 10^9$	$\sim 10^{18}$
Shell	8.885	577,152	$\sim 10^7$	$\sim 10^{17}$
UF-SL	8.960	26,208	$\sim 10^9$	$\sim 10^{13}$

4.6.3 Buckling of a Thin Cylinder

A thin cylinder with radius $R = 0.1$ m, $L = 1$ m and $t = 0.002$ m is now considered. Figure 4.18 shows its geometry. Boundary conditions are such that the edges are clamped. As presented in previous sections, stresses, buckling loads, shapes and efficiency are measured. A UF-SL model with 72 cross-section elements, 10 B4 beam elements and of order 3, is used. Details of the FE

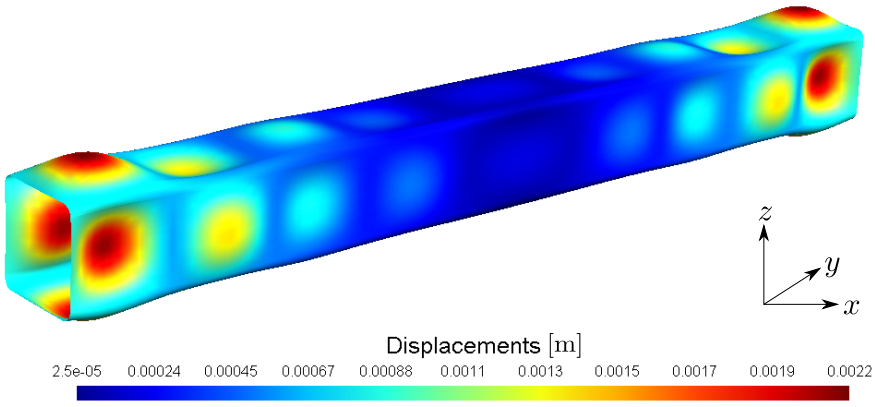

Figure 4.17: Buckling 3D shape of a thin box with curved edges. UF-SL model.

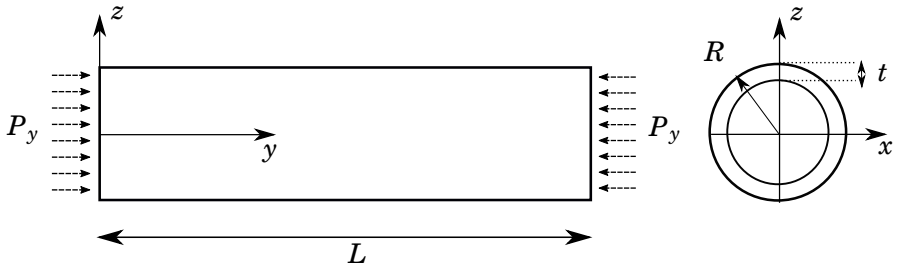

Figure 4.18: Thin cylinder geometry.

models can be found in Table 4.3.

4.6.3.1 Localised Stresses

During pre-buckling, axial normal stress σ_{yy} dominates; a plot of σ_{yy} along the span of the cylinder, and at middle top ($x = 0$ and $z = 0.1$), from the UF-SL and a Solid model is shown in Figure 4.19. The stress is constant up to approximately 5% from the boundaries.

For the modified geometry, maximum stresses are found at the same position where the maximum vertical (pre-buckling) displacements u_z develops, see Figure 4.19. Axial normal stress and hoop stress $\sigma_{\theta\theta}$ are measured through thickness at this position. Figure 4.20 shows the results. 3D plot distributions of axial normal stress σ_{yy} and hoop stress $\sigma_{\theta\theta}$ given by the UF-SL model are shown in Figure 4.21 and 4.22. The plots show one quarter of the structure and three different layers ($R = 0.1$, $R = 0.099$ and $R = 0.098$).

4.6.3.2 Buckling Load and Mode

The classical analytical solution for the buckling load of thin cylinder under axial compression is well known. If the structure is simply supported, the critical load per unit length is given

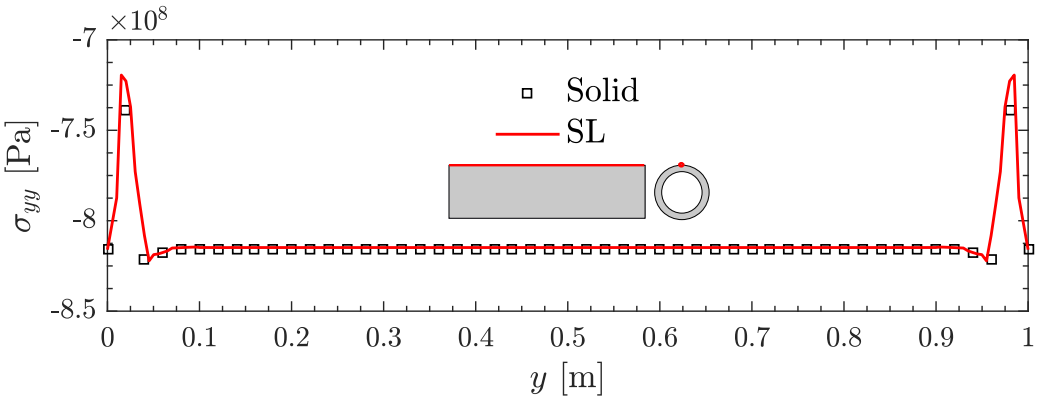

Figure 4.19: Pre-buckling axial stress σ_{yy} vs length y at $x = 0$ and $z = 0.1$. Cylinder.

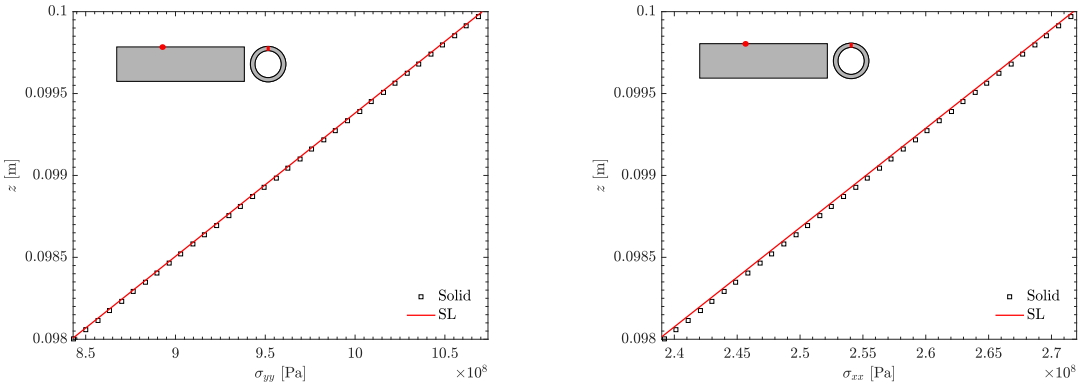

(a) Axial normal stress σ_{yy} through thickness.

(b) Hoop stress $\sigma_{\theta\theta}$ through thickness.

Figure 4.20: Modified structure axial and hoop stresses at $y = 0.4$ and $x = 0$ from $z = 0.098$ to $z = 0.1$. Cylinder.

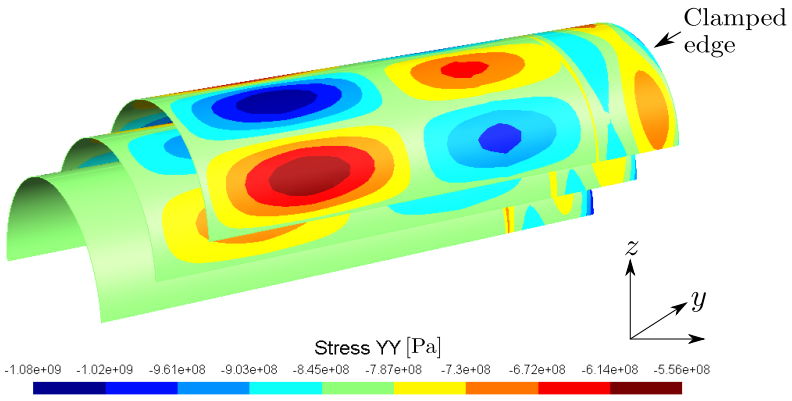

Figure 4.21: Axial normal stress σ_{yy} at three different layers ($R = 0.1$, $R = 0.099$ and $R = 0.098$). Cylinder, UF-SL model.

by [4, 54]:

$$N_{\text{cr}} = \frac{1}{\sqrt{3(1-\nu^3)}}\left(\frac{Et^2}{R}\right). \tag{4.15}$$

Even though this formula applies for the simply supported cylinder, it provides a good approximation of the buckling load for the case of clamped edges. Results for the critical loads using the three numerical models and the analytic solution, is found in Table 4.3. The three numerical analyses give similar results, within 1% of error. The buckling load from equation (4.15) is ~ 7% higher.

At buckling, $n = 8$ half-waves along the circumference and $m = 4$ along the length develop, as shown in Figure 4.23. Vertical displacement u_z at the top of the cylinder are shown in Figure 4.24. All three models give similar results.

The number of degrees of freedom required by the UF-SL to obtain converged results is

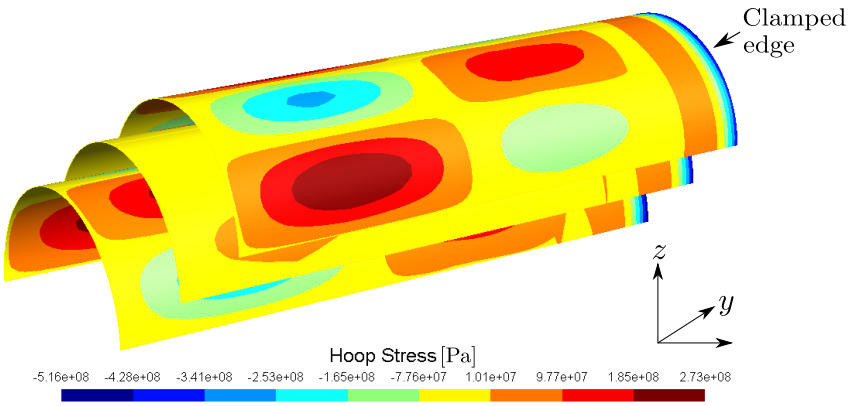

Figure 4.22: Hoop stress σ_{hp} at three different layers ($R = 0.1$, $R = 0.099$ amd $R = 0.098$). Cyliner, UF-SL model.

Table 4.3: Critical load, DOFs, Operations for Sparse and Eigenvalue Solvers for linear buckling analysis of a thin cylinder for three different models.

	P_{cr} [N] $\times 10^6$	DOFs #	Ops. Inversion #	Ops. Eigenvalue *#per iteration*
Model				
Solid	1.020	1,664,832	$\sim 10^9$	$\sim 10^{18}$
Shell	1.017	961,920	$\sim 10^7$	$\sim 10^{17}$
UF-SL	1.017	53,568	$\sim 10^{10}$	$\sim 10^{14}$
Analytical	1.091	$--$	$--$	$--$

approximately double compared with the previous examples. This is due to the fact that more elements are required to discretise the cylinder's cross-section. This had an impact on the number of operations for the inversion step, making the UF-SL model the most expensive. Nevertheless, UF-SL is the most efficient for the eigenvalue iteration step, followed by Shell and Solid models respectively.

4.6.4 Model as a Design Tool. Parametric Studies of a Stiffened Cylinder

This section is dedicated to show how the UF-SL model is used as an efficient and reliable design tool for performing linearised buckling analysis of complex structures. As discussed previously, obtaining good accuracy and precision may come with a high computational cost. Mostly in terms of degrees of freedom and computing time. Having a model that can keep both features, accuracy and efficiency, is desirable and useful in a design environment.

Three design examples are presented here. The first, a parametric study of the effect of the height of longitudinal stiffeners on buckling loads and modes of a cylinder. Second, a parametric study of the effect of width of the stiffeners on buckling loads, modes and structural weight. And

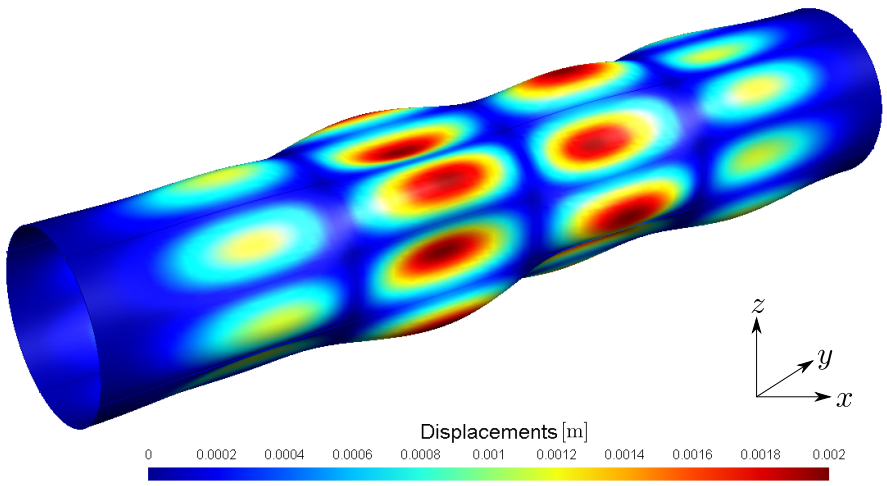

Figure 4.23: Buckling 3D shape of a cylinder. UF-SL model.

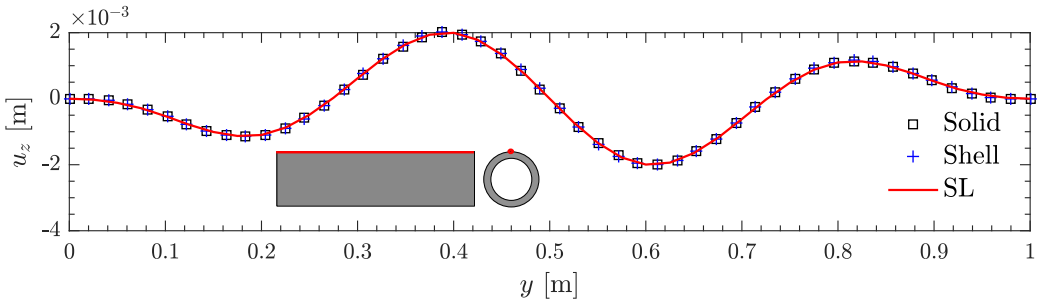

Figure 4.24: Vertical displacements u_z at buckling vs y at $x = 0$ and $z = 0.1$. Cylinder.

the third example shows the capability UF-SL model in capturing through thickness stresses, for the modified geometry, close to the singularities.

Same loading and boundary conditions used in Section 4.6.3 is used for this example.

4.6.4.1 Height of Longitudinal Stiffeners

It was shown in Section 4.6.3 that the structure develops eight half-waves along the circumference, and four half-waves along the span at the moment of buckling. Therefore, eight equally spaced longitudinal stiffeners are added to the structure. The position and geometry of the stiffeners is shown in Figure 4.25. Radius, thickness and angle are set to $R = 0.1$ m, $t = 0.002$ m and $\theta = 5^o$ respectively.

The models used are: a Solid model with 10,256,904 DOFs and a UF-SL model with 240 cross-section elements, 30 B4 beam elements and of order 5 with 884,520 DOFs.

Height h of the stiffeners was varied from $h = 0$ m (un-stiffened cylinder, $h/t = 0$) to $h = 0.018$ m ($h/t = 9$). The critical loads P_{st} and mode shapes of the stiffened structure are measured. Results

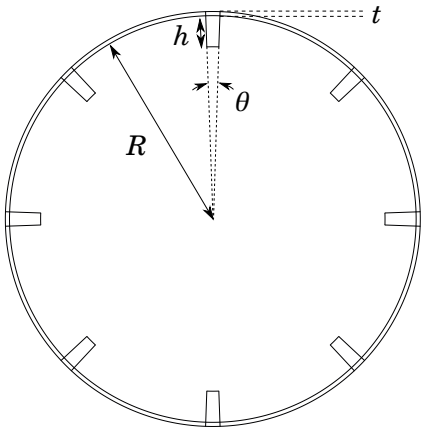

Figure 4.25: Cross-section view of the geometry and position of the longitudinal stiffeners.

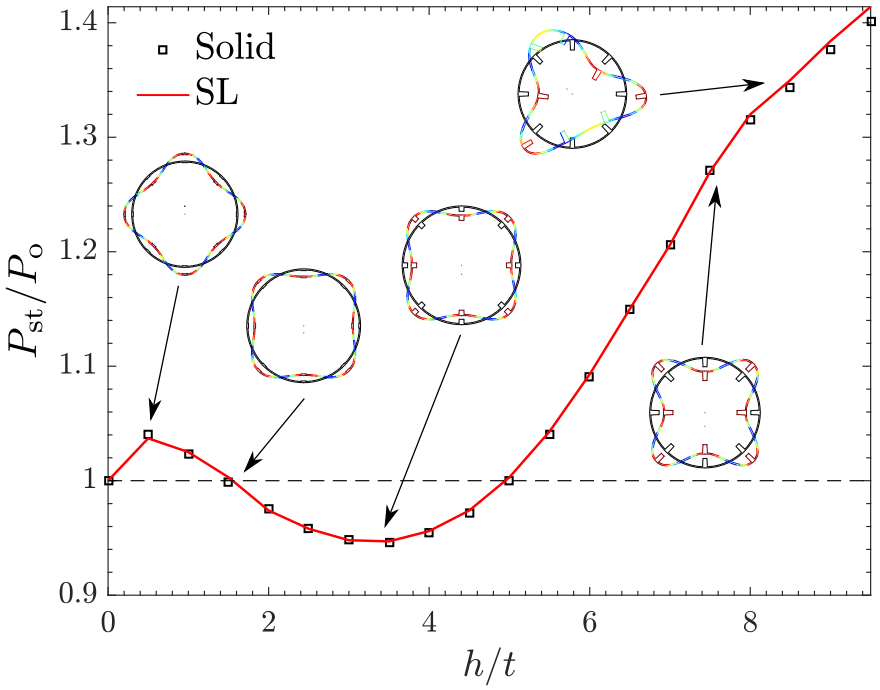

Figure 4.26: Relative buckling load vs relative size of stiffeners.

are shown in Figure 4.26. The vertical axis shows the relative buckling load P_{st}/P_o, with P_o the critical load of the un-stiffened cylinder, against the relative size of the stiffeners h/t. Cross-sectional deformations are also depicted for some cases. A reference value, $P_{st}/P_o = 1$ (un-stiffened cylinder), is also included.

Buckling load increases initially for $h/t \in [0, 0.4]$, where a local maximum is reached and the carrying capacity is increased $\sim 5\%$; in the range $h/t \in [0, 1.6]$ relative increase is strictly greater or equal to 1. For $h/t \in (1.6, 5]$ the buckling load is reduced regardless the presence of stiffeners.

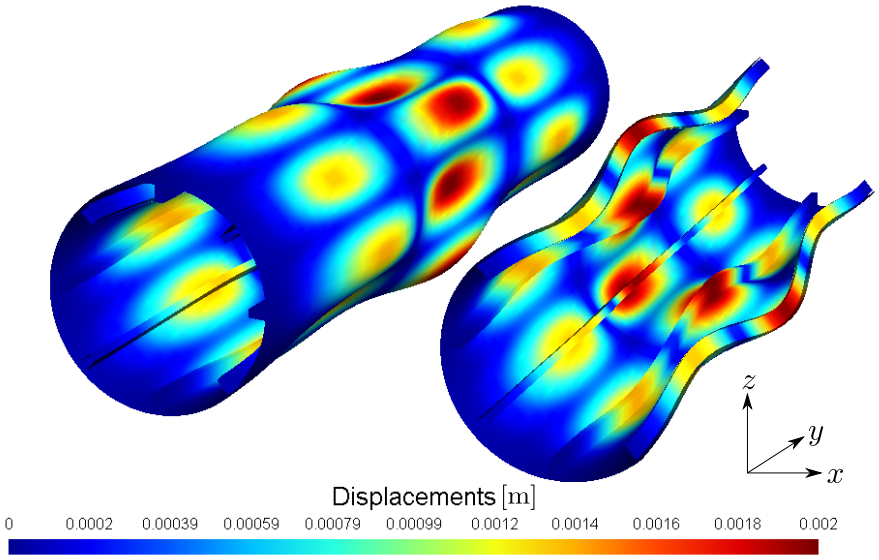

Figure 4.27: Buckling shape of a stiffened cylinder. Longitudinal cut. Case $h/t = 7.6$. UF-SL model.

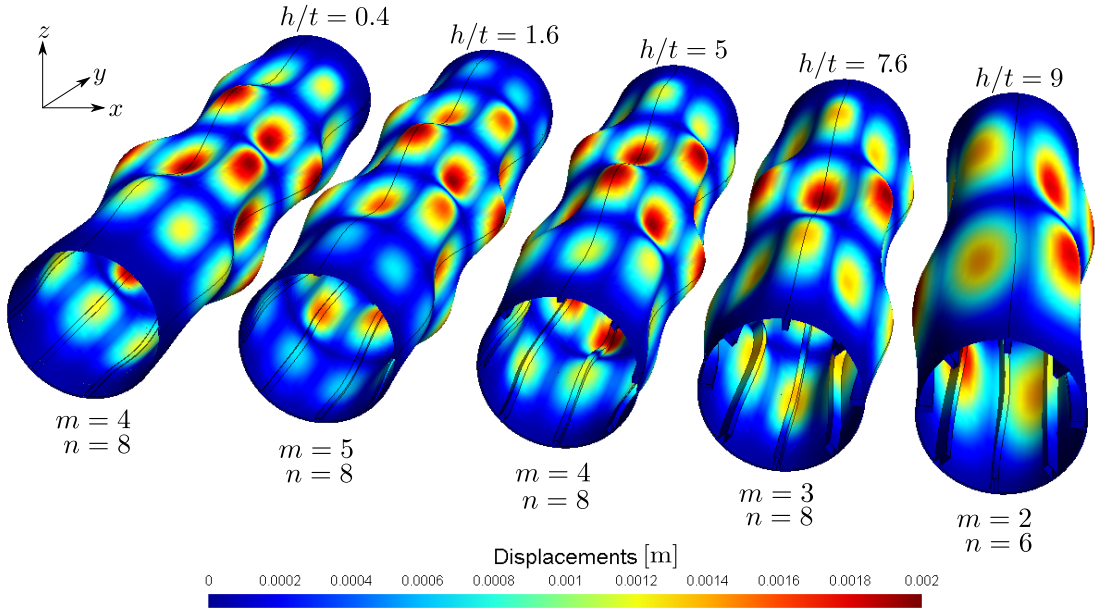

Figure 4.28: Number of half-waves along the span m and circumference n for various h/t. Stiffened cylinder, UF-SL model.

After this point, the critical load increases monotonically as h/t.

Regarding the mode shapes, in the interval from $h/t = 0$ to $h/t = 7.9$, the stiffeners undertake the maximum radial load and eight half-waves are developed on the circumference, as shown in Figure 4.27. For $h/t > 7.9$ the slope of the curve changes and, even though the buckling load continues to increase, the mode shapes change and the skin buckles. For this case six half-waves

appear instead of the original eight. Figure 4.28 shows the mode shapes and number of half waves for five different cases.

4.6.4.2 Thickness of Longitudinal Stiffeners

A second parametric study is performed. For this case the thickness θ of the stiffeners is varied. The radius, length and cylinder's thickness are as the previous example. The height of the stiffeners is chosen to be $h = 0.015$ m ($h/t = 7.5$). θ is varied from 1^o to 5^o. The effect on the buckling load and mass is reported. The same models used in previous example are employed.

Table 4.4: Parametric study of variable stiffener thickness. Stiffener thickness, relative mass and relative critical load for a stiffened cylinder.

θ [°]	M_{st}/M_o [–]	P_{st}/P_o [–]	P_{st}/P_o [–]
		Solid	**UF-SL**
1	1.15	1.047	1.049
2	1.30	1.089	1.088
3	1.45	1.139	1.138
4	1.60	1.203	1.201
5	1.76	1.263	1.261

Table 4.4 shows the results for the five cases. Mass is reported as M_{st}/M_o, where M_o is the mass of the un-stiffened cylinder. Results show that UF-SL results are close to those given by the Solid model.

4.6.4.3 Localised Stresses

When designing thin-walled structures the use of shell models is common practice. Shell models provide a tool that is both efficient and accurate. Nevertheless, their accuracy might be limited by the particular theory used, e.g. by plane stress assumptions. Therefore, shell models are rarely used to recover through thickness stress distributions. For this reason, a shell model is included here with the purpose of showing how this limitation is solved by UF-SL. On the other hand, solid models are too computationally expensive and slow for modelling thin structures. For more complex geometries, like a the thin cylinder with stiffeners, modelling becomes even more challenging, particularly if local stresses are to be computed. The aim of this section is to give evidence on how the UF-SL model can capture through thickness stresses, as in a Solid model, with the efficiency similar to that of a Shell model.

The three models were used to perform a linear buckling (for both, the original and modified geometry) of a cylinder with stiffeners of size $h/t = 7.6$. Table 4.5 shows the results for the predicted buckling load, the DOFs and the number of operations for each solver.

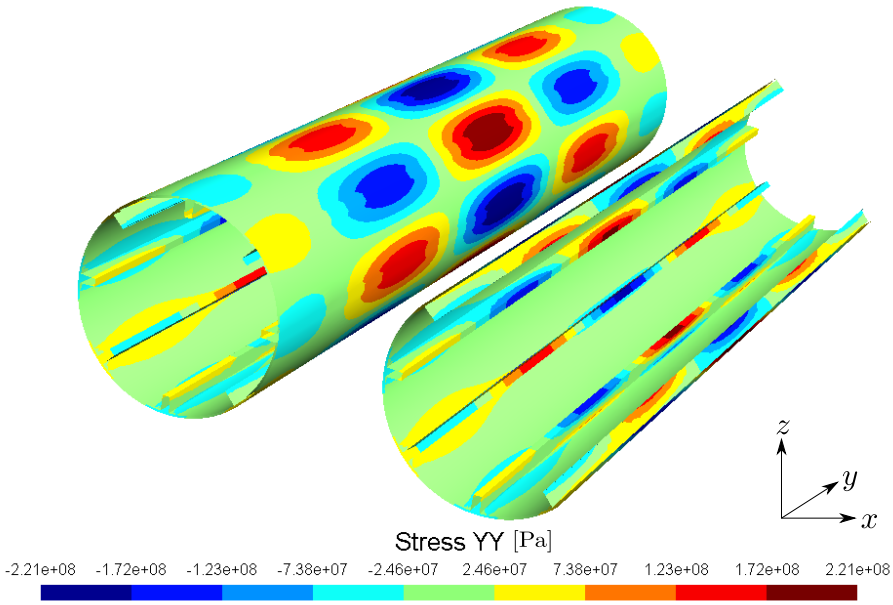

Figure 4.29: 3D axial stress σ_{yy} at buckling. Stiffened cylinder longitudinal cut. SL model.

The buckling load predicted by the UF-SL model is within ~ 1% relative the Solid solution. The shell model gives a load ~ 10% smaller.

For the modified geometry, axial and hoop stresses were measured, Figures 4.29 and 4.30 show the 3D plots of these given by the UF-SL. Notice that maximum stresses occur close to the

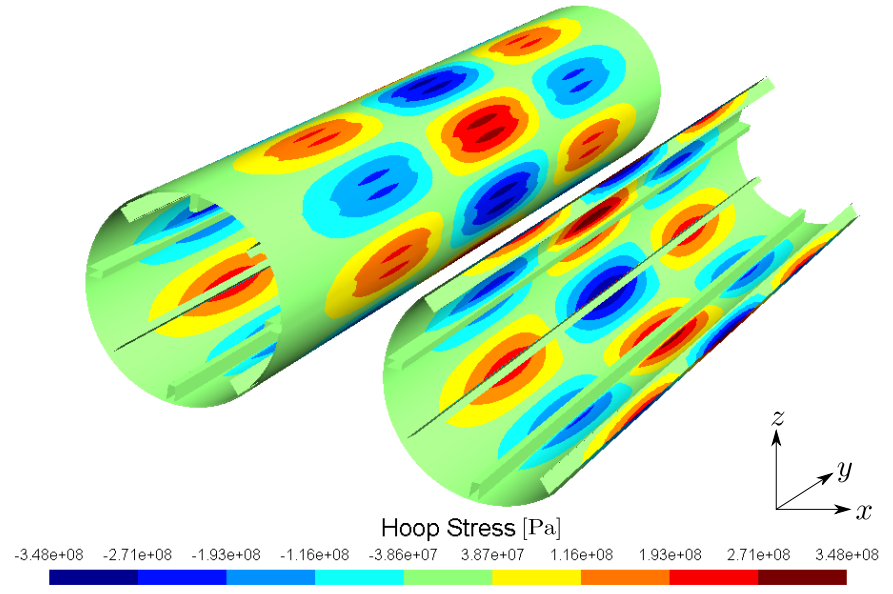

Figure 4.30: 3D hoop stress σ_{hp} at buckling. Stiffened cylinder longitudinal cut. SL model.

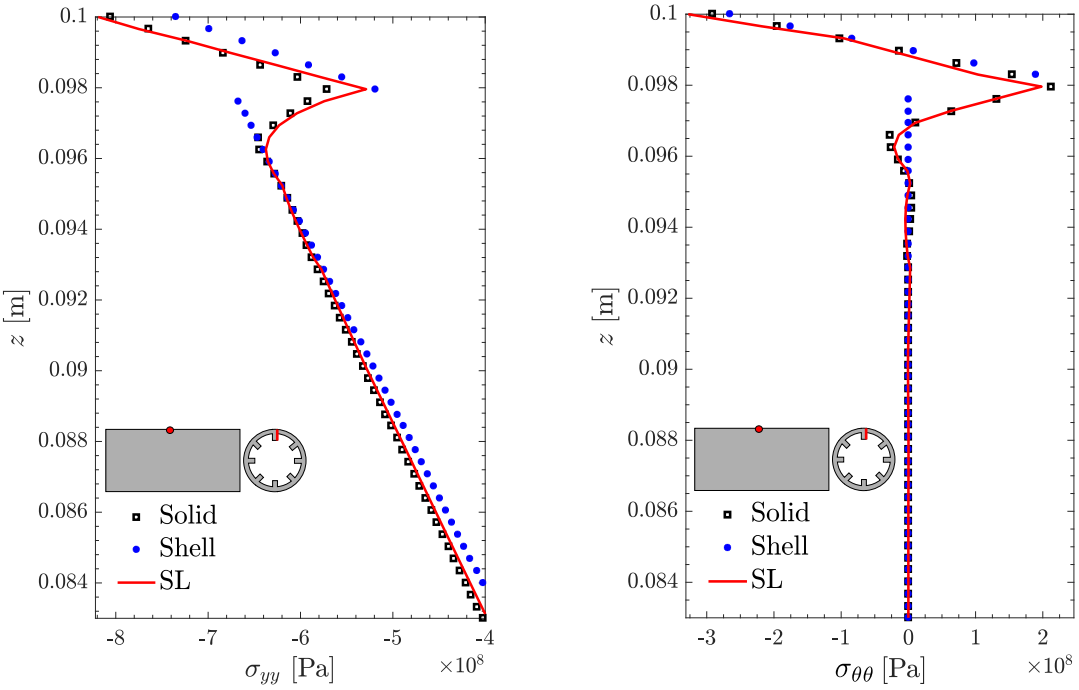

(a) Axial normal stress σ_{yy} through thickness at edge of the stiffener.

(b) Hoop stress $\sigma_{\theta\theta}$ through thickness at edge of the stiffener.

Figure 4.31: Normal σ_{yy} and hoop stress $\sigma_{\theta\theta}$ through thickness. Stiffened cylinder.

Table 4.5: Critical load, DOFs, Operations for Sparse and Eigenvalue Solvers for linear buckling analysis of a stiffened cylinder for three different models.

	P_o [N] $\times 10^6$	DOFs #	Ops. Inversion #	Ops. Eigenvalue *#per iteration*
Model				
Solid	1.29	4,879,032	$\sim 10^{10}$	$\sim 10^{20}$
Shell	1.16	712,176	$\sim 10^{8}$	$\sim 10^{17}$
UF-SL	1.28	884,520	$\sim 10^{14}$	$\sim 10^{17}$

edge of the stiffener (corner) and not at middle of it, as it is predicted by the Shell model and discussed further in this section. Figures 4.31(a) and 4.31(b) show through thickness stresses at this position. Take for instance σ_{yy}, UF-SL and Solid give a linear distribution, except close to the singularity. The Shell model predicts piecewise linear distribution throughout the thickness. Hoop stresses through thickness have a linear distribution along the skin. Stress is zero along the stiffener, except close to the corner. As mentioned before, the shell model only gives an approximate distribution close to the corner.

A third set of plots is provided, the stresses are measured at the top of the skin from stiffener

to stiffener. Figures 4.32(a) and 4.32(b) show the stresses in function of the arc length s. Both, UF-SL and Solid predict a discontinuity at the interface between the skin and stiffener. The Shell model is not able to capture the discontinuity and predicts a maximum concentration of stress at the middle of the stiffener.

Regarding the efficiency, the number of DOFs for the UF-SL model increased significantly compared to the previous cases. In this case 240 curved elements are used to discretise the cross-section. Shell model is the most efficient in terms of DOFs, followed by UF-SL and Solid model respectively. The number of operations for solving the system is highest for the UF-SL model. The number of operations for the iterative eigenvalue step is the same to that of the Shell model, and ~ 85% less than that of the Solid model.

4.7 Discussion

The Unified Formulation Linearised Buckling Model, combined with the Serendipity Lagrange Expansion model, provides the means for studying the linear buckling behaviour of complex shell-like structures. Moreover, it is able to capture localised three-dimensional stress fields, especially through thickness and in locations close to singularities, without the need of sub-modelling. To achieve the same results using finite element models requires fine meshes and a minimum number of elements through thickness (for the case of solid models).

For all of the different cases studied, the critical load predicted by the UF-SL model was within 1% of error compared with FEM models. Buckling shapes have shown to be also in accordance with the reference solutions. Showing the capability of the model for performing accurate buckling analysis. Stress distributions of a modified geometry resembling the initial post-buckled shape

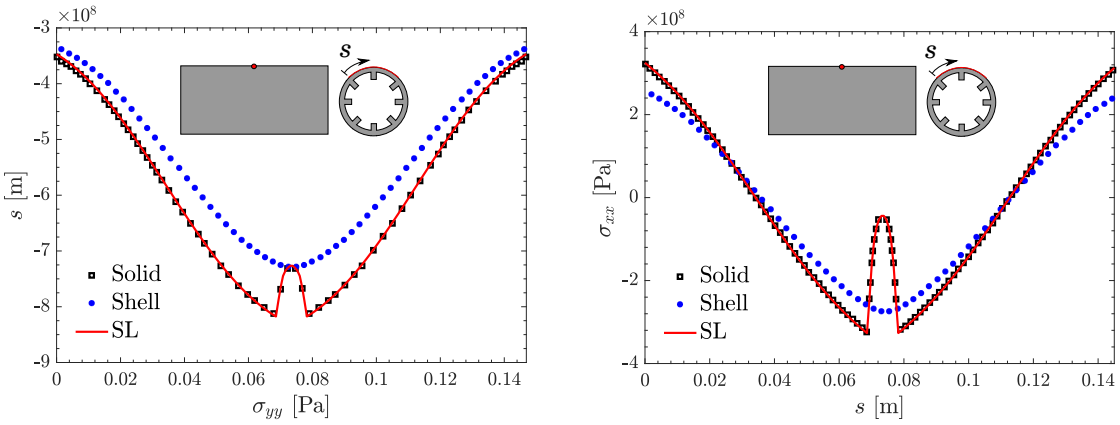

(a) Axial normal stress σ_{yy} vs s.

(b) Hoop stress $\sigma_{\theta\theta}$ vs s.

Figure 4.32: Normal σ_{yy} and hoop stress $\sigma_{\theta\theta}$ along the arc length $s \in [0, 0.14]$ (from stiffener to stiffener).

have also been presented[12]. The UF-SL model can predict stresses that are in agreement with FEM solutions, especially in regions close to corners and edges. In these regions, the Shell model may fail to capture accurate stress fields.

Efficiency was measured in terms of DOFs and number of operations (*time*) required for each step. For the first three cases the UF-SL models used at least one order of magnitude less DOFs compared with the other two models. For the case of the stiffened cylinder it was clear that the shell and UF-SL model performed similarly. This provides evidence of the model ability to reproduce results with the same degree of accuracy in a more efficient way. In terms of the number of operations for the inversion step, the UF-SL model showed the same performance as a Solid model, except for the case of a stiffened cylinder. The Shell model was the most efficient in every case. For the number of operations (*per iteration*) for the eigenvalue step, the UF-SL was the fastest, except for the last case where Shell and UF-SL models performed similarly.

The last section presented how the UF-SL model can be used in a design environment. Parametric studies for a stiffened cylinder was provided as an example. It was shown that the UF-SL model can achieve the same level of accuracy for buckling and stress analyses as that given by a Solid model, with the efficiency of a Shell model. And, in some cases, a better performance. Considering the accuracy of the buckling and stress analyses, together with the computational efficiency, makes the present model an attractive choice for industrial applications.

4.8 Concluding Remarks

The main aim was to provide an accurate, efficient and reliable design tool for performing linearised buckling analysis of complex thin-walled structures. The model is introduced within the Unified Formulation, in which the SL Expansion is adopted. Curved elements, with an exact geometrical representation, are used to discretise the cross-sections. Buckling analysis for a thin box, a thin box with round fillets, a thin cylinder and a stiffened cylinder have been carried out. The model was benchmarked against Solid and Shell finite element models. Critical loads, buckling modes, stresses and three different measures of efficiency (DOFs, time for inversion and time per iteration) were computed. The main findings can be summarised as follows:

1. For all cases, the critical loads were accurately predicted within 1% of error relative to FEM Shell and Solid models. Additionally, buckling shapes are in good agreement with the reference solutions.

2. Local stresses through thickness and close to corners were accurately captured. This was achieved without the need of sub-modelling.

[12]As mentioned before, this is not a proper initial post-buckling analysis, since second order effects are not taken into account.

3. The UF-SL model was the most efficient in terms DOFs for all the cases, except for the stiffened cylinder for which the efficiency was close to the Shell model.

4. For inversion time, the UF-SL model was the second fastest (two orders of magnitude less compared with Shell model time) for the box examples; performance was the slowest for the two cylinders (4 orders of magnitude compared with Solid model's time).

5. For the eigenvalue solver time (per iteration), the UF-SL model was the fastest for every case (between 1 and 4 orders of magnitude faster).

The proposed UF-SL Linearised Buckling Model proved to be an efficient, accurate and reliable tool for performing linear buckling and stress analysis of shell-like complex structures.

CHAPTER 5

UNIFIED FORMULATION 3D-BEAM MODEL

"Arc, amplitude, and curvature sustain a similar relation to each other as time, motion, and velocity, or as volume, mass, and density"

- Friedrich Gauss

In this chapter a novel three-dimensional beam model is proposed. The new element type is based on the Unified Formulation, which has proved to be an accurate and efficient model. The Unified Formulation Three-dimensional Beam Model (UF-3D) is a non-linear Total Lagrangian beam formulation that makes use of a three-dimensional shape mapping to model curved and non-prismatic geometries. Three sets of shape functions are used to describe both, the geometry and the kinematic field: first, a 3D function describing the solid beam-like geometry; second, a function defined in the element cross-section (which, in this case, is the Serendipity Lagrange Expansion); and third, a function defined in the element beam axis. The last two can be chosen and enriched independently, yet, they are linked to the 3D geometry via their gradients and a Jacobian transformation.

The work presented in this chapter is the outcome of secondment that took place between May and June 2018 in Delft University, The Netherlands. The need to model the non-linear behaviour of imperfect structures under buckling was the inspiration for this work. The contents of Section 5.3.2 and 5.4.4 were developed, and are shared, with my colleague Mayank Patni. The rest of the content is the personal contribution of the author.

5.1 Aim and Motivation

One known (and rarely discussed or mentioned) disadvantage of the Unified Formulation, in its current form, is that it works only for locally prismatic[1] structures. That is, tapered beams or structures with changing shape or size of cross-sections cannot be accurately described. Some progress in modelling tapered structures, using the Unified Formulation, has been made [104–106], where the tapered structures are described using non-rectangular cross-sections and prismatic beam geometries[2], rather than varying the cross-section along the the beam axis. Another feature that has not been completely developed is the ability to model curved beams. Recently, a curved-beam formulation using the Frenet-Serret description has been introduced in the Unified Formulation context [107]. The current Frenet-Serret approach has two limitations: first, is that the element cross-section cannot change shape or size along the beam direction; and second, it requires the exact description of the curved line defining the beam's axis. Additionally, the existing Unified Formulation models describing curved or tapered structures are linear models, which limits its range of applications, especially on the case of curved-beams.

The aim of this chapter is to provide a formulation, called Unified Formulation 3D Beam Model (UF-3D) from now on, that overcomes these limitations and have the following features:

1. Capability for modelling non-prismatic elements, particularly tapered structures.
2. Model structures with curved-beam axis.
3. Describe curved geometries using a three-dimensional shape mapping (similar to CAD) approach, without increasing the DOFs.
4. Fully non-linear Total Lagrangian formulation.
5. Include all the capabilities of the Unified Formulation[3], particularly the SL Expansion Model.

5.2 Introduction

Analysing beam-like curved structures is a challenging task, mainly due to the fact that their behaviour is often non-linear, and, in a finite element context, this is associated with a high computational cost. The difficulty of obtaining accurate solutions is particularly pronounced in the analysis of 3D curved beam structures. Namely because a general 3D non-linear formulation is not a simple extension of a 2D formulation. In a non-linear 3D analysis, large rotations, which are not vector quantities, have to be considered. In recent decades, many approaches that improve

[1] Meaning that each element has to be prismatic in the beam axis direction. Complex structures, e.g. stiffened panels, can be constructed by joining prismatic elements.

[2] that is, the tapered geometry is actually modelled as a "cross-section", and its width as the "beam axis".

[3] Efficiency, accuracy, versatility -shape functions-, etc.

the efficiency of three-dimensional beam FEM models have been proposed. One of the first was developed by Belytschko [108], who used the previous work on initially curved beams from Glaum [109], to develop a non-linear high-order co-rotational formulation. Bathe and Bolourch [110] presented a Total Lagrangian formulation in which Hermite shape functions are used to interpolate transverse bending displacements and linear functions elsewhere, effectively reducing the amount of variables needed to model a three-dimensional beam. At around the same time, Hodges et. al. [111, 112] proposed a model that coupled bending, torsion, shear deformation, extension and warping of initially twisted and curved beam structures. Later on, Crisfield [113] extended the co-rotational formulation to embed the strains associated with small-deflections into a continuously rotating frame. The method showed excellent numerical performance and a quadratic convergence rate, when combined with Newton-Raphson solvers. A similar approach by Surana and Sorem [114] uses the principal bending directions at the centroid of each element as a reference system to describe the kinematics of the beam (three rotations and three displacements). A slightly different approach, using Reissner's beam theory, was proposed by Ibrahimbegović and Frey [115, 116]. In this formulation, a hierarchical three-dimensional curved beam element is used to mitigate the shear and membrane locking caused by low order elements. Petrov and Géradin [117] developed a finite element theory for curved and twisted beams based on the exact solutions for three-dimensional solids. The theory includes all components of the stress tensor, in contrast to traditional beam theories that take into account only the stress resultants over the cross-sections. Pai and Nayfeh [118] developed an approach to model composite beams under large rotations and displacements that take into account three-dimensional stress effects, without the need of tensor operations or asymptotic expansions. Yu et al. [119] proposed a model for naturally curved anisotropic beams with thin-walled cross-sections. In their model, eigenfunctions are used to expand the displacement field as an expansion series, allowing torsion and warping effects to be accurately described. More recently, a linear curved-beam Unified Formulation for prismatic beams, using the Frenet-Serret description, has been introduced in the Unified Formulation context [107].

The Unified Formulation, due to its flexibility on choosing shape functions and/or order of expansion, has proven [12, 38, 120] to be an accurate tool for describing 3D-like beams. Recovering three-dimensional stress fields close to complicated regions is a known capability. As mentioned previously, one of the limitations of the current formulation is that curved beams and/or beams with changing shape of cross-sections are not accurately described. Furthermore, recent developments in the non-linear capabilities are still limited to prismatic structures [95, 121]. Herein an extension of the formulation to curved *and* non-prismatic elements, taking into account the non-linear behaviour, is presented.

5.3 Mathematical Formulation

The three-dimensional beam model is based on a non-linear, displacement-based finite element formulation. The displacement field is approximated using two different shape functions, one defined over the cross-section of the element, and the other defined on its axis. The three-dimensional geometry is described via an additional 3D-mapping, which allows to model general solid-like beam structures without adding additional degrees of freedom.

5.3.1 Non-Linear Finite Element Model

Let $\boldsymbol{u} = [u, v, w]^{\mathrm{T}}$ be the displacement field and consider the Green-Lagrange Stress tensor $\boldsymbol{E}$, whose components in Cartesian coordinates can be expressed as [7, 93]

$$E_{ij} = \frac{1}{2}\left(\boldsymbol{u}_{,i} \cdot \boldsymbol{g}_j + \boldsymbol{u}_{,j} \cdot \boldsymbol{g}_i + \boldsymbol{u}_{,i} \cdot \boldsymbol{u}_{,j}\right) \tag{5.1}$$

where comma denotes derivatives, $i, j = 1,2,3$ and $\boldsymbol{g}_1 = [1,0,0]^{\mathrm{T}}$, $\boldsymbol{g}_2 = [0,1,0]^{\mathrm{T}}$ and $\boldsymbol{g}_3 = [0,0,1]^{\mathrm{T}}$; its variation with respect to displacements is

$$\delta E_{ij} = \frac{1}{2}\left[\delta\boldsymbol{u}_{,i} \cdot (\boldsymbol{g}_j + \boldsymbol{u}_{,j}) + \delta\boldsymbol{u}_{,j} \cdot (\boldsymbol{g}_i + \boldsymbol{u}_{,i})\right]. \tag{5.2}$$

Elastic equilibrium is enforced via the Principle of Virtual Displacements, which, in a quasi-static setting, states that

$$\delta W_{\mathrm{int}} = \delta W_{\mathrm{ext}}, \tag{5.3}$$

where W_{int} and W_{ext} are the internal and external works, respectively. By definition, the internal energy is the work done by stresses over corresponding virtual strains. Noting that $W_{\mathrm{int}} = \sum_{\mathrm{e}} W_{\mathrm{int}}^{(\mathrm{e})}$ and letting $V_{(\mathrm{e})}$ be the volume of the generic element, then

$$\delta W_{\mathrm{int}}^{(\mathrm{e})} = \int_{V_{(\mathrm{e})}} \delta\boldsymbol{E} \cdot \boldsymbol{S}\, dV, \tag{5.4}$$

where $\boldsymbol{S}$ is the Second Piola Stress Tensor. $\boldsymbol{S}$ can be written in terms of $\boldsymbol{E}$ as [7].

$$\boldsymbol{S} = \mathscr{C}\boldsymbol{E} \tag{5.5}$$

with $\mathscr{C}$ the fourth-order elasticity tensor. For the sake of brevity, the reader is referred to [3] for an explicit definition of the coefficients in $\mathscr{C}$. If we now denote body forces per unit volume as $\boldsymbol{g}$, surface forces per unit area as $\boldsymbol{p}$, line forces per unit length as $\boldsymbol{q}$ and concentrated forces acting on Q as $\boldsymbol{P}$, the external work is

$$\delta W_{\mathrm{ext}}^{(\mathrm{e})} = \int_{V_{(\mathrm{e})}} \delta\boldsymbol{u}^{\mathrm{T}}\boldsymbol{g}\, dV + \int_S \delta\boldsymbol{u}^{\mathrm{T}}\boldsymbol{p}\, dS + \int_l \delta\boldsymbol{u}^{\mathrm{T}}\boldsymbol{q}\, dl + \delta\boldsymbol{u}^{\mathrm{T}}|_Q \boldsymbol{P}. \tag{5.6}$$

In a finite element context, the element displacement field is approximated by means of local shape functions, G_i, and generalised nodal displacements $\boldsymbol{u}_i$, such that

$$\boldsymbol{u}_{(\mathrm{e})}(x,y,z) = G_i(x,y,z)\boldsymbol{u}_i, \qquad \text{with} \qquad i = 1,\ldots,N, \tag{5.7}$$

where N is the number of degrees of freedom per element. Einstein summation convention for repeated indexes is implied hereafter. The shape function $G(x,y,z)$ is described in detail in the Section 5.3.2. With this definition, the components of the tensors in equation (5.1) and equation (5.2) can be written in Voigt notation as

$$\boldsymbol{E} = \mathscr{B}_i \boldsymbol{u}_i, \tag{5.8}$$

$$\delta\boldsymbol{E} = \mathscr{D}_j \delta\boldsymbol{u}_j, \tag{5.9}$$

where

$$\mathscr{B}_i = \begin{bmatrix} \frac{\partial G_i}{\partial x} + \frac{1}{2}\frac{\partial u}{\partial x}\frac{\partial G_i}{\partial x} & \frac{1}{2}\frac{\partial v}{\partial x}\frac{\partial G_i}{\partial x} & \frac{1}{2}\frac{\partial w}{\partial x}\frac{\partial G_i}{\partial x} \\ \frac{1}{2}\frac{\partial u}{\partial y}\frac{\partial G_i}{\partial y} & \frac{\partial G_i}{\partial y} + \frac{1}{2}\frac{\partial v}{\partial y}\frac{\partial G_i}{\partial y} & \frac{1}{2}\frac{\partial w}{\partial y}\frac{\partial G_i}{\partial y} \\ \frac{1}{2}\frac{\partial u}{\partial z}\frac{\partial G_i}{\partial z} & \frac{1}{2}\frac{\partial v}{\partial z}\frac{\partial G_i}{\partial z} & \frac{\partial G_i}{\partial z} + \frac{1}{2}\frac{\partial w}{\partial z}\frac{\partial G_i}{\partial z} \\ \frac{\partial u}{\partial y}\frac{\partial G_i}{\partial z} & \frac{\partial G_i}{\partial z} + \frac{\partial v}{\partial y}\frac{\partial G_i}{\partial z} & \frac{\partial G_i}{\partial y} + \frac{\partial w}{\partial y}\frac{\partial G_i}{\partial z} \\ \frac{\partial G_i}{\partial z} + \frac{\partial u}{\partial x}\frac{\partial G_i}{\partial z} & \frac{\partial v}{\partial x}\frac{\partial G_i}{\partial z} & \frac{\partial G_i}{\partial x} + \frac{\partial w}{\partial x}\frac{\partial G_i}{\partial z} \\ \frac{\partial G_i}{\partial y} + \frac{\partial u}{\partial x}\frac{\partial G_i}{\partial y} & \frac{\partial G_i}{\partial x} + \frac{\partial v}{\partial x}\frac{\partial G_i}{\partial y} & \frac{\partial w}{\partial x}\frac{\partial G_i}{\partial y} \end{bmatrix},$$

and

$$\mathscr{D}_i = \begin{bmatrix} x_1\frac{\partial G_j}{\partial x} & y_1\frac{\partial G_j}{\partial x} & z_1\frac{\partial G_j}{\partial x} \\ x_2\frac{\partial G_j}{\partial y} & y_2\frac{\partial G_j}{\partial y} & z_2\frac{\partial G_j}{\partial y} \\ x_3\frac{\partial G_j}{\partial z} & y_3\frac{\partial G_j}{\partial z} & z_3\frac{\partial G_j}{\partial z} \\ x_2\frac{\partial G_j}{\partial z} + x_3\frac{\partial G_j}{\partial y} & y_2\frac{\partial G_j}{\partial z} + y_3\frac{\partial G_j}{\partial y} & z_2\frac{\partial G_j}{\partial z} + z_3\frac{\partial G_j}{\partial y} \\ x_1\frac{\partial G_j}{\partial z} + x_3\frac{\partial G_j}{\partial x} & y_1\frac{\partial G_j}{\partial z} + y_3\frac{\partial G_j}{\partial x} & z_1\frac{\partial G_j}{\partial z} + z_3\frac{\partial G_j}{\partial x} \\ x_1\frac{\partial G_j}{\partial y} + x_2\frac{\partial G_j}{\partial x} & y_1\frac{\partial G_j}{\partial y} + y_2\frac{\partial G_j}{\partial x} & z_1\frac{\partial G_j}{\partial y} + z_2\frac{\partial G_j}{\partial x} \end{bmatrix},$$

with

$$x_1 = 1 + \frac{\partial u}{\partial x}, \qquad x_2 = \frac{\partial u}{\partial y}, \qquad x_3 = \frac{\partial u}{\partial z}, \tag{5.10}$$

$$y_1 = \frac{\partial v}{\partial x}, \qquad y_2 = 1 + \frac{\partial v}{\partial y}, \qquad y_3 = \frac{\partial v}{\partial z}, \tag{5.11}$$

$$z_1 = \frac{\partial w}{\partial x}, \qquad z_2 = \frac{\partial w}{\partial y}, \qquad z_3 = 1 + \frac{\partial w}{\partial z}. \tag{5.12}$$

With these, the element internal force equation (5.4) reads

$$\begin{aligned} \delta W^{(e)}_{\text{int}} &= \delta\boldsymbol{u}_j^{\mathrm{T}} \left(\int_{V_{(e)}} \mathscr{D}_j^{\mathrm{T}} \boldsymbol{C} \mathscr{B}_i \, dV \right) \boldsymbol{u}_i \\ &= \delta\boldsymbol{u}_j^{\mathrm{T}} \boldsymbol{K}^{(e)}_{ij} \boldsymbol{u}_i. \end{aligned} \tag{5.13}$$

Recasting equation (5.6) as $-\delta W^{(e)}_{\text{ext}} = \delta\boldsymbol{u}^{\mathrm{T}} \boldsymbol{f}_{(e)}$ and substituting with equation (5.13) into equation (5.3) we get

$$\delta\boldsymbol{u}_j^{\mathrm{T}} \boldsymbol{K}^{(e)}_{ij} \boldsymbol{u}_i = \delta\boldsymbol{u}_j^{\mathrm{T}} \boldsymbol{f}_{(e)}, \tag{5.14}$$

which is a statement of elastic equilibrium in weak form, where $\boldsymbol{K}^{(e)}_{ij}$ and $\boldsymbol{f}_{(e)}$ are, respectively, the structural *Secant Matrix* and the generalised load vector of the generic element. In a non-linear

finite element context, it is useful to have an expression for the *Tangent Matrix*, as it is used in non-linear solvers e.g. Newton-Raphson or Riks. The expression of this matrix can be deduced from the linearisation of the second variation of the internal work [122]:

$$\begin{aligned}\delta(\delta W_{\text{int}}^{(\text{e})}) &= \int_{V_{(\text{e})}} \delta\left(\delta\boldsymbol{E}\cdot\boldsymbol{S}\right), dV \\ &= \int_{V_{(\text{e})}} \delta\boldsymbol{E}\cdot\delta\boldsymbol{S}\, dV + \int_{V_{(\text{e})}} \delta(\delta\boldsymbol{E})\cdot\boldsymbol{S}\, dV.\end{aligned} \tag{5.15}$$

Substituting equation (5.5) and equation (5.9) into the first term of the right hand side give as result

$$\begin{aligned}\int_{V_{(\text{e})}} \delta\boldsymbol{E}\cdot\delta\boldsymbol{S}\, dV &= \delta\boldsymbol{u}_j^{\text{T}}\left(\int_{V_{(\text{e})}} \mathscr{D}_j^{\text{T}}\boldsymbol{C}\mathscr{D}_i\, dV\right)\delta\boldsymbol{u}_i \\ &= \delta\boldsymbol{u}_j^{\text{T}}\boldsymbol{K}_{(\text{O})ij}^{(\text{e})}\delta\boldsymbol{u}_i,\end{aligned} \tag{5.16}$$

which is the non-linear contribution to the *Tangent Matrix*. It is easy to prove (Appendix B) that the second term on the right hand side, called *Geometrical Stiffness Matrix*, can be written as [123]

$$\begin{aligned}\int_{V_{(\text{e})}} \delta(\delta\boldsymbol{E})\cdot\boldsymbol{S}\, dV &= \delta\boldsymbol{u}_j^{\text{T}}\left(\int_{V_{(\text{e})}} \mathscr{D}^{*\text{T}}_j\boldsymbol{\sigma}\boldsymbol{I}_i\, dV\right)\delta\boldsymbol{u}_i \\ &= \delta\boldsymbol{u}_j^{\text{T}}\boldsymbol{K}_{(\text{G})ij}^{(\text{e})}\delta\boldsymbol{u}_i,\end{aligned} \tag{5.17}$$

where $\boldsymbol{\sigma}^{\text{T}} = [\sigma_{xx},\sigma_{yy},\sigma_{zz},\sigma_{yz},\sigma_{xz},\sigma_{xy}]$ is a vector with the Second Piola stresses, $\boldsymbol{I}$ is a 3×3 identity matrix, and

$$\mathscr{D}_i^* = \begin{bmatrix} \frac{\partial G_i}{\partial x}\frac{\partial G_j}{\partial x} \\ \frac{\partial G_i}{\partial y}\frac{\partial G_j}{\partial y} \\ \frac{\partial G_i}{\partial z}\frac{\partial G_j}{\partial z} \\ \frac{\partial G_i}{\partial z}\frac{\partial G_j}{\partial y} + \frac{\partial G_i}{\partial y}\frac{\partial G_j}{\partial z} \\ \frac{\partial G_i}{\partial z}\frac{\partial G_j}{\partial x} + \frac{\partial G_i}{\partial x}\frac{\partial G_j}{\partial z} \\ \frac{\partial G_i}{\partial x}\frac{\partial G_j}{\partial y} + \frac{\partial G_i}{\partial y}\frac{\partial G_j}{\partial x} \end{bmatrix}.$$

Therefore, the element *Tangent Matrix* is given by

$$\boldsymbol{K}_{(\text{T})ij}^{(\text{e})} = \boldsymbol{K}_{(\text{O})ij}^{(\text{e})} + \boldsymbol{K}_{(\text{G})ij}^{(\text{e})}. \tag{5.18}$$

5.3.2 Curved Beam Formulation

Equation (5.7) describes the element displacement field in terms of the shape functions G_i, which, in principle, can take many functional forms. In the context of the Unified Formulation [11], two shape functions are used to describe the displacement field. The first defined over the cross-section $F(x,z)$, the second on the beam axis $N(y)$, as depicted in Figure 2.6. The shape function takes the product form

$$G(x,y,z) = F(x,z)N(y), \tag{5.19}$$

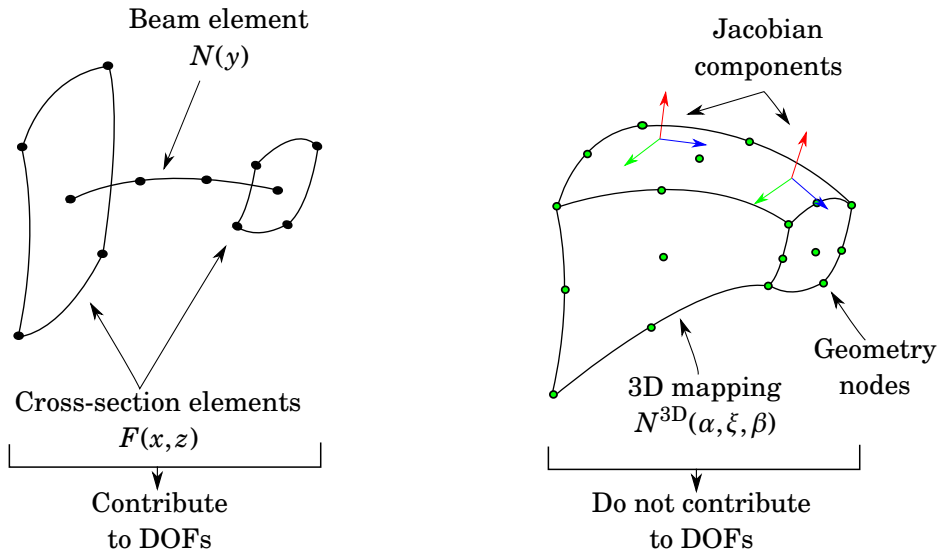

(a) Displacement field discretisation.

(b) 3D geometry description.

Figure 5.1: Discretisation and element mapping.

which allows the desired expansion function to be chosen independently, therefore, two subindices are needed: $\tau = 1,...,m$ (number of expansion terms) for the functions in the cross-section, and $i = 1,...,N_e$ (number of nodes in the beam element) for the those on the beam axis. The displacement field reads

$$\begin{aligned} \boldsymbol{u} &= F_\tau(x,z)N_i(y)\boldsymbol{u}_{i\tau} \\ &= G_{i\tau}\boldsymbol{u}_{i\tau}, \end{aligned} \tag{5.20}$$

with $\boldsymbol{u}_{i\tau}$ the generalised displacements. In this work we use the Serendipity Lagrange Expansion Model [12] as described in detail in Chapter 3, in which the cross-section expansions $F(\alpha,\beta)$, defined in the master element $[-1,1]^2$, are a combination of 2D Lagrange-type shape functions and hierarchical polynomials. The beam functions $N(\xi)$, defined in $[-1,1]$, are the traditional 1D Lagrange shape functions.

In the present work an approach for representing the geometry, by introducing a third shape function, which is independent of the displacement expansion functions, is presented. This function is used as a three-dimensional shape mapping, similar to the approach in Chapter 3. Let $N^{3D}(\alpha,\xi,\beta)$ be a function, defined in $[-1,1]^3$, describing the geometry such that the position vector $\boldsymbol{x}$ of any given point, in the global Cartesian system, can be represented as

$$\boldsymbol{x} = N_k^{3D}(\alpha,\xi,\beta)\boldsymbol{x}_k \tag{5.21}$$

where $\boldsymbol{x}_k \in \mathbb{R}^3$ are the position vectors of the nodes of the element, and $k = 1,...,N_{ne}$, with N_{ne} the number of nodes; 8-noded or 27-noded brick elements are used in this case. The number of nodes used to represent the element geometry is not related to those used for the discretisation

of the cross-section and beam axis, as the shape functions are independent from each other. Figure 5.1(a) shows the approximation of the displacement field, where the cross-section and beam axis elements[4] and shape functions are decoupled. The connection between the displacement shape functions $G(\alpha,\xi,\beta)$ (which contribute to the DOFs), the 3D-mapping function $N^{3D}(\alpha,\xi,\beta)$ (which do not contribute to the DOFs) and the structure's geometry is via the Jacobian matrix, defined as[5]:

$$\mathscr{J} = \begin{bmatrix} x_\alpha & y_\alpha & z_\alpha \\ x_\xi & y_\xi & z_\xi \\ x_\beta & y_\beta & z_\beta \end{bmatrix},$$

where the entries are the derivatives of equation (5.21), and can be interpreted as the local curvilinear basis vectors, as shown in Figure 5.1(b). The relationship reads

$$\begin{bmatrix} G_x \\ G_y \\ G_z \end{bmatrix} = \begin{bmatrix} x_\alpha & y_\alpha & z_\alpha \\ x_\xi & y_\xi & z_\xi \\ x_\beta & y_\beta & z_\beta \end{bmatrix}^{-1} \begin{bmatrix} G_\alpha \\ G_\xi \\ G_\beta \end{bmatrix}. \tag{5.22}$$

This simple expression changes the form of the Unified Formulation Fundamental Nucleus significantly. Particularly, it couples the gradients of the shape functions and adds new terms to the kernel. A comparison between the expressions of the gradients in the case of existing prismatic formulation and in the new 3D formulation is presented in Section 5.3.3.

Substituting equation (5.20) into equation (5.13) leads to

$$\begin{aligned} \delta W_{\text{int}}^{(e)} &= \delta \boldsymbol{u}_{js}^{\mathrm{T}} \left(\int_{V_{(e)}} \mathfrak{D}_{js}^{\mathrm{T}} \boldsymbol{C} \mathfrak{B}_{i\tau} \, dV \right) \boldsymbol{u}_{i\tau} \\ &= \delta \boldsymbol{u}_{js}^{\mathrm{T}} \boldsymbol{k}_{(e)}^{ij\tau s} \boldsymbol{u}_{i\tau}, \end{aligned} \tag{5.23}$$

and the element *Secant Matrix* is then:

$$\boldsymbol{k}_{(e)}^{ij\tau s} = \int_{V_{(e)}} \mathfrak{D}_{js}^{\mathrm{T}} \boldsymbol{C} \mathfrak{B}_{i\tau} \, dV \tag{5.24}$$

Similarly, substituting equation (5.20) into equation (5.15) results in the expression for the element *Tangent Matrix*:

$$\boldsymbol{\kappa}_{(\mathrm{T})}^{ij\tau s} = \boldsymbol{\kappa}_{(\mathrm{O})}^{ij\tau s} + \boldsymbol{\kappa}_{(\mathrm{G})}^{ij\tau s}. \tag{5.25}$$

As stated previously, most non-linear solvers need the *Tangent Matrix* as input exclusively, *Secant Matrix* is not necessarily required[6]. For this reason, only an explicit form of the *Tangent Matrix* is provided. The reader is referred to Appendix C for details. Note that this matrix is sufficient if a linear analysis is to be performed, since the *Secant Matrix* and *Tangent Matrix* coincide in this regime.

[4]This is different from a traditional Unified Formulation approach, since the element is curved and tapered, in contrast to what is explained in Chapters 3 and 4 where the element was prismatic and straight.

[5]The following expression should read: $x_{,\alpha}$, $y_{,\alpha}$, etc., denoting the derivative with a comma; for these expressions, the commas will be omitted from this point onwards.

[6]The *Secant Matrix* is commonly used only for computing the internal energy. This can be avoided by integrating the energy using the internal stress distribution. Therefore, the *Secant Matrix* is not needed.

5.3.3 Comparison of Shape Function Gradients

The main idea behind the Unified Formulation is the fact that the displacement field can be written as a separation of variables and in a compact way:

$$\boldsymbol{u} = F(x,z)N(y)\boldsymbol{u}_{\tau i}, \tag{5.26}$$

where F and N are defined over a master element and then mapped into the global coordinate system. The mapping will depend on the *a-priori* assumption of the element geometry (prismatic or not). In the existing prismatic formulation, the cross-section of the element does not change along the its axis, and the derivatives of the shape functions are written as (see Section 3.4):

$$\begin{aligned} N_y(y) &= \frac{1}{J^{1D}} N_\xi(\xi) \\ F_x(x,z) &= \frac{1}{J^{2D}} \left[z_\beta F_\alpha(\alpha,\beta) - z_\alpha F_\beta(\alpha,\beta) \right] \\ F_z(x,z) &= \frac{1}{J^{2D}} \left[x_\alpha F_\beta(\alpha,\beta) - x_\beta F_\alpha(\alpha,\beta) \right], \end{aligned} \tag{5.27}$$

where J^{1D} is the length of the 1D element and J^{2D} the determinant of

$$\mathcal{J} = \begin{bmatrix} x_\alpha & z_\alpha \\ x_\beta & z_\beta \end{bmatrix}.$$

With equation (5.27), the gradients of the displacement field for the prismatic case, equation (5.26) are

$$\begin{aligned} \boldsymbol{u}_x &= \frac{1}{J^{2D}} \left[z_\beta F_{\tau,\alpha} - z_\alpha F_{\tau,\beta} \right] N_i \boldsymbol{u}_{\tau i} \\ \boldsymbol{u}_y &= F_\tau \frac{1}{J^{1D}} N_{i,\xi} \boldsymbol{u}_{\tau i} \\ \boldsymbol{u}_z &= \frac{1}{J^{2D}} \left[x_\alpha F_{\tau,\beta} - x_\beta F_{\tau,\alpha} \right] N_i \boldsymbol{u}_{\tau i}. \end{aligned} \tag{5.28}$$

Now, if the element is non-prismatic, the product $F(x,z)N(y)$ has to be taken as a whole unit G, equation (5.19), and its derivatives are computed using equation (5.22). Therefore, the gradients of the displacement field for the non-prismatic case take the form

$$\begin{aligned} \boldsymbol{u}_x &= \frac{1}{J^{3D}} \left[y_\beta z_\alpha F_\tau N_{i,\xi} - y_\xi z_\alpha F_{\tau,\beta} N_i - y_\alpha z_\beta F_\tau N_{i,\xi} + y_\xi z_\beta F_{\tau,\alpha} N_i + y_\alpha z_\xi F_{\tau,\beta} N_i - y_\beta z_\xi F_{\tau,\alpha} N_i \right] \boldsymbol{u}_{\tau i} \\ \boldsymbol{u}_y &= -\frac{1}{J^{3D}} \left[x_\beta z_\alpha F_\tau N_{i,\xi} - x_\xi z_\alpha F_{\tau,\beta} N_i - x_\alpha z_\beta F_\tau N_{i,\xi} + x_\xi z_\beta F_{\tau,\alpha} N_i + x_\alpha z_\xi F_{\tau,\beta} N_i - x_\beta z_\xi F_{\tau,\alpha} N_i \right] \boldsymbol{u}_{\tau i} \\ \boldsymbol{u}_z &= \frac{1}{J^{3D}} \left[x_\beta y_\alpha F_\tau N_{i,\xi} - x_\xi y_\alpha F_{\tau,\beta} N_i - x_\alpha y_\beta F_\tau N_{i,\xi} + x_\xi y_\beta F_{\tau,\alpha} N_i + x_\alpha y_\xi F_{\tau,\beta} N_i - x_\beta y_\xi F_{\tau,\alpha} N_i \right] \boldsymbol{u}_{\tau i}, \end{aligned} \tag{5.29}$$

where J^{3D} is the determinant of equation (5.22).

Equation (5.28) shows that in the expressions for the derivatives of the displacement field, the geometric information from the cross-section and element axis (that is, the components of the local curvilinear basis vectors x_α, z_β, etc.) can be written as a decoupled product of gradients. A change

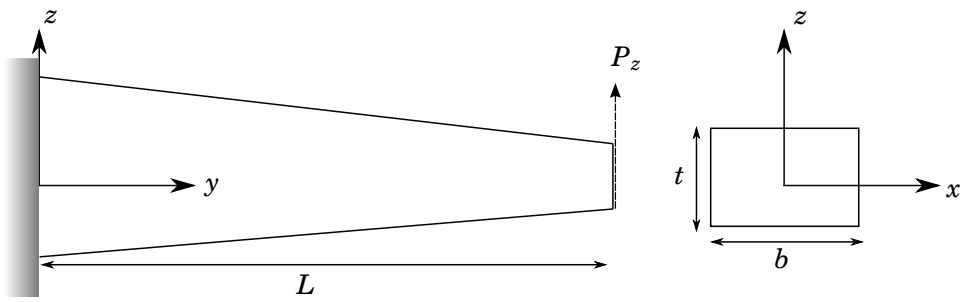

Figure 5.2: Tapered beam geometry.

in curvature in the cross-section is not related to a change in geometry in the axial direction, and vice-versa. On the other hand, equation (5.29) shows that the derivatives of displacements depend on a combination of the components of the basis in all directions. In other words, it couples the gradients of the shape functions, and a change in curvature in one direction, say in axial direction, will inevitably affect the behaviour in the cross-section direction, and vice-versa.

This is the key point of the UF-3D formulation, even though the shape functions in the cross-section and beam axis can be chosen and enriched independently, the product is taken as a whole unit, and changes in geometry in any direction will have an effect on gradients in all directions.

5.4 Numerical Results

In this section, several examples are presented with the aim of testing the model's main capabilities: (1) model of beams with changing cross-sections, particularly tapered beams; (2) modelling highly curved structures; (3) performing large displacements non-linear analyses.

The first example is an isotropic cantilever tapered beam in bending. The model is benchmarked against known results, including a semi-analytical method, a 3D FEM and experimental data. The second case, a thin initially-curved plate made of both, isotropic and composite materials. Results are compared with a known high-order finite element model. The third case is a functionally-graded, tapered and initially-curved beam under buckling. Data are benchmarked against results in literature. The fourth and last example, is a set of three anisotropic and highly-curved corrugated structures under axial extension. Results are compared with 3D FEM models and experimental results. All cases are studied in the geometrically non-linear regime.

Materials, geometric dimensions, loading and boundary conditions are described in each particular case.

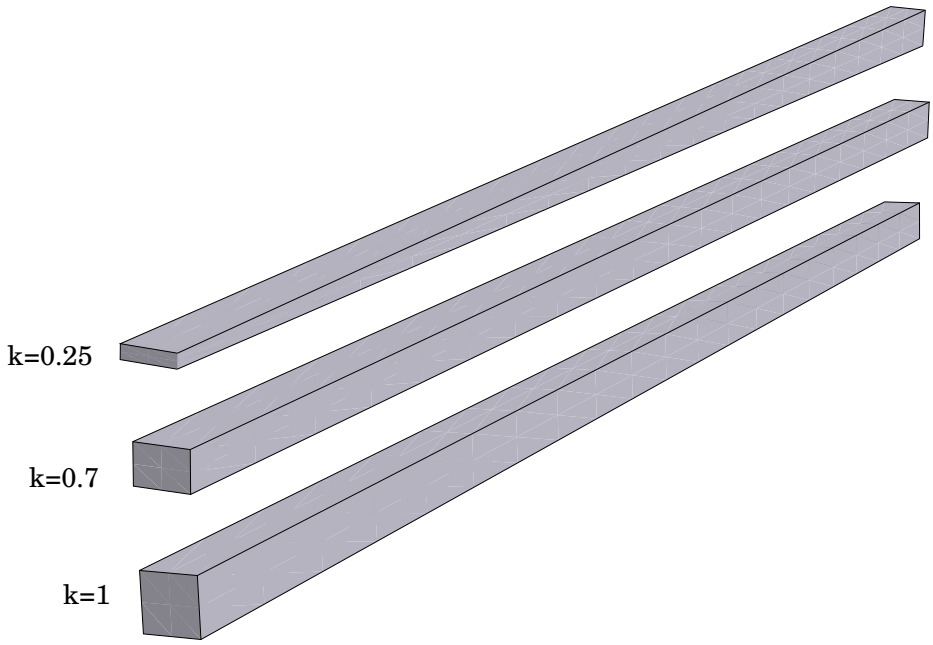

Figure 5.3: Three tapered beams considered.

5.4.1 Isotropic Tapered Beam

Consider a cantilever, linearly tapered beam as shown in Figure 5.2. The structure has a square cross-section with width $b = 2$ in, length $L = 40$ in, the thinner edge has a width of $b = 2$ in and thickness $t \in \{2\,, 1.4\,, 0.5\}$ in. The tapering ratio is defined as $k = \frac{t}{b}$, therefore, the three cases studied are $k = 1\,, 0.7\,, 0.25$. A three-dimensional view of the tapered beams is shown in Figure 5.3. The material is isotropic with Young's modulus of $E = 4.2 \times 10^5$ psi and Poisson's ratio of $\nu = 0.3$.

In order to simplify the discussion the following non-dimensional quantities are defined

$$\tilde{u}_z = \frac{u_z}{L} \qquad \delta = \frac{L - u_y}{L} \qquad \tilde{P} = \frac{P_z L^2}{EI}, \tag{5.30}$$

where u_z is the vertical displacement, u_y is the axial displacement, P_z is the vertical bending force applied at the tip and I is the second moment of area of the clamped (square) edge.

A UF-3D model with a fifth order SL expansion, 4 cross-section elements and 20 beam elements is used to describe the structure. The converged UF-3D model has a total of 12,627 DOFs. A second model is used, an `ANSYS` solid model with 189,405 DOFs. Additionally, numerical and experimental results from a work by Kemper [6] are also included.

Non-dimensional applied force vs tip vertical displacements for the three cases are shown in Figure 5.4(a). Results show that, for all cases, the model provides close agreement compared to the solid FEM model's results. For the prismatic ($k = 1$) and shallowly tapered ($k = 0.7$), and for relative small forces $0 \leq P_z \leq 0.4$, the results differ slightly from Kemper. Nevertheless, UF-3D and FEM models are closer to the experimental data. The three models predict the same behaviour for $k = 0.25$. Results for the relative shortening, Figure 5.4(b), show a good agreement

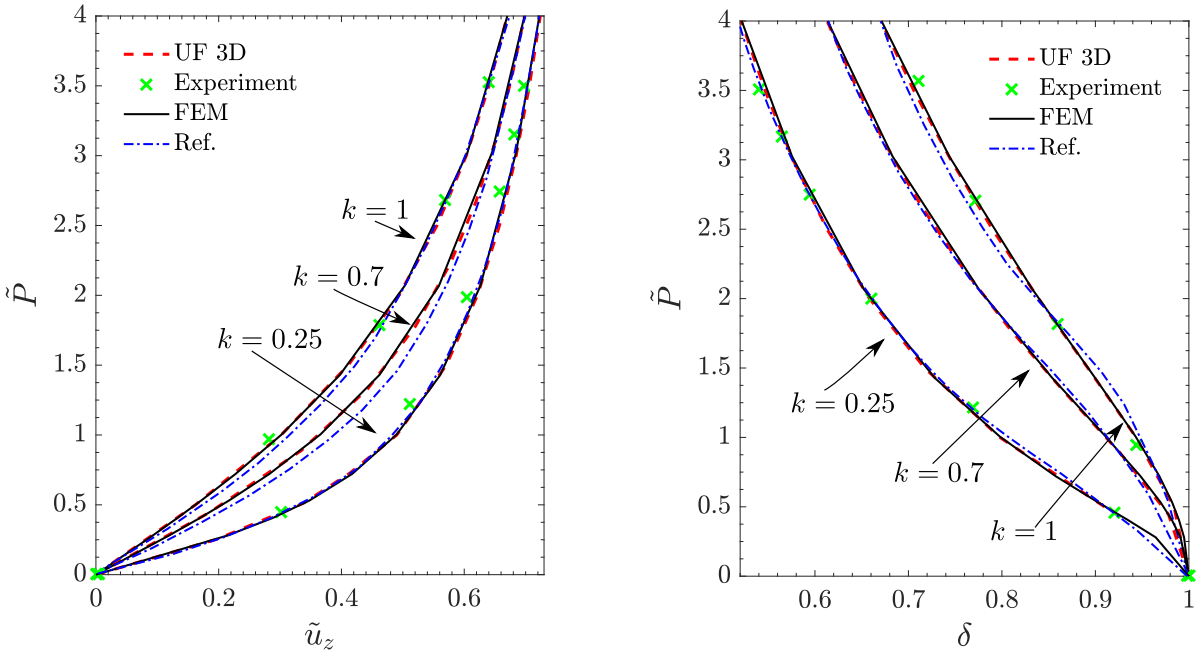

(a) Centre tip, force vs vertical displacement

(b) Centre tip, force vs shortening

Figure 5.4: Force vs displacements at centre tip. Reference and experimental results from Kemper [6]. Tapered beam.

with the FEM solution. The UF-3D model predicts shortenings closer the experimental data as well. Figure 5.5 shows a colour plot of the non-linear bending for the tapered case $k = 0.25$.

In order to show the capability of the model in recovering stresses, the bending stress σ_{yy} and shear stress σ_{yz} through thickness are measured for the case of $k = 0.25$. Figure 5.6 shows the results for σ_{yy} and σ_{yz} in local coordinates for five different load cases: $\tilde{P}_z^1 = \frac{4}{5}$, $\tilde{P}_z^2 = \frac{8}{5}$, $\tilde{P}_z^3 = \frac{12}{5}$, $\tilde{P}_z^4 = \frac{16}{5}$ and $\tilde{P}_z^5 = 4$. Results from FEM are shown only for the last step. Data shows that the model predicts the stresses accurately, particularly at the last and highest load step, where it coincides perfectly with the FEM solution.

5.4.2 Thin Plate

The purpose of this example is to show two capabilities of the model: (1) how it can be used for studying the non-linear bending of thin composite plate structures; (2) how a curved beam element is used to introduce an initial geometrical imperfection when studying post-buckling behaviour.

Results are benchmarked against a high-order shell finite element formulation with 3D capabilities developed by Payette & Reddy [7]. The model, known as *Seven-Parameter spectral/hp model*, is known to be as accurate as 3D finite elements when applied to thin structures, as well

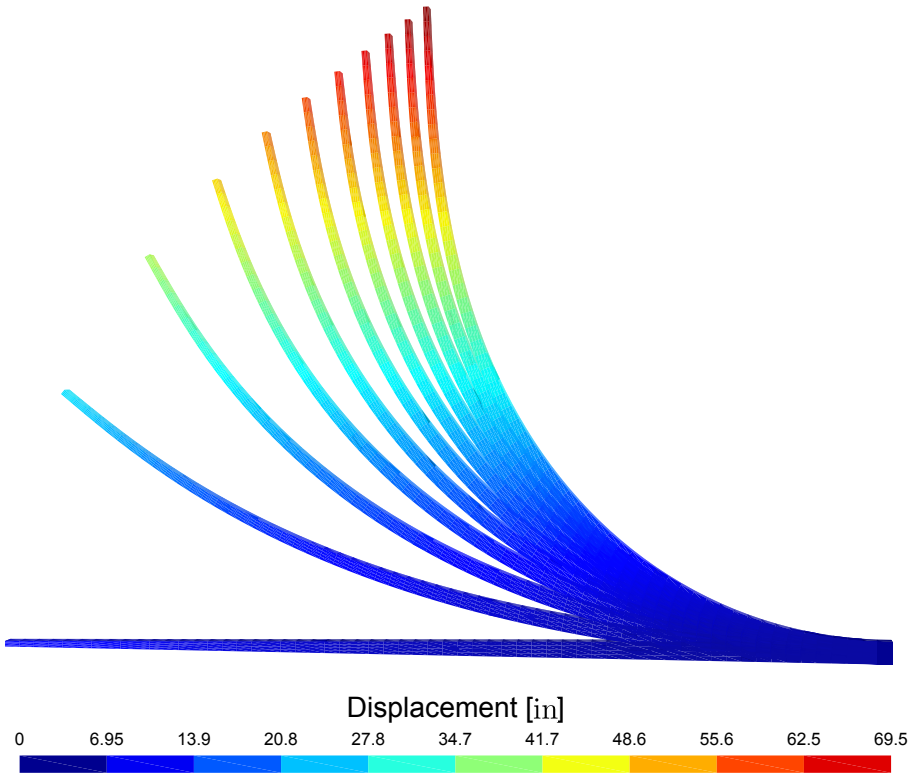

Figure 5.5: Non-linear bending for tapered case $k = 0.25$.

as its numerical efficiency [93]. For the two examples, a UF-3D model with a second order SL expansion, 32 cross-section elements and 10 beam elements is used. The size of the UF-3D-model is 11,253 DOFs.

The boundary condition is clamped at one edge and free at the other. The structure is shown in Figure 5.7. Specifics of the dimensions and materials used are specified in each case.

5.4.2.1 Thin Composite Plate Under Bending

A plate with dimensions $L = 10$ m, $b = 1$ m and $h = 0.1$ m is now studied. A distributed vertical load of $\tilde{P}_z$ is applied to the free edge of the plate. A multi-layered composite laminate with material properties given as

$$\begin{array}{lll} E_x = 3 \times 10^5 \text{ Pa} & E_y = 1 \times 10^6 \text{ Pa} & E_z = 3 \times 10^5 \text{ Pa} \\ G_{yz} = 1.5 \times 10^5 \text{ Pa} & G_{xz} = 1.2 \times 10^5 \text{ Pa} & G_{xy} = 1.5 \times 10^5 \text{ Pa} \\ \nu_{yz} = 0.25 & \nu_{xz} = 0.25 & \nu_{xy} = 0.075 \end{array} ,$$

is considered.

Four different layups are used: [0/90/0], [30/-60/-60/30], [90/0/90], [-45/45/-45/45]. An isotropic case with $E = 1.2$ MPa is also included. Force versus non-dimensionalised vertical displacement

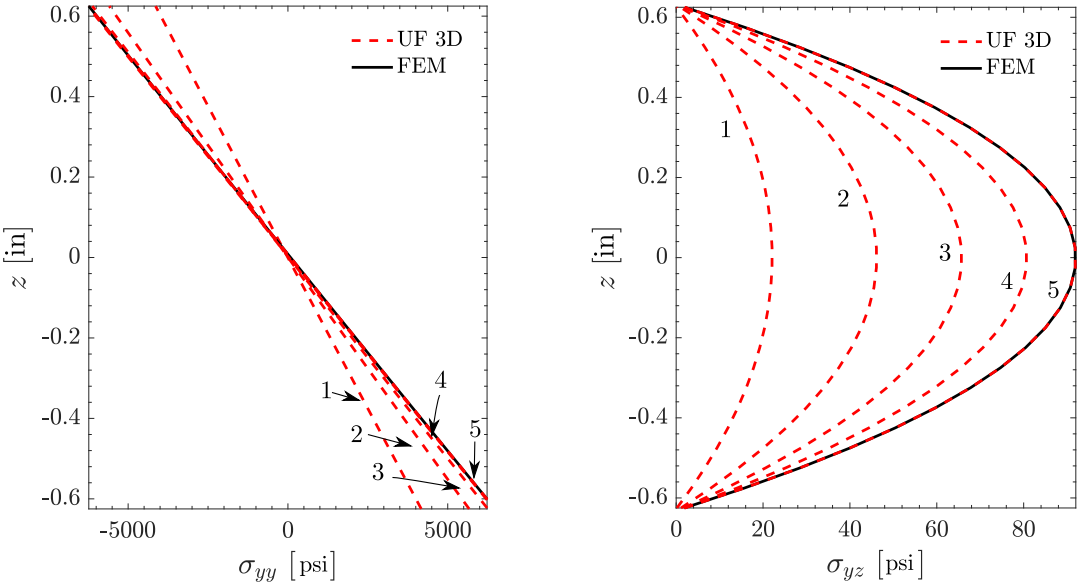

(a) Through thickness bending stress at mid span.

(b) Through thickness shear stress at mid span

Figure 5.6: Through thickness bending and shear stress for tapered case $k = 0.25$. Five equally spaced force steps in the range $\frac{4}{5} \leq \tilde{P}_z \leq 4$ are shown.

$\tilde{u}_z = \frac{u_z}{L}$ is measured at the plate centre tip, Figure 5.8. Results show that the two models predict exactly the same bending profile for all the cases. The plate with stacking sequence [90/0/90] is the most flexible and [0/90/90] showing the greatest stiffness, as expected.

5.4.2.2 Post-buckling of an Initially Curved Plate

For this example the plate dimensions take the values of: $L = 0.5$ m, $b = 0.075$ m and $h = 0.0045$ m. Material is isotropic with Young's modulus $E = 200$ GPa and Poisson's ratio of $\nu = 0.3$. The loading condition is in the axial direction applied at the tip. In order to trigger the post-buckling behaviour, an initial geometric imperfection is introduced. The imperfection is modelled as an initially curved beam (plate), for which the magnitude of the deviation is written in terms of the thickness h as:

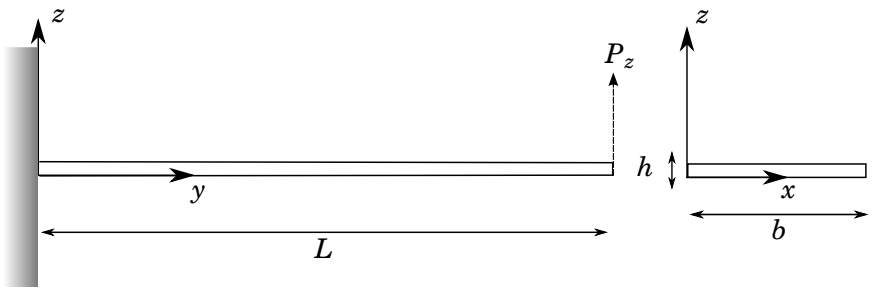

Figure 5.7: Thin plate geometry.

$c \times h$ where $0 \leq c \leq 1$, as shown in Figure 5.9.

Four different magnitudes of curved imperfections are tested: $c = 1,\ 10,\ 50,\ 100\,\%$. Results, in terms of normalised vertical ($\tilde{u}_z = \frac{u_z}{L}$) and axial ($\tilde{u}_y = \frac{u_y}{L}$) displacements vs applied force, are measured at the centre tip of the plate. For comparison purposes, the solution from Payette & Reddy's model is also presented. Figure 5.10 shows the normalised vertical and axial displacements at centre tip for both models. An amplified plot of the region close to the buckling point is also shown. From here it can be seen that both models predict very similar results, particularly in the deep post-buckling regime ($\sim 4000 \geq P_y$). Close to the buckling point, which occurs approximately at $P_y = 1024$, according to Euler's formula, a slight difference between Seven-Parameter model and UF-3D is observed. The structure's vertical displacement, $\tilde{u}_z$, is more sensitive to imperfections than the axial displacement, $\tilde{u}_y$. The sensitive region, approximately $-0.1 \leq u \leq 0.1$, is located around the buckling point, and for higher displacements the effect is negligible. A 3D plot of the post-buckled deformed thin-plate is shown in Figure 5.11.

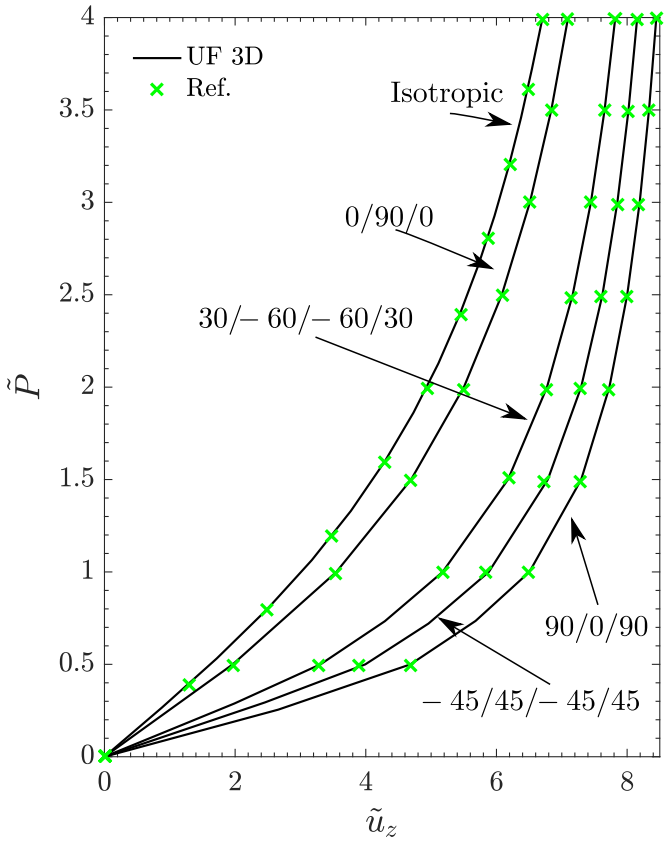

Figure 5.8: Non-linear bending of a composite thin plate. Force vs displacement at centre tip. Reference results from Payette & Reddy [7].

5.4.3 Tapered Functionally Graded Beam

The purpose of this example is to take some ingredients from the previous two: a tapered and initially curved beam geometry. The effect of the functionally gradient power law in the bending

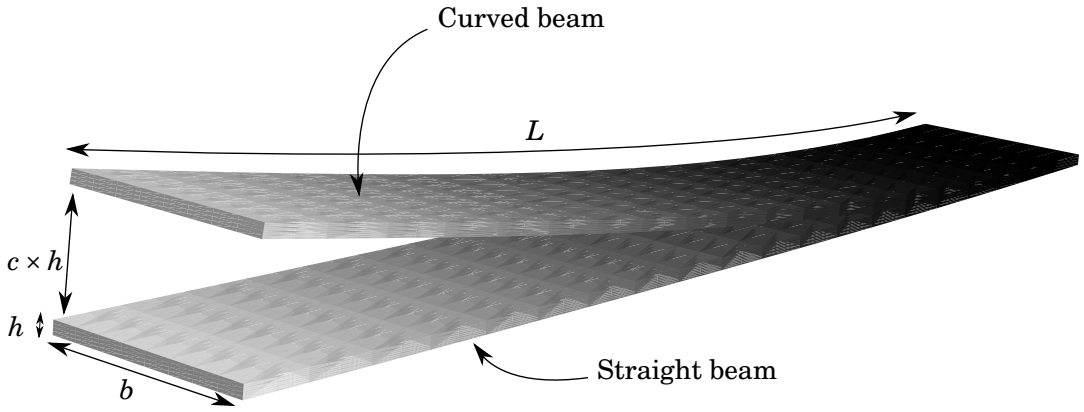

Figure 5.9: Initially imperfect plate modelled as a curved-beam.

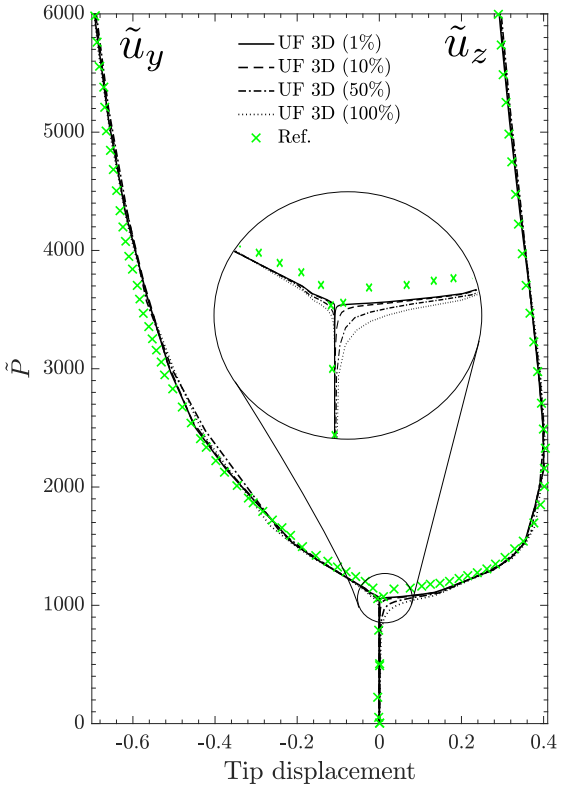

Figure 5.10: Post-buckling behaviour of a thin-plate. Applied force vs vertical and axial displacements at centre tip. Reference results from Payette & Reddy [7].

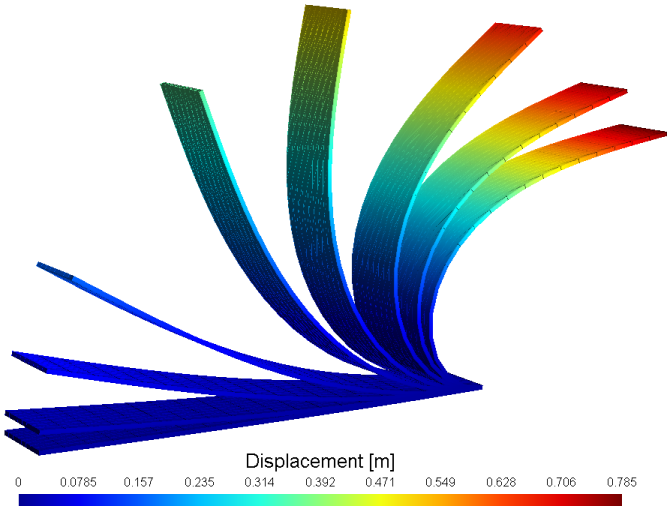

Figure 5.11: Post-buckling behaviour of a thin-plate.

and post-buckling behaviour of the composite structure is studied. The available literature on the analysis of large displacements of functionally graded tapered beams is limited. Therefore, it has been decided to compare results with those by Nguyen [8], in which he has used a co-rotational beam element, based on first-order shear deformation beam theory, to study large deflections of tapered FGM beams under various loading conditions.

Refer to Figure 5.2, the dimensions for the structure are: $L = 80$ m, $b = 2$ m and $t = 1$ m. The structure is linearly tapered with tapering ratio of $k = 0.5$. The material is functionally graded along the axial direction according to the power rule

$$E(y) = (E_a - E_s)\left(\frac{y}{L}\right)^n + E_s, \tag{5.31}$$

where $E_a = 70$ GPa is the Young's modulus for Aluminium, $E_s = 200$ GPa for steel and n is a strictly positive number. The cases studied are $n = 0.2$, 1, 5. A plot of the material distribution along the length, for the three cases, is shown in Figure 5.12.

5.4.3.1 Bending of a FGM Tapered Beam

A clamped tapered FGM beam is subject to a vertical bending load applied at the tip. Five different material distributions are used, three using the FGM rule with $n = 0.2$, 1, 5, and two isotropic structures with E_a and E_s. Applied force vs vertical and axial displacements are measured at centre tip. The normalisation rules, equations (5.30), are used here. The solution is shown in Figure 5.13.

Several conclusions can be deduced from the results. First, is that displacements coincide exactly with those of the reference solution; secondly, as the n parameter in the power rule increases, the structure becomes stiffer. Is interesting to note that for the case of $n = 5$, the result

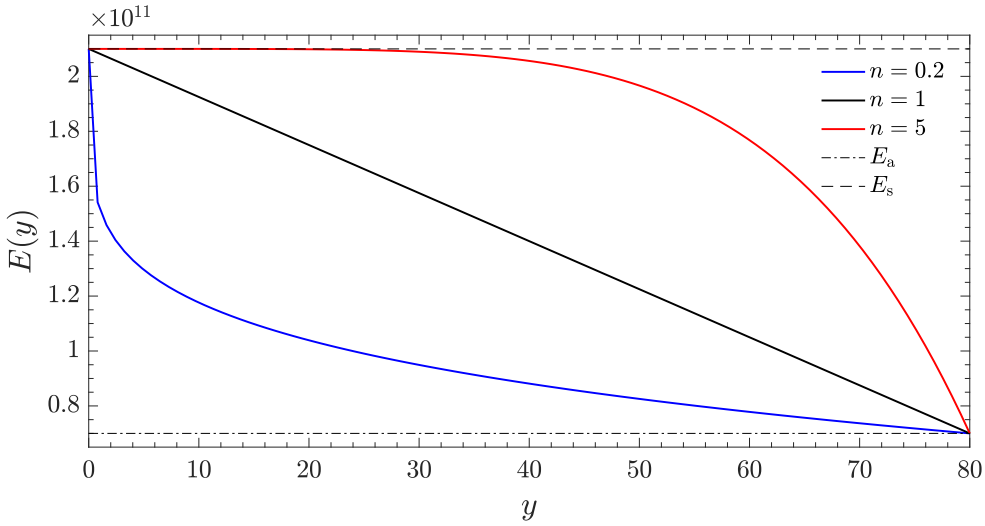

Figure 5.12: Functionally graded power rule.

is almost the same as if the beam is made entirely of steel, even though it only occurs at the root (~ 50% of beam length) with, the rest is made of a softer material.

5.4.3.2 Post-buckling of a FGM Tapered Beam

The second example is a FGM tapered beam subject to an axial load applied at the tip. The same three n-cases are studied. Due to the nature of the loading and boundary conditions, the structure becomes unstable at the buckling point, in order to trigger the post-buckling behaviour a geometrical imperfection is introduced. The new geometry consists of an initially curved-beam, the magnitude of the imperfection is given in terms of the hight of the free edge t by: $c \times t$, where $c = 0.01$ (or 1%), which is enough to induce buckling. The imperfect (curved) geometry is shown in Figure 5.14. Regarding the reference solution, the authors have used a different approach to trigger buckling. Their model is based on a beam formulation and part of the kinematic field are translations and rotations, therefore it is possible to induce buckling by applying a special type of load. Instead of using a geometric imperfection, Nguyen [8] used an axial force in combination with a moment of magnitude $\frac{P_y t}{2}$ to trigger buckling. In here, only the general overall behaviour is discussed.

Figure 5.15 shows the effect of the parameter n in the post-buckling behaviour of the tapered beam. Even though the loading conditions are not exactly the same (UF-3D predicts ~ 5% higher loads), both models show the same global behaviour, as n increases the buckling point increases. Nguyen's loading condition results in the beam's behaviour as if it had a big initial geometrical imperfection. In terms of buckling load, the maximum is achieved with $n = 5$. For this case, the structure's buckling load has approximately doubled compared with the case of $n = 0.2$. A 3D plot of the deformed geometry for $n = 0.2$ is shown in Figure 5.16.

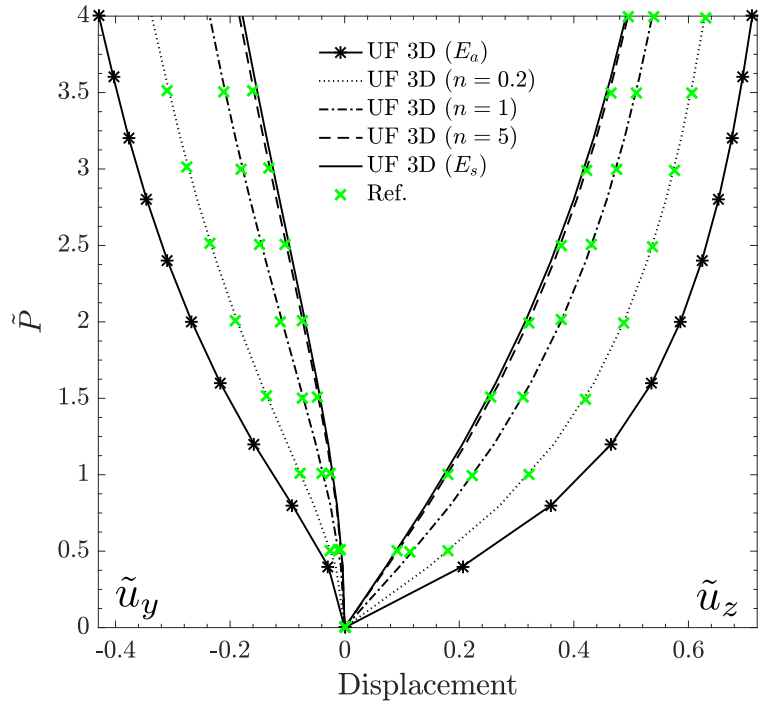

Figure 5.13: Applied force vs vertical and axial displacement at centre tip. FGM Tapered beam under bending. Reference results from Nguyen [8].

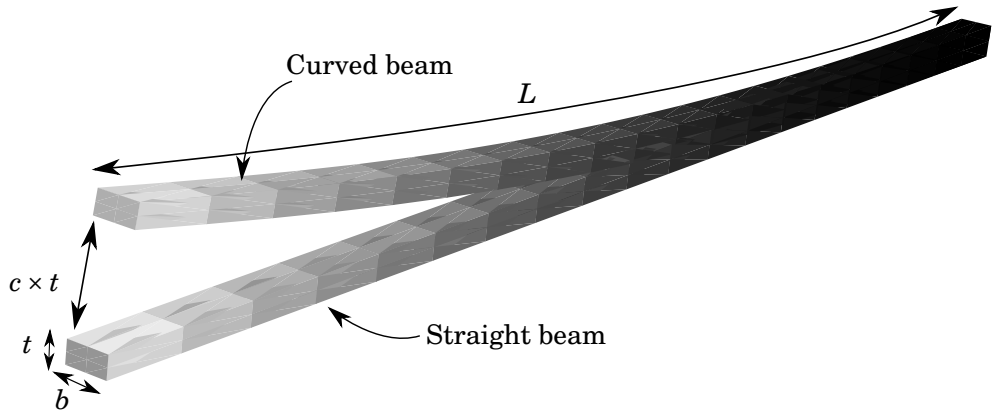

Figure 5.14: Initially imperfect tapered FGM structure modelled as a curved-beam.

5.4.4 Corrugated Beam

In the last example a set of three anisotropic and highly-curved beam structures studied by Thurnherr et al. [124] are considered. The purpose is to show how the UF-3D beam formulation is capable of model these complex structures and to describe accurately their non-linear behaviour.

A corrugation pattern consisting on three unit cells with two circular sections is now described.

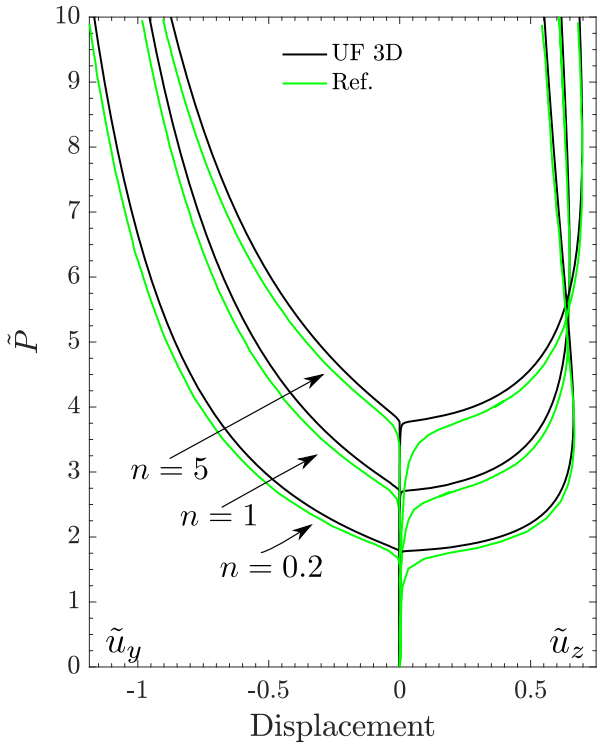

Figure 5.15: Post-buckling behaviour of a FGM tapered beam. Applied force vs vertical and axial displacements at centre tip. Reference results from Nguyen [8].

The elementary cell unit is shown in Figure 5.17, together with the definition of its parameters: the radius of curvature R , the radius of the cell c, the length p, the arc-length parameter s and the coordinates $(y(s), z(s))$ of a point in the mid plane. The coordinates of any point in the mid surface are given by the parametric equation [9, 125]:

$$\begin{aligned} y(s) &= R\left[\sin(\psi(s)) + (2+m)\sin(\psi_0)\right] \\ z(s) &= -mR\left[\cos(\psi(s)) - \cos(\psi_0)\right], \end{aligned} \tag{5.32}$$

where m switches the sign between the first and second unit cell. It is $+1$ for the first half and -1 for the second half. The radius of curvature R is

$$R = \frac{16c^2 + p^2}{32c}, \tag{5.33}$$

cell's curvature $\kappa = \frac{1}{R}$,

$$\psi_0 = \begin{cases} \arcsin\left(\frac{p}{4R}\right) & \text{if } c \le \frac{p}{4} \\ \arccos\left(\frac{p}{4R}\right) + \frac{\pi}{2} & \text{if } c > \frac{p}{4}, \end{cases} \tag{5.34}$$

and

$$\psi(s) = \kappa s - (2-m)\psi_0. \tag{5.35}$$

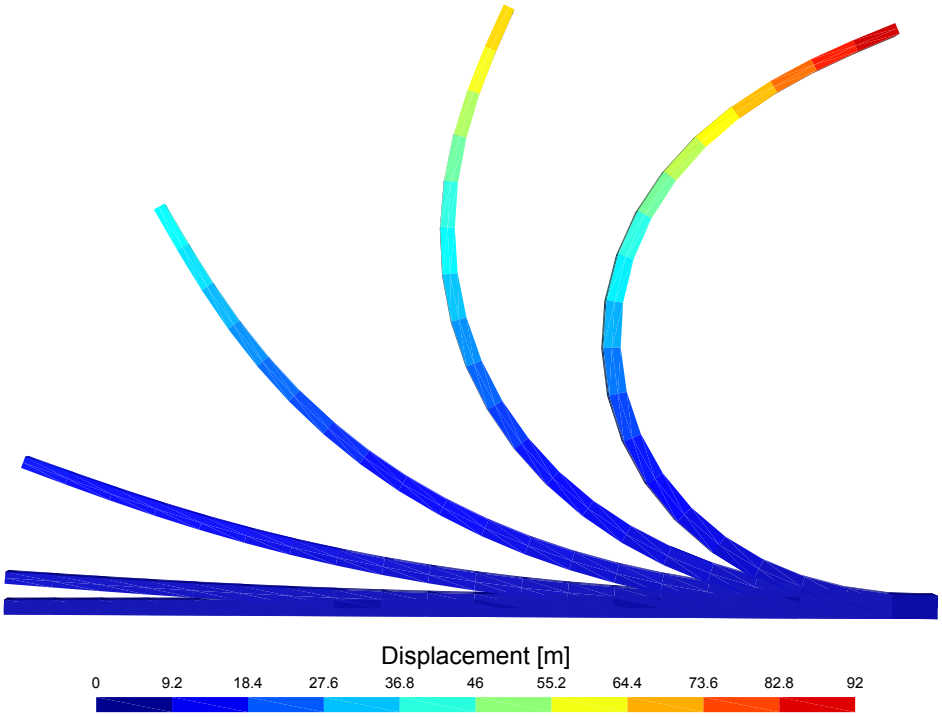

Figure 5.16: Post-buckling behaviour of a tapered FGM beam. Case $n = 0.2$.

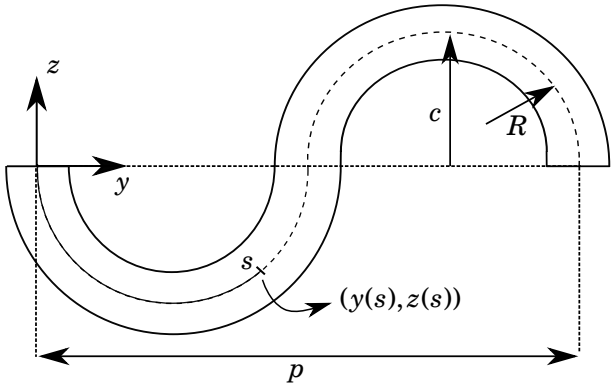

Figure 5.17: Unit cell geometry definition.

Three different structures with four unit cells are studied: (1) one with $c = 5$ mm, $p = 40$ mm, width $b = 25$ mm and thickness $t = 0.52$ mm; (2) a cell with $c = 10$ mm, $p = 40$ mm, width $b = 25$ mm and thickness $t = 0.59$ mm; and (3) a cell with $c = 30$ mm, $p = 40$ mm, width $b = 25$ mm and thickness $t = 1$ mm. The three-dimensional structures, geometry definitions and boundary & loading conditions are shown in Figure 5.18.

The specimens for the experiment performed by Thurnerr et al. were 3D printed and made of an anisotropic material, PolyLactic acid. Nevertheless, due to the tensile loading, the response is governed by the stiffness in the axial direction, therefore an isotropic material can be used as good

approximation [9]. The constitutive material parameters are: Young's modulus $E = 3.5$ GPa and Poisson's ratio of $\nu = 0.346$. The structure is clamped at one end and a tensile load in y-direction is applied at the other end.

Three sets of results are presented: one using the UF-3D model, second a 3D FEM ANSYS solid model and experimental results from Thurnherr et al. [9]. A linear solution given by a linearised version of the UF-3D model is also provided. Each case is discussed separately.

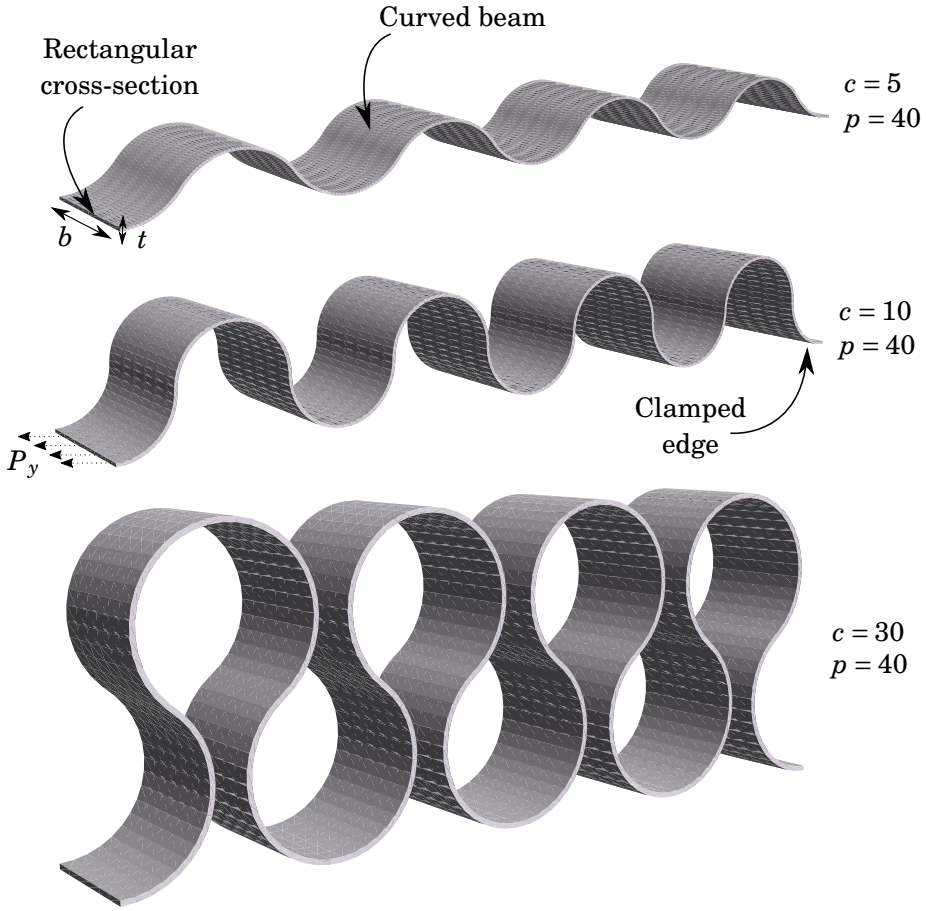

Figure 5.18: Corrugated structures modelled as curved beams. Geometry definitions and boundary & loading conditions.

5.4.4.1 Case $c = 5$ mm & $p = 40$ mm.

For this geometry the model used is a fourth order UF-3D model with an SL expansion, 3 elements in the cross-section and 140 elements in the beam direction. The size of the model is 35,364 DOFs. Results are compared with an ANSYS solid model with 217,323 DOFs and experimental data.

Figure 5.19(a) shows the applied force vs displacement measured at the centre tip of the beam. Results show a good agreement with FEM model; a good match between experiments and

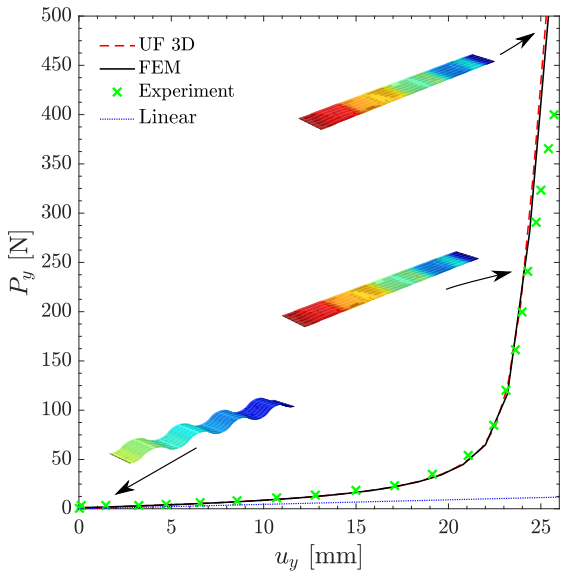

(a) Case $c = 5$ mm & $p = 40$ mm

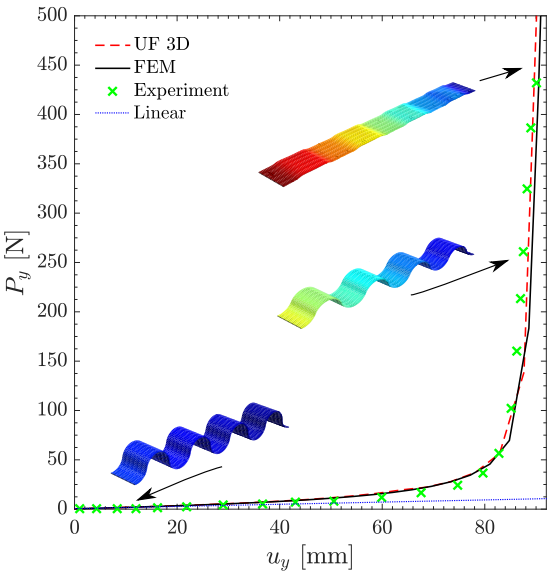

(b) Case $c = 10$ mm & $p = 40$ mm

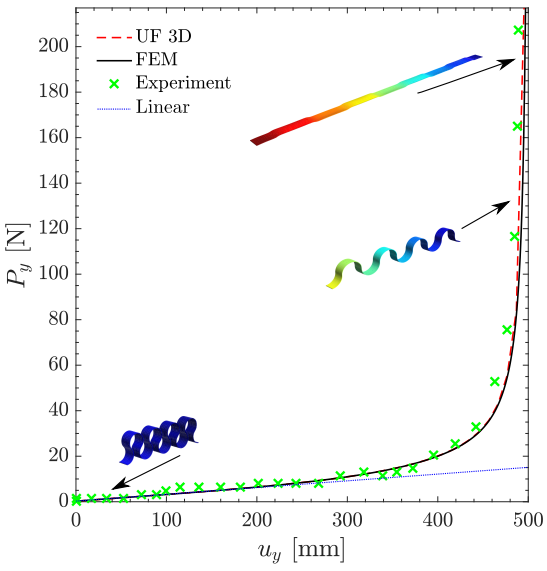

(c) Case $c = 30$ mm & $p = 40$ mm

Figure 5.19: Force vs displacement for the three corrugated structures. Experimental results from Thurnherr *et al.* [9].

the simulations is also evident up to a displacement ~ 23 mm, where it deviates slightly from both models. It is evident that the mechanics is highly non-linear, especially close to the knee (~ 20 mm), where the slope of the curve changes drastically. Before this point, the amplitude of the corrugation decreases due to bending, afterwards, in approximately 30% – 40% of the applied

force, the mechanism that drives the deformation is stretching, and the structure becomes almost fully extended and stiffer. A comparison of the deformed geometries at several loading steps is presented in Figure 5.20.

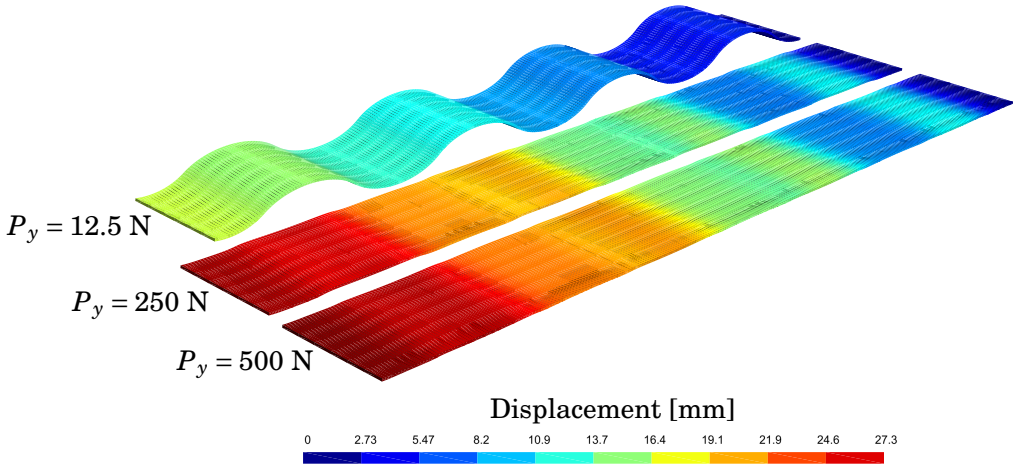

Figure 5.20: Deformation at several loads steps, case $c = 5$ mm & $p = 40$ mm.

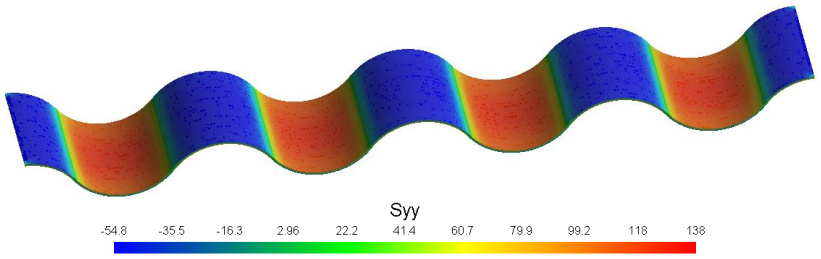

(a) ANSYS.

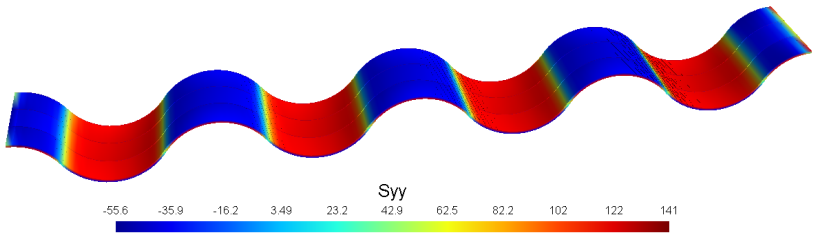

(b) UF-3D

Figure 5.21: Axial stress σ_{yy}, case $c = 5$ mm & $p = 40$ mm.

The UF-3D model is also capable of recovering three-dimensional stresses. A plot of the leading axial stress σ_{yy} is shown in Figure 5.21, a comparison with the result from ANSYS model is also included. It can be seen that the overall stress for both models is the same, a small difference or $\sim 2\%$ for the maximum and minimum values is observed. This difference is mainly

due to the stress concentrations close to the singularity (clamped edge).

5.4.4.2 Case $c = 10$ mm & $p = 40$ mm.

For this structure a third order UF-3D model with an SL expansion, 3 elements in the cross-section, 200 beam elements and 50,484 DOFs is used. A 3D FEM ANSYS solid model with 220,059 DOFs is used for comparison. Experimental results are also provided.

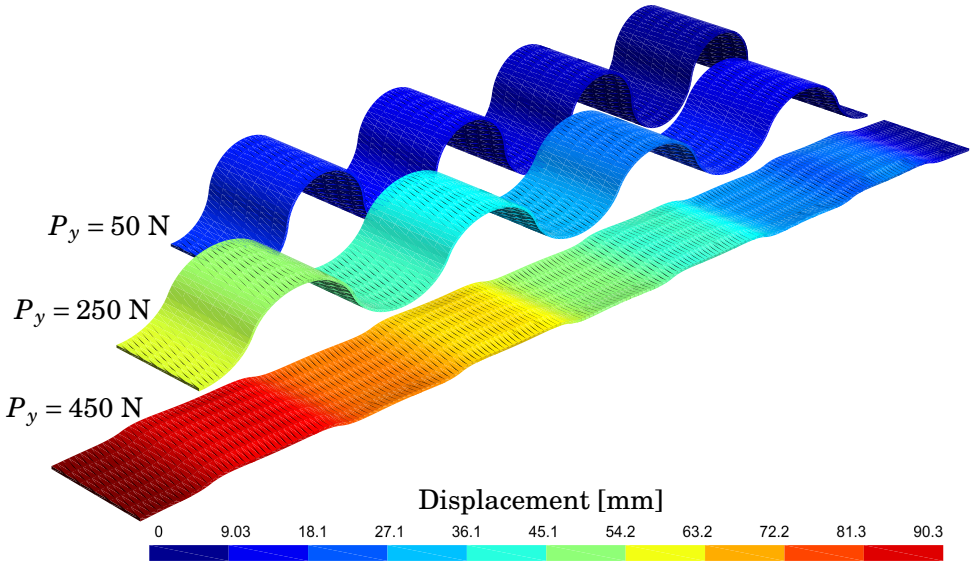

Figure 5.22: Deformation at several loads steps, case $c = 10$ mm & $p = 40$ mm.

The same displacements as in the previous case are measured. Figure 5.19(b) shows the force vs displacement for the three sets of results. A good agreement between the proposed model, FEM and experiments is evident. As in the previous case, a non-linear behaviour is observed. In contrast with the previous example, the bending mechanism governs the deformation up to approximately 50% of the applied force, where the corrugation amplitude is still visible. Afterwards stretching takes place and the structure becomes almost fully flat. A three-dimensional view of the deformed geometry for several steps is shown in Figure 5.22.

A plot of the leading axial stress σ_{yy} is shown in Figure 5.21, a comparison with the result from ANSYS model is also included. A difference in maximum and minimum values of $\sim 5\%$ is again observed, and as mention before this is due to numerical inaccuracies and localised stress concentrations close to the boundary.

5.4.4.3 Case $c = 30$ mm & $p = 40$ mm.

The last case is a highly-curved structure which is modelled using a third order UF-3D model with an SL expansion, 3 elements in the cross-section and 250 beam elements. The model size is

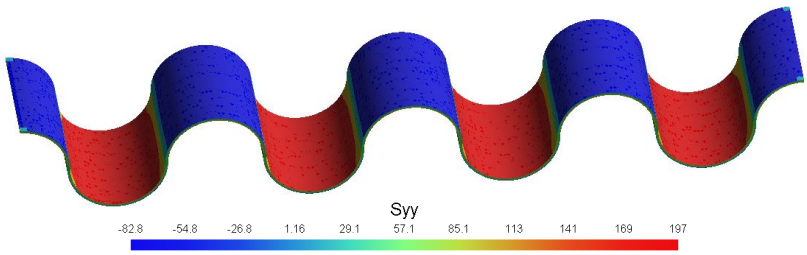

(a) ANSYS

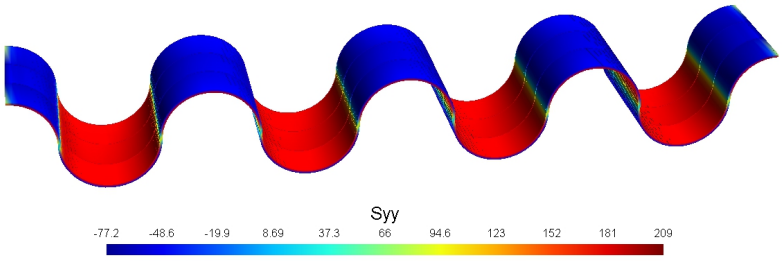

(b) UF-3D

Figure 5.23: Axial stress σ_{yy}, case $c = 5$ mm & $p = 40$ mm.

63,084 DOFs. As comparison an ANSYS solid model with 308,295 DOFs, experimental results and a linear solution are provided.

Due to its high-curvature a non-linear behaviour governed mostly by bending is expected. This is confirmed by the results shown in Figure 5.19(c), where it can be seen that, up to approximately $\sim 60-70\%$ of the applied load, the structure's cell amplitudes are still visible. Afterwards it starts to stretch until is almost fully flat, at approximately half of the load required by the cases $c = 5$ mm and $c = 10$ mm. In terms of axial displacement, its final length is about 20 times higher than that of the $c = 5$ mm case, and 5 times compared to the $c = 10$ mm case. A plot of the deformed structure, for several load steps, is shown in Figure 5.24. Three-dimensional plot of the axial stress from UF-3D and 3D FEM is shown in Figure 5.25.

The results presented in this section show that for the highly-curved structures considered herein, it is non-sense to use a linear model, since it leads to extremely high errors when large displacements are expected. Non-linear formulations are required to model accurately the mechanics, something that the UF-3D model has shown to be capable of. Efficiency is also a key feature of the model, since for each case only $\sim 5\%$ of DOFs (compared with a 3D FEM model) was required to obtain accurate results.

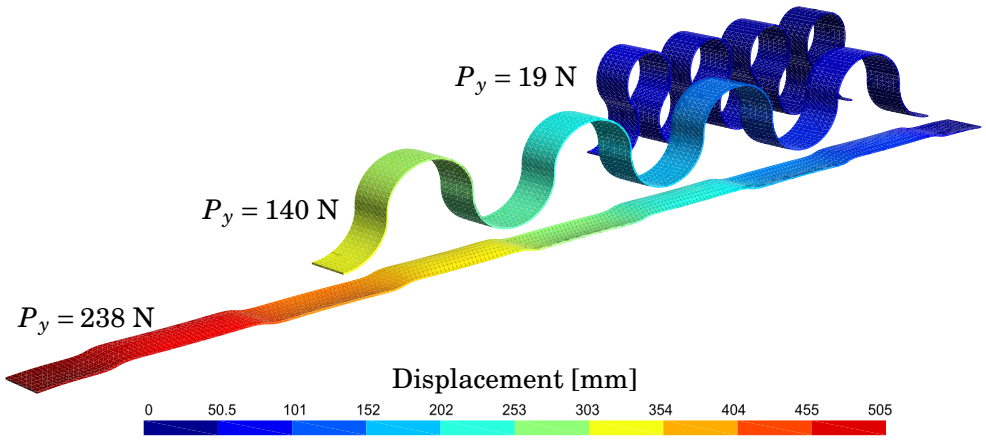

Figure 5.24: Deformation at several loads steps, case $c = 30$ mm & $p = 40$ mm.

5.5 Discussion

The Unified Formulation Three-dimensional Beam Model (UF-3D) combined with the Serendipity Lagrange Expansion, provides the means for studying the non-linear mechanics of curved beam-like three-dimensional structures in an accurate and efficient way. The new formulation is based on an element that can be curved in the cross-section direction as well as in the axial direction. Moreover, the element has the capability of connecting different shapes of cross-sections by a three-dimensional mapping. This mapping takes into account the geometrical spatial variation of the structure via a Jacobian transformation computed using a CAD-like approach, which in addition, does not contribute to the DOFs needed for analysis. Therefore, a set of three shape functions are needed, one is the 3D-map for the geometry $N^{3D}(\alpha,\xi,\beta)$, the shape functions defined in the cross-section $F(x,z)$ and the functions defined in the beam direction $N(y)$. The last two can be chosen and enriched independently; their gradients are coupled and linked with the geometry shape functions.

Different geometries and cases were analysed. In the first, large displacements of a tapered beam under bending was studied and compared with FEM, semi-analytical and some experimental results. The main purpose of this example was to test its capability of modelling structures with varying cross-section along the axial direction. Data showed that UF-3D can provide results that are in good agreement with the reference models and with experiments. The proposed model used only ~ 6% of the DOFs compared with `ANSYS`.

The second example was a thin plate under two different loading conditions, and made of various materials. Two main purposes were targeted: (1) to show its capability of modelling composite structures, particularly of those under bending load; and (2) to study the post-buckling behaviour of initially curved (imperfect) structures. In the case of bending, the results matched exactly with the reference solutions; for the post-buckling case, the model predicted very similar results to the reference, particularly in the deep post-buckling regime.

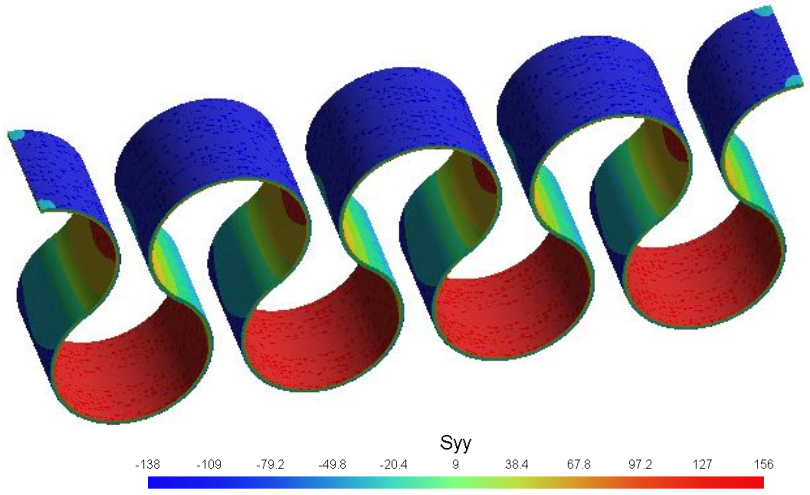

(a) ANSYS

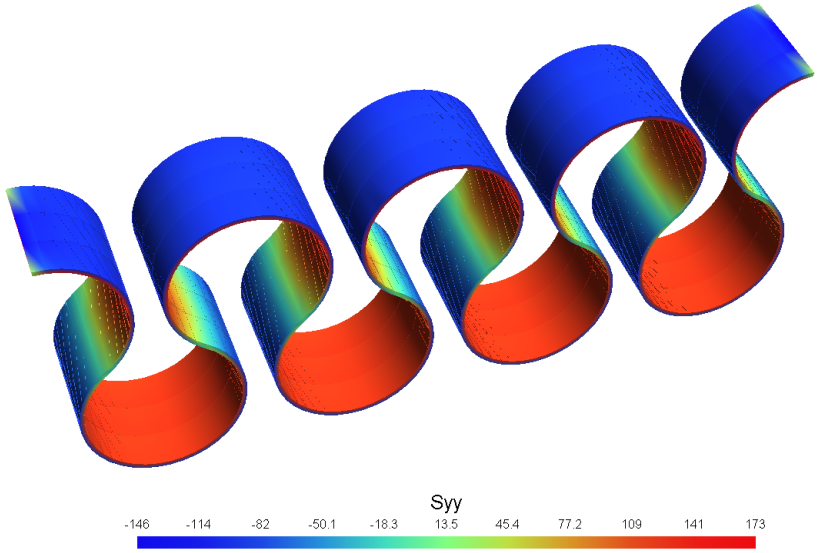

(b) UF-3D

Figure 5.25: Axial stress σ_{yy}, case $c = 30$ mm & $p = 40$ mm.

The third example was a more complex structure: a tapered beam made of functionally graded material. The purpose was to take some ingredients from the first two examples: tapered geometry and curved axis. The effect of the grading parameter was studied. Results were benchmarked against a known non-linear FGM tapered beam formulation. The first loading condition was a bending load, for which the model predicted accurately how, by increasing the power low parameter (more steel close to the root), the structure becomes stiffer and behaves as if it was made entirely of steel. The second set of results had the purpose of studying the effect of the same power rule in the post-buckling behaviour. In order to trigger buckling, the structure was modelled

as an initially curved beam. Results showed the same pattern, as the power parameter is greater (closer to steel), the structure becomes stiffer and the buckling load is nearly double (relative to the less stiff distribution). When compared with the reference data, some discrepancies were found, about ~ 5% higher results. Nevertheless, the same global response was predicted.

The last example was a set of highly-curved corrugated structures. The purpose was to show the capabilities of modelling beams with high curvatures, for which geometrical non-linearities have to be included. Results were compared with 3D FEM model, linear UF-3D model and available experimental results from literature. The agreement between all of these was evident. UF-3D model used a fraction (~ 5%) of the DOFs compared with solid 3D formulation. This gives evidence of the effectiveness and accuracy of the new formulation. In terms of the mechanics predicted by the proposed model, it can be seen that the corrugated structures studied were governed by two main mechanisms: for relative small values of the load, the structure shows local bending, and its curvature decreases until is almost flat; followed by a membrane stretching and high increase in stiffness. This effects can be captured only with non-linear models.

In summary, the Unified Formulation Three-dimensional Beam Model is capable of performing full Total Lagrangian non-linear analysis for curved and tapered 3D beam-like structures, in an accurate and effective way.

5.6 Concluding Remarks

The aim was to provide a non-linear three-dimensional beam model based on the Unified Formulation capable of performing large deformation analysis of curved and tapered structures. Combined with the Serendipity Lagrange expansion and the 3D element description, the model provides the means of performing the desired analyses in an accurate and efficient way. The main findings can be summarised as follows:

1. Non-linear total Lagrangian analysis can be performed on beam-like structures with tapered and curved geometries.

2. A three-dimensional shape mapping can be used to describe the three-dimensional beam element without increasing the DOFs.

3. For the cases that apply, the model used only a small fraction (~ 5%) of the DOFs compared with 3D FEM models.

4. For the case of the tapered beam under bending, the results showed a good agreement with the FEM model and experiments. Agreement with the semi-analytical model was, in general, satisfactory. Moreover, shear and normal stresses through thickness were accurately predicted by the model.

5. The predictions for the bending behaviour of a thin composite plate under bending was in excellent agreement with the reference solution. Buckling and post-buckling of an initially imperfect (curved) structure was modelled correctly as well.

6. Non-linear modelling of complex structures with tapered, curved and made of composite material (FGM) was also performed in an accurate way.

7. The non-linear behaviour of highly-curved corrugated structures was correctly and efficiently predicted by the model. Results match with 3D FEM and are close to those to the available experimental results as well.

With the Unified Formulation Beam Model (UF-3D) the capabilities of the Unified Formulation have been expanded, and new and more complex structures can now be modelled with this approach.

CHAPTER 6

LOCAL NOMINAL STIFFNESS METHOD

"A very small cause which escapes our notice determines a considerable effect that we cannot fail to see, and then we say that the effect is due to chance"

- Henri Poincaré

Thin-walled structures are used extensively in aerospace, automotive and mechanical engineering applications. Their buckling performance and structural weight makes them an excellent solution for members subject to compression loads. However, the manufacturing process may introduce localised regions of reduced stiffness/strength that can compromise their performance. Considering the sensitivity to these nominal stiffness areas, especially their spatial distribution over the entire structure, can be highly important. Identifying the mentioned regions can aid engineers in the design process. We propose a new methodology, the *Localised Nominal Stiffness Method* (LNS), which allows physical regions of sensitivity to be first identified and then mapped. The underpinning idea involves a series of linearised buckling analyses, in which a localised nominal stiffness region is introduced in each analysis and where the buckling response of the structure is recorded. The process is repeated for all discrete locations until the entire shell surface has been represented. In practice, each discrete location corresponds to a unique element in a finite element mesh. The overall data provides a continuous distribution on regions on sensitivity to localised stiffness variations. This distribution is then used to find areas where material can be removed, without affecting the buckling and post-buckling behaviour significantly. The methodology does not depend on any particular finite element formulation, however, the nature of the eigenvalue analysis can be computationally expensive. For this reason, we have adopted the Linearised Buckling Model of Chapter 4, in order to reduce overall computational effort. To exemplify our methodology, we study three different structures: a flat simply-supported plate,

a simply-supported thin box and a thin curved panel with two different boundary conditions, simply-supported and clamped-clamped.

6.1 Aim and Motivation

Designing lightweight thin structures against buckling can be a complex task. The problem of reducing mass of a structure given a target buckling load can be approached is different ways. The most common solution is to use an optimisation routine with stability constraints, however this method can be difficult to implement and computationally costly. The main motivation for the developments of the present chapter is to provide an alternative methodology for designing lighter structures without compromising their buckling and post-buckling performance.

The aims can be summarised as follows:

- To develop a methodology for identifying and mapping regions where the structure might be more sensitive to localised nominal stiffness imperfections, and its relationship with the buckling performance.
- To create contour-like plots that can be used for designing purposes, particularly to identify regions where material might be removed, e.g. by introducing cut-outs, without affecting significantly the buckling and post-buckling performance.
- The methodology has to exploit the efficiency and accuracy features of the SL Unified Formulation Linearised Buckling model, however it should not depend on it.

6.2 Introduction

Thin-walled structures are extensively used in environments where high compression loads are expected. However, undesirable material inhomogeneities introduced during the manufacturing process may compromise their performance. Taking into account the sensitivity to these in the design process, especially for lightweight applications, is of paramount importance.

Even though imperfection sensitivity of shells has been extensively studied over recent decades [48, 59, 126–129], the design challenges remain a research topic to this day, particularly the studies regarding localised stiffness variations. In order to design the structure against buckling, one has to understand the effects of local low stiffness inhomogeneities, especially their spatial distribution over the entire structure. Identifying regions where the structure is insensitive to these areas can aid engineers in the design process. One of the first works related to the design of structures against buckling, using spatial sensitivity distributions, came from the context of composite materials. Hyer & Lee [60] used a sensitivity analysis and a gradient technique to find the fibre orientation in different regions of a plate that increases its buckling load. The sensitivity analysis was used to determine those regions of the structure that have

the most influence on buckling load, and the gradient method was used for maximising the critical load. Nowadays the use of high performance computers and commercial finite element software allows more detailed and extensive studies to be performed. Stochastic, parametric and exhaustive methods are of common use. Take for example the work by Papadopoulos et al. [130], who used random non-Gaussian distribution of spatial distribution of variable thickness to study its influence on the buckling load in an imperfect structure. A similar work, performed by Broggi & Schuëller [131] and Kepple et al. [132], studied variations in material properties due to variable thickness. They used the *Moving Window Technique*, which consists of averaging properties in a chessboard-like pattern of imperfections, to study the effect on the buckling performance of cylinders. More recently Hu & Burgueño [133–135] used two different methods, *Seeded Geometric Imperfection* (SID) and *Non-Uniform Stiffeness* (NSD), to study the influence of imperfection fields on buckling response. The latter is of more interest to the present work, where a random and discrete patch-like pattern of stiffness imperfections is pre-assigned to a structure, for the purpose of studying its buckling behaviour. They proved that some structures can be tailored or *nudged* to have a desired buckling performance and be less sensitive to imperfections. A more recent and extensive work on modal nudging can be found in a work by Cox et al. [62].

In this chapter an approach for studying and tailoring structures against buckling is presented. A simple and novel method, the *Localised Nominal Stiffness Method* (LNS)[1], for identifying and mapping regions where the structure is insensitive to local variation of low stiffness properties, is introduced and discussed. The method entails simulating a localised *cut-out* via the introduction of a low stiffness finite element. A series of linear buckling analyses (eigenvalue problems) are performed, where on each run, a patch-like nominal stiffness property is assigned to a single element. The purpose is to find a contour-like pattern which represents *regions of sensitivity*. The result can then be used as a baseline for reducing the mass of structures by introducing cut-outs, without significantly[2] compromising on buckling and post-buckling performance. Particularly, for structures that behave linearly[3], the aim is to reduce the mass without affecting its critical load; on the other hand, for non-linear cases, the aim is to tailor the structure such that it is lighter and its post-buckling behaviour is approximately the same as the original. In addition, and for some cases, to reduce the sensitivity to geometrical imperfections. The LNS can be, potentially, combined with the method proposed by White & Weaver [61], in which they have used variable angle-tow laminae to design imperfection-insensitive shell structures against buckling.

The proposed methodology *does not* depend on a particular finite element formulation. However, the nature of the eigenvalue algorithm can lead to computationally costly models, since a repeated number of eigenvalue analyses have to be performed. This process can lead to a potential and undesirable bottle-neck. For this reason, the Unified Formulation Linearised Buckling Model

[1] The definition of *nominal* is a very small, or far below the real, value.

[2] *Significantly* is a relative concept, which depends on the context. A more detail explanation and definition is given in subsequent sections.

[3] i.e. if the critical load computed using a linear buckling analysis and a non-linear analysis are approximately the same.

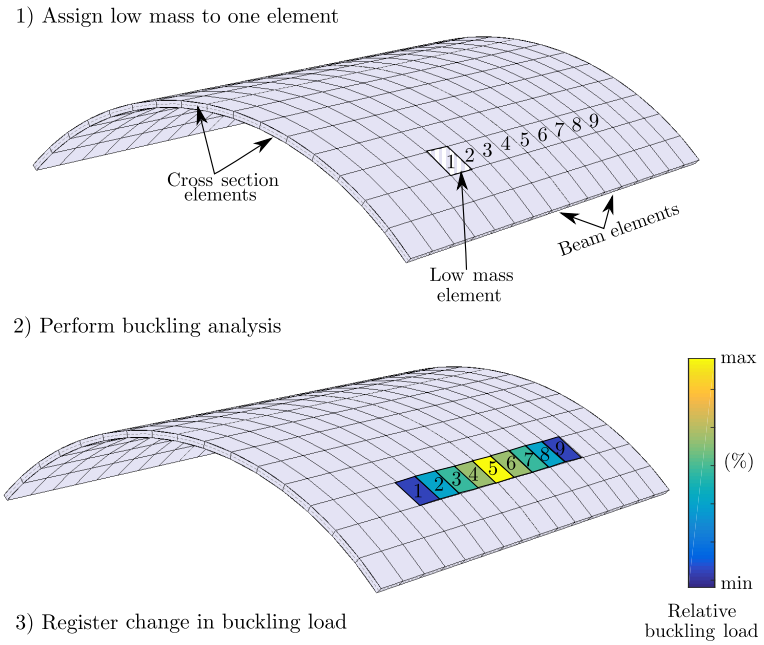

Figure 6.1: Schematic summary of the steps of the sensitivity analysis: Nominal mass element location vs buckling load.

presented in Chapter 4 is adopted, in order to reduce overall computational effort. The linear buckling model reduces the computational cost significantly, in terms of degrees of freedom (DOFs) and time for each convergence step.

6.3 Sensitivity Analysis: *Localised Nominal Stiffness Method*

The purpose of understanding a sensitivity analysis that involves locating a single nominal stiffness element is to identify well defined regions where the effect of the stiffness reduction on the buckling load is insignificant. The nominal stiffness property is simulated via a nominal value of Young's modulus, in this case $E/100$, where E is the modulus of the unperturbed structure. This approximation of a *hole* is used in many practical applications. In topology optimisation problems with buckling constraints, the method may lead to a phenomenon called *Singular Topology*. Singular Topology was first reported in 1968 by Sved and Ginos [136] and states that if an optimisation routine[4] is performed involving the removal of material by taking its size as zero, the solution may not converge to the exact optimum [137, 138]. Despite this difficulty, this approach is widely used. By way of a cautionary note, even though no optimisation routines were employed in our current work, results must be interpreted carefully and should only be considered as approximations.

[4]For example: Gradient method or Genetic Algorithms.

In a finite element analysis a linear system must be solved, i.e. inverted. The use of large areas (compared with the overall size of the structure) with low levels of density may cause numerical instabilities [139] and ill-conditioned systems. This problem arises because of the introduction of zeros in the main diagonal of the stiffness and geometrical stiffness matrices. Several authors have proposed techniques to mitigate such difficulties, including ignoring some degrees of freedom or by using a penalization method [140]. However, the problem becomes negligible if the affected area is small. In the present case, only a single finite element is modified and the meshes used are fine, therefore it is assumed that the ensuing solution is appropriate. Results in Section 6.4 provide evidence for this assumption.

The process utilised in *Localised Nominal Stiffness Method* (LNS) is now explained; refer to Figure 6.1. The structure is discretised by meshing the cross-section and the longitudinal axis. A reduced material stiffness is assigned to a single finite element, Step (1). Afterwards, a linear buckling analysis is performed, Step (2). The new buckling load is compared with the load of the unperturbed structure and registered using a colour scale, Step (3). The process is repeated until all elements have been considered. The steps may be repeated with a finer mesh to ensure convergence of the coloured distribution. The final result is a contour-like pattern that relates a *nominal stiffness location with buckling load reduction*. It is important to emphasise that only one element at a time is altered to avoid numerical instabilities. As presented later, this process provides approximate regions where removing material may have little or no effect on the buckling performance.

6.4 Numerical Examples

This section shows how LNS is used to find regions in the structure which are relatively insensitive to localised material changes. The aim is to find locations where cut-outs can be introduced such that mass can be reduced without affecting its buckling and post-buckling performance, significantly. For the case of structures that have a linear behaviour[5] the allowed value for the decrease of the buckling load is set to 1%. Any change in the load less or equal to this is considered to be acceptable. On the other hand, for non-linear cases, the goal is to design a structure whose post-buckling behaviour is approximately the same as the original structure, in terms of deformed shape and sensitivity to geometrical imperfections.

Convergence[6] of LNS, buckling modes and loads are reported and compared. Additionally, the change in buckling load is measured via an *Optimality Factor*, defined as the ratio between the new and original buckling load ($OF = \frac{\lambda}{\lambda_o}$), or in some cases as the relative reduction $s_\lambda = 1 - OF$. Similarly, the decrease in mass is given as the ratio of the new to original structural mass ($\frac{M}{M_o}$).

[5] Meaning that the critical load, computed using a linear eigenvalue and a non-linear analysis, are approximately the same.

[6] Convergence is assumed to be achieved if the contour pattern does not change significantly, this is verified visually.

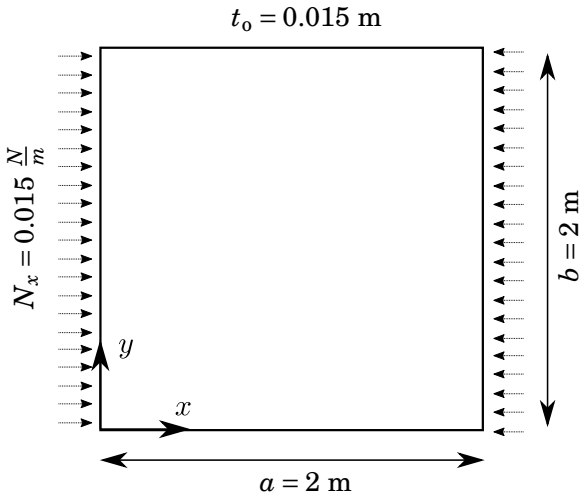

Figure 6.2: Flat plate geometry.

A comparison between UF-SL and ABAQUS's DOFs[7], complexity of the solution algorithms and approximate CPU time for the iterative step is also included in our comparison studies. Measuring *time* directly is not an appropriate comparison, as it depends on the particular implementation, language and code architecture (which in the case of ABAQUS is effectively a black-box for our purposes), even though, data is given for purposes of completeness.

Three cases are studied, the first example is a typical benchmark problem in topology optimisation analysis for buckling resistant structures: a simply-supported flat plate. The second case is a more complex structure, a thin box. The last is a curved thin panel with two different sets of boundary conditions. All the geometry specifications, materials and boundary conditions are provided for each example. Without lost of generality, the density is taken as $\rho = 1$ kg/m^3.

For all examples the UF-SL is used to perform the computationally intensive part of the analysis: the sensitivity convergence. Once the structure has been re-designed, and to check robustness, a non-linear analysis is performed on the tailored structure with an ABAQUS model[8].

6.4.1 Simply-Supported Flat Plate

Consider a flat square plate with side dimensions $a = b = 2$ m and thickness $t = 0.015$ m, uniaxially compressed with a force per unit length of $N_x = 0.015$ N/m, along the x direction, as shown in Figure 6.2. An isotropic material with Young's modulus of $E = 200$ GPa and Poisson's ratio, $\nu = 0.3$ is considered. All of the plate's edges are simply-supported (SSSS) and allowed to move in the in-plane direction. Table 6.1 shows the DOFs, complexity of the algorithms and approximate CPU time for: an ABAQUS Shell model with 40,000 elements and a UF-SL model of order 2 with a

[7]Needed for the convergence of both: buckling load (eigenvalue) and buckling mode (eigenvector) -in terms of number and relative size of half waves-.

[8]We have use an ABAQUS model since the current code implementation of the UF-SL model does not support structures with holes.

Table 6.1: DOFs, Number of operations for Sparse Inversion & Eigenvalue Solvers and CPU time for linear buckling analysis of a flat plate.

	DOFs [#]	Ops. Inversion [#]	Ops. Eigenvalue [# *per iteration*]	~Inversion Time [secs.]	~Eigenvalue Time [secs.]
Model					
ABAQUS	242,406	$\sim 10^7$	$\sim 10^{16}$	< 1	200
UF-SL	18,849	$\sim 10^9$	$\sim 10^{13}$	< 1	5

mesh of 20×20. As a baseline for comparison, two different geometrical configurations are used: a plate without cut-outs and a plate with a central cut-out [141]. These are compared with a tailored structure obtained as a result of the proposed methodology: a plate with four distributed cut-outs, which is designed such that the area of the cut-outs is the same as the case of a plate with a central hole.

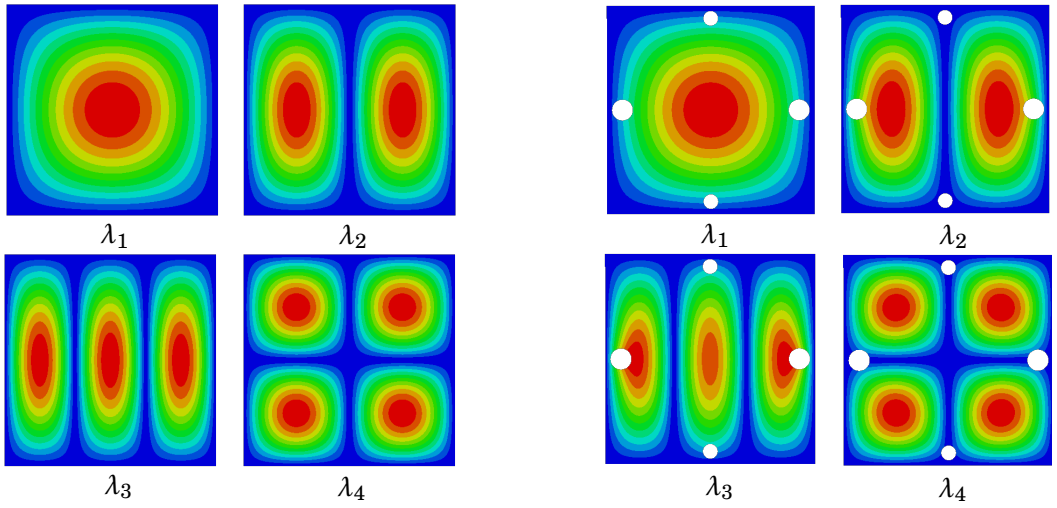

(a) Plate without cut-outs

(b) Plate with distributed cut-outs.

Figure 6.3: First four buckling modes. Simply-Supported Plate.

The shell model is used to analyse the buckling performance of the first two structures. The

Table 6.2: First four buckling loads. SSSS Plate.

	λ_1 $[\text{N/m}] \times 10^5$	λ_2 $[\text{N/m}] \times 10^5$	λ_3 $[\text{N/m}] \times 10^5$	λ_4 $[\text{N/m}] \times 10^5$
Geometry				
No cut-out	6.06	9.48	16.88	24.22
Four cut-outs	6.01	9.20	15.88	23.03

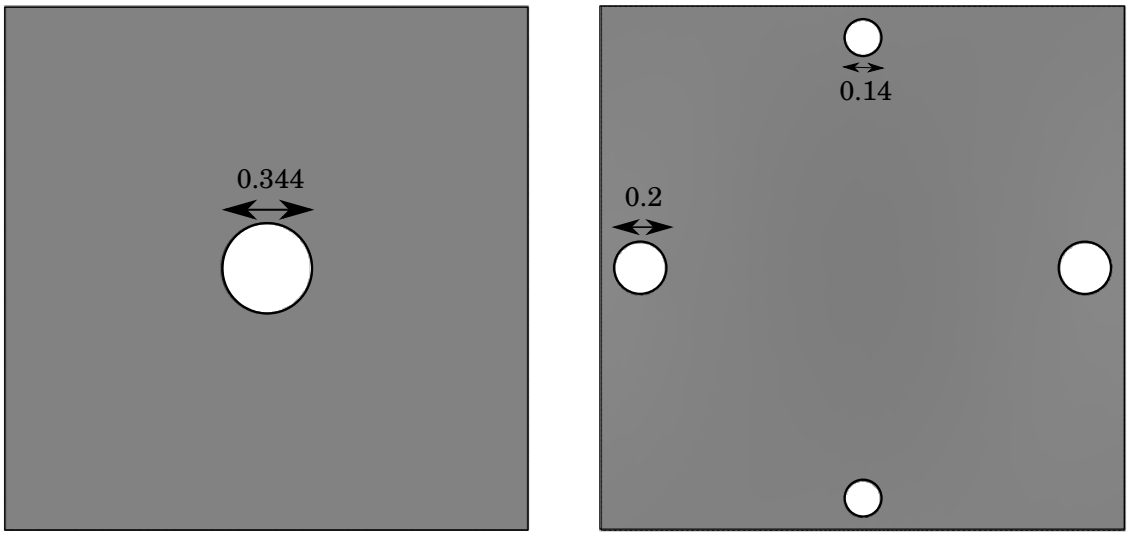

(a) Plate with centre cut-out.

(b) Plate with distributed cut-outs.

Figure 6.4: Equivalent area cut-outs. SSSS plate.

first four buckling loads can be found in Table 6.2. Buckling modes are shown in Figure 6.3(a). As seen in the table, the critical load (λ_1) obtained for the plate without cut-outs is $\lambda_o = 6.06 \times 10^5$ N/m. The buckling load for the plate with a circular cut-out, Figure 6.4(a), is $\lambda = 5.51 \times 10^5$, that is $OF = 0.91$, a decrease of $\sim 9\%$ relative to the original plate. This result is close to the one reported by Ritchie & Rhodes [141], $OF = 0.93$. Reduction of the surface area is $\sim 3\%$.

Now, the LNS is used for finding regions of relative insensitivity. A convergence analysis is performed using a UF-SL model of order 4 with four different mesh sizes: 8×8, 18×18, 28×28 and 38×38 elements. Results in Figure 6.5 show converged and well-defined sensitivity regions. Horizontal and vertical numbers depict the number of beam and cross-sectional elements respectively. Colours represent the relative reduction of the buckling load s_λ. Four areas where the effect of cut-outs might have a minimum effect are located: two largish regions close to the loaded edges, and two smaller near the unloaded edges. Four circular cut-outs are introduced such that the decrease in surface area is 3%: two with radius of $r_b = 0.1$ m, and two with radius $r_s = 0.07$ m. These are located at a distance of 0.05 m from the edges as shown in Figure 6.4(b). The new geometry is analysed where both, linear and non-linear methods are performed. The resulting first four buckling loads are shown in Table 6.2. Figure 6.3(b) depicts the buckling shapes of the plate with distributed cut-outs. Comparing the critical load of the original structure to the one with distributed cut-outs, the $OF \sim 1$, that is, the buckling load is not affected significantly. Table 7.7 summarises the results for the critical loads and mass reduction for the three cases.

A post-buckling geometrical sensitivity analysis was then performed for the original and tailored structures. The first buckling mode is used for seeding an initial geometrical imperfection. Four cases are studied, the original structure and three others where the normalised eigenvectors

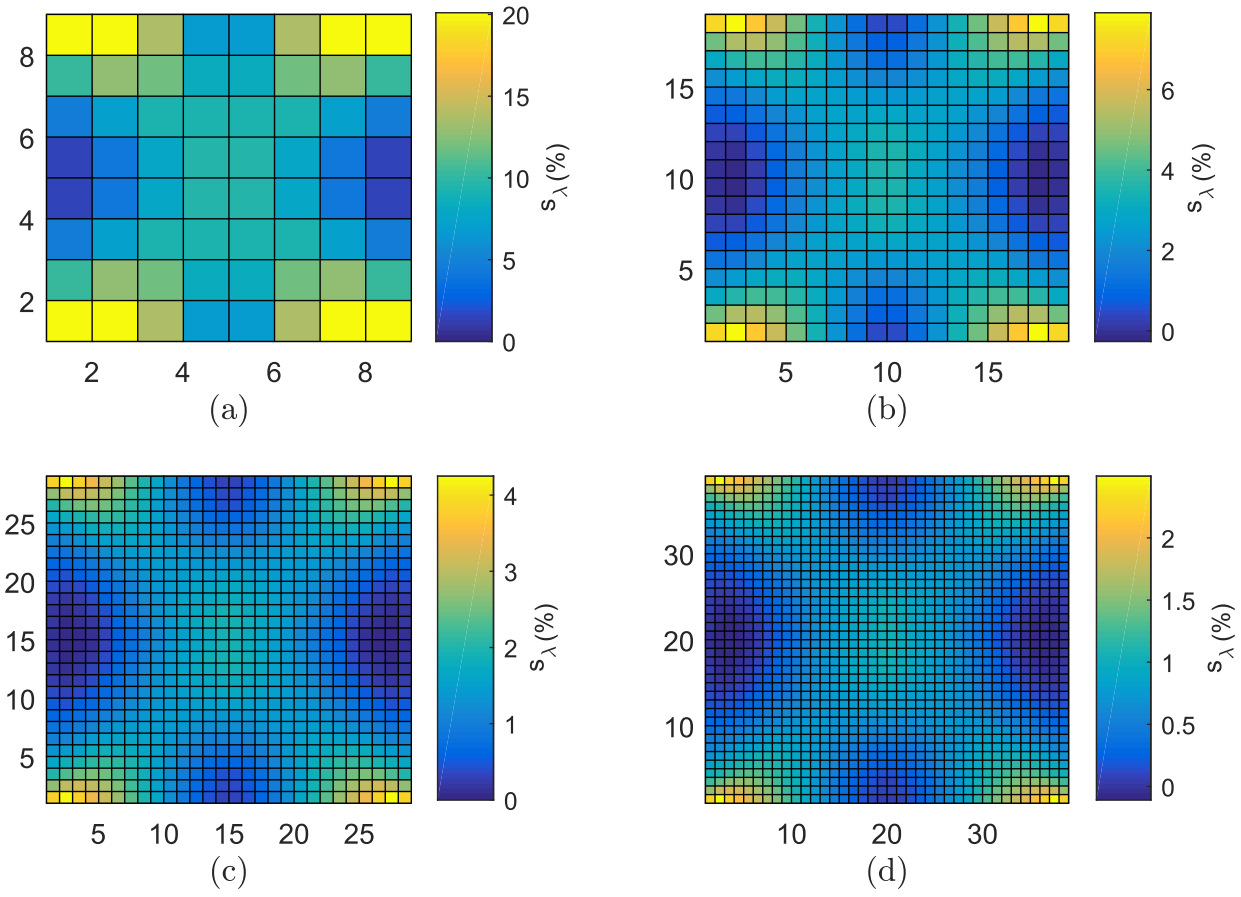

Figure 6.5: Convergence of sensitivity analysis: (a) 8×8, (b) 18×18, (c) 28×28 and (d) 38×38 elements. SSSS plate.

are added to original mesh. The scale factor is interpreted as percentage relative to the structure's thickness t. Figure 6.6 shows the load-displacement curves measured at the centre of the plate, for the cases: original, 1%, 10% and 50% (only stable paths are shown). Mode shapes at some locations are also depicted. A comparison of the post-buckling behaviour for the three geometries

Table 6.3: Buckling load, Optimal Factor, mass and relative mass. SSSS Plate.

	λ [N/m] $\times 10^5$	OF	M [Kg] $\times 10^{-4}$	M/M_o
Geometry				
No cut-out	6.06	1.00	6.00	1.00
Centre cut-out	5.51	0.91	5.86	0.97
Four cut-outs	6.01	1.00	5.86	0.97

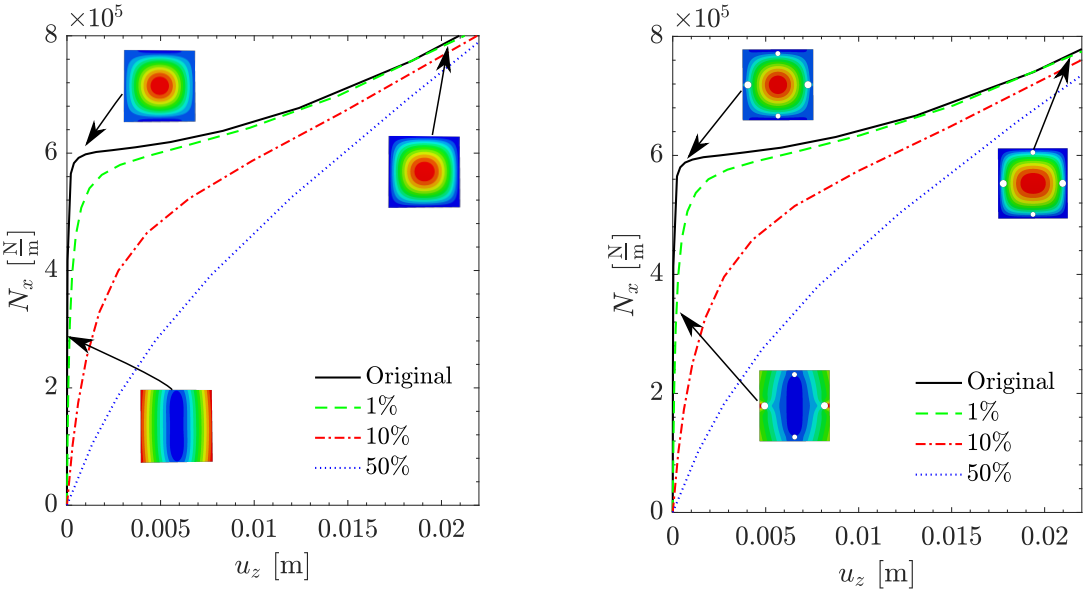

(a) Plate without cut-outs.

(b) Plate with distributed cut-outs.

Figure 6.6: Post-buckling geometrical imperfection analysis. Plate.

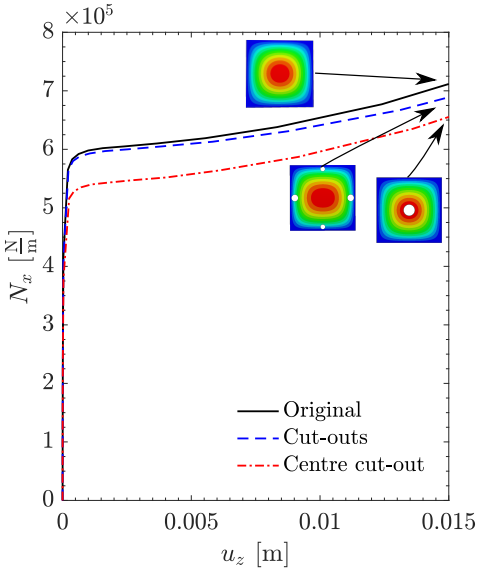

Figure 6.7: Comparison of the post-buckling path for the three plate geometries.

is shown in Figure 6.7.

In this case, it was possible to identify regions of potential insensitivity to variations in localised nominal stiffness where cut-outs were introduced. Results show that the plate with distributed cut-outs effectively maintained the critical load within the allowed value. Moreover,

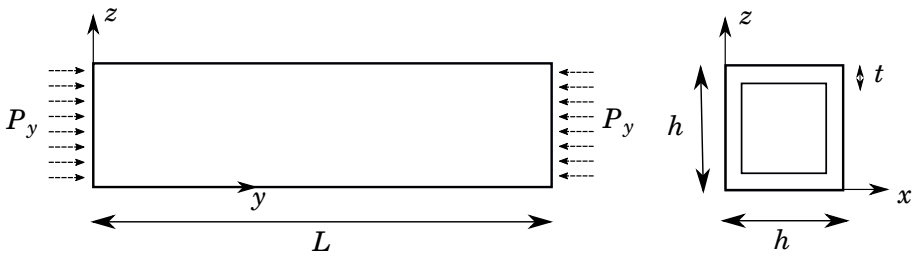

Figure 6.8: Thin box geometry.

the post-buckling behaviour is approximately the same, showing a better performance than the structure with equivalent mass, but with a central cut-out.

6.4.2 Thin Box

The second case considers a more complicated structure, namely a thin box of length $L = 1$ m, width and height of $h = 0.1$ m and thickness $t = 0.002$ m. Figure 6.8 shows the geometry. An isotropic material with Young's modulus of $E = 71$ GPa and Poisson's ratio, $\nu = 0.33$ is considered. The structure is loaded axially with a unit force applied to the edges. Boundary conditions are such that the loaded edges can move only in the y-axis direction. Table 6.4 shows the DOFs, complexity and approximate CPU time of the algorithms for: an `ABAQUS` shell model with 48,160 elements and a UF-SL model of order 2 with a mesh of 48×48. The first buckling loads given by a linear buckling analysis are shown in Table 6.5; buckling modes are depicted in Figure 6.9(a).

Table 6.4: DOFs, Number of operations for Sparse Inversion & Eigenvalue Solvers and CPU time for linear buckling analysis of a thin box.

	DOFs \#	Ops. Inversion \#	Ops. Eigenvalue \# *per iteration*	~Inversion Time secs.	~Eigenvalue Time secs.
Model					
`ABAQUS`	288,960	$\sim 10^7$	$\sim 10^{16}$	< 1	580
UF-SL	104,400	$\sim 10^{11}$	$\sim 10^{15}$	1.5	60

A convergence of the buckling sensitivity analysis is performed with a UF-SL model of order 2 with four mesh sizes: 20×20, 32×32, 40×40 and 48×48 elements. Figure 6.10 shows the results. Several potential regions for the location of cut-outs are identified, mainly towards the centre of the structure. With this in mind, three cut-outs, one ellipse and two circles, are chosen to be located on each of the four faces. Dimensions and exact locations can be found in Figure 6.11. The new geometry is tested with, linear and non-linear analyses are performed. The first four buckling loads and buckling modes are computed and shown in Table 6.5 and Figure 6.9(b), respectively.

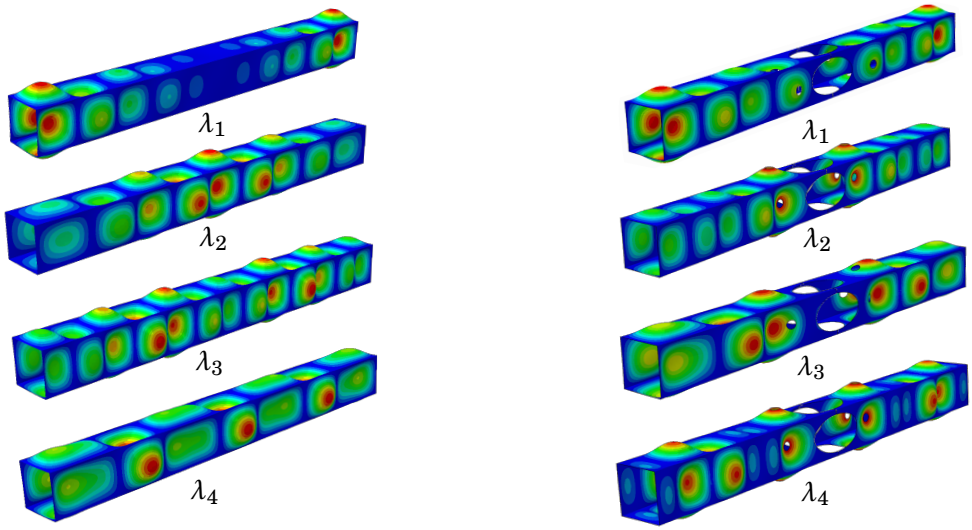

(a) Box without cut-outs

(b) Box with distributed cut-outs.

Figure 6.9: First four buckling modes. Thin box.

Table 6.5: First four buckling loads. Thin box.

	λ_1 [N/m] $\times 10^5$	λ_2 [N/m] $\times 10^5$	λ_3 [N/m] $\times 10^5$	λ_4 [N/m] $\times 10^5$
Geometry				
No cut-out	2.17	2.23	2.32	2.50
Cut-outs	2.16	2.23	2.40	2.49

Table 6.6: Buckling load, Optimal Factor, mass and relative mass. Thin box.

	λ [N/m] $\times 10^5$	OF	M [Kg] $\times 10^{-4}$	M/M_o
Geometry				
No cut-out	2.17	1.00	8.00	1.00
Cut-outs	2.16	0.99	7.24	0.90

The critical load is $\lambda_1 = 2.16 \times 10^5$ N/m or equivalently $OF = 0.99$. That is, a decrease of 1%, which is still acceptable, relative to the standards defined previously. Even though the buckling load decreased, the reduction in total mass is significant: 10%. Table 6.6 summarises the results.

A post-buckling geometrical sensitivity analysis is also performed. A common practice for sensitivity (geometrical) analysis of shells, is to use the first eigenvector as geometrical imperfection. Therefore, we have used this to seed an initial imperfection to the structure. Figure 6.12 shows

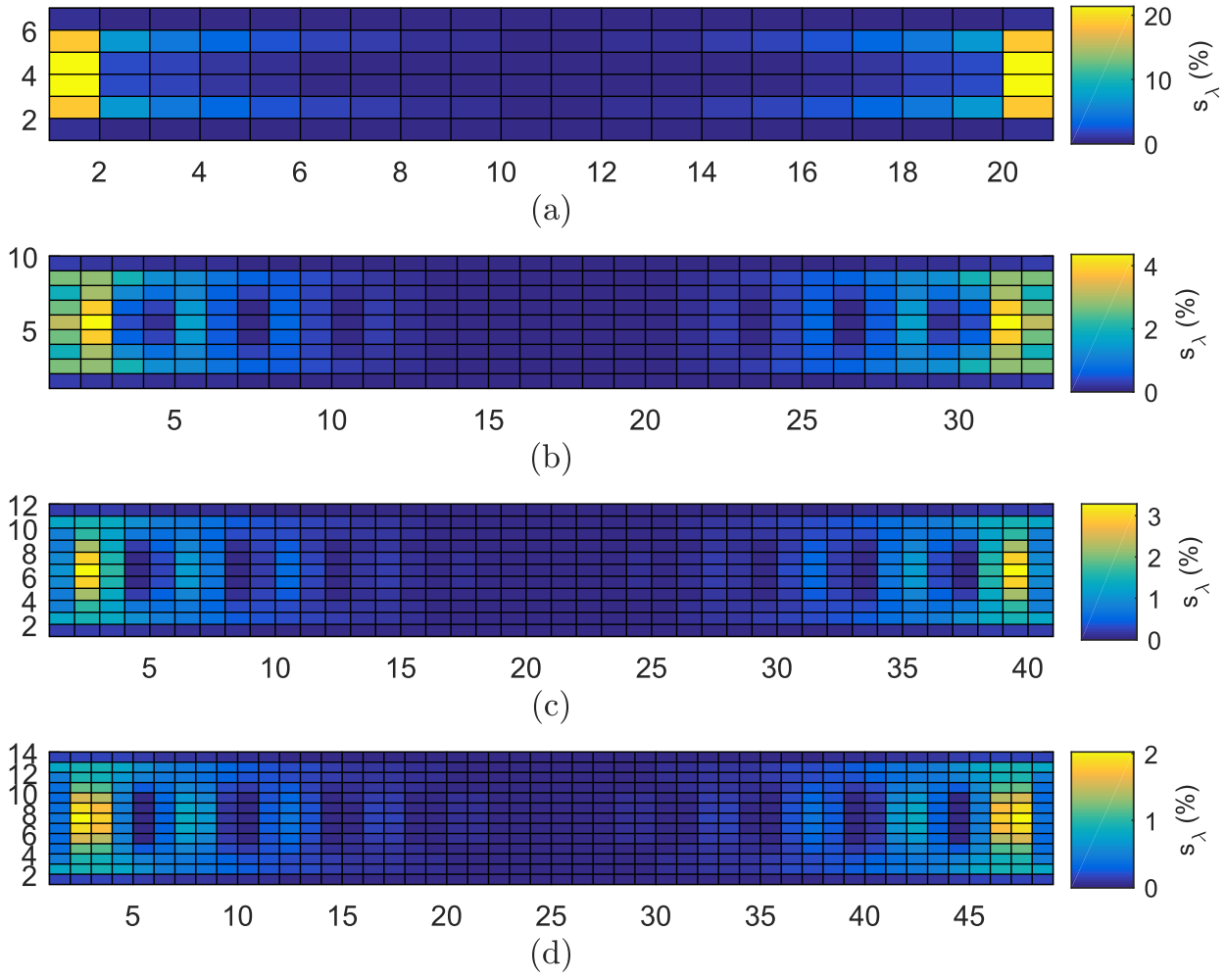

Figure 6.10: Convergence of sensitivity analysis: (a) 20×20, (b) 32×32, (c) 40×40 and (d) 48×48 elements. Thin box (top view).

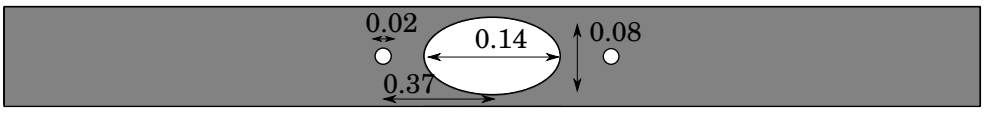

Figure 6.11: Box with cut-outs. Top view.

the load vs maximum displacement results for four cases[9]: 0% (unstable path), 1%, 10% and 50%. It can be seen that the introduction of cut-outs in the specified location does not have an effect on the buckling load (a bifurcation point). The post-buckling load-displacement curve for both cases is the same, nevertheless, the deformed shapes do change, especially for the unstable path.

[9]Magnitude of imperfection relative to the box's thickness t

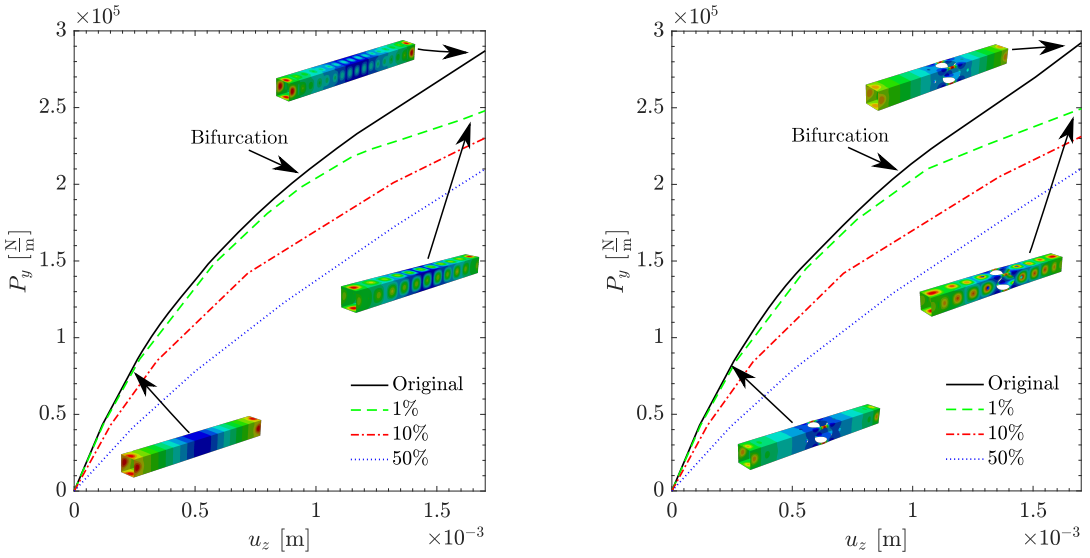

(a) Box without cut-outs.

(b) Box with distributed cut-outs.

Figure 6.12: Post-buckling geometrical imperfection analysis. Plate.

6.4.3 Curved Panel

The purpose of this example is to show the following important results: (1) how the distribution of varying local stiffness sensitivity may change if boundary conditions are changed; (2) how these can be used to make the structure lighter, without compromising its post-buckling performance significantly; and (3) for the structure which presents a negative stiffness after its limit-load (simply-supported case), the method provides the means to tailor it such that the resulting structure is less imperfection sensitive (geometrically), compared with the original.

A curved panel is now considered. The panel is axially loaded and two sets of boundary conditions are used: clamped-clamped (CC) curved edges and simply-supported (SS) curved edges. Straight edges are free for both cases. The material is the same as that considered for the case of the box. Geometry and dimensions are shown in Figure 6.13.

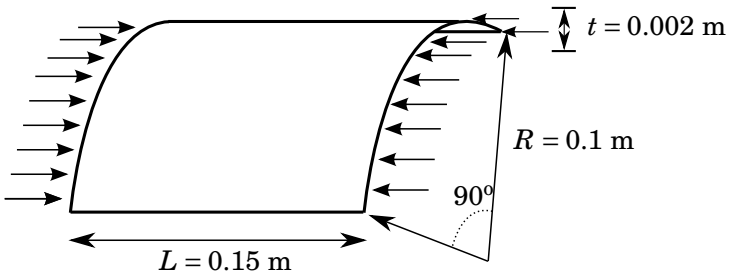

Figure 6.13: Geometry of the curved thin panel.

Table 6.7: First four buckling loads. Curved Panel.

	λ_1 [N] $\times 10^4$	λ_2 [N] $\times 10^4$	λ_3 [N] $\times 10^4$	λ_4 [N] $\times 10^4$
Geometry				
Clamped-Clamped				
No cut-out	7.11	7.98	8.66	8.75
Cut-outs	7.13	7.98	8.69	8.80
Simply-Supported				
No cut-out	4.11	4.87	7.51	7.62
Cut-outs	4.10	4.61	7.31	7.41

Table 6.8: DOFs, Number of operations for Sparse Inversion & Eigenvalue Solvers and CPU time for linear buckling analysis of a curved panel.

	DOFs #	Ops. Inversion #	Ops. Eigenvalue # *per iteration*	~Inversion Time secs.	~Eigenvalue Time secs.
Model					
ABAQUS	277,500	$\sim 10^6$	$\sim 10^{16}$	< 1	220
UF-SL	73,689	$\sim 10^{11}$	$\sim 10^{14}$	< 1	4

6.4.3.1 Clamped-Clamped Panel

An ABAQUS shell model with 45,692 elements is used to find the buckling modes and loads of the structure without cut-outs. Table 6.7 shows the results for the linear buckling loads. Figure 6.14(a) depicts the buckling modes.

A convergence study of the LNS is performed for both cases. A UF-SL model of order 2 and with four different geometry discretisations: 10×10, 20×20, 30×30 and 40×40 elements along both, cross-section and beam axis directions are used. Figure 6.15 show the results. Table 6.8 shows the DOFs, complexity and approximate CPU time of the algorithms.

For this case, the regions with minimum loss in performance are located towards the centre and close to the curved loaded edges. Six elliptical cut-outs are distributed on the surface as shown in Figure 7.34(a).

The new structure is tested before where both linear and non-linear analyses are carried out. The critical load is now $\lambda_1 = 7.13 \times 10^4$, that is $OF = 1$, therefore, the linear buckling performance is not affected. The mass reduction is $\sim 2\%$. The mode shapes are shown in Figure 6.14(b). A post-buckling geometrical imperfection analysis, using the first eigenvector as seeded geometrical imperfection, is carried out. A load vs vertical displacement curve, measured at centre of the straight edge, is shown in Figure 6.17. The figure shows the results for four imperfection cases, with scale factors relative to the panel's thickness: original, 1%, 10% and 50%. As shown here, the limit load is $\sim 8\%$ less than that predicted by the linear buckling analysis. Therefore, the

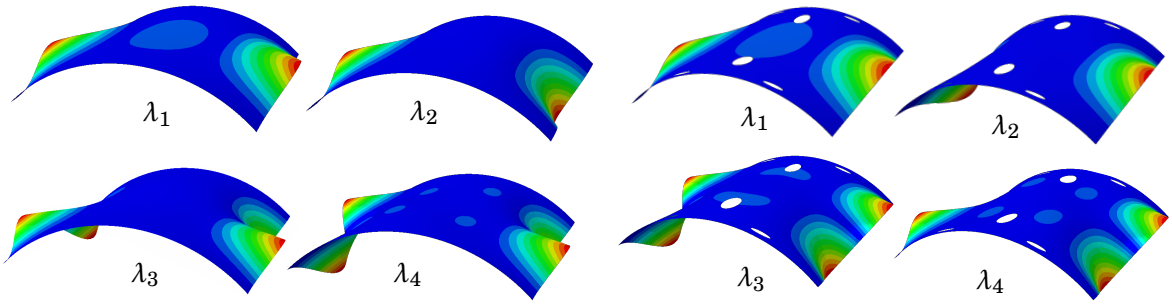

(a) Panel without cut-outs.

(b) Panel with distributed cut-outs.

Figure 6.14: First four buckling modes. CC Curved panel.

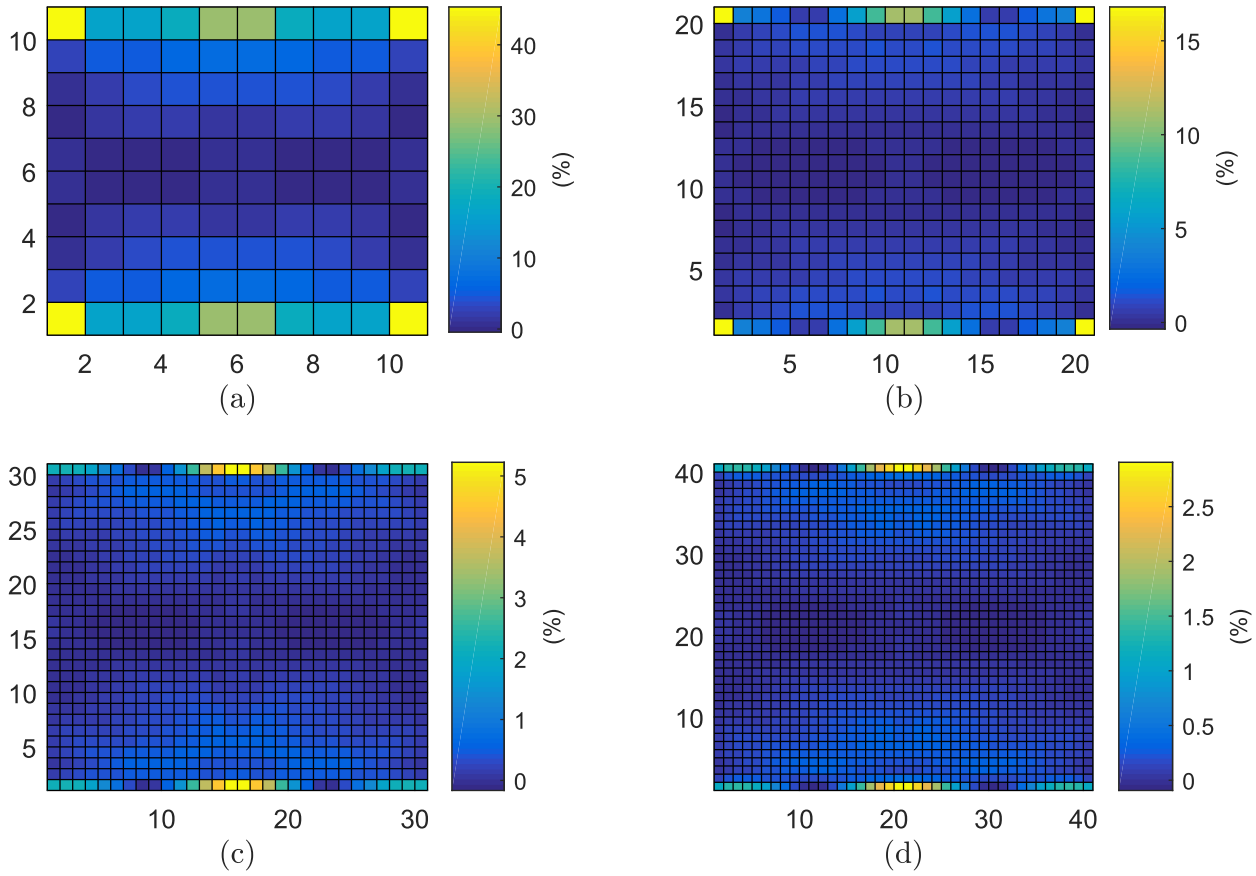

Figure 6.15: Sensitivity analysis: nominal mass element vs relative load reduction. CC curved panel with (a) 10×10, (b) 20×20, (c) 30×30 and (d) 40×40 elements.

structure is considered to have a more pronounced non-linear behaviour compared with the case of a plate and a box. The structure with cut-outs behaves similar to the original one, particularly

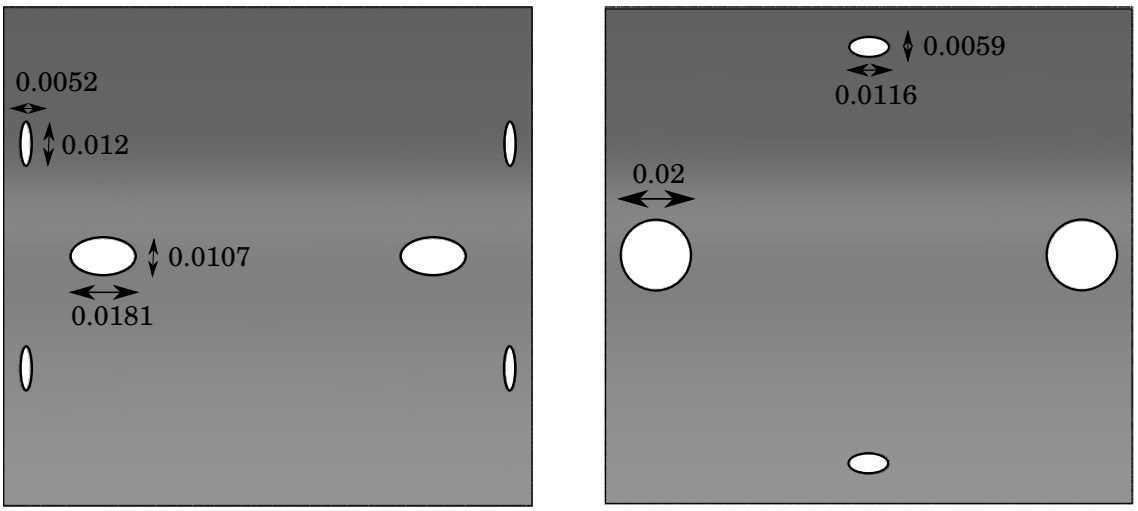

(a) CC panel with distributed cut-outs.

(b) SS panel with distributed cut-outs.

Figure 6.16: Curved panel with cut-outs for two different boundary conditions.

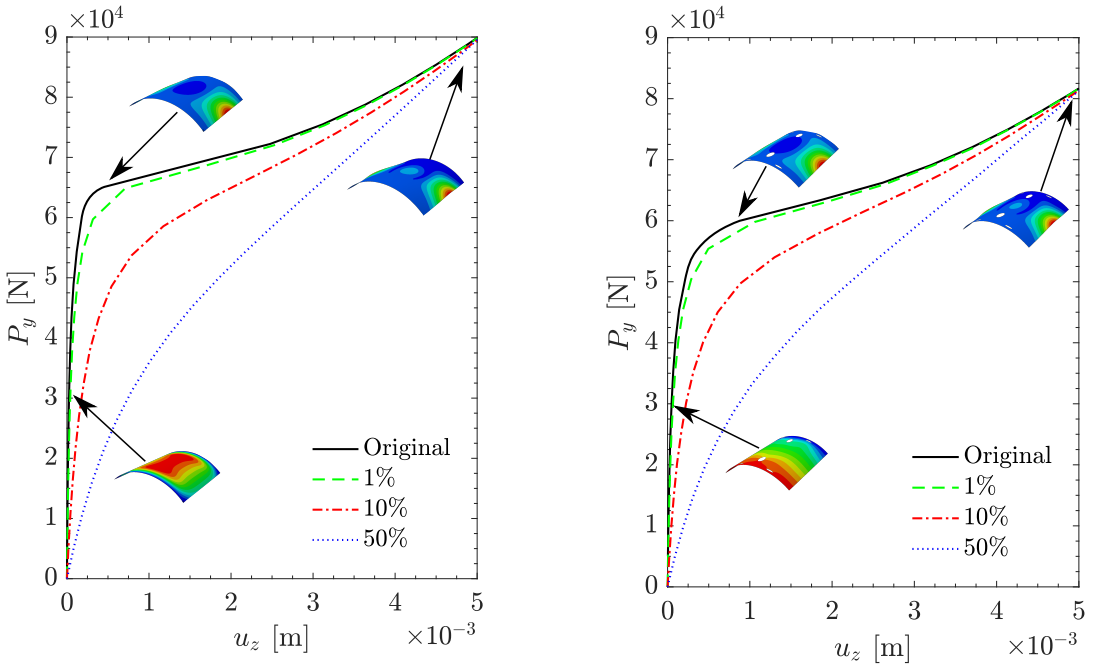

(a) Panel without cut-outs.

(b) Panel with distributed cut-outs.

Figure 6.17: Post-buckling geometrical imperfection analysis. CC panel.

its deformed shape. The limit-load of the tailored structure is ~ 5% less to that of the panel without holes.

For comparison purposes, a third structure is studied. A curved panel with a central cut-out

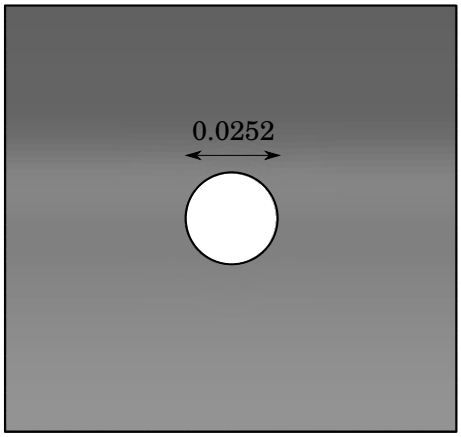

Figure 6.18: Panel with a centre cut-out.

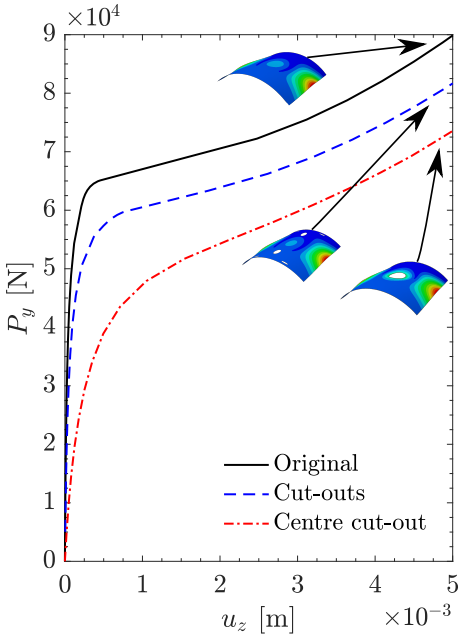

Figure 6.19: Comparison of the post-buckling path for the three CC panel geometries.

with an area equal to that of the distributed cut-out case. Figure 6.18 shows the geometry. In Figure 6.19 the load vs maximum vertical displacement for the three cases is shown. This shows that, even though the tailored structure reduces the limit-load point, the load carrying capability is higher compared with the case of an equivalent centre-holed structure.

6.4.3.2 Simply-Supported Panel

A linear buckling analysis is performed for the SS case, the first buckling loads and modes are presented in Table 6.7 and Figure 6.20(a) respectively. A stiffness sensitivity analysis is also

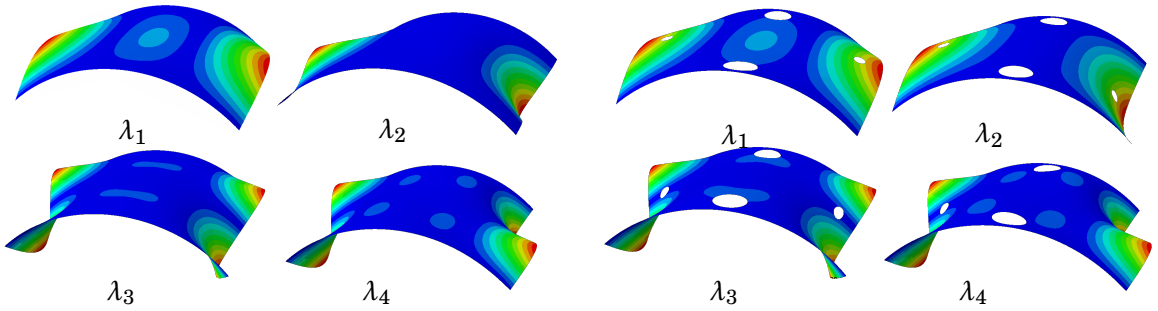

(a) Panel without cut-outs. (b) Panel with distributed cut-outs.

Figure 6.20: First four buckling modes. SS Curved panel.

carried out, with the converged result shown in Figure 6.21. For the SS-panel the resulting pattern is different compared to that of the CC case. Apart from regions close to the curved edges, two smaller regions appear towards the straight edges. Therefore, only four cut-outs, two ellipses and two circles, are removed from the geometry, Figure 6.16(b).

Linear and non-linear analyses are carried out for the tailored structure. The first four buckling loads and modes are shown in Table 6.7 and Figure 6.20(b) respectively. In this case, the limit load predicted by a linear analysis is $\lambda_1 = 4.10 \times 10^4$ N, i.e. a $OF = 0.99$. The mass reduction is greater than that of the CC case, $\sim 4\%$.

A geometrical non-linear analyses with imperfections, using the first eigenvector as seeded imperfection, is now considered. As before, the load vs vertical displacement plot for four cases are presented: original, 1%, 10% and 50%. Results in Figure 6.22 show that, after the limit load, the stiffness is negative and the load carrying capacity is diminished. Structures like these are more likely to be imperfection (geometrically) sensitive. Therefore, a more detailed analysis of geometrical-imperfection sensitivity is carried out.

Table 6.9: Buckling load, Optimal Factor, mass and relative mass. Curved Panel.

	λ	OF	M	M/M_o
	[N] $\times 10^4$		[Kg] $\times 10^{-5}$	
Geometry				
Clamped-Clamped				
No cut-out	7.11	1.00	4.71	1.00
Cut-outs	7.13	1.00	4.62	0.98
Simply-Supported				
No cut-out	4.11	1.00	4.71	1.00
Cut-outs	4.10	0.99	4.56	0.96

Different combinations of the first three linear buckling modes are used to seed the structure

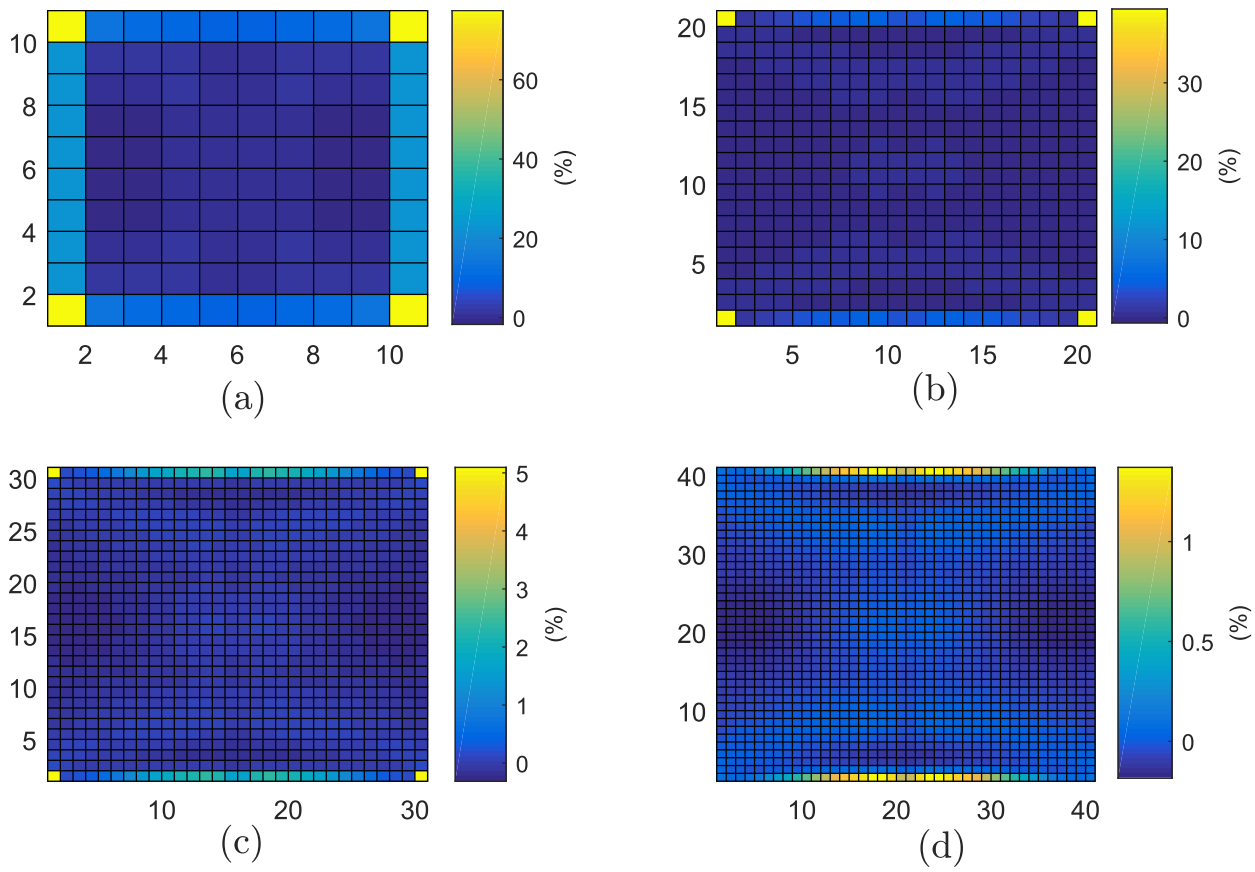

Figure 6.21: Sensitivity: nominal mass element vs relative load reduction. SS with (a) 10×10, (b) 20×20, (c) 30×30 and (d) 40×40 elements.

with imperfections. Eight cases are studied, the relative contribution (scale 0 to 1)[10] of the three eigenvectors is shown in Figure 6.23. A load vs displacement curve, measured at the middle of the straight edge, for the eight cases is presented in Figure 6.24, for the structure without cut-outs, and Figure 6.25 for the one with cut-outs. These figures show that the original panel can be considered to be less sensitive imperfections, since three different mode shapes develop depending on the combination of the modes. On the other hand, the panel with distributed holes is less sensitive; the paths are all similar and only two different modes develop.

As in the case of the CC panel, we include a third structure with a centre cut-out. The mass is the same as that of the tailored structure. A comparison of the load vs vertical displacement path is shown in Figure 6.26. Lastly, a summary of the main results of the section is presented in Table 7.8.

[10]This can be interpreted as a percentage of contribution. The maximum combined imperfection is equal to 1% of the thickness t of the panel.

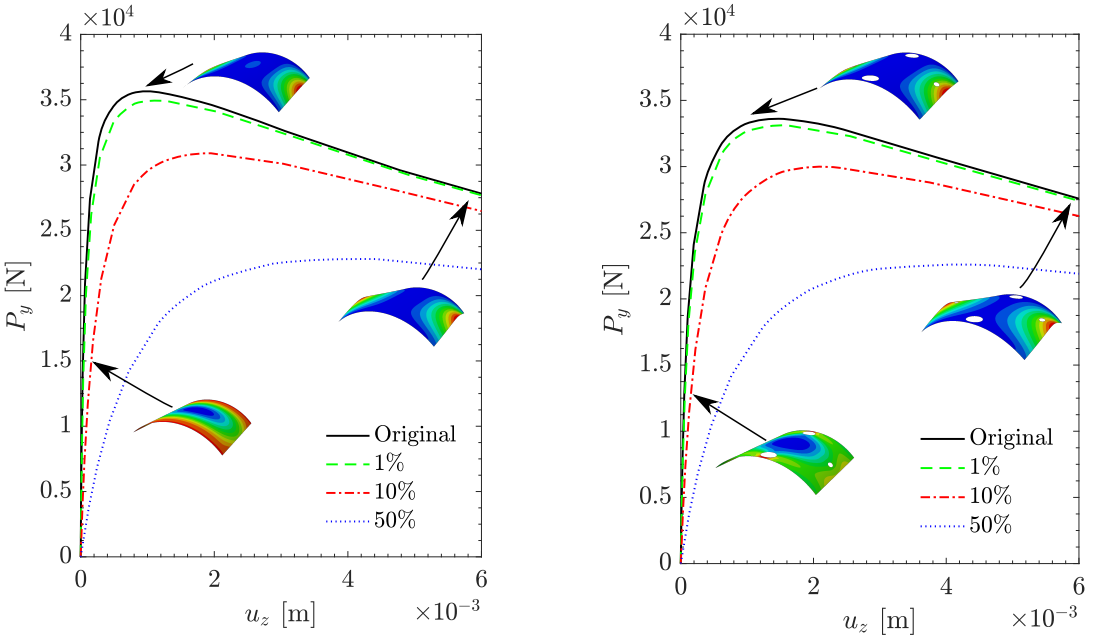

(a) Panel without cut-outs.

(b) Panel with distributed cut-outs.

Figure 6.22: Post-buckling geometrical imperfection analysis. SS panel.

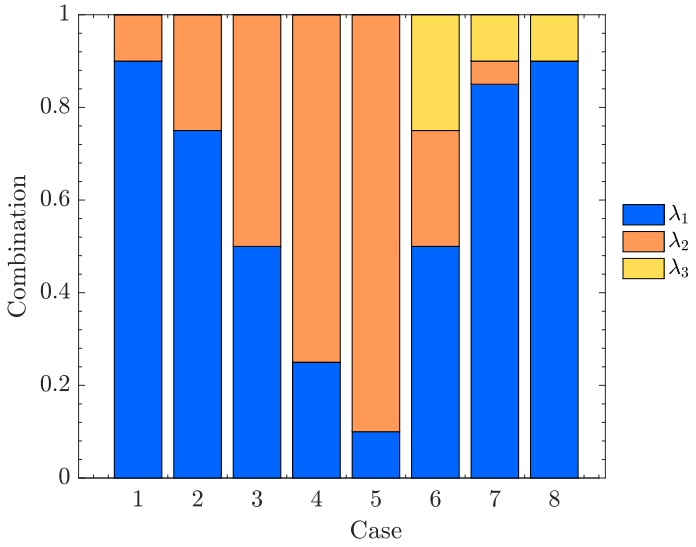

Figure 6.23: Relative combination of the first three linear eigenvectors. SS panel.

6.5 Discussion

The Localised Nominal Stiffness Method has been shown to be a simple and effective process for finding regions in a structure that are relatively insensitive to localised areas of low stiffness. The method relates locations of localised hole-like regions to a change in buckling load. It relies on a

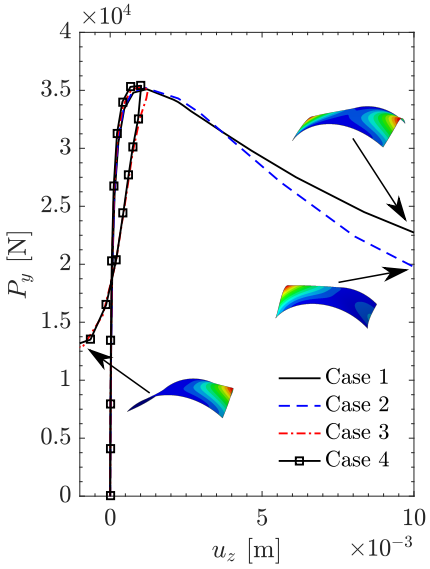

(a) Cases 1 to 4.

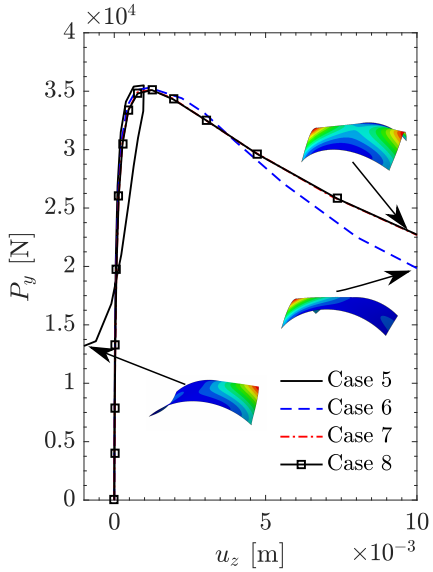

(b) Cases 5 to 8.

Figure 6.24: Load vs vertical displacement for eight geometrically imperfect cases. Panel without cut-outs.

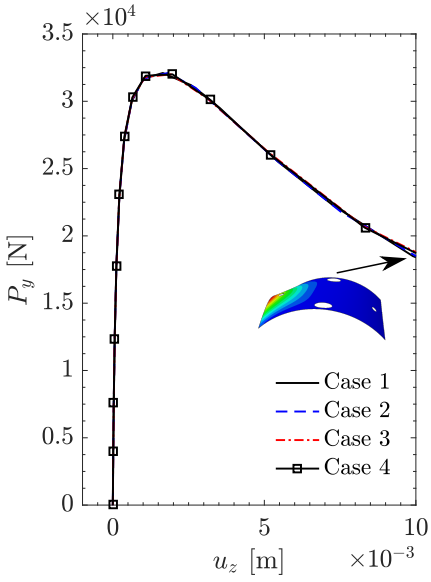

(a) Cases 1 to 4.

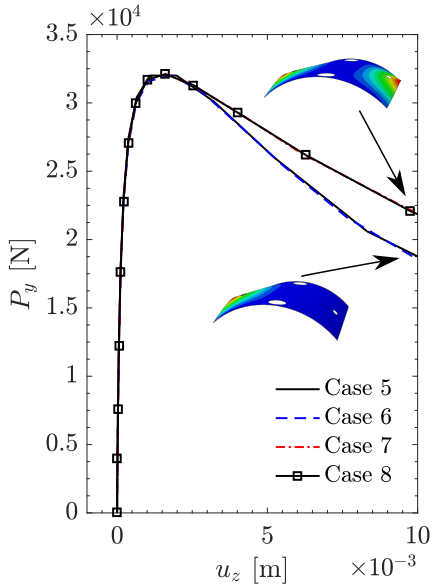

(b) Cases 5 to 8.

Figure 6.25: Load vs vertical displacement for eight geometrically imperfect cases. Panel with cut-outs.

series of linear buckling analyses where, in each run, an individual finite element is modified to have a nominal material stiffness. The method can be computationally costly if the finite element

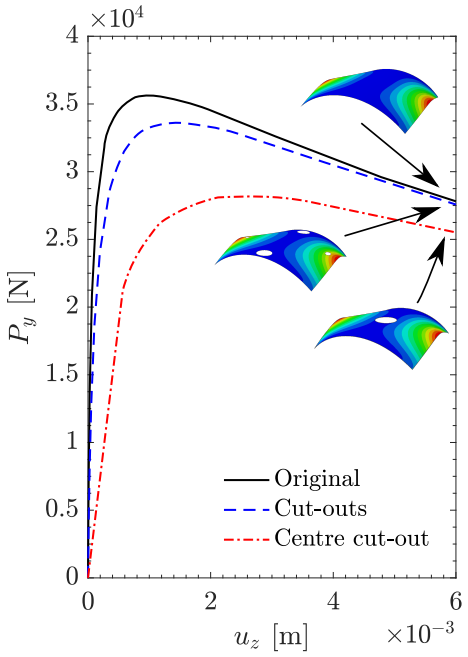

Figure 6.26: Comparison of the post-buckling path for the three SS panel geometries.

mesh is fine, which justifies the use of the computationally-efficient UF-SL Linearised Buckling Model being adopted for the iterative part of the process. Even though the method uses this particular formulation, it does not depend on it because any finite element formulation can be used.

Regarding the UF-SL model, results show that adopting this formulation does improve the efficiency of the method. For all cases, the number of operations required for inverting the system was more for the UF-SL model, nevertheless, the time to do so was less than one second for both methods. On the other hand, the number of operations for solving the eigenvalue problem was significantly less for the UF-SL model, resulting in an improvement on the total time used for the iterative part of the method.

For the cases studied it was possible to use the buckling sensitivity analysis to locate regions, within a thin-walled structure, where cut-outs had little or no effect on the buckling and post-buckling performance. For structures that behaved linearly (plate and box), the method provided the means for tailoring them such that the critical bifurcation load remains the same. For the non-linear structures (curved panels), it was possible to maintain a similar post-buckling behaviour, and in the case of the SS panel, to make the structure less imperfection sensitive to geometrical imperfections.

Results may depend on the size of the finite element mesh and boundary conditions, therefore close attention to these aspects is important. In all of the examples considered, structural weight was reduced. The final shape, locations and size of the cut-outs were ultimately decided

upon by the set-input (i.e. the skill of the designer), solely based on the result of the LNS. The solutions[11] proposed may not be unique, and possibly not optimal, but despite this relative lack of mathematical rigour, our goal of reducing weight without compromising on its buckling and post-buckling performance was achieved.

The two main advantages of the method are: (1) simple implementation, as only one parameter is changed per run; (2) removal of a single element reduces the risk of the phenomenon called *singular topology*, as long as the mesh is sufficiently fine. Results showed that a good approximation can be obtained using a relatively coarse mesh, which is desirable because many consecutive analysis have to be performed. Computational effort could be further improved if the structure, material stiffness distribution, boundary conditions and critical load are symmetric, by modelling only a representative part of the geometry.

The structures considered in this work are single-moded, i.e. only the first buckling mode and load are considered, and the iterative analysis is linear. It is also assumed that localised elements do not interact, with other localised regions.

6.6 Concluding Remarks

By using the Localised Nominal Stiffness Method it is possible to locate structural regions that are insensitive to localised low stiffness areas and relate these to the corresponding change in buckling load. By using this method it was possible to reduce the mass of a structure without affecting the buckling and post-buckling performance significantly. The mass was reduced by removing material from the areas where the sensitivity was minimal. The shape, size and dimensions of the cut-outs are ultimately chosen by the designer relying solely on the output distribution of sensitivity. The solutions presented here are most probably not strictly optimal, but they satisfy the prescribed requirement: (1) for structures that behave linearly, to reduce the mass without affecting significantly their critical bifurcation point; and (2) for non-linear structures, to achieve a similar post-buckling behaviour, and as a further gain, to make the structure less sensitive to geometrical imperfections.

The summarised results per case is as follows:

- Flat plate: mass reduction of 3% and no significant reduction of buckling load;
- Thin box with simply-supported edges: mass reduction of ~ 10% and buckling load decrease of 1%;
- Panel with clamped curved edges: mass reduction of ~ 2% and maintain a similar post-buckling behaviour;

[11] Structures with cut-outs.

- Panel with simply-supported curved edges: mass reduction of ~ 4%, maintaining a similar post-buckling behaviour and the resultant structure is less sensitive to geometrical imperfections;

Adopting the UF-SL model improved the efficiency of the iterative step, especially for the eigenvalue solver, for which the solution time was reduced significantly. Nevertheless, the proposed LNS method does not require a particular finite element implementation.

The method relies on single-moded structures, i.e. only the first buckling mode and load are considered, and on an iterative linear buckling analysis. The method presented here provides a fast and intuitive way for choosing potential areas for material removal yet caution should be applied as the skill of the designer is relied upon to use it most effectively.

The check-board patterned obtained by the present method can also be used as baseline for tailoring the *thickness* of the structure, with the aim of improving its performance, as discussed next in Chapter 7.

CHAPTER 7

EIGENSTRESS METHOD

"For since the fabric of the universe is most perfect, and is the work of a most wise Creator, nothing whatsoever takes place in the universe in which some relation of maximum and minimum does not appear."

- L. Euler

Designing a structure for buckling resistance can involve increasing the buckling load for a given structural weight, or alternatively, reducing the structural weight for a given buckling load. Both cases are of interest here. Where no analytical solution is available, iterative optimisation routines such as Gradient-based or Genetic Algorithms are widely employed. However, in the first stages of design, these methods can be complex to use and time-consuming. Moreover, at these stages, an improved, yet sub-optimal, solution may suffice. Therefore, a new intuitive method for: (1) designing topologies that improve buckling loads for a given mass; or (2) reducing structural weight via cut-outs, without affecting the critical load significantly, is proposed. The design method relies on resultant stress fields corresponding to the first eigenvector as computed by linearised buckling analyses. Herein, this quantity is referred to as an *eigenstress*. Two classical benchmark problems are investigated: a circular cross-section beam with three boundary conditions (clamped simply-supported, clamped-free and clamped-clamped) and a square flat plate with both simply-supported, and clamped edges; the final example concerns a curved thin panel with various boundary conditions. Of particular note, is that all resulting topologies enhance specific buckling strength (critical load to mass ratio), while also being manufacturable.

7.1 Aim and Motivation

One of the objectives of the present work was to identify the role of localised stiffness variations in the buckling performance of thin structures. This was one of the motivations of Chapter 6. The LNS Method provides a chessboard-like pattern that gives information on regions where the effect of local variations may be negligible. This pattern looks very familiar: it resembles a *stress* profile. Taking the first eigenvector given by the linear buckling analysis of the perfect structure (the one with out the local stiffness variation) and post-processing the stresses, it was found that one particular stress profile matched the sensitivity pattern closely: the resultant stress. Figure 7.1 shows an overlap of the patterns of sensitivity to local stiffness variations, the chessboard pattern, and the resultant stress (showing von Mises) recovered from the first eigenvector, namely, one of the eigenstresses. This was the inspiration for the Eigenstress Method. So, instead of performing many linear eigenvalue analysis (as many as elements in the mesh), as in the LNS Method, is it possible to do just *one* and get the same information?

This chapter gives evidence that this might be possible. The following points summarise the aims of this chapter:

1. To develop an intuitive and non-iterative methodology for improving the buckling performance of structures.

2. To develop a method that provides a good approximation of the optimal topology that maximises the buckling load.

3. To provide an alternative to the LNS Method.

7.2 Introduction

Topology optimisation comprises a family of algorithmic methods to determine the layout of material inside a design domain for given loads and boundary conditions. With the use of robust methodologies and high strength materials, structural designs are becoming more slender and thinner, which makes them susceptible to buckling phenomena. In recent decades, optimisation with stability constraints [139, 142–145] has found application in many fields and has proven to be a useful tool in the design of structures, mechanical parts, composite materials, trusses [146, 147] and micro-electromechanical [148] to name but a few areas. The use of optimisation routines can be computationally expensive and time consuming, which can become a bottleneck in the design process. Nevertheless, in many applications or at the first stages of design, a sub-optimal and easy-to-compute solution might be sufficient. We focus our attention in finding a fast and intuitive methodology for designing topologically enhanced structures against buckling.

The problem of finding the optimum shape of a column to give the maximum buckling load for a fixed volume was first tackled by Lagrange [149]. Weinberger and Clausen [150] solved the

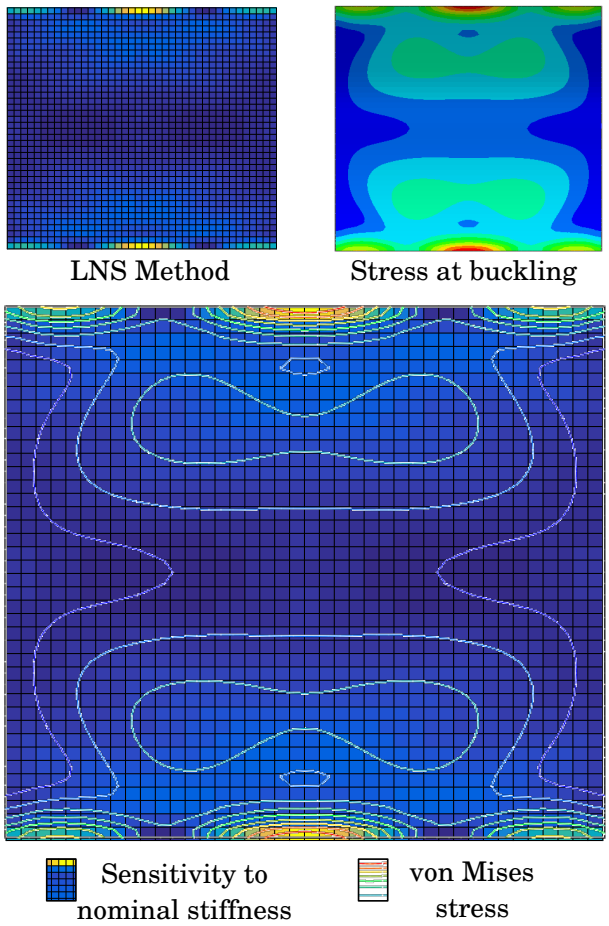

Figure 7.1: Motivation for the Eigenstress Method. Top left: Chessboard pattern of sensitivity; Top right: eigenstress pattern; Bottom: overlap of both patterns.

problem for circular cross-section simply-supported beams. More recently, Keller [151], found that the cross-sectional shape that maximises the load, for a simply-supported beam (see [151–153]), is an equilateral triangle. Tadjbakhsh and Keller [153] extended this result to other boundary conditions. Using an analytical approach based on Euler-Bernoulli (EB) beam theory, and taking into account only one eigenvector, they found an expression for the cross-sectional area in terms of its location along the length of the beam assuming clamped-clamped boundary conditions. Their solution predicts 33.3% increase in the buckling load. Olhoff and Rasmussen [154] used a variational approach to re-analyse the problem, and considered both, single and bi-modal behaviour. Their conclusion was that Keller's solution was not optimal because it introduced a new instability at a lower buckling load. Their solution predicts a marginally lower gain in buckling load, 32.6%; Olhoff's and Rasmussen's solution, however, is also non-optimal, because other columns exist with the same mass, but different geometries [154], that carry higher buckling loads. Bi-modal solutions were also studied by Seyranian and Privolona [155, 156], Masur [157] and Seyranian and Olhoff [158] among others. Szyszkowski and Watson [159], who worked on

single buckling mode columns, proposed an iterative method, based on minimum bending energy, to optimise the buckling load, which results in a gain of 25.2%. Manickarajah et al. [160] used an iterative Finite Element Method (FEM) that gradually shifts material from the stiffest to the most flexible part while keeping the weight constant. Their conclusions were similar in content to that of Olhoff and Rasmussen. Maalawi [161] tackled the problem of finding the topology that maximises the buckling load of a structure which can be *practically manufactured*. He proposed an analytical approach for segmented beams. The reported increase in buckling load was 29.4%. In this work we propose a fast and intuitive methodology for designing enhanced structures against buckling. We benchmark our results against optimal designs by Tadjbakhsh & Keller, Olhoff & Rasmussen and Maalawi.

For the case of the plate the problem is more complex. Several authors have proposed different strategies. Spillers and Levy [162] proposed a method based on Keller's classical solution. Using an analytical variational approach they derived an optimality condition which relates topology to strain energy density. Their solutions feature thickness distributions, which result in local buckling and reduced load-carrying capacity. Pandey and Sherbourne [163] re-analysed Levy's plate using a Rayleigh-Ritz method with Fourier series, and proposed a different thickness distribution which increases the buckling load by 28.4% for a simply-supported plate, and by 204% for a plate with all edges clamped. Later, Levy and Sokolinsky [164], using an iterative Rayleigh-Ritz method, provided two possible thickness distributions: one based on a double cosine distribution, with a 23.4% increase, and a hybrid double sine symmetric plate, with an increase of 32.3%. Manickarajah et al. [10] used an Evolutionary Structural Optimisation method (ESO) and obtained a topology that increases the buckling load by 37% for a simply supported plate and 86% for the clamped case. Here, we compare our results with those of Levy & Sokolinsky, Pandey & Sherbourne and Manickarajah et al..

Many engineering applications require lightweight structures with a certain buckling performance, mainly in terms of critical load. Therefore, it seems sensible to reduce mass by removing material where it is less needed (i.e. where it is less stressed). One simple way of doing this is to introduce cut-outs. Cut-outs may also be desirable for other reasons, e.g. water drainage, access or holes for fasteners. However, the introduction of cut-outs may inadvertently result in an undesirable decrease in buckling resistance. The effect on buckling performance of cut-outs on plates subject to axial loading has been widely studied and documented [141, 165, 166].

In recent years topological design with stability criteria has become an important part of the design process of lightweight structures, especially in aerospace, automotive and wind energy industries. Preventing buckling of these complex structures requires a combination in many strategies. Take for instance a wind turbine blade made of composite materials. Its performance can be improved by changing its topology [167], but also by optimising its material properties. Relatively complex optimisation techniques can be developed and adapted for this purpose [168–170]. However, topology optimisation problems with stability constraints are difficult to solve.

For some simple cases analytical solutions are available, but for more complex cases, which can still be relatively simple, iterative numerical techniques are usually employed. These techniques, which are commonly based on FEM, can be computationally expensive since the process requires the solution of two analyses (static and eigenvalue analysis) at each optimisation step.

The problem of designing a structure topologically for buckling resistance may be defined either as finding the maximum value of the buckling load for a given structural weight, or alternatively, as minimising structural weight maintaining a certain buckling load. Herein, we propose an alternative and intuitive method, based on the resultant stresses recovered from the displacement eigenvector obtained from a linear buckling analysis, to design an enhanced structure against buckling. Henceforth, these stresses are referred to as *eigenstresses*. When improving the buckling capability, the method produces a sub-optimal geometry whose topology closely resembles that of the optimum shape for all cases we have examined so far, even though the topologies obtained do not necessarily maximise the buckling load in the mathematically formal sense, they tend to perform within a few percents of the optimal values. The consistency of these results gives credence to the viability and usefulness of the Eigenstress Method, for design purposes. When reducing the structural weight, the model provides a good indication of the regions where mass can be removed by introducing cut-outs. The resulting buckling performance of the structure with cut-outs is similar to that of the original.

In order to benchmark our approach, we compare our solutions with analytical results in the literature. Three different geometries are considered: a circular cross-section beam, a flat square plate and a curved panel. In so doing, we demonstrate that our method provides a relatively simple topology design strategy to enhance the buckling performance of a structure.

The remainder of chapter is divided into four sections. Section 7.3 explains the concept of eigenstresses and their use in topological design. Several case studies are then presented in Section 7.4: a circular cross-section beam, a flat plate and a curved panel with different boundary conditions. Results are discussed in Section 7.5, while concluding remarks are given in Section 7.6.

7.3 Eigenstress Method

Bochenek & Tajs-Zielińska [171] found that, for the case of a column, the topology that maximises the buckling load given a mass has the property of making the maximum bending stress (at buckling) constant along the axis (see Taylor and Liu [172]). They translated the topology optimisation problem with an instability criteria to a minimum compliance problem (stress based) [173] by means of an equivalent moment distribution [156]. This suggests that the rigidity of the structure is such that it redistributes the load accordingly. Therefore, a redistribution of the *material* may increase the buckling resistance, as long as it is located in the correct regions. For doing this, it is necessary to identify the proper locations where mass can be reduced and those where it can be added. Our hypothesis is that it is possible to approximate these locations

by means of the resultant stresses recovered from the displacements of the buckled structure. That is, only one[1] linear buckling analysis (i.e. the eigenvector) is needed to approximate a new topology that improves the buckling performance with a given structural weight.

The main idea is to use the normalised resultant stress recovered from the first eigenvector[2] of the *original* structure (e.g. prismatic beam or flat plate) as an approximation of the rigidity distribution of the enhanced geometry. Consider the eigenvalue problem

$$(\boldsymbol{K} + \lambda_i \boldsymbol{K}_{\mathrm{G}})\,\boldsymbol{v}_i = \boldsymbol{0}, \tag{7.1}$$

where the symbols $\boldsymbol{K}$, $\boldsymbol{K}_{\mathrm{G}}$, λ_i and $\boldsymbol{v}_i$ denote the stiffness and geometric operators, the ith eigenvalue, and the corresponding eigenvector, respectively. The expressions for $\boldsymbol{K}$, $\boldsymbol{K}_{\mathrm{G}}$ and $\boldsymbol{v}_i$ depend on how the problem is modelled. In finite element analyses, the operators are written as matrices and the eigenvectors represents nodal displacements. For analytical approaches, $\boldsymbol{K}$ and $\boldsymbol{K}_{\mathrm{G}}$ are differential operators, whilst the eigenvector is a real function. Examples for both cases are provided. Buckling is associated with critical value of the load factors. In particular, buckling occurs at the onset of instability corresponding to the smallest eigenvalue λ. The associated eigenvector $\boldsymbol{v}$ gives the shape of the buckled structure up to a multiplicative constant, therefore its magnitude is meaningless. This eigenvector can be used to compute strains using the differential relation

$$\boldsymbol{e} = \mathscr{B}\boldsymbol{v}, \tag{7.2}$$

where

$$\mathscr{B} = \begin{bmatrix} \frac{\partial}{\partial x} & 0 & 0 \\ 0 & \frac{\partial}{\partial y} & 0 \\ 0 & 0 & \frac{\partial}{\partial z} \\ 0 & \frac{\partial}{\partial z} & \frac{\partial}{\partial y} \\ \frac{\partial}{\partial z} & 0 & \frac{\partial}{\partial x} \\ \frac{\partial}{\partial y} & \frac{\partial}{\partial x} & 0 \end{bmatrix}.$$

Using Hooke's law and the material's stiffness matrix $\boldsymbol{C}$, the six components of the Cauchy stress tensor

$$\boldsymbol{\sigma} = \left\{\sigma_{xx}, \sigma_{yy}, \sigma_{zz}, \tau_{yz}, \tau_{zx}, \tau_{xy}\right\}^{\mathrm{T}},$$

are computed using the relation

$$\boldsymbol{\sigma} = \boldsymbol{C}\boldsymbol{e}. \tag{7.3}$$

Since the stresses $\boldsymbol{\sigma}$ are computed using the eigenvector $\boldsymbol{v}$, their magnitude is meaningless as well. Therefore, from this point onwards we distinguish between *stresses*, which refer to *true* physical

[1] or only a few, as it is explained in the examples.

[2] Our method is related to that of Bochenek & Tajs-Zielińska [171], who used the first eigenvector to find an equivalent moment distribution in a beam and employed an optimisation routine. Nevertheless, our methodology is different, since the stress recovered from the buckling mode is used directly to find an enhanced topology without any optimisation method. We applied this on beams, plates and panels.

stresses, and *eigenstresses* which refer to the stresses of the buckled structure recovered from the eigenvectors. With the components of $\boldsymbol{\sigma}$ a scalar resultant[3] normalised eigenstress distribution $\hat{\sigma}$ can be computed. This can be used as an approximation of the (normalised) distribution of the structure's rigidity D

$$\hat{\sigma} \propto D \tag{7.4}$$

With this profile it is possible to recover the area (or thickness) distribution, i.e. the topology, and by setting a proper scaling, to fix desired volume. The approach taken in this work is to choose the eigenstresses because it provides an idea on how the stress will be redistributed at buckling. Nevertheless, other approaches like taking the *eigen-strains*, or a combination of these, might also be appropriate. The process is now explained in more detail for the case of a beam and a plate.

7.3.1 Beam Case

The equilibrium of the beam is described by the boundary value problem [4, 54]

$$\frac{d^2}{dx^2}\left(EI\frac{d^2v}{dx^2}\right)+P\frac{d^2v}{dx^2}=0 \tag{7.5}$$

where v, I, E, x and P are the, vertical displacements, second moment of area, Young's modulus, axial coordinate and applied axial force respectively. In here we study three different boundary conditions: clamped edges (CC), clamped-free (CF) and clamped-hinged (CH). For the sake of brevity we do not include the boundary conditions related to equation (7.5), these can be found in [4, 54].

Equation (7.5) shows that buckling of a beam is governed entirely by the flexural rigidity EI, and if the material is isotropic, by the second moment of area. If we consider structures whose second moment of area satisfies[4] $I \propto A^2$ then equation (7.4) is equivalent to

$$\hat{\sigma} \propto A^2 \tag{7.6}$$

where the proportionality factor is chosen such that the volume of the structure is kept constant as is explained further in this section. This distribution represents a normalised approximation of the desired axial distribution of areas along the beam axis. I.e. the material has to be redistributed to satisfy this area profile and doing so will improve the buckling performance keeping the same volume.

[3]This is explained in more detail further in this section. The expressions for resultant stress are slightly different for the case of a beam or a plate.

[4]There is a strong theoretical basis for this relation, which, when written as a ratio, becomes Ashby's shape factor for structural efficiency. Ashby [174] and then Weaver and Ashby [175] showed that this ratio directly governed structural efficiency.

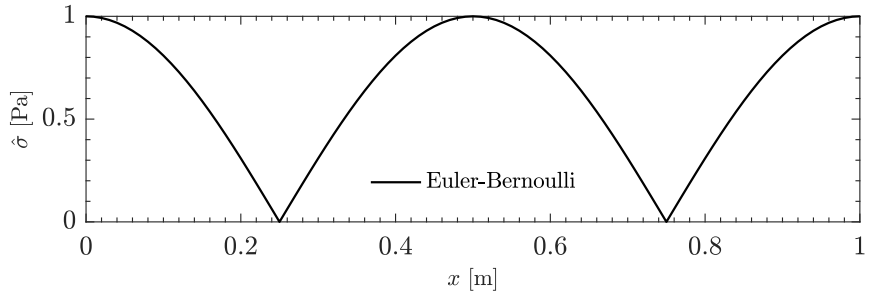

Figure 7.2: Maximum eigenstress distribution. CC beam.

Clamped-clamped beam For the case of clamped edges (CC) the solution to equation (7.5), if EI is constant, is given by [54]

$$v(x) = c\left[1 - \cos\left(\frac{2\pi x}{L}\right)\right], \tag{7.7}$$

which represents the buckling shape and where c is an arbitrary constant. The corresponding buckling load is given by $P_{\text{cr}} = 4\pi^2 EI/L^2$, with L the length of the beam. The maximum axial eigenstress is derived to be [54]

$$\begin{aligned} \sigma_x &= -zE\frac{d^2v}{dx^2} \\ &= -zEc\left(\frac{2\pi}{L}\right)^2 \cos\left(\frac{2\pi x}{L}\right), \end{aligned} \tag{7.8}$$

from which the normalised resultant eigenstress distribution is defined as

$$\hat{\sigma} = \left|\cos\left(\frac{2\pi x}{L}\right)\right|. \tag{7.9}$$

Figure 7.2 shows a plot of equation (7.9). Using relation (7.6) the axial distribution of areas is given by $A(x) = c\hat{\sigma}$, with c a proportionality factor. If the volume of the beam is set to V_{o}, then the following relation should be satisfied

$$\int_0^L A(x)\,dx = \int_0^L c\sqrt{\hat{\sigma}}\,dx = V_{\text{o}}. \tag{7.10}$$

Solving the elliptic integral numerically the area distribution takes the form:

$$A(x) = \frac{2\pi V_{\text{o}}}{\gamma_{\text{o}} L}\sqrt{\hat{\sigma}}, \tag{7.11}$$

with[5] $\gamma_{\text{o}} = 4.79256$.

The axial area distribution given by equation (7.11) is not physically correct, since at two points it takes the value of zero (see Figure 7.2). To avoid null area, we define a new area distribution as the linear map

$$A(x) = (A_{\max} - A_{\min})\sqrt{\hat{\sigma}} + A_{\min}, \tag{7.12}$$

[5]At least four significant figures are needed for getting the correct volume.

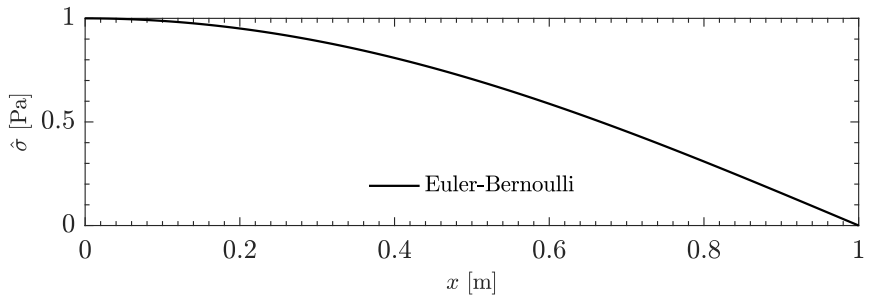

Figure 7.3: Maximum eigenstress distribution. CF beam.

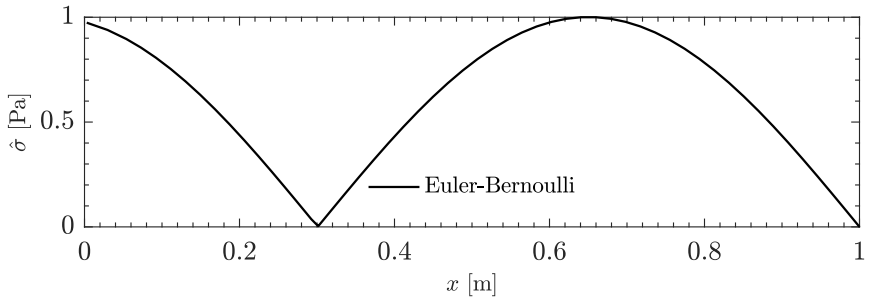

Figure 7.4: Maximum eigenstress distribution. CH beam.

where $A_{\min}$ and $A_{\max}$ are minimum and maximum allowed areas. In order to keep the volume constant these areas should satisfy[6]

$$A_{\max} = \frac{2\pi V_o}{\gamma_o L} + \left(1 + \frac{2\pi}{\gamma_o}\right) A_{\min}. \tag{7.13}$$

Clamped-free beam For clamped-free (CF) boundary conditions the solution to equation (7.5) is given by [54]

$$v(x) = c\left[1 - \cos\left(\frac{\pi x}{2L}\right)\right], \tag{7.14}$$

and the maximum normalised resultant stress (using equation (7.8)) is

$$\hat{\sigma} = \cos\left(\frac{\pi x}{2L}\right). \tag{7.15}$$

A plot of the latter is shown in Figure 7.3. The axial area distribution is given by equation (7.11) with $\gamma_o = 1.1981$ and using equation (7.15).

Clamped-hinged beam For clamped-hinged (CH) boundary conditions the solution to equation (7.5) is given by [54]

$$v(x) = c\left[\sin\left(\frac{kx}{L}\right) - k\cos\left(\frac{kx}{L}\right) - kx + k\right], \tag{7.16}$$

[6] the following expression is deduced using a similar procedure as the one for equation (7.10).

with $k = 4.493$, and the maximum normalised resultant stress (using equation (7.8)) is

$$\hat{\sigma} = \frac{1}{\sigma_{\max}} \left(k^3 \cos\left(\frac{kx}{L}\right) - k^2 \sin\left(\frac{kx}{L}\right) \right), \tag{7.17}$$

$\sigma_{\max} = 92.8610$, Figure 7.4. The area profile is given by

$$A(x) = c\sqrt{\hat{\sigma}}, \tag{7.18}$$

with $c = \frac{V_o k \sqrt{\sigma_{\max}}}{\gamma o L}$, $\gamma o = 9.6364$.

7.3.2 Plate Case

A similar idea applies to the case of a plate, the eigenstress is used to redistribute material and improve the buckling performance. The normalised resultant eigenstress $\hat{\sigma}$ is taken as proportional to the rigidity of the structure. The rigidity of a plate is proportional to the cube of the thickness $D \propto t^3$, therefore we propose a slightly different relation based on the eigenstress:

$$t \propto \hat{\sigma}^{\frac{n}{3}}, \tag{7.19}$$

with $n = 1,2,3$ or 4. Ashby and Weaver [175] found a similar expression to equation (7.19), but with $n = \frac{3}{2}$, and showed that it is directly related to buckling resistance efficiency. All of these cases are studied in Section 7.4. In order to avoid potential zero thickness the following distribution is used:

$$t(x,y) = (t_{\max} - t_{\min})\hat{\sigma}^{\frac{n}{3}} + t_{\min}, \tag{7.20}$$

with $t_{\max}$ and $t_{\min}$ maximum and minimum allowed thickness's respectively. In order to keep the volume constant these should satisfy[7]

$$t_{\max} = \frac{t_o ab}{q} - \frac{t_{\min}}{q}(ab - q), \tag{7.21}$$

with t_o the original thickness, a and b the width and height of the plate and $q = \int_0^b \int_0^a \hat{\sigma}^{\frac{n}{3}}\, dxdy$. Note, take the maximum resultant eigenstress as the normalised von Mises[8] stress computed as follows[9]:

$$\hat{\sigma} = \frac{1}{\sigma^{\max}} \sqrt{\frac{3}{2}\sigma_{ij}\sigma_{ij} - \frac{1}{2}(\sigma_{kk})^2}, \tag{7.22}$$

where σ_{ij} are the components of (7.3) and $\sigma^{\max}$ is a number such that the maximum of $\hat{\sigma}$ is 1.

[7] From the relation $\int\int t(x,y)\,dxdy = V_o$.

[8] Here we are taking the von Mises as an estimate of the total resultant stress, this is not a mandatory requirement as other metrics might be also used.

[9] Einstein's summation convention is implied.

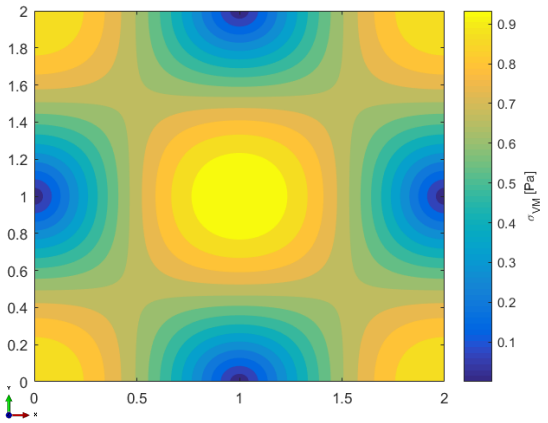

Figure 7.5: Reultant eigenstress distribution ($n = 3$, equivalent to von Mises). Plate SSSS.

Simply-supported plate For the case of an isotropic plate with all of its edges simply-supported and uniaxially compressed, the corresponding eigenstresses are [54] (at $z = t_o/2$):

$$\begin{aligned}
\sigma_{xx} &= \frac{\alpha c}{(1-\nu)} \sin\left(\frac{\pi x}{a}\right) \sin\left(\frac{\pi y}{b}\right) \\
\sigma_{yy} &= \frac{\alpha c}{(1-\nu)} \sin\left(\frac{\pi x}{a}\right) \sin\left(\frac{\pi y}{b}\right) \\
\sigma_{xy} &= \frac{\alpha c}{2(1+\nu)} \cos\left(\frac{\pi x}{a}\right) \cos\left(\frac{\pi y}{b}\right)
\end{aligned} \tag{7.23}$$

with $\alpha = E t_o \pi^2 / 2ab$, E the Young's modulus. It then follows that

$$\begin{aligned}
\hat{\sigma} = \Bigg[&\sin^2\left(\frac{\pi x}{a}\right) \sin^2\left(\frac{\pi y}{b}\right) \\
&+3\left(\frac{1-\nu}{1+\nu}\right)^2 \cos^2\left(\frac{\pi x}{a}\right) \cos^2\left(\frac{\pi y}{b}\right) \Bigg]^{\frac{1}{2}},
\end{aligned} \tag{7.24}$$

whose distribution is shown in Figure 7.5, i.e. $n = 3$. Figure 7.6 shows a schematic summary of the main rationale of the method.

7.4 Examples

This section demonstrates the Eigenstress Method through a series of examples. In the examples, the topology of the structures under consideration is altered to improve their specific buckling strength, i.e. the buckling load per unit mass, by: (a) increasing the critical load keeping weight approximatively constant; or, alternatively, reducing mass maintaining the critical load within 1% of the original one. Three geometries, with different boundary conditions, are used as test cases. In all the analyses, the response is taken as single-modal[10], only the first critical load and the corresponding eigenvalue and eigenvector are considered.

[10] i.e. that the second buckling mode occurs at a much higher buckling load than the first, such that the likelihood of modal interaction is remote and, therefore, buckling is governed by the first mode.

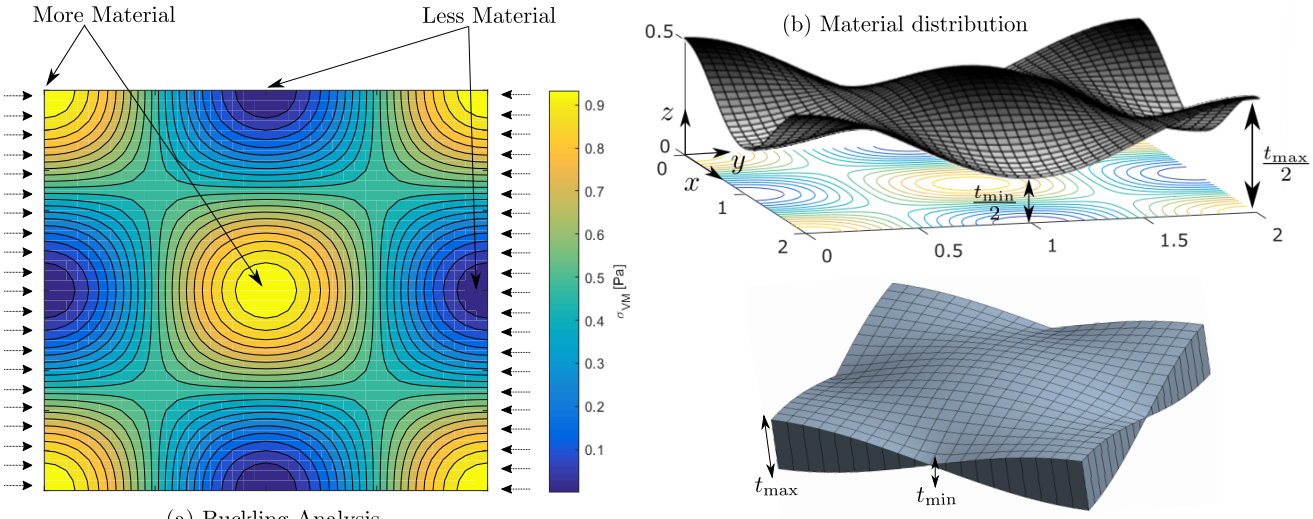

(a) Buckling Analysis
von Mises eigentress

(c) Final geometry

Figure 7.6: Exemplification of the Eigenstress Method steps for the case of a plate. Showing $n = 3$.

7.4.1 Circular Cross-Section Beam. Clamped-Clamped (CC).

Let us consider a circular cross-section beam of Figure 7.7. The beam is compressed axially by a unit force, P_y. One end is clamped, while the other one is free to move longitudinally[11]. The constituent material is isotropic with Young's modulus $E = 71$ GPa and Poisson's ratio $\nu = 0.33$.

Figure 7.2 shows the normalised maximum eigenstress as computed analytically. As explained previously, it is hypothesised that this distribution gives an approximation of the second moment of area of the column that maximises the buckling performance. That is, the mass has to be redistributed from the areas where the eigenstress is minimum, to those where it is maximum. The square root of equation (7.9) provides a distribution of the cross-section areas, i.e. the topology, of the beam that increases the buckling performance. As explained in Section 7.3, for the CC case the eigenstress method gives an optimal area distribution that is not physically possible, since it takes the value of zero at two locations. We name this case as Eig. 1; for this reason, an alternative area distribution is given by equation (7.12), we called this case Eig. 2. Figure 7.8 shows the result for the normalised area distribution given by the present method. Solutions from Tadjbakhsh & Keller's [153] and Olhoff & Rasmussen's [154] are given for comparison purposes. Results show that Eig. 1 coincides with Keller's and that Eig 2 result is close to the one by Olhoff's.

For the particular dimensions and geometry considered here, and taking as reference the area profile, the radii distribution along the axial direction is easily derived. Figure 7.9 shows the radii

[11]The free edge remains flat and is not allowed to rotate.

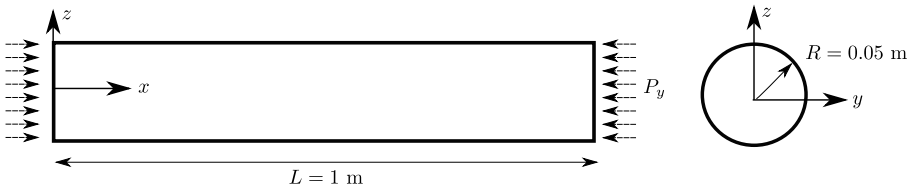

Figure 7.7: Geometry of the circular cross-section beam

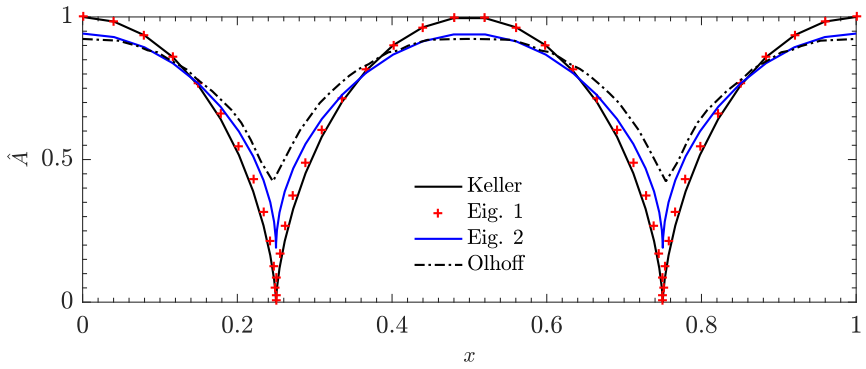

Figure 7.8: Normalised area distribution. CC beam.

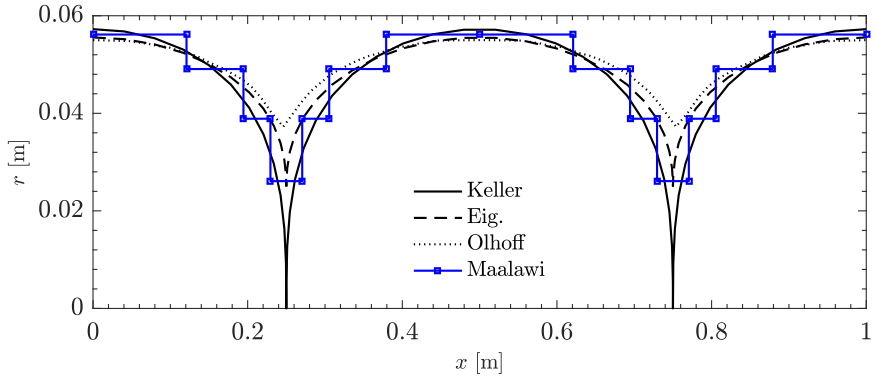

Figure 7.9: Radii distribution. CC beam.

distribution given by the eigenstress method for the case of non-zero areas. Reference results derived from [153, 154, 161] are also provided. The proposed geometry is shown in Figure 7.10.

Figure 7.10: Proposed geometry. CC beam.

The performance of the new geometry is assessed and compared with known results. The

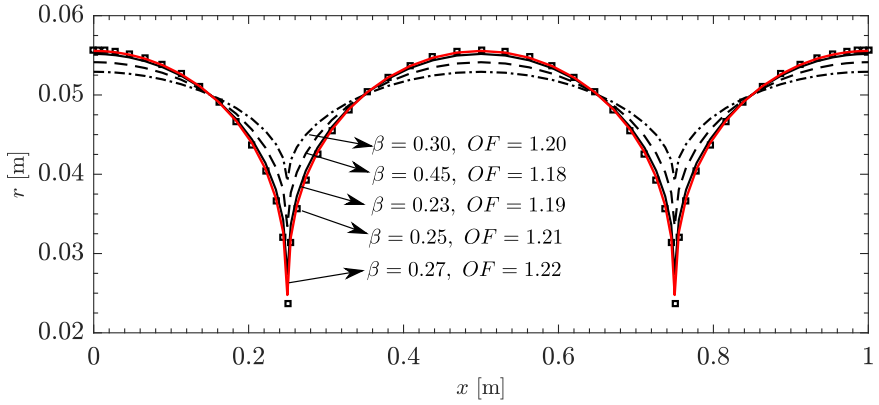

Figure 7.11: Optimal Factors for different radius distributions. CC beam.

critical buckling load of the new structure, λ, is compared quantitatively against the critical load (first buckling load) of the original structure, λ_o, by defining an *Optimality Factor* (OF) as

$$OF = \frac{\lambda}{\lambda_o}. \tag{7.25}$$

[154] and [160] have demonstrated that, if only one eigenvector is considered, then the optimum distribution of cross-sections can be found if the parameter $\beta = A_{\min}L/V_o$, where V_o is the original volume, is in the range $0.28 \leq \beta \leq 1$. This parameter relating the beam's minimum cross-section with its length and volume can then be used to inform our choice of $A_{\min}$ and $A_{\max}$, such that equation (7.13) is satisfied. Buckling loads were computed using an `ABAQUS` solid model with 68800 `C3D8R` elements. Figure 7.11 shows the OFs for five different geometries.

The case $\beta = 0.27$ ($A_{\min} = 0.00193$ and $A_{\max} = 0.0097$ m^2) gives as result a buckling load of 1.60×10^7 N, which represents a Optimality Factor of $OF = 1.22$. The first four buckling eigenvectors are shown in Figure 7.12.

Table 7.1 resumes the results for our best case and other reference results. We can see from here that our method does improve the buckling load by 22%, and it is close to the solution given by Maalawi [161].

7.4.2 Circular Cross-Section Beam. Clamped-Free (CF).

Consider the same original geometry and dimensions described in the previous section. Different boundary conditions are considered for this case: clamped-free. Figure 7.3 shows the normalised resultant eigenstress for this case. As discussed previously, this is used (its square root) to compute the area distribution. Figure 7.13 shows the normalised area profile using our method, results for the theoretical maximum (Tadjbakhsh & Keller [153]) and from Zhang et. al. [176] are also provided.

The radii axial distribution can be found from the area profile easily, the result is shown in Figure 7.14. This distribution satisfies equation (7.10), that is the volume of the structure

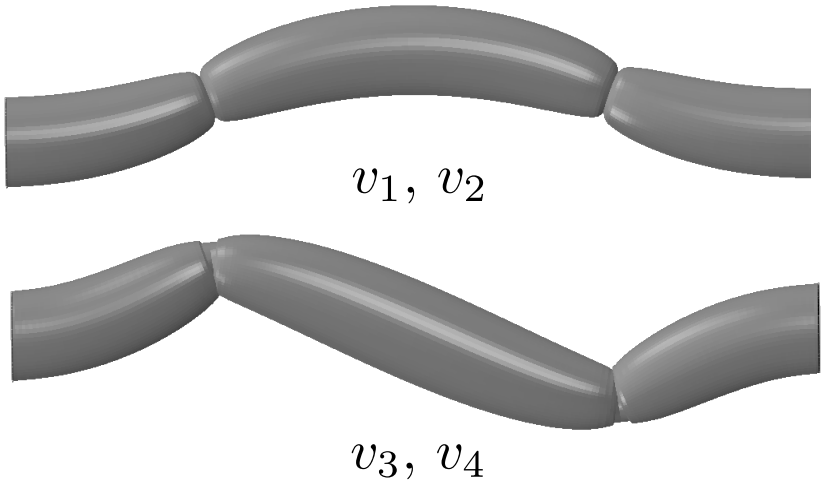

Figure 7.12: First four buckling shapes corresponding to the loads: $\lambda_1 = \lambda_2 = 1.60 \times 10^6$ N and $\lambda_3 = \lambda_4 = 1.63 \times 10^6$ N.

Table 7.1: Buckling load and Optimality Factor for CC beam.

	λ	OF
	[N] $\times 10^6$	[-]
Method		
Prismatic	1.32	1.00
Eigenstress	1.60	1.22
Keller et. al.	1.76	1.33
Olhoff et. al.	1.76	1.33
Maalawi	1.70	1.29

is kept constant. This shows that our method provides an area distribution very close to that of the theoretical maximum (Keller's results), except for a region close to the tip. The proposed geometry can bee seen in Figure 7.15.

The buckling behaviour is analysed using an ABAQUS FEM model is used to compute the first four buckling modes and loads. The shape of the first four modes is shown in Figure 7.16. Table 7.2 summarises the buckling loads and Optimality Factor for the cases presented. This shows that the proposed geometry improves the buckling performance (31%) almost to the theoretical maximum of 33%.

7.4.3 Circular Cross-Section Beam. Clamped-Hinged (CH).

The same procedure is repeated for the case of clamped-hinged beam. The same dimensions, material and original geometry are used. From the resultant eigenstress distribution, Figure (7.3), the normalised area profile is given, shown in Figure 7.17. For the particular geometry, i.e.

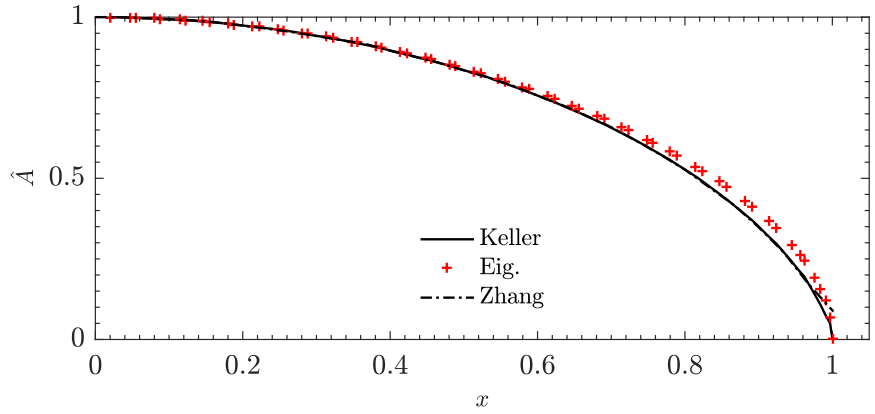

Figure 7.13: Normalised area distribution. CF beam.

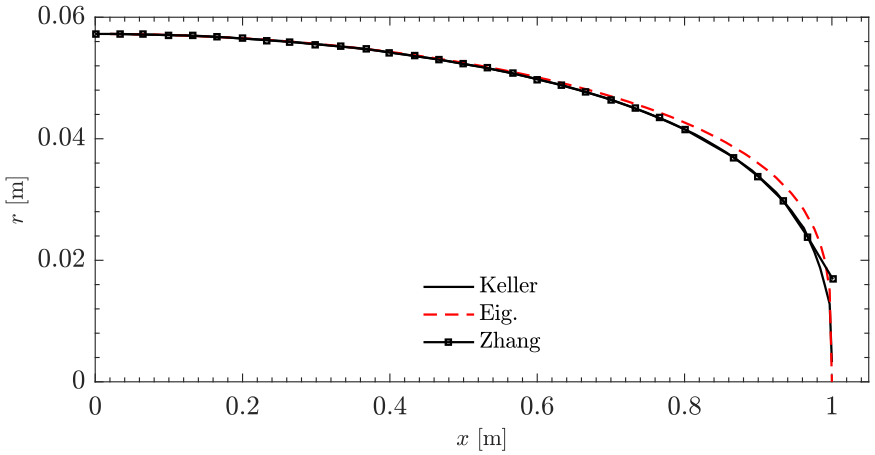

Figure 7.14: Radii distribution. CF beam.

Figure 7.15: Proposed geometry. CF beam.

circular beam, the axial distribution of the radii can be easily computed, shown in Figure 7.18. The theoretical maximum, computed from Keller's result, is also provided as reference. We can see from here that the distribution is similar, except for a difference close to 25% of the beam's length. The proposed geometry that improves the buckling performance with a given volume (i.e. satisfies equation (7.10)) is shown in Figure 7.19.

To assess the viability of this structure an ABAQUS FEM model is used to compute the first four buckling modes and loads. The shape of the first four modes is shown in Figure 7.20. Table 7.3 summarises the buckling loads and optimality factor for the cases presented. The improvement

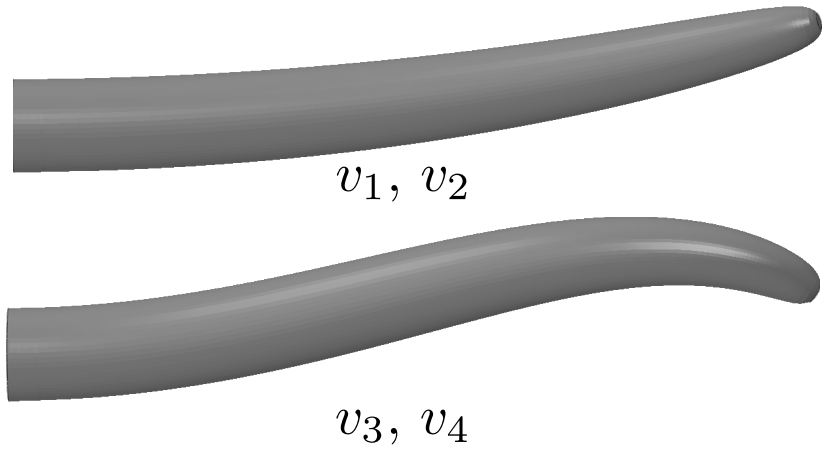

Figure 7.16: First four buckling shapes corresponding to the loads: $\lambda_1 = \lambda_2 = 1.13 \times 10^6$ N and $\lambda_3 = \lambda_4 = 5.96 \times 10^6$ N.

Table 7.2: Buckling load and Optimality Factor for CF beam.

	λ [N] $\times 10^5$	OF [-]
Method		
Prismatic	8.56	1.00
Eigenstress	11.25	1.31
Keller et. al.	11.39	1.33
Zhang et. al.	11.39	1.33

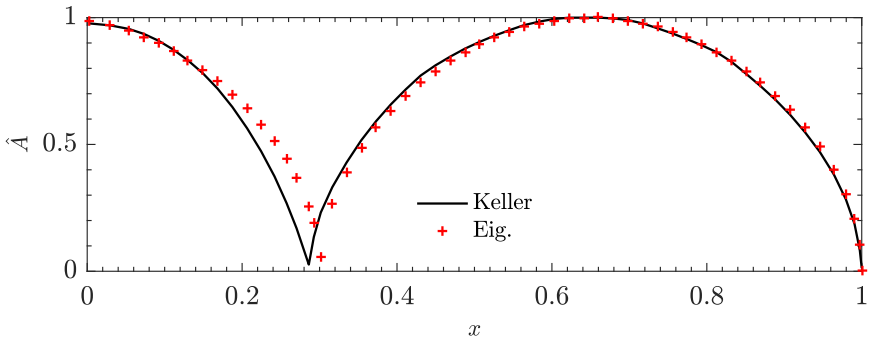

Figure 7.17: Normalised area distribution. CH beam.

in buckling load is around 24%.

7.4.4 Simply-Supported Square Plate

The next case is a flat square plate with sides of length $a = b = 2$ m and thickness $t_o = 0.015$ m. The geometry is shown in Figure 7.21. The Young's modulus is $E = 200$ GPa, with Poisson's ratio

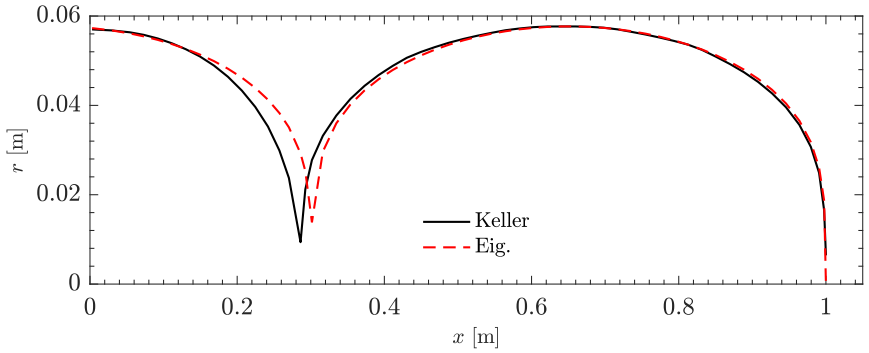

Figure 7.18: Radii distribution. CH beam.

Figure 7.19: Proposed geometry. CH beam.

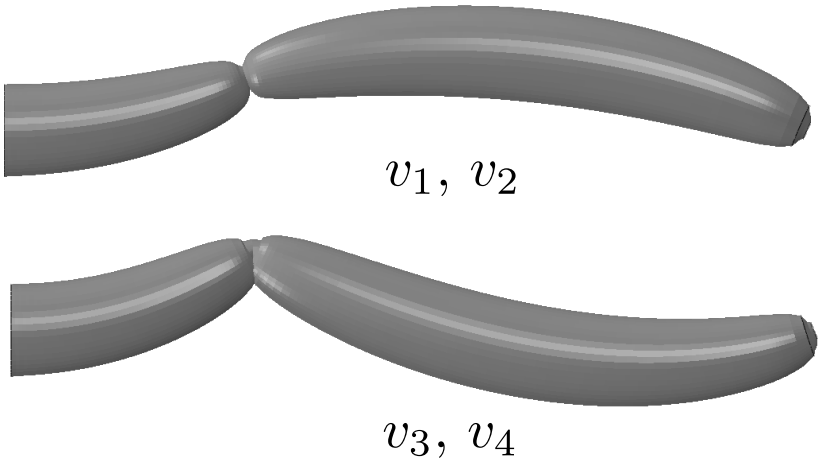

Figure 7.20: First four buckling shapes corresponding to the loads: $\lambda_1 = \lambda_2 = 8.48 \times 10^6$ N and $\lambda_3 = \lambda_4 = 10.0 \times 10^6$ N.

$\nu = 0.3$. All edges are simply-supported[12] (SSSS) and the plate is compressed uni-axially in the x direction by a force per unit length, N_x, of 0.015 N/m the x direction.

As explained in Section 7.3, a power $(n/3)$ of the resultant eigenstress is taken as proportional to the cube of the plate thickness. Four cases are studied here: $n = 1, 2, 3$ and 4. For each case, a sample set of combinations of[13] $t_{\min}/t_{\max} \in [0, 1]$, which satisfies equation (7.21) (i.e. constant volume) is taken. Optimality factor for each sample point is given. For the best $t_{\min}/t_{\max}$, four eigenvalues and eigenvectors are computed.

[12] i.e. all edges are restricted out of plane, in-plane movement and rotations are allowed
[13] i.e. minimum thickness is varied from $t_{\min} = 0$ to $t_{\min} = t_{\max}$

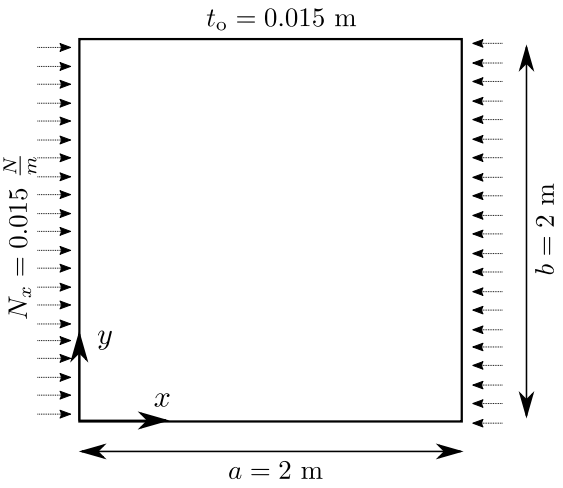

Figure 7.21: Geometry of flat plate.

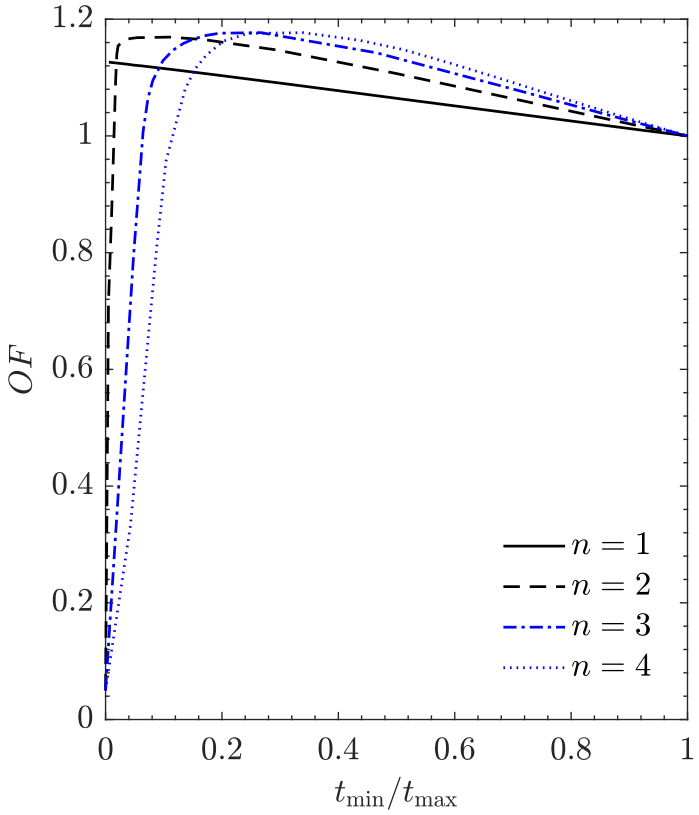

Figure 7.22: OF vs $t_{\max}/t_{\min}$ for SSSS plate.

Table 7.3: Buckling load and Optimality Factor for CH beam.

	λ [N] $\times 10^6$	OF [-]
Method		
Prismatic	6.86	1.00
Eigenstress	8.48	1.24
Keller et. al.	9.12	1.33

Table 7.4: First four buckling loads and Optimality Factor for the best case per n. SSSS plate.

	$t_{\min}/t_{\max}$ [-]	λ_1 N/m $\times 10^5$	λ_2 N/m $\times 10^5$	λ_3 N/m $\times 10^5$	λ_4 N/m $\times 10^5$	OF [-]
n						
1	0.01	6.83	9.43	16.20	23.40	1.13
2	0.11	7.09	8.81	14.10	20.00	1.17
3	0.27	7.13	8.67	14.30	21.00	1.18
4	0.44	7.07	8.93	15.40	23.70	1.17

Structural performance is assessed using an `ABAQUS` shell model with 40000 `S4R` elements. Figure 7.22 shows the results for the OF. The maximum gain in buckling load ($OF = 1.18$), is obtained for $n = 3$ (which coincides with the von Mises eigenstress) and $t_{\min}/t_{\max} = 0.27$ or equivalently $t_{\max} = 0.020$ and $t_{\min} = 0.005$, that is, a ratio of $\sim 4:1$. We can see that only the case of $n = 1$ (that is, taking the eigenstress proportional to the rigidity) gives an improvement regardless of the thickness ratio. Nevertheless, it does not provide the maximum gain, which is obtained for $n = 3$. For $n = 2,3,4$ there are combinations of thicknesses that decrease the buckling load, as shown in Figure 7.22 for values of $t_{\min}/t_{\max} < 0.1$.

Table 7.4 summarises the first four buckling loads for the best OF of each n case. Figure 7.23 shows the first four buckling modes for each best case. The plot shows that for every n case the first and second buckling modes remain similar, nevertheless the last two change significantly.

Lets take the best result, that is the geometry for $n = 3$ and $t_{\min}/t_{\max} = 0.27$. The thickness distribution can be seen in Figure 7.24(a). The proposed geometry is now compared with results from literature. Take, for example, the thickness distribution given by [10] which was obtained using the iterative Evolutionary Method:

$$\begin{aligned} t(r) &= 4\,t_{\min} - 3\,t_{\min}\left(\frac{2r}{a}\right)^2 \qquad \text{when } r \le a/2 \\ t(r) &= 4\,t_{\min} - 3\,t_{\min}\left(\frac{\sqrt{2}-2r/a}{\sqrt{2}-1}\right)^2 \quad \text{when } r > a/2, \end{aligned} \tag{7.26}$$

with $t_{\min} = 0.005$, $t_{\max} = 0.025$, and with r being the radius measured from the centre of the plate, and a the width of the plate. The optimality factor reported in [10] is $OF = 1.37$. A comparison

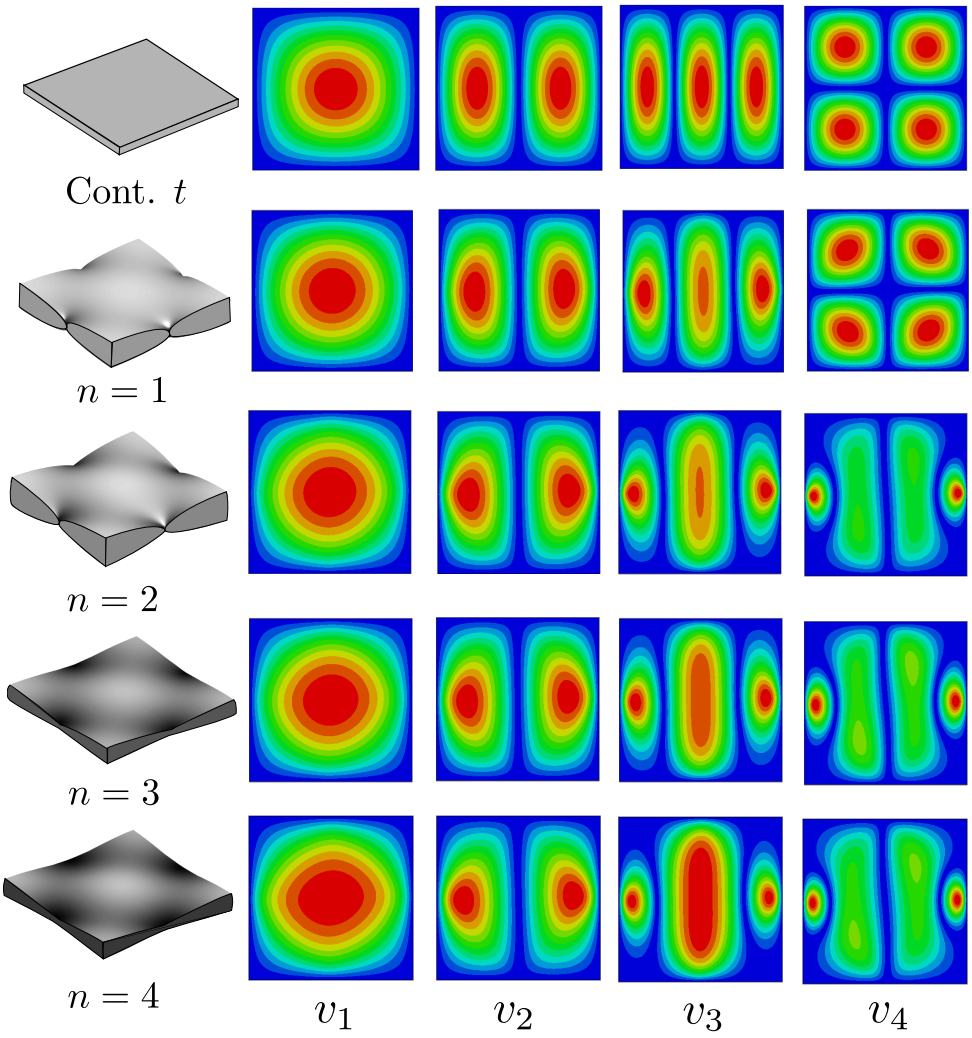

Figure 7.23: Buckling modes and geometry for best OF result (scale factor of 30). SSSS plate.

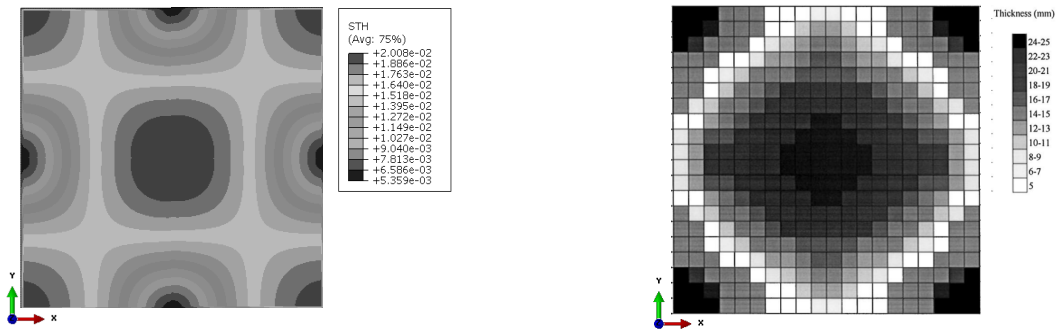

(a) Eigenstress Method $OF = 1.18$

(b) Evolutionary Method $OF = 1.37$ (adapted from [10])

Figure 7.24: Comparison of thickness distribution. Plate SSSS.

of the thickness distribution proposed here and Manickarajah's is shown in Figure 7.24. The solutions show similar features, where mass is redistributed to the corners and centre of the structure. Now, we provide three additional solutions given by [164] and [163]:

Levy & Sokolinsky-(a)

$$t(x,y) = t_o \left[1 - 0.295\cos\left(\frac{2\pi x}{a}\right)\right] \times \left[1 - 0.295\cos\left(\frac{2\pi y}{b}\right)\right]. \tag{7.27}$$

Levy & Sokolinsky-(b)

$$t(x,y) = c_1 \left[1 - c_2 \sin\left(\frac{2\pi x}{a}\right)\right]\left[1 - c_2 \sin\left(\frac{2\pi y}{b}\right)\right], \tag{7.28}$$

where c_1 and c_2 are parameters depending on the original thickness t_o.

Pandey & Sherbourne

$$t(x,y) = \frac{t_o}{\left[1 + \frac{2(N_v-1)}{\pi}\right]^2}\left[1 + (N_v - 1)\sin\left(\frac{2\pi x}{a}\right)\right] \times \left[1 + (N_v - 1)\sin\left(\frac{2\pi y}{b}\right)\right], \tag{7.29}$$

where N_v is a constant called the *thickness distribution shape parameter*.

Figure 7.25 depicts the topologies and the OFs obtained from equations (7.27), (7.28) and (7.29). Table 7.5 provides a further comparison in terms of OF for all of the above mentioned cases. Some of the solutions presented in the table were obtained using a semi analytical Rayleigh-Ritz method, and differ significantly with those from the more robust FE method, particularly for the CCCC case discussed in the following example. Therefore, we compare our results with those obtained using FEM presented by [10].

7.4.5 Clamped Square Plate

An improved design for uni-axially loaded square plates with all edges clamped[14] (CCCC) is sought using the proposed method. Plate dimensions and material coefficients are the same as of those for the SSSS plate. The purpose of this example is to show that the expression $\hat{\sigma}$ need not be given by an analytical equation. It can be approximated numerically from eigenvectors from linear buckling analysis in FEM. An `ABAQUS` shell model with 40000 `S4R` elements is used.

The resultant normalised eigenstress distribution used for $\hat{\sigma}$ is shown in Figure 7.26. The thickness distribution is prescribed to have the same general form as that for the SSSS case and the volume is constrained again; this time satisfying equation (7.21), which is obtained by integrating $q = \int_0^b \int_0^a \hat{\sigma}^{\frac{n}{3}}\, dxdy$ numerically.

[14] Edges are restricted out-of-plane and no rotations are allowed.

Table 7.5: Comparison of Optimality Factors obtained using different methods. Plate SSSS.

	Method	OF
Case		
SSSS – Plate		
Manickarajah et al. [10]	Evolutionary	1.37
Levy and Sokolinsky-(a)[164]	Rayleigh–Ritz	1.23
	FEM*	1.21
Levy and Sokolinsky-(b) [164]	Rayleigh–Ritz	1.32
	FEM*	1.30
Pandey and Sherbourne [163]		
($N_v = 2$)	Rayleigh–Ritz	1.28
	FEM*	1.24
Present ($n = 3$)	Eigenstress	1.18
CCCC – Plate		
Manickarajah et al. [10]	Evolutionary	1.86
Pandey and Sherbourne [163]		
($N_v = 0.5$)	Rayleigh–Ritz	2.05
	FEM*	0.13
Pandey and Sherbourne [163]		
($N_v = 0.25$)	Rayleigh–Ritz	1.45
	FEM*	0.50
Pandey and Sherbourne [163]		
($N_v = 2$)	Rayleigh–Ritz	0.73
	FEM*	1.22
Present		
($n = 2$)	Eigenstress	1.37

*From [10]

Thicknesses are varied within $t_{\min}/t_{\max} \in [0,1]$, n is varied from 1 to 4 and the OFs are computed for each case. Figure 7.27 shows the results. The maximum $OF = 1.37$ is found for $t_{\min}/t_{\max} = 0.18$ and $n = 2$, i.e. a ratio of $\sim 5:1$, which is higher than the SSSS case. We can see that only the case of $n = 1$ (that is, taking the eigenstress proportional to the rigidity) gives an improvement regardless of the thickness ratio. Nevertheless, it does not provide the maximum gain, which is obtained for $n = 2$. For $n = 1,3,4$ there are combinations of thicknesses that decrease the buckling load.

Table 7.6 shows the first four buckling loads and OFs for the best solution of each case. Figure 7.28 presents the buckling modes and geometries for each of best case. We can see here that the buckling modes do change significantly (the order in which they appear) depending on the n factor. For the best case, $n = 2$, the first and second mode swap relative to the original case.

Table 7.5 shows the comparison of our best solution with other known results. Considering the results obtained using FEM, our best result is higher than the best by Pandey & Sherbourne

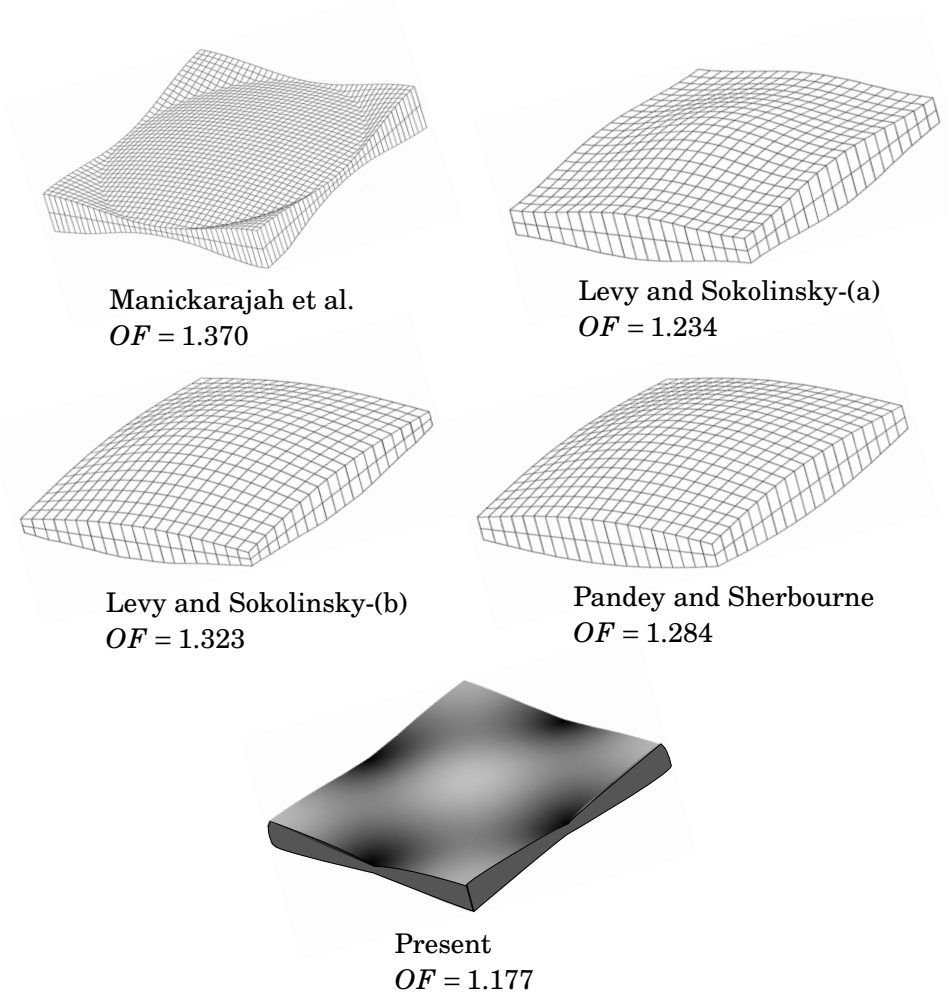

Figure 7.25: Optimised topologies for SSSS plate (dimensions exaggerated); Figure adapted from [10])

(OF = 1.216), and the second highest. Our result is still far from the optimum reported by Manickarajah et al. (OF = 1.86).

Figure 7.29 shows the comparison of the thickness distribution given in [10] and the present solution (n = 2 and $t_{\text{min}}/t_{\text{max}}$ = 0.18). Both topologies are similar, material is removed from the corners and added to the centre and toward the edges perpendicular to those where the load is applied. The proposed geometry is depicted in Figure 7.30. The possible cause for the difference between these solutions is that our thickness distribution varies smoothly whilst in [10] it is stepwise constant; the latter effectively allowing much sharper changes.

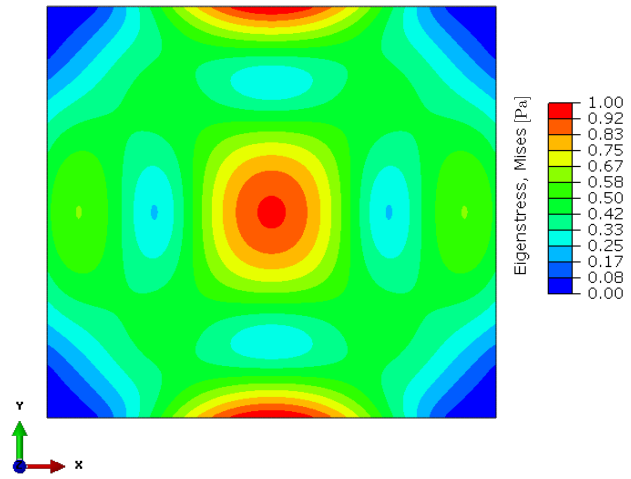

Figure 7.26: Resultant eigenstress distribution (showing $n = 3$) obtained from linear buckling analysis. CCCC plate.

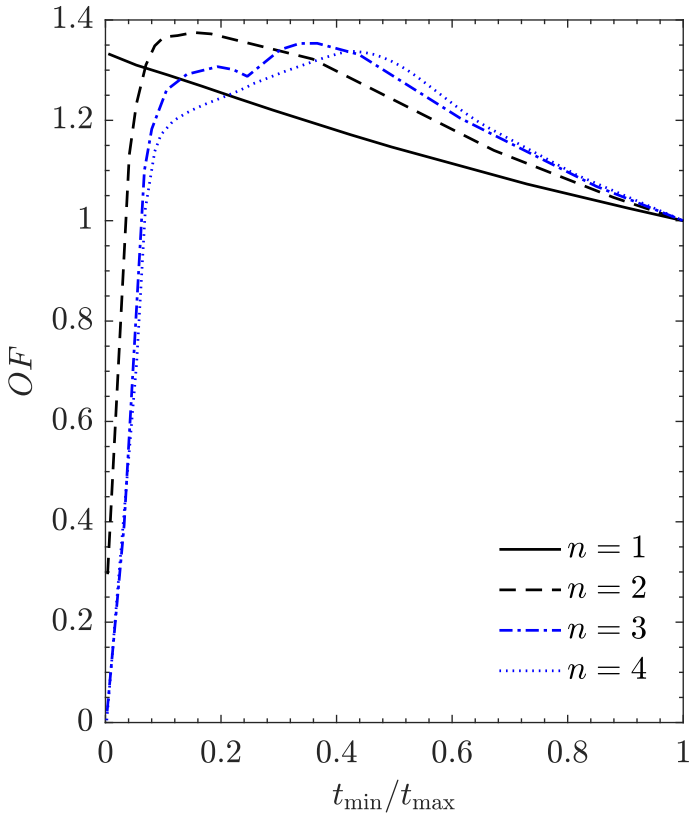

Figure 7.27: OF vs $t_{\max}/t_{\min}$ for SSSS plate.

Table 7.6: First four buckling loads and Optimality Factor for the best case per n. CCCC plate.

	t_{min}/t_{max} [-]	λ_1 N/m $\times 10^6$	λ_2 N/m $\times 10^6$	λ_3 N/m $\times 10^6$	λ_4 N/m $\times 10^6$	OF [-]
n						
1	0.00	3.26	3.46	5.69	6.62	1.33
2	0.18	3.36	3.53	5.69	6.58	1.37
3	0.37	3.32	3.40	5.68	6.52	1.35
4	0.46	3.28	3.28	5.66	6.45	1.34

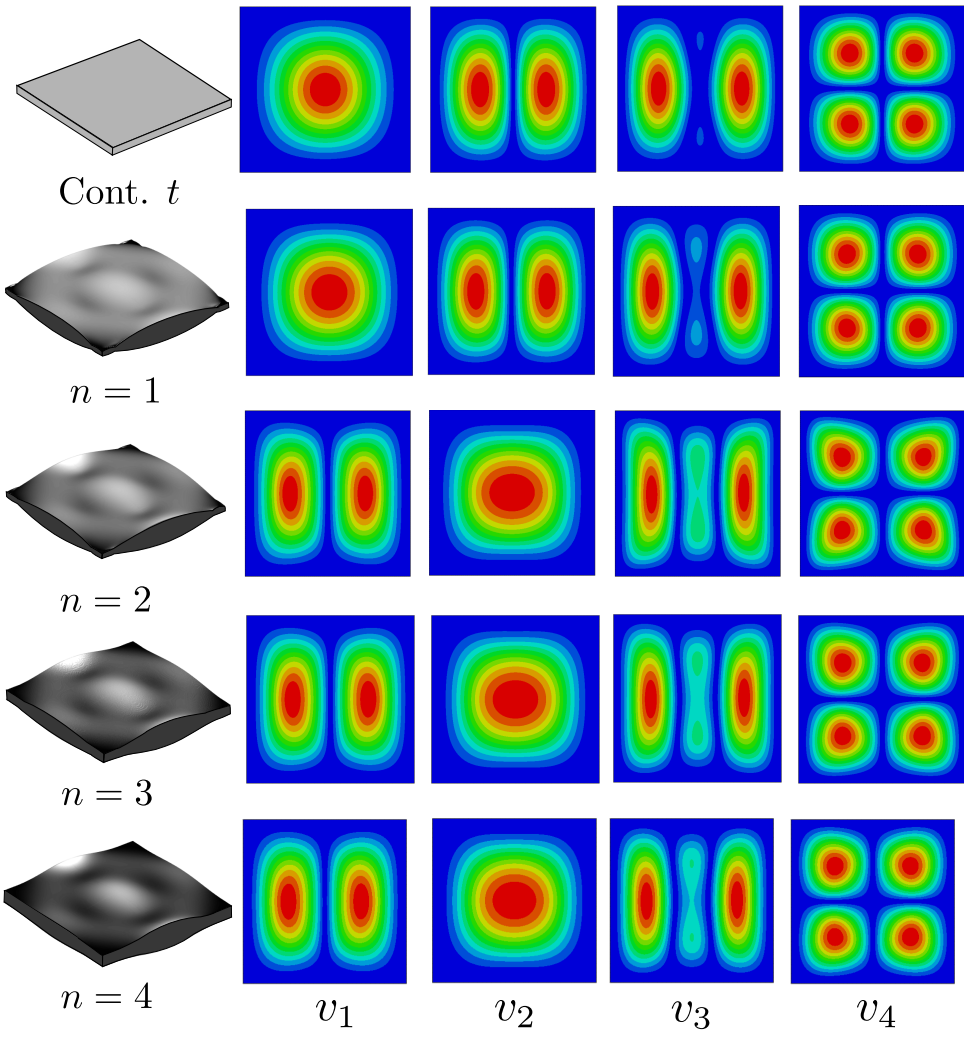

Figure 7.28: Buckling modes and geometry for best OF result (scale factor of 40). CCCC plate.

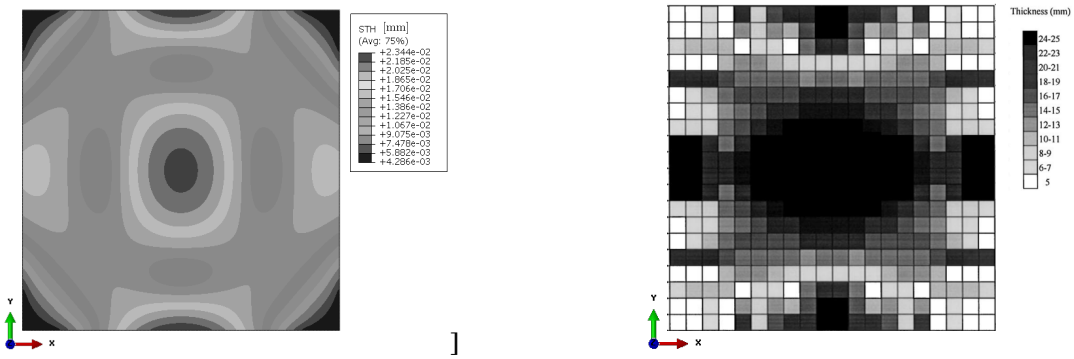

(a) Eigenstress Method $OF = 1.37$

(b) Evolutionary Method $OF = 1.86$ (Adapted from [10])

Figure 7.29: Comparison of thickness distribution. Plate CCCC.

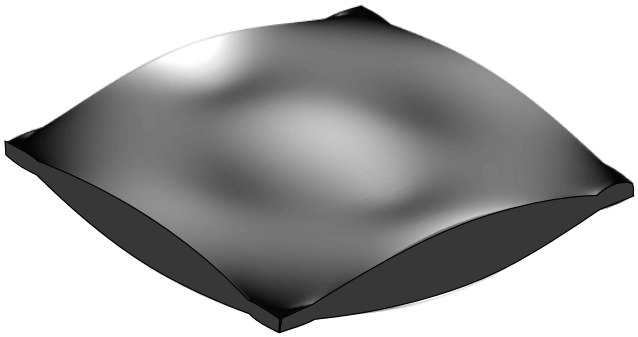

Figure 7.30: Improved design for CCCC plate (scale factor 40). Eigenstress Method ($OF = 1.37$).

7.4.6 SSSS Square Plate with Cut-outs

In the remaining examples we reverse the design approach and increase the specific buckling strength by removing mass while aiming to maintain the load carrying capacity. Mass is removed from the original structure by introducing cut-outs where eigenstresses are minimum. The purpose is to introduce cut-outs whose final dimensions and locations are chosen by the designer, therefore only the approximate regions where the resultant eigenstress is minimum are needed. For this reason, it is sufficient to use $n = 3$ (von Mises eigenstress) to find these. For the example described in this section, dimensions, material and boundary conditions are the same as those used in Section 7.4.4. Two different plates are considered: one with a single cut-out, which provides a reference for comparison; and one with four distributed cut-outs. These structures are designed such that the area of the cut-outs is the same for both cases.

The single cut-out is located at the centre of the plate and given a radius $r = 0.172$ m, as shown in Figure 7.31(a). For this case, the buckling load is $\lambda = 5.31 \times 10^5$ N/m, that is $OF = 0.9$, which is a decrease of ~ 10% relative to the original plate. This result is similar to that reported by [141]: $OF = 0.93$. Reduction of the volume is ~ 3%. Now, based on the distribution of the eigenstress

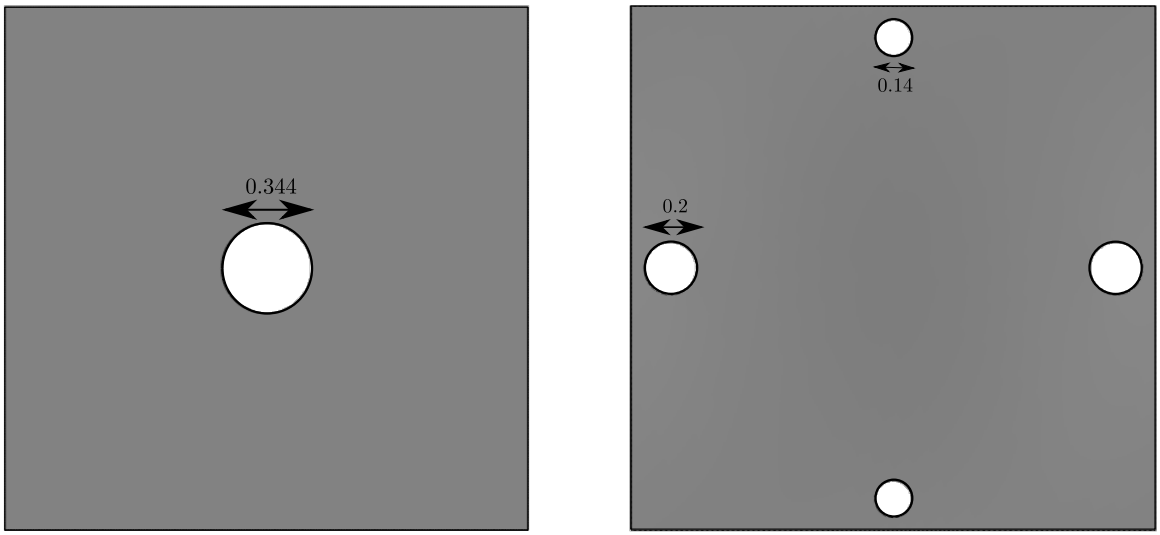

(a) Plate with centre cut-out (b) Plate with distributed cut-outs

Figure 7.31: Equivalent area cut-outs. SSSS plate ($a = b = 2$ m and $t = 0.015$ m).

Table 7.7: Buckling load, Optimality Factor, volume and relative volume. SSSS Plate.

	λ [N/m] $\times 10^5$	OF [-]	V [m^3] $\times 10^{-3}$	V/V_o [-]
Geometry				
No cut-out	5.89	1.00	6.00	1.00
Centre cut-out	5.31	0.90	5.86	0.97
Four cut-outs	5.92	1.01	5.86	0.97

shown in Figure 7.5, four potential regions where cut-outs could be located are identified, all towards the edges of the plate. Four circular cut-outs are designed into the structure, two with radius of $r_b = 0.1$ m, and two with radius $r_s = 0.07$ m, located at from the edges, Figure 7.31(b) shows the proposed topology. For this geometry, the resultant buckling load is $\lambda = 3.95 \times 10^5$ N/m, corresponding to $OF = 1$, i.e. the critical load is the same as that for the plate without cut-outs. Table 7.7 summarises the results in terms of buckling load, Optimality Factor, volume (V) and relative volume (V/V_o, with $V_o = abt$) for the three cases.

7.4.7 Curved Panel with Cut-outs

The last example highlights a more complex case, an axially loaded thin curved panel. Geometry and dimensions are shown in Figure 7.32. Two sets of boundary conditions are considered for the curved edges: clamped-clamped (CC) and simply-supported (SS). The straight edges are free in both cases. The constituent material is isotropic with Young's modulus $E = 71$ GPa and Poisson's

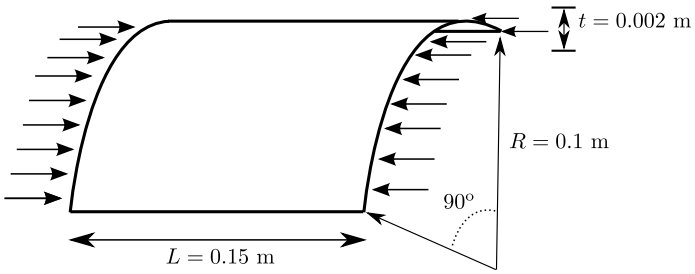

Figure 7.32: Curved panel geometry

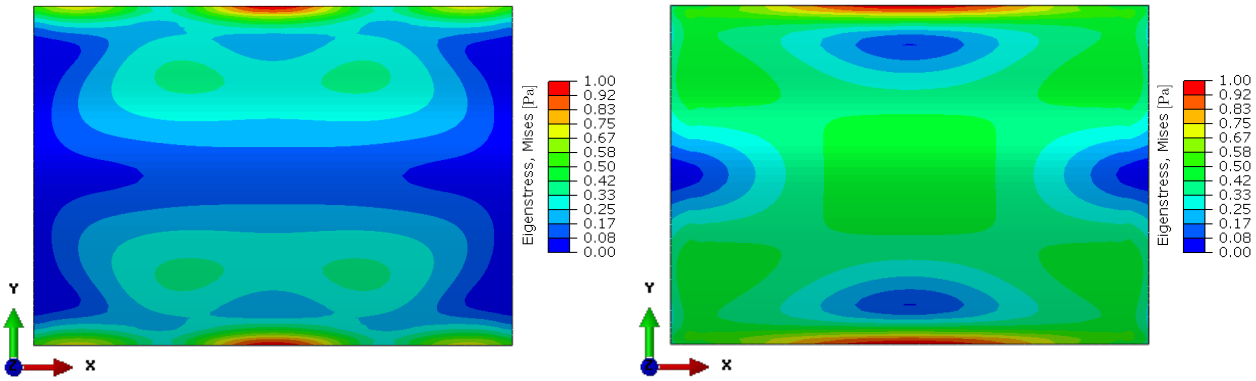

(a) CC panel

(b) SS panel

Figure 7.33: Resultant eigenstress distribution ($n = 3$) for curved panel

ratio $\nu = 0.33$. Again, cut-outs are designed into the structure to remove mass.

A converged ABAQUS shell model with 22181 S4R elements is used to identify buckling mode, resultant eigenstress ($n = 3$) and critical load. For the CC and SS panels without cut-outs the buckling load are $\lambda_o = 7.11 \times 10^4$ N and $\lambda_o = 4.11 \times 10^4$ N, respectively. The resultant eigenstress distributions for each case is shown in Figure 7.33.

For the CC-panel, regions where cut-outs can be located gravitate towards the centre and close to the curved loaded edges, as shown in Figure 7.33(a). For the SS-panel the distribution is different; the regions for cut-outs are clearly shown in blue Figure 7.33(b). For the CC-panel, six elliptical cut-outs are distributed on the surface. In contrast, for the SS-panel four cut-outs are introduced: two ellipses and two circles. Dimensions and locations are shown in Figure 7.34(a) and 7.34(b).

The performance of the two panels is assessed by computing the buckling resistance. The critical load for the CC-panel is $\lambda = 7.13 \times 10^4$ N, that is $OF = 1$, i.e. the buckling performance is not affected. The volume reduction is $\sim 2\%$. The buckling load of the SS-panel is $\lambda = 4.10 \times 10^4$ N or $OF = 0.99$. In this case, the load decreased by $\sim 1\%$, but volume reduction is greater than for the CC case, $\sim 4\%$. Table 7.8 shows the summary of the buckling load, Optimality Factor, volume and relative volume for the four cases discussed herein.

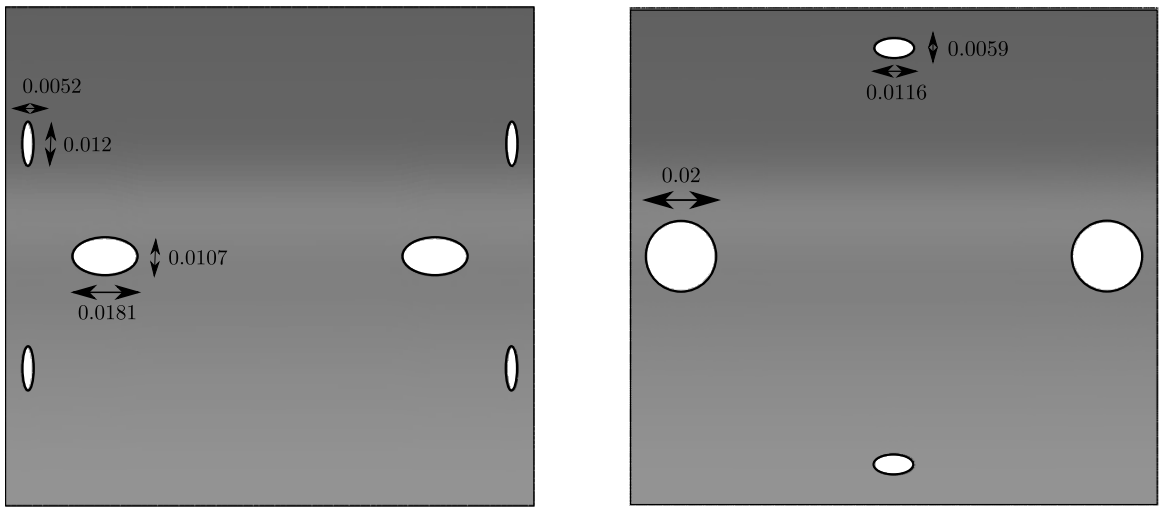

(a) CC panel with distributed cut-outs

(b) SS panel with distributed cut-outs

Figure 7.34: Curved panel with cut-outs for two different boundary conditions

Table 7.8: Buckling load, Optimality Factor, volume and relative volume. Curved Panel.

	λ [N] $\times 10^4$	OF [-]	V [m^3] $\times 10^{-5}$	V/V_o [-]
Geometry				
CC				
No cut-out	7.11	1.000	4.71	1.000
Cut-outs	7.13	1.002	4.62	0.980
SS				
No cut-out	4.11	1.000	4.71	1.000
Cut-outs	4.10	0.997	4.56	0.968

7.5 Discussion

For the cases considered in Section 7.4, it was possible to build a topological profile based on the resultant eigenstress to enhance the structure's specific buckling strength. In this particular case, the resultant eigenstress has been used since it is an estimate on how the stress are redistributed at buckling. If it is a beam, then the resultant eigenstress is taken as a normalised approximation of the distribution of the rigidity of the structure whose geometry maximises the buckling performance. If it is a plate, then the eigenstress[15] is taken as a *power* of the normalised approximation of the rigidity. The normalised eigenstress distribution can be obtained by either analytical or numerical means. The process has two main advantages: first, even though

[15]Here we are taking the von Mises eigentress as estimate of the resultant stress, nevertheless, this option might be changed by a more appropriate metric.

the method relies on the correct Eigentress pattern, it is sufficient to use an approximation, where localised features close to singularities can be ignored. Take for instance the case of beam and the SSSS-plate; it was possible to obtain an enhanced structural design using the results from classical theories, which are known to have good accuracy only far from singular points. Second, as the eigentresses are normalised, the same pattern could be used for structures with congruent[16] geometries, but with different dimensions, as long as they are subject to the same boundary and loading conditions. Additionally, the distribution can be calculated from the output of a single linear buckling analysis, in contrast to iterative methods where many analyses have to be performed to achieve convergence.

The method can be used as a design tool for the two most common optimisation problems with stability criteria: (1) to improve the buckling resistance for a given mass, as we have done in the first three examples; and (2) to decrease the structural weight for a given buckling load, as for the last two cases.

Increase buckling load Aiming to keep overall mass unchanged, the requirements of the problem dictate constraints for the maximum and minimum values of the geometric parameters defining (the radius of the beam, or thickness in the case of the plate) the new topology. Finding an appropriate relationship between these parameters may be challenging, depending on the complexity of the geometry. For the cases presented, a constraint equation relating the dimension parameters (e.g. radii or thicknesses) was considered. The equation defines a set of values for which the volume is kept constant. The exact value of the parameters that gives the maximum possible buckling load is not known, therefore, a series of trial runs have to be performed in order to find the best case within the set[17] (which could be a set of allowed areas or a power coefficient). This process may increase the computational effort of the method. A similar case may occur if the limitation is due to manufacturing reasons. If the constant-volume constraint is not a factor (meaning mass can be added as needed), the method automatically provides regions where material can be added. Another advantage is that eigenstress distributions give a clear indication of how the optimum topology should look like, without performing any calculation other than the resultant eigenstress.

Decrease structural weight The resultant eigenstresses give approximate regions where the decrease in stiffness, due to removal of mass, may not have significant impact on the buckling performance. In the cases studied, the distribution served as an aid for locating the desired cut-outs. As in the case of mass redistribution, a series of trials may be needed to find the geometry of the cut-outs that result in the desired performance Results show that, depending on the boundary conditions, a decrease in the structural weight may or may not be accompanied by

[16] Two geometries are *congruent* if they have the same shape but different size.

[17] It is worth to mention that this process is *not* iterative, since one solution does not depend on any previous result, nevertheless, it may required repeated runs to find the best case.

a reduction of buckling load. Either way, an increase of specific buckling strength was show to be possible as the removal of mass was more pronounced than the potential, if any, decrease in load.

In general, independently from the optimisation objective, implementation of the model is straightforward, once the eigenstresses are available. This simplicity makes it possible to, potentially, combine the model with existing optimisation routines.

A limitation of the model is that it could result in non-physical or unreasonable geometries, with thicknesses close to zero or with steep gradients. If this situation occurs additional computations, with different parameter constraints, may avoid the issue. Another limitation is that the method, as presented here, is using the resultant von Mises eigenstress. This is probably not the best choice. A normalised strain energy density (hence an *eigen-energy* approach) would provide a suitable alternative (and possibly more information-rich) metric. All examples presented here are single-modal, and only the first eigenvalue and eigenvector are used, as a note of caution this method may not apply, in its current form, to multi-modal structures.

7.6 Concluding Remarks

With the Eigenstress Method, we have provided an intuitive and straightforward approach for improving the buckling resistance of a structure by changing its topology, without affecting its structural weight. Alternatively, the method can be used to decrease the structural weight without significantly altering the buckling performance. In the former case, we were able to improve buckling loads by redistributing mass, as the method was shown to give material distribution patterns closely matching optimal ones, obtained using analytical or iterative methods. In the latter case, it was possible to introduce cut-outs in regions where their effect on critical load-carrying capacity could be minimised. The results are summarised as follows:

- The general formula for the redistribution of material to increase the buckling load is:

$$h = (h_{\max} - h_{\min})\hat{\sigma}^{\frac{n}{3}} + h_{\min} \tag{7.30}$$

  where h is interpreted as geometric parameter defining the topology of the structure (the radius in the case of the circular cross-section beam, and as the thickness in the case of the flat plate). $n = 3/2$ for a beam or $n = 1, 2, 3$ or 4 for a plate;

- The expression for $\hat{\sigma}$ can be an analytical expression or a numerical approximation obtained from FEM;

- The maximum *Optimality Factor* obtained for the case of the circular cross-section beam with clamped edges is 1.22;

- The maximum *Optimality Factor* obtained for the case of the circular cross-section beam with clamped-free boundary condition is 1.32;

- The maximum *Optimality Factor* obtained for the case of the circular cross-section beam with clamped-hinged boundary condition is 1.24;
- The maximum *Optimality Factor* obtained for the case of the SSSS square plate is 1.18. Which is obtained with $n = 3$ and $t_{\min}/t_{\max} = 0.27$.
- The maximum *Optimality Factor* obtained for the case of the CCCC square plate is 1.37. Which is obtained with $n = 2$ and $t_{\min}/t_{\max} = 0.18$. $\hat{\sigma}$ is obtained from a FEM linear buckling analysis in FEM.
- For the SSSS plate, it was possible to reduce the mass ~ 3% by introducing distributed cut-outs as in Figure 7.31(b), without affecting the buckling load.
- For the CC panel, it was possible to reduce the mass ~ 2% by introducing distributed cut-outs as in Figure 7.34(a), without affecting the buckling load.
- For the SS panel, the introduction of cut-outs, as in Figure 7.34(b), resulted in a decrease of ~ 4% of mass accompanied by a reduction of buckling load of ~ 1%.

The geometries with redistributed mass are sub-optimal, but for every case, the buckling load was improve by at least ~ 20%. For structures with cut-outs, mass was decreased by at least ~ 2% with a maximum critical load loss of ~ 1%.

CHAPTER 8

CONCLUDING REMARKS

In the present work a high-fidelity and efficient advanced finite element model, based on the Unified Formulation, has been developed. The proposed model has the capability of correctly modelling the mechanical response of beam-like and thin-walled structures. Special attention has been given to modelling the buckling, initial post-buckling and large deflection behaviour. In addition, two new methodologies for designing buckling resistant structures have been presented. The following points summarise in more detail the main findings for the cases studied in this work:

1. A novel expansion model for displacement-based finite element analysis, based on Serendipity Lagrange (SL) polynomials, was developed. The new expansion has shown to provide accurate results, especially for localised stress distributions, in a very efficient way compared with traditional FEM models. It was also shown that, by using this expansion, the systems involved are less ill-conditioned, improving the numerical stability. The SL expansion has the property of being hierarchical within a discrete element, given the possibility of enriching the kinematics by increasing the order of expansion as well as the level of refinement. This provides much more control on the modelling process and gives the designer the capability of choosing the correct refinement in places where is needed the most, effectively, reducing the computational effort.

2. A Linearised Buckling Model, suitable for modelling the buckling of curved (cross-section) and thin-walled structures, was developed. In order to describe structures with curved cross-sections accurately, a method that makes use of an exact geometrical description was also presented. The model, which makes use of the SL expansion, was shown to provide accurate results for displacements and localised stress profiles. Moreover, it was shown

that the model improves significantly the efficiency in terms of DOFs and time, which was measured and compared using the complexity of the algorithms involved. This justified the use of the UF-SL linear buckling model for problems that involved repeated number of steps, like eigenvalue solvers or iterative methods.

3. A novel three-dimensional beam finite element model was also presented. The new model extends the known capabilities of the Unified Formulation framework to non-prismatic and curved (cross-section and beam) structures. It provides the means for performing non-linear and large displacement analyses of 3D-like composite beam structures. In order to accurately describe the three-dimensional geometry, 3D Lagrange shapes functions are employed. In addition, this mapping does not contribute to extra DOFs apart from those related to the cross-section (SL) and beam expansions. These last two can be chosen and enriched independently. The three shape functions are linked via their gradients, which allows to them to be all used within a non-prismatic element.

4. A new iterative, and easy to implement, method for identifying and mapping regions sensitive to stiffness variations, has been presented. The method exploits the efficiency of the UF-SL linear buckling model. Nevertheless, the method does not rely on any particular analysis framework. The methodology provides a contour-like pattern which relates regions of sensitivity to nominal stiffness to buckling performance. This chessboard-like pattern is then used to design buckling resistant structures. Results showed that, for structures that behave linearly, it was possible to reduce the mass by introducing cut-outs without altering its buckling performance. On the other hand, for structures that behave non-linearly, it was possible to tailor the structure such that its post-buckling performance was not significantly affected. In addition, in some cases it was possible to reduce the structure's sensitivity to geometrical imperfections.

5. Lastly, a novel and intuitive method for designing topologically efficient buckling-resistant structures was developed. By using the resultant stress distribution, recovered from the first eigenvector of the linear buckling analysis, it was possible to tailor the structure to improve (increase) its critical load. The method provided a topology that closely resembles that of the optimum case, keeping its weight constant. The same result can be used to reduce the mass by introducing cut-outs.

CHAPTER 9

FUTURE WORK

Based on the results and new ideas proposed throughout the manuscript, new research tracks and future work is now described.

1. The Serendipity Lagrange Expansion model used as the main tool can be improved in several ways: (1) it is possible to extend the hierarchical property to the beam axis shape functions as well. (2) One of the requirements of the cross-section discretisation is that elements had to be connected by the cross-section nodes (element edge nodes), this condition can be relaxed if transition elements are developed. These type of transition elements may also be used to connect elements with different number of nodes, say a 4-node element to a 3-node element. These kind of features are usually required for problems involving failure or delamination, among others. (3) The SL expansion idea may be extended to shell-like models, where the expansion is not in the cross-section (or through-thickness in this case), but to the in-plane interpolation, which may ease locking phenomena.

2. The capabilities of the Linearised Buckling Model, in particular its efficiency in terms of computational time, can be exploited for studying more complex geometries, load cases and boundary conditions. Moreover, it can be modified to study eigenvalue problems involving non-linearities, such as for finding bifurcation points.

3. The three-dimensional beam finite element model can be used to study problems involving beam-like structures made of composite materials, in particular wind turbine blades. When designing wind turbine blades, one of the most common bottlenecks encountered is that the models are too computationally expensive when combining them with optimisation routines. A common practice is to use reduced models (EB or TB) for this part of the process.. After

a desired optimised target is reached, 2D or 3D FEM models are use to sub-model parts of the blade. The 3D Beam Model developed here could be used as a single tool for both processes, optimisation and stress-analysis, without the need of using different models.

4. The Local Nominal Stiffness Method can be extended and improved in several ways as well. (1) To perform non-linear eigenvalue analyses for each of the steps (i.e. for each local nominal stiffness element) instead of a linear buckling analysis. (2) Extending the capabilities for studying any three-dimensional problem, not only for shell-like problems. (3) Including more buckling modes and their interactions prior to re-designing the topology.

5. Lastly, the Eigenstress Method can be extended to include non-linearities and multi-modal problems, which would allow to study and design more complex structures subject to different loading cases and boundary conditions.

The models presented in this work can be re-implemented and coded in a user-friendly and open-source software, with pre-post processing features and analysis capabilities. In the mid-term, this software can be distributed and shared among other researches, companies or to anyone that may find a good use of it.

APPENDIX A

SERENDIPITY LAGRANGE EXPANSION SHAPE FUNCTIONS

This section provides the explicit form of the Serendipity Lagrange shape functions. The polynomials and their first derivatives in each of the variables, for the first five orders, are presented.

A.1 Shape Functions

The explicit form of the shape functions presented on Section 3.3.1.2 are as follows:

Order One:

$$L_1^{(\mathrm{I})} = \frac{1}{4}(1-\alpha)(1-\beta)$$
$$L_2^{(\mathrm{I})} = \frac{1}{4}(1+\alpha)(1-\beta)$$
$$L_3^{(\mathrm{I})} = \frac{1}{4}(1+\alpha)(1+\beta)$$
$$L_4^{(\mathrm{I})} = \frac{1}{4}(1-\alpha)(1+\beta)$$

Order Two:

$$L_5^{(\mathrm{IIA})} = \frac{1}{2}(1-\beta)(\alpha^2-1)$$
$$L_6^{(\mathrm{IIA})} = \frac{1}{2}(1+\alpha)(\beta^2-1)$$
$$L_7^{(\mathrm{IIB})} = \frac{1}{2}(1+\beta)(\alpha^2-1)$$
$$L_8^{(\mathrm{IIB})} = \frac{1}{2}(1-\alpha)(\beta^2-1)$$

Order Three:

$$L_9^{(\mathrm{IIA})} = \frac{1}{2}(1-\beta)(\alpha^3-\alpha)$$
$$L_{10}^{(\mathrm{IIA})} = \frac{1}{2}(1+\alpha)(\beta^3-\beta)$$
$$L_{11}^{(\mathrm{IIB})} = \frac{1}{2}(1+\beta)(\alpha^3-\alpha)$$
$$L_{12}^{(\mathrm{IIB})} = \frac{1}{2}(1-\alpha)(\beta^3-\beta)$$

Order Four:

$$L_{13}^{(\mathrm{IIA})} = \frac{1}{2}(1-\beta)(\alpha^4-\frac{10}{9}\alpha^2+\frac{1}{9})$$
$$L_{14}^{(\mathrm{IIA})} = \frac{1}{2}(1+\alpha)(\beta^4-\frac{10}{9}\beta^2+\frac{1}{9})$$
$$L_{15}^{(\mathrm{IIB})} = \frac{1}{2}(1+\beta)(\alpha^4-\frac{10}{9}\alpha^2+\frac{1}{9})$$
$$L_{16}^{(\mathrm{IIB})} = \frac{1}{2}(1-\alpha)(\beta^4-\frac{10}{9}\beta^2+\frac{1}{9})$$
$$L_{17}^{(\mathrm{III})} = (\alpha^2-1)(\beta^2-1)$$

Order Five:

$$L_{18}^{(\mathrm{IIA})} = \frac{1}{2}(1-\beta)(\alpha^5-\frac{5}{4}\alpha^3+\frac{1}{4}\alpha)$$
$$L_{19}^{(\mathrm{IIA})} = \frac{1}{2}(1+\alpha)(\beta^5-\frac{5}{4}\beta^3+\frac{1}{4}\beta)$$
$$L_{20}^{(\mathrm{IIB})} = \frac{1}{2}(1+\beta)(\alpha^5-\frac{5}{4}\alpha^3+\frac{1}{4}\alpha)$$
$$L_{21}^{(\mathrm{IIB})} = \frac{1}{2}(1-\alpha)(\beta^5-\frac{5}{4}\beta^3+\frac{1}{4}\beta)$$
$$L_{22}^{(\mathrm{III})} = (\alpha^2-1)(\beta^3-\beta)$$
$$L_{23}^{(\mathrm{III})} = (\beta^2-1)(\alpha^3-\alpha)$$

A.2 Derivatives of Shape Functions

The first derivatives in terms of α and β are presented below. Comma denotes partial derivative.

Order One:

$$L_1^{(\mathrm{I})},_\alpha = -\frac{1}{4}(1-\beta) \qquad L_1^{(\mathrm{I})},_\beta = -\frac{1}{4}(1-\alpha)$$
$$L_2^{(\mathrm{I})},_\alpha = \frac{1}{4}(1-\beta) \qquad L_2^{(\mathrm{I})},_\beta = -\frac{1}{4}(1+\alpha)$$
$$L_3^{(\mathrm{I})},_\alpha = \frac{1}{4}(1+\beta) \qquad L_3^{(\mathrm{I})},_\beta = \frac{1}{4}(1+\alpha)$$
$$L_4^{(\mathrm{I})},_\alpha = -\frac{1}{4}(1+\beta) \qquad L_4^{(\mathrm{I})},_\beta = \frac{1}{4}(1-\alpha)$$

Order Two:

$$L_5^{(\mathrm{IIA})},_\alpha = \frac{1}{2}(1-\beta)(2\alpha) \qquad L_5^{(\mathrm{IIA})},_\beta = -\frac{1}{2}(\alpha^2-1)$$
$$L_6^{(\mathrm{IIA})},_\alpha = \frac{1}{2}(\beta^2-1) \qquad L_6^{(\mathrm{IIA})},_\beta = \frac{1}{2}(1+\alpha)(2\beta)$$
$$L_7^{(\mathrm{IIB})},_\alpha = \frac{1}{2}(1+\beta)(2\alpha) \qquad L_7^{(\mathrm{IIB})},_\beta = \frac{1}{2}(\alpha^2-1)$$
$$L_8^{(\mathrm{IIB})},_\alpha = -\frac{1}{2}(\beta^2-1) \qquad L_8^{(\mathrm{IIB})},_\beta = \frac{1}{2}(1-\alpha)(2\beta)$$

Order Three:

$$L_9^{(\mathrm{IIA})},_\alpha = \frac{1}{2}(1-\beta)(3\alpha^2-1) \qquad L_9^{(\mathrm{IIA})},_\beta = -\frac{1}{2}(\alpha^3-\alpha)$$
$$L_{10}^{(\mathrm{IIA})},_\alpha = \frac{1}{2}(\beta^3-\beta) \qquad L_{10}^{(\mathrm{IIA})},_\beta = \frac{1}{2}(1+\alpha)(3\beta^2-1)$$
$$L_{11}^{(\mathrm{IIB})},_\alpha = -\frac{1}{2}(1+\beta)(3\alpha^2-1) \qquad L_{11}^{(\mathrm{IIB})},_\beta = -\frac{1}{2}(\alpha^3-\alpha)$$
$$L_{12}^{(\mathrm{IIB})},_\alpha = \frac{1}{2}(\beta^3-\beta) \qquad L_{12}^{(\mathrm{IIB})},_\beta = -\frac{1}{2}(1-\alpha)(3\beta^2-1)$$

Order Four:

$$L_{13}^{(\mathrm{IIA})},_\alpha = \frac{1}{2}(1-\beta)(4\alpha^3-\frac{20}{9}\alpha) \qquad L_{13}^{(\mathrm{IIA})},_\beta = -\frac{1}{2}(\alpha^4-\frac{10}{9}\alpha^2+\frac{1}{9})$$
$$L_{14}^{(\mathrm{IIA})},_\alpha = \frac{1}{2}(\beta^4-\frac{10}{9}\beta^2+\frac{1}{9}) \qquad L_{14}^{(\mathrm{IIA})},_\beta = \frac{1}{2}(1+\alpha)(4\beta^3-\frac{20}{9}\beta)$$
$$L_{15}^{(\mathrm{IIB})},_\alpha = \frac{1}{2}(1+\beta)(4\alpha^3-\frac{20}{9}\alpha) \qquad L_{15}^{(\mathrm{IIB})},_\beta = \frac{1}{2}(\alpha^4-\frac{10}{9}\alpha^2+\frac{1}{9})$$
$$L_{16}^{(\mathrm{IIB})},_\alpha = -\frac{1}{2}(\beta^4-\frac{10}{9}\beta^2+\frac{1}{9}) \qquad L_{16}^{(\mathrm{IIB})},_\beta = \frac{1}{2}(1-\alpha)(4\beta^3-\frac{20}{9}\beta)$$
$$L_{17}^{(\mathrm{III})},_\alpha = (2\alpha)(\beta^2-1) \qquad L_{17}^{(\mathrm{III})},_\beta = (\alpha^2-1)(2\beta)$$

Order Five:

$$L_{18}^{(\mathrm{IIA})},_{\alpha} = \frac{1}{2}(1-\beta)(5\alpha^4 - \frac{15}{4}\alpha^2 + \frac{1}{4}) \qquad L_{18}^{(\mathrm{IIA})},_{\beta} = -\frac{1}{2}(\alpha^5 - \frac{5}{4}\alpha^3 + \frac{1}{4}\alpha)$$

$$L_{19}^{(\mathrm{IIA})},_{\alpha} = \frac{1}{2}(\beta^5 - \frac{5}{4}\beta^3 + \frac{1}{4}\beta) \qquad L_{19}^{(\mathrm{IIA})},_{\beta} = \frac{1}{2}(1+\alpha)(5\beta^4 - \frac{15}{4}\beta^2 + \frac{1}{4})$$

$$L_{20}^{(\mathrm{IIB})},_{\alpha} = -\frac{1}{2}(1+\beta)(5\alpha^4 - \frac{15}{4}\alpha^2 + \frac{1}{4}) \qquad L_{20}^{(\mathrm{IIB})},_{\beta} = -\frac{1}{2}(\alpha^5 - \frac{5}{4}\alpha^3 + \frac{1}{4}\alpha)$$

$$L_{21}^{(\mathrm{IIB})},_{\alpha} = \frac{1}{2}(\beta^5 - \frac{5}{4}\beta^3 + \frac{1}{4}\beta) \qquad L_{21}^{(\mathrm{IIB})},_{\beta} = -\frac{1}{2}(1-\alpha)(5\beta^4 - \frac{15}{4}\beta^2 + \frac{1}{4})$$

$$L_{22}^{(\mathrm{III})},_{\alpha} = (2\alpha)(\beta^3 - \beta) \qquad L_{22}^{(\mathrm{III})},_{\beta} = (\alpha^2 - 1)(3\beta^2 - 1)$$

$$L_{23}^{(\mathrm{III})},_{\alpha} = (\beta^2 - 1)(3\alpha^2 - 1) \qquad L_{23}^{(\mathrm{III})},_{\beta} = (2\beta)(\alpha^3 - \alpha)$$

APPENDIX B

DERIVATION OF THE LINEARISED BUCKLING MODEL NUCLEUS

This section provides the details of the derivation of the Geometric Matrix nucleus used in the Linearised Buckling Model. Using the assumptions given in Section 4.3 the value of the stress and strain at the incremental load step $t+\Delta t$ are written as the value at time t plus the incremental (Δ) value. For example, the stress at the loading step is $\boldsymbol{\sigma}_{t+\Delta t} = \boldsymbol{\sigma}_t + \Delta\boldsymbol{\sigma}$. Values at time t are considered constant, thus, $\delta\boldsymbol{\sigma}_{\Delta t+t} = \delta\Delta\boldsymbol{\sigma}$, where δ refers to variation. The strains are written as a sum of a linear and a non-linear term

$$\boldsymbol{\varepsilon} = \boldsymbol{e} + \boldsymbol{\nu}, \tag{B.1}$$

where $\boldsymbol{\nu}$ is the non-linear part of the stress tensor. The last equation, together with the constant values at time t, yields $\delta\boldsymbol{e}_{t+\Delta t} = \delta\Delta\boldsymbol{e}$ and $\delta\boldsymbol{\nu}_{t+\Delta t} = \delta\Delta\boldsymbol{\nu}$. Using these relations the internal work at the incremental step is expanded as

$$\begin{aligned}
\delta W_{\text{int}}^{t+\Delta t} &= \int_V \delta\boldsymbol{\varepsilon}_{t+\Delta t}^{\mathrm{T}}\boldsymbol{\sigma}_{t+\Delta t}\,dV \\
&= \int_V \delta\boldsymbol{\varepsilon}_{t+\Delta t}^{\mathrm{T}}(\boldsymbol{\sigma}_t + \Delta\boldsymbol{\sigma})\,dV \\
&= \int_V \delta\boldsymbol{\varepsilon}_{t+\Delta t}^{\mathrm{T}}\Delta\boldsymbol{\sigma} + \delta\boldsymbol{\varepsilon}^{\mathrm{T}}\boldsymbol{\sigma}_t\,dV \\
&= \int_V \delta\Delta\boldsymbol{\varepsilon}^{\mathrm{T}}\boldsymbol{C}\Delta\boldsymbol{\varepsilon} + \delta(\boldsymbol{e}_{t+\Delta t} + \boldsymbol{\nu}_{t+\Delta t})^{\mathrm{T}}\boldsymbol{\sigma}_t\,dV \\
&= \int_V \delta(\Delta\boldsymbol{e} + \Delta\nu)^{\mathrm{T}}\boldsymbol{C}(\Delta\boldsymbol{e} + \Delta\boldsymbol{\nu}) + \delta(\boldsymbol{e}_{t+\Delta t} + \boldsymbol{\nu}_{t+\Delta t})^{\mathrm{T}}\boldsymbol{\sigma}_t\,dV \\
&= \int_V \delta\Delta\boldsymbol{e}^{\mathrm{T}}\boldsymbol{C}\Delta\boldsymbol{e} + \delta\Delta\boldsymbol{e}^{\mathrm{T}}\boldsymbol{C}\Delta\boldsymbol{\nu} + \Delta\boldsymbol{\nu}^{\mathrm{T}}\boldsymbol{C}\Delta\boldsymbol{e} + \Delta\boldsymbol{\nu}^{\mathrm{T}}\boldsymbol{C}\Delta\boldsymbol{\nu} \\
&\quad + \delta(\boldsymbol{e}_{t+\Delta t} + \boldsymbol{\nu}_{t+\Delta t})^{\mathrm{T}}\boldsymbol{\sigma}_t\,dV,
\end{aligned} \tag{B.2}$$

where V is the volume of the solid. The second, third and fourth terms of equation (B.2) can be linearised, since they are at least quadratic in $\Delta\boldsymbol{u}$, this gives

$$\delta W_{\text{int}}^{t+\Delta t} = \int_V \delta\Delta\boldsymbol{e}^{\mathrm{T}}\boldsymbol{C}\Delta\boldsymbol{e} + \delta\Delta\boldsymbol{e}^{\mathrm{T}}\boldsymbol{\sigma}_t + \delta\Delta\boldsymbol{v}^{\mathrm{T}}\boldsymbol{\sigma}_t\, dV. \tag{B.3}$$

If an external force $\boldsymbol{f}_{\text{ext}}$ is applied, then

$$\delta W_{\text{ext}}^{t+\Delta t} = \delta\Delta\boldsymbol{u}^{\mathrm{T}}\boldsymbol{f}_{\text{ext}}, \tag{B.4}$$

and by the Principle of Virtual Displacements

$$\int_V \delta\Delta\boldsymbol{e}^{\mathrm{T}}\boldsymbol{C}\Delta\boldsymbol{e} + \delta\Delta\boldsymbol{e}^{\mathrm{T}}\boldsymbol{\sigma}_t + \delta\Delta\boldsymbol{v}^{\mathrm{T}}\boldsymbol{\sigma}_t\, dV = \delta\Delta\boldsymbol{u}^{\mathrm{T}}\boldsymbol{f}_{\text{ext}}. \tag{B.5}$$

Substituting the stress-strain relation and equation (4.3) into equation (B.5) gives the relation at element level [1]

$$\delta\boldsymbol{u}_{js}^{\mathrm{T}}\left(\int_{V_{(\mathrm{e})}} \mathfrak{B}_{js}^{\mathrm{T}}\boldsymbol{C}\mathfrak{B}_{i\tau} + \phi^{\mathrm{T}}\boldsymbol{\sigma}_t\boldsymbol{I}\, dV\right)\boldsymbol{u}_{i\tau} = \delta\boldsymbol{u}_{js}^{\mathrm{T}}\left(\boldsymbol{f}_{\text{ext}} - \int_{V_{(\mathrm{e})}} \mathfrak{B}_{js}\boldsymbol{\sigma}_t\, dV\right) \tag{B.6}$$

where $\phi^{\mathrm{T}}\boldsymbol{\sigma}_t\boldsymbol{I}$ is a 3×3 matrix and $\mathfrak{B}$ is the differential matrix, relating stress and strain, applied to the shape functions. The explicit form of ϕ^{T} is derived further in this section. Note that the terms in parenthesis in equation (B.6) are independent of $\delta\boldsymbol{u}_{js}^{\mathrm{T}}$. This expression is used to study the stability of the structure. At the point of buckling, several stable (or unstable) configurations appear, mathematically speaking, the equation has more than one solution. Assuming that the pre-buckling behaviour of the structure is linear, and that the applied force is proportional to a reference force:

$$\boldsymbol{f}_{\text{ext}} = \lambda\boldsymbol{f}_{\text{ref}}, \tag{B.7}$$

then the stress distribution is $\lambda\boldsymbol{\sigma}_o$ with $\boldsymbol{\sigma}_o$ the stress due to the application of $\boldsymbol{f}_{\text{ref}}$. If the load is the critical load, then at least two possible solutions exist, $\boldsymbol{u}_{i\tau}^{(1)}$ and $\boldsymbol{u}_{i\tau}^{(2)}$ such that

$$\begin{aligned}\left(\int_{V_{(\mathrm{e})}} \mathfrak{B}_{js}^{\mathrm{T}}\boldsymbol{C}\mathfrak{B}_{i\tau} + \lambda\phi^{\mathrm{T}}\boldsymbol{\sigma}_o\boldsymbol{I}\, dV\right)\boldsymbol{u}_{i\tau}^{(1)} &= \left(\lambda\boldsymbol{f}_{\text{ref}} - \int_{V_{(\mathrm{e})}} \mathfrak{B}_{js}\boldsymbol{\sigma}_t\, dV\right)\\ \left(\int_{V_{(\mathrm{e})}} \mathfrak{B}_{js}^{\mathrm{T}}\boldsymbol{C}\mathfrak{B}_{i\tau} + \lambda\phi^{\mathrm{T}}\boldsymbol{\sigma}_o\boldsymbol{I}\, dV\right)\boldsymbol{u}_{i\tau}^{(2)} &= \left(\lambda\boldsymbol{f}_{\text{ref}} - \int_{V_{(\mathrm{e})}} \mathfrak{B}_{js}\boldsymbol{\sigma}_t\, dV\right).\end{aligned} \tag{B.8}$$

Subtracting these equations one gets

$$\begin{aligned}\left(\int_{V_{(\mathrm{e})}} \mathfrak{B}_{js}^{\mathrm{T}}\boldsymbol{C}\mathfrak{B}_{i\tau} + \lambda\phi^{\mathrm{T}}\boldsymbol{\sigma}_o\boldsymbol{I}\, dV\right)\left(\boldsymbol{u}_{i\tau}^{(1)} - \boldsymbol{u}_{i\tau}^{(2)}\right) &= \boldsymbol{0}\\ \left(\boldsymbol{k}_{(\mathrm{e})}^{ij\tau s} + \lambda\boldsymbol{\kappa}_{(\mathrm{e})}^{ij\tau s}\right)\left(\boldsymbol{u}_{i\tau}^{(1)} - \boldsymbol{u}_{i\tau}^{(2)}\right) &= \boldsymbol{0},\end{aligned} \tag{B.9}$$

where

$$\boldsymbol{\kappa}_{(\mathrm{e})}^{ij\tau s} = \int_{V_{(\mathrm{e})}} \phi^{\mathrm{T}}\boldsymbol{\sigma}_o\boldsymbol{I}\, dV \tag{B.10}$$

[1] From this point the symbol Δ is dropped.

is the elemental geometrical stiffness matrix. After assembly

$$(\boldsymbol{K} + \lambda \boldsymbol{K}_{\mathrm{G}})(\boldsymbol{u}^{(1)} - \boldsymbol{u}^{(2)}) = \boldsymbol{0}. \tag{B.11}$$

Equation (B.11) has non-trivial solution if and only if

$$\det(\boldsymbol{K} + \lambda \boldsymbol{K}_{\mathrm{G}}) = 0. \tag{B.12}$$

The solution of this gives, by construction, the buckling loads (eigenvalues) λ and the buckling shapes (eigenvectors).

Geometrical Stiffness Matrix In order to derive the Geometrical Stiffness matrix it is necessary to write the third term of equation (B.5) in the form

$$\int_{V_{(\mathrm{e})}} \delta \boldsymbol{\nu}^{\mathrm{T}}_{ij\tau s} \boldsymbol{\sigma}_t \, dV = \delta \boldsymbol{u}^{\mathrm{T}}_{js} (\cdot) \boldsymbol{u}_{i\tau}. \tag{B.13}$$

An expression of the variation of the non-linear term $\boldsymbol{\nu}$ is now derived. In its general form, the non-linear part of the stress tensor reads

$$\boldsymbol{\nu} = \frac{1}{2} \begin{bmatrix} (\frac{\partial u}{\partial x})^2 & (\frac{\partial v}{\partial x})^2 & (\frac{\partial w}{\partial x})^2 \\ (\frac{\partial u}{\partial y})^2 & (\frac{\partial v}{\partial y})^2 & (\frac{\partial w}{\partial y})^2 \\ (\frac{\partial u}{\partial z})^2 & (\frac{\partial v}{\partial z})^2 & (\frac{\partial w}{\partial z})^2 \\ \frac{\partial u}{\partial y}\frac{\partial u}{\partial z} & \frac{\partial v}{\partial y}\frac{\partial v}{\partial z} & \frac{\partial w}{\partial y}\frac{\partial w}{\partial z} \\ \frac{\partial u}{\partial x}\frac{\partial u}{\partial z} & \frac{\partial v}{\partial x}\frac{\partial v}{\partial z} & \frac{\partial w}{\partial x}\frac{\partial w}{\partial z} \\ \frac{\partial u}{\partial x}\frac{\partial u}{\partial y} & \frac{\partial v}{\partial x}\frac{\partial v}{\partial y} & \frac{\partial w}{\partial x}\frac{\partial w}{\partial y} \end{bmatrix},$$

where u, v, w are the components of the displacement vector. It can be proved that, after substitution of equation (4.3), the variation $\delta\boldsymbol{\nu}$ can be expressed as

$$\delta \boldsymbol{\nu}_{ij\tau s} = \begin{bmatrix} \left(N_i N_j F_{\tau,x} F_{s,x}\right)\left(\delta u_{js} u_{i\tau} + \delta v_{js} v_{i\tau} + \delta w_{js} w_{i\tau}\right) \\ \left(N_{i,y} N_{j,y} F_\tau F_s\right)\left(\delta u_{js} u_{i\tau} + \delta v_{js} v_{i\tau} + \delta w_{js} w_{i\tau}\right) \\ \left(N_i N_j F_{\tau,z} F_{s,z}\right)\left(\delta u_{js} u_{i\tau} + \delta v_{js} v_{i\tau} + \delta w_{js} w_{i\tau}\right) \\ \left(N_i N_{j,y} F_{\tau,z} F_s + N_{i,y} N_j F_\tau F_{s,z}\right)\left(\delta u_{js} u_{i\tau} + \delta v_{js} v_{i\tau} + \delta w_{js} w_{i\tau}\right) \\ \left(N_i N_j F_{\tau,z} F_{s,x} + N_i N_j F_{\tau,x} F_{s,z}\right)\left(\delta u_{js} u_{i\tau} + \delta v_{js} v_{i\tau} + \delta w_{js} w_{i\tau}\right) \\ \left(N_{i,y} N_j F_\tau F_{s,x} + N_i N_{j,y} F_{\tau,x} F_s\right)\left(\delta u_{js} u_{i\tau} + \delta v_{js} v_{i\tau} + \delta w_{js} w_{i\tau}\right) \end{bmatrix} \tag{B.14}$$

where the subscripts with a comma denote first derivatives. The product of $\delta\boldsymbol{\nu}_{ij\tau s}$ and $\boldsymbol{\sigma}_t^{\mathrm{T}} = \{\sigma_{xx}, \sigma_{yy}, \sigma_{zz}, \tau_{yz}, \tau_{zx}, \tau_{xy}\}$ can be written as

$$\delta \boldsymbol{\nu}_{ij\tau s} \boldsymbol{\sigma}_t = \delta \boldsymbol{u}^{\mathrm{T}}_{js} \left(\phi^{\mathrm{T}} \boldsymbol{\sigma}_t \boldsymbol{I}\right) \boldsymbol{u}_{i\tau} \tag{B.15}$$

if ϕ is defined to be

$$\phi = \begin{bmatrix} N_i N_j F_{\tau,x} F_{s,x} \\ N_{i,y} N_{j,y} F_\tau F_s \\ N_i N_j F_{\tau,z} F_{s,z} \\ N_i N_{j,y} F_{\tau,z} F_s + N_{i,y} N_j F_\tau F_{s,z} \\ N_i N_j F_{\tau,z} F_{s,x} + N_i N_j F_{\tau,x} F_{s,z} \\ N_{i,y} N_j F_\tau F_{s,x} + N_i N_{j,y} F_{\tau,x} F_s \end{bmatrix} \tag{B.16}$$

and $\boldsymbol{I}$ is the 3×3 identity matrix. So, the third term of equation (B.5) is then

$$\int_{V_{(e)}} \delta \boldsymbol{\nu}_{ij\tau s}^{\mathrm{T}} \boldsymbol{\sigma}_t \, dV = \delta \boldsymbol{u}_{js}^{\mathrm{T}} \left(\int_{V_{(e)}} \phi^{\mathrm{T}} \boldsymbol{\sigma}_t \boldsymbol{I} \, dV \right) \boldsymbol{u}_{i\tau}, \tag{B.17}$$

and the elemental geometrical stiffness matrix takes is final form by multiplying ϕ^{T}, $\boldsymbol{\sigma}_o$ and $\boldsymbol{I}$:

$$\begin{aligned} \boldsymbol{\kappa}_{(e)}^{ij\tau s} &= \int_{V_{(e)}} \phi^{\mathrm{T}} \boldsymbol{\sigma}_o \boldsymbol{I} \, dV \\ &= \kappa^{ij\tau s} \begin{bmatrix} 1 & 0 & 0 \\ 0 & 1 & 0 \\ 0 & 0 & 1 \end{bmatrix} \end{aligned} \tag{B.18}$$

with

$$\begin{aligned} \kappa^{ij\tau s} = \int_{V_{(e)}} & \sigma_{xx} N_i N_j F_{\tau,x} F_{s,x} + \sigma_{yy} N_{i,y} N_{j,y} F_\tau F_s + \sigma_{zz} N_i N_j F_{\tau,z} F_{s,z} + \\ & \sigma_{yz} (N_i N_{j,y} F_{\tau,z} F_s + N_{i,y} N_j F_\tau F_{s,z}) + \\ & \sigma_{xz} (N_i N_j F_{\tau,z} F_{s,x} + N_i N_j F_{\tau,x} F_{s,z}) + \\ & \sigma_{xy} (N_{i,y} N_j F_\tau F_{s,x} + N_i N_{j,y} F_{\tau,x} F_s) \, dV \end{aligned} \tag{B.19}$$

APPENDIX C

3D BEAM MODEL TANGENT NUCLEUS

In this appendix an explicit form of the non-linear Tangent Matrix nucleus described in Section 5.3 is provided. If the equations are linearised, then the Tangent Nucleus coincides with the Linear Stiffness Fundamental Nucleus described in Chapters 2 and 3.

C.1 Tangent Nucleus

The Cartesian metric components are written as

$$
\begin{aligned}
x_1 &= 1+\frac{\partial u}{\partial x} & y_1 &= \frac{\partial v}{\partial x} & z_1 &= \frac{\partial w}{\partial x}\\
x_2 &= \frac{\partial u}{\partial y} & y_2 &= 1+\frac{\partial v}{\partial y} & z_2 &= \frac{\partial w}{\partial y}\\
x_2 &= \frac{\partial u}{\partial z} & y_2 &= \frac{\partial v}{\partial z} & z_2 &= 1+\frac{\partial w}{\partial z},
\end{aligned}
$$

where u, v and w are the components of the displacement field. Let τ & s be the indexes related to the cross-section expansion functions $F(x,z)$ and i & j indexes for the beam functions $N(y)$ and define the following terms:

$$
\begin{aligned}
T_1 &= G_{jsy}x_1+G_{jsx}x_2 & T_2 &= G_{jsz}x_1+G_{jsx}x_3 & T_3 &= G_{jsz}x_2+G_{jsy}x_3\\
T_4 &= G_{i\tau z}x_2+G_{i\tau y}x_3 & T_5 &= G_{i\tau z}x_1+G_{i\tau x}x_3 & T_6 &= G_{i\tau y}x_1+G_{i\tau x}x_2\\
T_7 &= G_{i\tau y}y_1+G_{i\tau x}y_2 & T_8 &= G_{i\tau z}y_1+G_{i\tau x}y_3 & T_9 &= G_{i\tau z}y_2+G_{i\tau y}y_3\\
T_{10} &= G_{i\tau y}z_1+G_{i\tau x}z_2 & T_{11} &= G_{i\tau z}z_1+G_{i\tau x}z_3 & T_{12} &= G_{i\tau z}z_2+G_{i\tau y}z_3\\
T_{13} &= G_{jsy}y_1+G_{jsx}y_2 & T_{14} &= G_{jsz}y_1+G_{jsx}y_3 & T_{15} &= G_{jsz}y_2+G_{jsy}y_3\\
T_{16} &= G_{jsy}z_1+G_{jsx}z_2 & T_{17} &= G_{jsz}z_1+G_{jsx}z_3 & T_{18} &= G_{jsz}z_2+G_{jsy}z_3,
\end{aligned}
$$

where G and its derivatives are defined in equation (5.20) and equation (5.22) respectively. Taking C_{kl}, with $k,l = 1,...,6$, as the components of the 6×6 material matrix the following terms are defined:

$$
\begin{aligned}
T_{19} &= C_{11}G_{jsx}x_1 + C_{12}G_{jsy}x_2 + C_{16}T_1 + C_{13}G_{jsz}x_3 + C_{15}T_2 + C_{14}T_3 \\
T_{20} &= C_{12}G_{jsx}x_1 + C_{22}G_{jsy}x_2 + C_{26}T_1 + C_{23}G_{jsz}x_3 + C_{25}T_2 + C_{24}T_3 \\
T_{21} &= C_{13}G_{jsx}x_1 + C_{23}G_{jsy}x_2 + C_{36}T_1 + C_{33}G_{jsz}x_3 + C_{35}T_2 + C_{34}T_3 \\
T_{22} &= C_{14}G_{jsx}x_1 + C_{24}G_{jsy}x_2 + C_{46}T_1 + C_{34}G_{jsz}x_3 + C_{45}T_2 + C_{44}T_3 \\
T_{23} &= C_{15}G_{jsx}x_1 + C_{25}G_{jsy}x_2 + C_{56}T_1 + C_{35}G_{jsz}x_3 + C_{55}T_2 + C_{45}T_3 \\
T_{24} &= C_{16}G_{jsx}x_1 + C_{26}G_{jsy}x_2 + C_{66}T_1 + C_{36}G_{jsz}x_3 + C_{56}T_2 + C_{46}T_3 \\
T_{25} &= C_{11}G_{jsx}y_1 + C_{12}G_{jsy}y_2 + C_{16}T_{13} + C_{13}G_{jsz}y_3 + C_{15}T_{14} + C_{14}T_{15} \\
T_{26} &= C_{12}G_{jsx}y_1 + C_{22}G_{jsy}y_2 + C_{26}T_{13} + C_{23}G_{jsz}y_3 + C_{25}T_{14} + C_{24}T_{15} \\
T_{27} &= C_{13}G_{jsx}y_1 + C_{23}G_{jsy}y_2 + C_{36}T_{13} + C_{33}G_{jsz}y_3 + C_{35}T_{14} + C_{34}T_{15} \\
T_{28} &= C_{14}G_{jsx}y_1 + C_{24}G_{jsy}y_2 + C_{46}T_{13} + C_{34}G_{jsz}y_3 + C_{25}T_{45} + C_{44}T_{15} \\
T_{29} &= C_{15}G_{jsx}y_1 + C_{25}G_{jsy}y_2 + C_{56}T_{13} + C_{35}G_{jsz}y_3 + C_{55}T_{14} + C_{45}T_{15} \\
T_{30} &= C_{16}G_{jsx}y_1 + C_{26}G_{jsy}y_2 + C_{66}T_{13} + C_{36}G_{jsz}y_3 + C_{56}T_{14} + C_{46}T_{15} \\
T_{31} &= C_{11}G_{jsx}z_1 + C_{12}G_{jsy}z_2 + C_{16}T_{16} + C_{13}G_{jsz}z_3 + C_{15}T_{17} + C_{14}T_{18} \\
T_{32} &= C_{12}G_{jsx}z_1 + C_{22}G_{jsy}z_2 + C_{26}T_{16} + C_{23}G_{jsz}z_3 + C_{25}T_{17} + C_{24}T_{18} \\
T_{33} &= C_{13}G_{jsx}z_1 + C_{23}G_{jsy}z_2 + C_{36}T_{16} + C_{33}G_{jsz}z_3 + C_{35}T_{17} + C_{34}T_{18} \\
T_{34} &= C_{14}G_{jsx}z_1 + C_{24}G_{jsy}z_2 + C_{46}T_{16} + C_{34}G_{jsz}z_3 + C_{45}T_{17} + C_{44}T_{18} \\
T_{35} &= C_{15}G_{jsx}z_1 + C_{25}G_{jsy}z_2 + C_{56}T_{16} + C_{35}G_{jsz}z_3 + C_{55}T_{17} + C_{45}T_{18} \\
T_{36} &= C_{16}G_{jsx}z_1 + C_{26}G_{jsy}z_2 + C_{66}T_{16} + C_{36}G_{jsz}z_3 + C_{56}T_{17} + C_{46}T_{18}
\end{aligned}
$$

and

$$
\begin{aligned}
k_s = {} & \sigma_{xx}G_{i\tau x}G_{jsx} + \sigma_{yy}G_{i\tau y}G_{jsy} + \sigma_{zz}G_{i\tau z}G_{jsz} \\
& + \sigma_{yz}\left(G_{i\tau z}G_{jsy} + G_{i\tau y}G_{jsz}\right) \\
& + \sigma_{xz}\left(G_{i\tau x}G_{jsz} + G_{i\tau z}G_{jsx}\right) \\
& + \sigma_{xy}\left(G_{i\tau x}G_{jsy} + G_{i\tau y}G_{jsx}\right).
\end{aligned}
$$

With these, the entries of the Tangent Matrix

$$
\boldsymbol{\kappa}^{ij\tau s}_{(\mathrm{T})} = \begin{bmatrix} k_{11} & k_{12} & k_{13} \\ k_{21} & k_{22} & k_{23} \\ k_{31} & k_{32} & k_{33} \end{bmatrix}
$$

are computed as follows:

$$
\begin{aligned}
k_{11} &= \int_{V_{(e)}} G_{i\tau x} x_1 T_{19} + G_{i\tau y} x_2 T_{20} + G_{i\tau z} x_3 T_{21} + T_4 T_{22} + T_5 T_{23} + T_6 T_{24} + k_s \, dV \\
k_{12} &= \int_{V_{(e)}} G_{i\tau x} y_1 T_{19} + G_{i\tau y} y_2 T_{20} + G_{i\tau z} y_3 T_{21} + T_{24} T_7 + T_8 T_{23} + T_{22} T_9 \, dV \\
k_{13} &= \int_{V_{(e)}} G_{i\tau x} z_1 T_{19} + G_{i\tau y} z_2 T_{20} + G_{i\tau z} z_3 T_{21} + T_{24} T_{10} + T_{11} T_{23} + T_{22} T_{12} \, dV \\
k_{21} &= \int_{V_{(e)}} G_{i\tau x} x_1 T_{25} + G_{i\tau y} x_2 T_{26} + G_{i\tau z} x_3 T_{27} + T_4 T_{28} + T_5 T_{29} + T_6 T_{30} \, dV \\
k_{22} &= \int_{V_{(e)}} G_{i\tau x} y_1 T_{25} + G_{i\tau y} y_2 T_{26} + G_{i\tau z} y_3 T_{27} + T_9 T_{28} + T_8 T_{29} + T_7 T_{30} + k_s \, dV \\
k_{23} &= \int_{V_{(e)}} G_{i\tau x} z_1 T_{25} + G_{i\tau y} z_2 T_{26} + G_{i\tau z} z_3 T_{27} + T_{30} T_{10} + T_{11} T_{29} + T_{28} T_{12} \, dV \\
k_{23} &= \int_{V_{(e)}} G_{i\tau x} z_1 T_{25} + G_{i\tau y} z_2 T_{26} + G_{i\tau z} z_3 T_{27} + T_{30} T_{10} + T_{11} T_{29} + T_{28} T_{12} \, dV \\
k_{31} &= \int_{V_{(e)}} G_{i\tau x} x_1 T_{31} + G_{i\tau y} x_2 T_{32} + G_{i\tau z} x_3 T_{33} + T_4 T_{34} + T_5 T_{35} + T_6 T_{36} \, dV \\
k_{32} &= \int_{V_{(e)}} G_{i\tau x} y_1 T_{31} + G_{i\tau y} y_2 T_{32} + G_{i\tau z} y_3 T_{33} + T_8 T_{35} + T_5 T_{35} + T_7 T_{36} \, dV \\
k_{33} &= \int_{V_{(e)}} G_{i\tau x} z_1 T_{31} + G_{i\tau y} z_2 T_{32} + G_{i\tau z} z_3 T_{33} + T_{12} T_{34} + T_{11} T_{35} + T_{10} T_{36} + k_s \, dV.
\end{aligned}
$$

By setting the metric components to

$$
\begin{array}{lll}
x_1 = 1 & y_1 = 0 & z_1 = 0 \\
x_2 = 0 & y_2 = 1 & z_2 = 0 \\
x_2 = 0 & y_2 = 0 & z_2 = 1,
\end{array}
$$

and $k_s = 0$, the Tangent Nucleus reduces to the Linear Stiffness Fundamental Nucleus $\boldsymbol{k}^{(e)}_{ij\tau s}$ described in Chapters 2 and 3.

BIBLIOGRAPHY

[1] S. Timoshenko, History of strength of materials: with a brief account of the history of theory of elasticity and theory of structures, Courier Corporation, 1983.

[2] R. Ballarini, The Da Vinci-Euler-Bernoulli beam theory?, 2003, Mechanical Engineering Magazine Online (2003).

[3] J.N. Reddy, Mechanics of laminated composite plates and shells: theory and analysis (2003).

[4] C. M. Wang, C. Y. Wang, J. Reddy, Exact solutions for Buckling of Structural Members, Vol. 6, CRC press, 2004.

[5] B. Szabó, I. Babuška, Introduction to Finite Element Analysis: Formulation, Verification and Validation, Wiley, 2011.

[6] J. D. Kemper, Large deflections of tapered cantilever beams, International Journal of Mechanical Sciences 10 (6) (1968) 469–478.

[7] G. Payette, J. Reddy, A seven-parameter spectral/hp finite element formulation for isotropic, laminated composite and functionally graded shell structures, Computer methods in applied mechanics and engineering 278 (2014) 664–704.

[8] D. K. Nguyen, Large displacement response of tapered cantilever beams made of axially functionally graded material, Composites Part B: Engineering 55 (2013) 298–305.

[9] C. Thurnherr, New analysis methods for corrugated laminates, Ph.D. thesis, ETH Zurich (2017).

[10] D. Manickarajah, Y. Xie, G. Steven, An evolutionary method for optimization of plate buckling resistance, Finite Elements in Analysis and Design 29 (3) (1998) 205 – 230. doi:https://doi.org/10.1016/S0168-874X(98)00012-2.

[11] E. Carrera, M. Cinefra, M. Petrolo, E. Zappino, Finite Element Analysis of Structures through Unified Formulation, John Wiley & Sons Ltd., West Sussex, United Kingdom, 2014.

[12] S. Minera, M. Patni, E. Carrera, M. Petrolo, P. Weaver, A. Pirrera, Three-dimensional stress analysis for beam-like structures using Serendipity Lagrange shape functions, International Journal of Solids and Structures 141 (2018) 279–296.

[13] S. Minera, M. Patni, A. Pirrera, P. Weaver, Buckling-resistant topological design using sensitivities to variations in localised nominal stiffness, To be submitted to: Thin-Walled Structures (2018).

[14] S. Minera, M. Patni, A. Pirrera, P. Weaver, Design of topologically efficient buckling-resistant structures using eigenstresses, To be submitted to: Thin-Walled Structures (2018).

[15] I. Todhunter, A History of the Theory of Elasticity and of the Strength of Materials, Cambridge University Press, 2014.

[16] L. Euler, Methodus inveniendi lineas curvas maximi minimive proprietate gaudentes sive solutio problematis isoperimetrici latissimo sensu accepti, Vol. 1, Springer Science & Business Media, 1952.

[17] D. Mucichescu, Bounds for stiffness of prismatic beams, Journal of Structural Engineering 110 (1984) 1410–1414.

[18] S. P. Timoshenko, J. N. Goodier, Theory of Elasticity, New York: McGraw-Hill, 1970.

[19] G. R. Cowper, The shear coefficient in Timoshenko's beam theory, Journal of Applied Mechanics 33.2 (1966) 335–340.

[20] I. S. Sokolnikoff, Mathematical Theory of Elasticity, New York: McGraw-Hill, 1956.

[21] K. Washizu, Variational methods in elasticity and plasticity, International Series of Monographs in Aeronautics and Astronautics (1968).

[22] R. Schardt, Eine erweiterung der technischen biegetheorie zur berechnung prismatischer faltwerke. der stahlbau 35 (1966), pp. 161–171.

[23] W. Kanok-Nukulchai, Y. S. Shin, Versatile and improved higher-order beam element, Journal of Structural Engineering 110 (9) (1984) 2234–2249.

[24] J. N. Reddy, A simple higher-order theory for laminated composite plates, Journal of applied mechanics 51 (4) (1984) 745–752.

[25] E. Reissner, On a certain mixed variational theorem and a proposed application, International Journal for Numerical Methods in Engineering 20 (7) (1984) 1366–1368.

[26] V. Giavotto, M. Borri, P. Mantegazza, G. Ghiringhelli, V. Carmaschi, G. Maffioli, F. Mussi, Anisotropic beam theory and applications, Computers & Structures 16 (1-4) (1983) 403–413.

[27] P. . Ladevèze, J. Simmonds, De nouveaux concepts en théorie des poutres pour des charges et des géométries quelconques, Comptes Rendus de l'Académie des Sciences 332 (1996) 445–462.

[28] P. Ladevèze, J. Simmonds, New concepts for linear beam theory with arbitrary geometry and loading, European Journal of Mechanics, A/Solids 17 (3) (1998) 377–402.

[29] K. Surana, S. Nguyen, Two-dimensional curved beam element with higher-order hierarchical transverse approximation for laminated composites, Computers and Structures 36 (1990) 499 – 511.

[30] R. Kameswara, Y. M. Desai, M. R. Chitnis, Free vibrations of laminated beams using mixed theory, Composite Structures 52 (2001) 149–160.

[31] V. Berdichevsky, Equations of the theory of anisotropic inhomogeneous rods, Doklady Akademii Nauk 228 (1976) 558–561.

[32] V. L. Berdichevsky, E. Armanios, A. Badir, Theory of anisotropic thin-walled closed-cross-section beams, Composites Engineering 2.5-7 (1992) 411–432.

[33] W. Yu, V. Volovoi, D. Hodges, X. Hong, Validation of the variational asymptotic beam sectional analysis, The American Institute of Aeronautics and Astronautics 40(10) (2010) 2105–2112.

[34] W. Yu, D. H. Hodges, J. C. Ho, Variational asymptotic beam sectional analysis - an updated version, International Journal of Engineering Science 59 (2012) 40–64.

[35] N. Silvestre, D. Camotim, First-order generalised beam theory for arbitrary orthotropic materials, Thin Walled Structures 40.9 (2002) 791–820.

[36] E. Carrera, A. Pagani, M. Petrolo, E. Zappino, Recent developments on refined theories for beams with applications, Mechanical Engineering Reviews 2 (2) (2015) 14–00298.

[37] E. Carrera, G. Giunta, Refined beam theories based on a unified formulation, International Journal of Applied Mechanics 02 (2010) 117–143.

[38] E. Carrera, G. Giunta, M. Petrolo, A Modern and Compact Way to Formulate Classical and Advanced Beam Theories, Saxe-Coburg Publications, United Kingdom, 2010.

[39] E. Carrera, Theories and finite elements for multilayered, anisotropic, composite plates and shells, Archives of Computational Methods in Engineering 9 (2002) 87–140.

[40] E. Carrera, M. Filippi, E. Zappino, Laminated beam analysis by polynomial, trigonometric, exponential and zig-zag theories, European Journal of Mechanics, A/Solids 41 (2013) 58–69.

[41] M. Filippi, A. Pagani, M. Petrolo, G. Colonna, E. Carrera, Static and free vibration analysis of laminated beams by refined theory based on chebyshev polynomials, Composite Structures 132 (2015) 1248–1259.

[42] A. Pagani, A. G. de Miguel, M. Petrolo, E. Carrera, Analysis of laminated beams via unified formulation and legendre polynomial expansions, Composite Structures 156 (2016) 78–92.

[43] E. Reissner, On a mixed variational theorem and on shear deformable plate theory, International Journal for Numerical Methods in Engineering 23 (2) (1986) 193–198.

[44] E. Carrera, Evaluation of layerwise mixed theories for laminated plates analysis, AIAA journal 36 (5) (1998) 830–839.

[45] E. Carrera, Mixed layer-wise models for multilayered plates analysis, Composite Structures 43 (1) (1998) 57–70.

[46] A. M. Lyapunov, The general problem of motion stability, Annals of Mathematics Studies 17 (1892).

[47] R. Thom, R. Thom, R. Thom, F. Mathématicien, R. Thom, F. Mathematician, Stabilité structurelle et morphogénèse: essai d'une théorie générale des modèles, WA Benjamin Reading, Mass., 1972.

[48] T. v. Karman, The buckling of thin cylindrical shells under axial compression, Journal of the Aeronautical Sciences 8 (8) (1941) 303–312.

[49] T. V. Karman, The buckling of spherical shells by external pressure, Journal of the Aeronautical Sciences 7 (2) (1939) 43–50.

[50] T. v. Karman, The influence of curvature on the buckling characteristics of structures, Journal of the Aeronautical Sciences 7 (7) (1940) 276–289.

[51] W. T. Koiter, Over de stabiliteit van het elastisch evenwicht (1945).

[52] W. T. Koiter, Elastic Stability of Solids and Structures, Cambridge University Press, 2008. doi:10.1017/CBO9780511546174.

[53] B. Budiansky, Theory of buckling and post-buckling behavior of elastic structures, in: Advances in applied mechanics, Vol. 14, Elsevier, 1974, pp. 1–65.

[54] S. Timoshenko, M. Gere, Theory of Elastic Stability, Dover Publications, Inc., 1961.

[55] H. Wagner, Torsion and buckling of open sections (1936).

[56] N. S. Trahair, Flexural-torsional buckling of structures, Routledge, 2017.

[57] R. K. Livesley, D. B. Chandler, Stability Functions for Structural Frameworks, Manchester University Press, 1956.

[58] A. Kromm, K. Marguerre, Behavior of a plate strip under shear and compressive stresses beyond the buckling limit, NASA Technical Report (1938).

[59] L. H. Donnell, A new theory for the buckling of thin cylinders under axial compression and bending, Trans. Asme 56 (11) (1934) 795–806.

[60] M. W. Hyer, H. Lee, The use of curvilinear fiber format to improve buckling resistance of composite plates with central circular holes, Composite Structures 18 (3) (1991) 239–261.

[61] S. White, P. Weaver, Towards imperfection insensitive buckling response of shell structures-shells with plate-like post-buckled responses, The Aeronautical Journal 120 (1224) (2016) 233–253.

[62] B. Cox, R. Groh, D. Avitabile, A. Pirrera, Modal nudging in nonlinear elasticity: Tailoring the elastic post-buckling behaviour of engineering structures, Journal of the Mechanics and Physics of Solids 116 (2018) 135–149.

[63] Z. Bažant, Stability of elastic, anelastic, and disintegrating structures: a conspectus of main results, ZAMM-Journal of Applied Mathematics and Mechanics/Zeitschrift für Angewandte Mathematik und Mechanik: Applied Mathematics and Mechanics 80 (11-12) (2000) 709–732.

[64] E. Carrera, G. Giunta, M. Petrolo, Beam Structures: Classical and Advanced Theories, John Wiley and Sons, 2011.

[65] P. F. Pai, M. J. Schulz, Shear correction factors and an energy-consistent beam theory, International journal of solids and structures 36 (10) (1999) 1523–1540.

[66] F. Gruttmann, R. Sauer, W. Wagner, Shear stresses in prismatic beams with arbitrary cross-sections, International journal for numerical methods in engineering 45 (7) (1999) 865–889.

[67] F. Gruttmann, W. Wagner, Shear correction factors in timoshenko's beam theory for arbitrary shaped cross-sections, Computational Mechanics 27 (3) (2001) 199–207.

[68] S. P. Timoshenko, Lxvi. on the correction for shear of the differential equation for transverse vibrations of prismatic bars, The London, Edinburgh, and Dublin Philosophical Magazine and Journal of Science 41 (245) (1921) 744–746.

[69] E. Carrera, M. Maiar, M. Petrolo, Component-wise analysis of laminated anisotropic composites, International Journal of Solids and Structures 49 (2012) 1839 – 1851.

[70] E. Carrera, M. Petrolo, Refined One-Dimensional Formulations for Laminated Structure Analysis, AIAA Journal 50 (1) (2012) 176–189.

[71] W. D. Callister, D. G. Rethwisch, Materials science and engineering, Vol. 5, John Wiley & Sons NY, 2011.

[72] T. V. Galambos, Guide to Stability Design Criteria for Metal Structures, John Wiley & Sons, 1998.

[73] W.-F. Chen, E. M. Lui, Structural stability: theory and implementation (1987).

[74] S. P. Timoshenko, Einige stabilitätsprobleme der elastizitätstheorie, Zeitschrift für Mathematik und Physik 58 (4) (1910) 337–385.

[75] R. Lorenz, Achsensymmetrische verzerrungen in dünnwandigen hohlzylindern, Zeitschrift des Vereines Deutscher Ingenieure 52 (43) (1908) 1706–1713.

[76] E. Kreyszig, Advanced Engineering Mathematics, Wiley, 2011.

[77] G. B. Arfken, H. J. Weber, F. E. Harris, Mathematical Methods for Physicists, 2013.

[78] A. Pagani, A. G. de Miguel, E. Carrera, Cross-sectional mapping for refined beam elements with applications to shell-like structures, Computational Mechanics 59 (6) (2017) 1031–1048.
doi:10.1007/s00466-017-1390-7.

[79] C. Geuzaine, J.-F. Remacle, Gmsh: A 3-d finite element mesh generator with built-in pre-and post-processing facilities, International Journal for Numerical Methods in Engineering 79 (11) (2009) 1309–1331.

[80] E. Carrera, A. de Miguel, A. Pagani, Extension of mitc to higher-order beam models and shear locking analysis for compact, thin-walled, and composite structures, International Journal for Numerical Methods in Engineering 112 (13) (2017) 1889–1908.

[81] J. Boyd, R. Petschek, The relationships between chebyshev, legendre and jacobi polynomials: The generic superiority of chebyshev polynomials and three important exceptions., Journal of Scientific Computing 59 (1) (2014) 1–27.

[82] S. Arora, B. Barak, Computational Complexity: A Modern Approach, Cambridge University Press, 2009.

[83] H. Wilf, Algorithms and complexity, Prentice-Hall international editions, Prentice-Hall, 1986.

[84] V. Weingarten, P. Seide, P. JP, Buckling of thin-walled circular cylinders, NASA SP-8007 National Aeronautics and Space Administration (1968).

[85] R. Sullins, G. Smith, S. EE, Manual for structural stability analysis of sandwich plates and shells, NASA CR-1457 National Aeronautics and Space Administration (1968).

[86] R. Degenhardt, A. Kling, A. Bethge, J. Orf, L. Kärger, R. Zimmermann, K. Rohwer, A. Calvi, Investigations on imperfection sensitivity and deduction of improved knock-down factors for unstiffened cfrp cylindrical shells, Composite Structures 92 (8) (2010) 1939 – 1946.

[87] M. C. Lee, R. M. Payne, D. W. Kelly, R. S. Thomson, Determination of robustness for a stiffened composite structure using stochastic analysis, Composite Structures 86 (1) (2008) 78 – 84, fourteenth International Conference on Composite Structures.

[88] S. C. White, G. Raju, P. M. Weaver, Initial post-buckling of variable-stiffness curved panels, Journal of the Mechanics and Physics of Solids 71 (1) (2014) 132–155. doi:10.1016/j.jmps.2014.07.003.

[89] G. Raju, Z. Wu, B. C. Kim, P. M. Weaver, Prebuckling and buckling analysis of variable angle tow plates with general boundary conditions, Composite Structures 94 (2012) 2961–2970. doi:10.1016/j.compstruct.2012.04.002.

[90] A. C. Orifici, C. Bisagni, Perturbation-based imperfection analysis for composite cylindrical shells buckling in compression, Composite Structures 106 (2013) 520–528. doi:10.1016/j.compstruct.2013.06.028.

[91] E. Carrera, A. Pagani, J. Banerjee, Linearized buckling analysis of isotropic and composite beam-columns by Carrera Unified Formulation and dynamic stiffness method, Mechanics of Advanced Materials and Structures 23 (9) (2016) 1092–1103. doi:10.1080/15376494.2015.1121524.

[92] S. M. Ibrahim, E. Carrera, M. Petrolo, E. Zappino, Buckling of composite thin walled beams by refined theory, Composite Structures 94 (2) (2012) 563–570. doi:10.1016/j.compstruct.2011.08.020.

[93] J. N. Reddy, An Introduction to Nonlinear Finite Element Analysis: with Applications to Heat transfer, Fluid mechanics, and Solid mechanics, OUP Oxford, 2014.

[94] V. Ciampi, M. Crisfield, Non-linear finite element analysis of solids and structures, Meccanica 32 (6) (1997) 586–587.

[95] A. Pagani, E. Carrera, Unified formulation of geometrically nonlinear refined beam theories Unified formulation of geometrically nonlinear refined beam theories, Mechanics of Advanced Materials and Structures 6494 (September) (2016) 0–17.
doi:10.1080/15376494.2016.1232458.

[96] X.-m. Jiang, H. Chen, J. Y. R. Liew, R. de Borst, M. a. M. Crisfield, J. J. C. Remmers, C. V. Verhoosel, Non-linear finite element analysis of solids and structures, Volume 1, East 58 (1991) 193–212.
doi:10.1017/CBO9781107415324.004.

[97] T. A. Davis, Direct methods for sparse linear systems, SIAM, 2006.

[98] Y. Saad, Iterative methods for sparse linear systems, SIAM, 2003.

[99] K.-J. Bathe, The subspace iteration method – revisited, Computers & Structures 126 (Supplement C) (2013) 177 – 183.
doi:https://doi.org/10.1016/j.compstruc.2012.06.002.

[100] P. Arbenz, D. Kressner, D. Zürich, Lecture notes on solving large scale eigenvalue problems, D-MATH, EHT Zurich 2 (2012).

[101] Y. Saad, Numerical Methods for Large Eigenvalue Problems, Manchester University Press, 1992.

[102] J. Thorson, Gaussian elimination on a banded matrix, SEP-Report 20 (1979) 143–154.

[103] B. N. Parlett, The symmetric eigenvalue problem, SIAM, 1998.

[104] S. M. Ibrahim, S. H. Alsayed, H. Abbas, E. Carrera, Y. A. Al-Salloum, T. H. Almusallam, Free vibration of tapered beams and plates based on unified beam theory, Journal of Vibration and Control 20 (16) (2014) 2450–2463.

[105] E. Zappino, A. Viglietti, E. Carrera, The analysis of tapered structures using a component-wise approach based on refined one-dimensional models, Aerospace Science and Technology 65 (2017) 141–156.

[106] A. Viglietti, E. Zappino, E. Carrera, Free vibration analysis of locally damaged aerospace tapered composite structures using component-wise models, Composite Structures 192 (2018) 38–51.

[107] G. De Pietro, A. G. de Miguel, E. Carrera, G. Giunta, S. Belouettar, A. Pagani, Strong and weak form solutions of curved beams via carrera's unified formulation, Mechanics of Advanced Materials and Structures (2018) 1–12.

[108] T. Belytschko, L. W. Glaum, Applications of higher order corotational stretch theories to nonlinear finite element analysis, Computers & Structures 10 (1-2) (1979) 175–182.

[109] L. W. Glaum, Direct iteration and perturbation methods for the analysis of nonlinear structures., Ph.D. thesis, University of Illinois at Chicago (1976).

[110] K. J. Bathe, S. Bolourchi, Large displacement analysis of three-dimensional beam structures, International journal for numerical methods in engineering 14 (7) (1979) 961–986.

[111] D. H. Hodges, Proper definition of curvature in nonlinear beam kinematics, AIAA Journal 22 (12) (1984) 1825–1827.

[112] D. A. Danielson, D. H. Hodges, Nonlinear beam kinematics by decomposition of the rotation tensor, Journal of Applied Mechanics 54 (2) (1987) 258–262.

[113] M. A. Crisfield, A consistent co-rotational formulation for non-linear, three-dimensional, beam-elements, Computer Methods in Applied Mechanics and Engineering 81 (2) (1990) 131–150.

[114] K. S. Surana, R. M. Sorem, Geometrically non-linear formulation for three dimensional curved beam elements with large rotations, International Journal for Numerical Methods in Engineering 28 (1) (1989) 43–73.

[115] A. Ibrahimbegović, On finite element implementation of geometrically nonlinear reissner's beam theory: three-dimensional curved beam elements, Computer Methods in Applied Mechanics and Engineering 122 (1-2) (1995) 11–26.

[116] A. Ibrahimbegović, F. Frey, Finite element analysis of linear and non-linear planar deformations of elastic initially curved beams, International Journal for Numerical Methods in Engineering 36 (19) (1993) 3239–3258.

[117] E. Petrov, M. Géradin, Finite element theory for curved and twisted beams based on exact solutions for three-dimensional solids part 1: Beam concept and geometrically exact nonlinear formulation, Computer Methods in Applied Mechanics and Engineering 165 (1-4) (1998) 43–92.

[118] P. F. Pai, A. H. Nayfeh, A fully nonlinear theory of curved and twisted composite rotor blades accounting for warpings and three-dimensional stress effects, International Journal of Solids and Structures 31 (9) (1994) 1309–1340.

[119] A. Yu, J. Yang, G. Nie, X. Yang, An improved model for naturally curved and twisted composite beams with closed thin-walled sections, Composite Structures 93 (9) (2011) 2322–2329.

[120] M. Patni, S. Minera, R. Groh, A. Pirrera, P. Weaver, Three-dimensional stress analysis for laminated composite and sandwich structures, Composites Part B: Engineering 155 (2018) 299–328.

[121] A. Pagani, E. Carrera, Large-deflection and post-buckling analyses of laminated composite beams by carrera unified formulation, Composite Structures 170 (2017) 40–52.

[122] M. A. Crisfield, J. J. Remmers, C. V. Verhoosel, et al., Nonlinear Finite Element Analysis of Solids and Structures, John Wiley & Sons, 2012.

[123] A. Pagani, E. Carrera, Unified formulation of geometrically nonlinear refined beam theories, Mechanics of Advanced Materials and Structures 25 (1) (2018) 15–31.

[124] C. Thurnherr, L. Ruppen, G. Kress, P. Ermanni, Non-linear stiffness response of corrugated laminates in tensile loading, Composite Structures 157 (2016) 244–255.

[125] C. Thurnherr, L. Ruppen, S. Brändli, C. M. Franceschi, G. Kress, P. Ermanni, Stiffness analysis of corrugated laminates under large deformation, Composite Structures 160 (2017) 457–467.

[126] C. Calladine, Understanding imperfection-sensitivity in the buckling of thin-walled shells, Thin-Walled Structures 23 (1-4) (1995) 215–235.

[127] M. Freeland, G. Thurston, Buckling of imperfect cylinders under axial compression, Nasa Contractor Report, NASA, 1966. (1966).

[128] D. Bushnell, Computerized Buckling Analysis of Shells, Vol. 9, Springer Science & Business Media, 2012.

[129] C. R. Calladine, Shell buckling, without 'imperfections', Advances in Structural Engineering (2018) 1369433217751585.

[130] V. Papadopoulos, G. Stefanou, M. Papadrakakis, Buckling analysis of imperfect shells with stochastic non-gaussian material and thickness properties, International Journal of Solids and Structures 46 (14-15) (2009) 2800–2808.

[131] M. Broggi, G. Schuëller, Efficient modeling of imperfections for buckling analysis of composite cylindrical shells, Engineering Structures 33 (5) (2011) 1796–1806.

[132] J. Kepple, M. Herath, G. Pearce, G. Prusty, R. Thomson, R. Degenhardt, Improved stochastic methods for modelling imperfections for buckling analysis of composite cylindrical shells, Engineering Structures 100 (2015) 385–398.

[133] N. Hu, R. Burgueño, Tailoring the elastic postbuckling response of cylindrical shells: A route for exploiting instabilities in materials and mechanical systems, Extreme Mechanics Letters 4 (2015) 103–110.

[134] N. Hu, R. Burgueño, Elastic postbuckling response of axially-loaded cylindrical shells with seeded geometric imperfection design, Thin-Walled Structures 96 (2015) 256–268.

[135] N. Hu, R. Burgueño, Harnessing seeded geometric imperfection to design cylindrical shells with tunable elastic postbuckling behavior, Journal of Applied Mechanics 84 (1) (2017) 011003.

[136] G. Sved, Z. Ginos, Structural optimization under multiple loading, International Journal of Mechanical Sciences 10 (10) (1968) 803–805.

[137] M. Zhou, Difficulties in truss topology optimization with stress and local buckling constraints, Structural and Multidisciplinary Optimization 11 (1) (1996) 134–136.

[138] G. I. Rozvany, Difficulties in truss topology optimization with stress, local buckling and system stability constraints, Structural and Multidisciplinary Optimization 11 (3) (1996) 213–217.

[139] M. Neves, H. Rodrigues, J. Guedes, Generalized topology design of structures with a buckling load criterion, Structural and Multidisciplinary Optimization 10 (2) (1995) 71–78.

[140] M. P. Bendsøe, O. Sigmund, Topology optimization by distribution of isotropic material, in: Topology Optimization, Springer, 2004, pp. 1–69.

[141] D. Ritchie, J. Rhodes, Buckling and post-buckling behaviour of plates with holes, The Aeronautical Quarterly 26 (4) (1975) 281–296.

[142] S. Min, N. Kikuchi, Optimal reinforcement design of structures under the buckling load using the homogenization design method, Structural Engineering and Mechanics 5 (5) (1997) 565–576.

[143] H.-C. Cheng, K.-N. Chiang, T.-Y. Chen, Optimal configuration design of elastic structures for stability, in: High Performance Computing in the Asia-Pacific Region, 2000. Proceedings. The Fourth International Conference/Exhibition on, Vol. 2, IEEE, 2000, pp. 1112–1117.

[144] M. Zhou, Topology optimization for shell structures with linear buckling responses, WCCM VI, Beijing, China (2004) 5–10.

[145] B.-c. Bian, Y.-k. Sui, Topology optimization of continuum structures under buckling and displacement constraints, in: Information Technology and Computer Science, 2009. ITCS 2009. International Conference on, Vol. 2, IEEE, 2009, pp. 417–420.

[146] X. Guo, G. Cheng, N. Olhoff, Optimum design of truss topology under buckling constraints, Structural and Multidisciplinary Optimization 30 (3) (2005) 169–180.

[147] D. Bojczuk, Z. Mróz, Optimal topology and configuration design of trusses with stress and buckling constraints, Structural optimization 17 (1) (1999) 25–35.

[148] J. D. Deaton, R. V. Grandhi, A survey of structural and multidisciplinary continuum topology optimization: post 2000, Structural and Multidisciplinary Optimization 49 (1) (2014) 1–38.

[149] J. L. de Lagrange, Sur la figure des colonnes, Miscellanea Taurinensia V (1770-1773) 123.

[150] T. Clausen, Uber die form architektonischer saulen, Bulletin physieo-mathematiques el Astronumiques 1 (1849-1853) 279–294.

[151] J. B. Keller, The shape of the strongest column, Archive for Rational Mechanics and Analysis 5 (1) (1960) 275–285.
doi:10.1007/BF00252909.

[152] E. Nikolai, The Lagrange problem on optimal shape of a column, izv, St.-Petersbourg Politechn. Inst. VIII (1) (1907) 255–288.

[153] I. Tadjbakhsh, J. Keller, Strongest columns and isoperimetric inequalities for eigenvalues, Journal of Applied Mechanics 29 (1) (1962) 159–164.

[154] N. Olhoff, S. H. Rasmussen, On single and bimodal optimum buckling loads of clamped columns, International Journal of Solids and Structures 13 (7) (1977) 605 – 614.
doi:https://doi.org/10.1016/0020-7683(77)90043-9.

[155] A. Seyranian, On a problem of Lagrange, Mechanics of Solids 19 (2) (1984) 100–111.

[156] A. Seyranian, O. Privalova, The Lagrange problem on an optimal column: old and new results, Structural and multidisciplinary optimization 25 (5-6) (2003) 393–410.

[157] E. Masur, Optimal structural design under multiple eigenvalue constraints, International Journal of Solids and Structures 20 (3) (1984) 211–231.

[158] N. Olhoff, A. P. Seyranian, Bifurcation and post-buckling analysis of bimodal optimum columns, International Journal of Solids and Structures 45 (14-15) (2008) 3967–3995.

[159] W. Szyszkowski, L. Watson, Optimization of the buckling load of columns and frames, Engineering Structures 10 (4) (1988) 249–256.

[160] D. Manickarajah, Y. Xie, G. Steven, Optimisation of columns and frames against buckling, Computers & Structures 75 (1) (2000) 45 – 54.
doi:https://doi.org/10.1016/S0045-7949(99)00082-6.

[161] K. Y. Maalawi, Buckling optimization of flexible columns, International Journal of Solids and Structures 39 (23) (2002) 5865–5876.

[162] W. Spillers, R. Levy, Optimal design for plate buckling, Journal of Structural Engineering 116 (3) (1990) 850–858.

[163] M. D. Pandey, A. N. Sherbourne, Mechanics of shape optimization in plate buckling, Journal of Engineering Mechanics 118 (6) (1992) 1249–1266.

[164] R. Levy, V. Sokolinsky, Prebuckling optimal design of orthotropic variable thickness plates for inplane loading, Structural Optimization 9 (2) (1995) 96–104.
doi:10.1007/BF01758826.
URL https://doi.org/10.1007/BF01758826

[165] P.-L. Larsson, On buckling of orthotropic compressed plates with circular holes, Composite Structures 7 (2) (1987) 103–121.

[166] M. P. Nemeth, Buckling and postbuckling behavior of compression-loaded isotropic plates with cutouts, AIAA Journal 29 (2) (1991) 313–314.

[167] N. Buckney, S. Green, A. Pirrera, P. M. Weaver, On the structural topology of wind turbine blades, Wind Energy 16 (4) (2013) 545–560.

[168] J. Stegmann, E. Lund, Discrete material optimization of general composite shell structures, International Journal for Numerical Methods in Engineering 62 (14) (2005) 2009–2027.

[169] E. Lund, Buckling topology optimization of laminated multi-material composite shell structures, Composite Structures 91 (2) (2009) 158–167.

[170] Z. Wu, P. M. Weaver, G. Raju, B. C. Kim, Buckling analysis and optimisation of variable angle tow composite plates, Thin-Walled Structures 60 (2012) 163 – 172.
doi:https://doi.org/10.1016/j.tws.2012.07.008.

[171] B. Bochenek, K. Tajs-Zielińska, Minimal compliance topologies for maximal buckling load of columns, Structural and Multidisciplinary Optimization 51 (5) (2015) 1149–1157.

[172] C. Liu, J. Taylor, Optimal design of columns., AIAA Journal 6 (8) (1968) 1497–1502.

[173] B. Bochenek, K. Tajs-Zielińska, Novel local rules of cellular automata applied to topology and size optimization, Engineering Optimization 44 (1) (2012) 23–35.

[174] M. Ashby, Overview no. 92: materials and shape, Acta Metallurgica et Materialia 39 (6) (1991) 1025–1039.

[175] P. Weaver, M. Ashby, Material limits for shape efficiency, Progress in Materials Science 41 (1-2) (1997) 61–128.

[176] H. Zhang, C. Wang, N. Challamel, E. Ruocco, Semi-analytical solutions for optimal design of columns based on hencky bar-chain model, Engineering Structures 136 (2017) 87–99.